

MAGNETIC RESONANCE IMAGING  
OF COLONIC FUNCTION

Elisa Placidi

Thesis submitted to the University of Nottingham  
for the degree of Doctor of Philosophy

---

July 2011

# Contents

<b>Abstract</b>	<b>vi</b>
<b>List of publications</b>	<b>viii</b>
<b>Acknowledgments</b>	<b>xiii</b>
<b>Abbreviations</b>	<b>xiv</b>
<b>1 Introduction</b>	<b>1</b>
1.1 Thesis overview . . . . .	2
<b>2 Nuclear Magnetic Resonance</b>	<b>5</b>
2.1 Introduction . . . . .	5
2.2 NMR basic principles . . . . .	6
2.2.1 Atomic structure and MR active nuclei . . . . .	6
2.2.2 Boltzmann statistics . . . . .	6
2.2.3 Precession and Larmor frequency . . . . .	7
2.2.4 Resonance and MR signal . . . . .	8
2.2.5 Relaxation . . . . .	10
2.2.6 Relaxometry . . . . .	16
2.2.7 Chemical shift . . . . .	19
2.2.8 Susceptibility . . . . .	19
2.2.9 Contrast agents . . . . .	21

---

<b>3</b>	<b>Magnetic Resonance Imaging</b>	<b>24</b>
3.1	Introduction . . . . .	24
3.2	Gradients . . . . .	24
3.3	Slice selection . . . . .	26
3.4	In plane spatial encoding . . . . .	28
3.4.1	Frequency encoding . . . . .	28
3.4.2	Phase encoding . . . . .	30
3.5	k-space . . . . .	31
3.6	Gradient echo sequence . . . . .	32
3.7	Spin echo . . . . .	35
3.8	Echo planar imaging . . . . .	35
3.9	Fast spin echo . . . . .	38
3.10	Fast imaging in the steady state . . . . .	40
3.10.1	Fast field echo . . . . .	41
3.10.2	Balanced turbo field echo . . . . .	43
3.11	Image contrast . . . . .	44
3.12	Artifacts . . . . .	45
3.12.1	Image acquisition related . . . . .	45
3.12.2	Patient-related . . . . .	47
3.12.3	Gradient-related . . . . .	48
3.12.4	Magnetic susceptibility . . . . .	48
<b>4</b>	<b>Instrumentation</b>	<b>50</b>
4.1	Introduction . . . . .	50
4.2	Main magnet . . . . .	50
4.3	Shim coils . . . . .	52
4.4	Gradient coils . . . . .	52
4.5	RF coils . . . . .	53
4.5.1	Body coil . . . . .	53
4.5.2	Fluorine coil . . . . .	54

4.6	Safety . . . . .	55
<b>5</b>	<b>MRI of the gastrointestinal tract</b>	<b>59</b>
5.1	The gastrointestinal tract . . . . .	60
5.1.1	Anatomy and physiology of the gastrointestinal tract . .	60
5.1.2	Definition of colon regions . . . . .	64
5.1.3	Colonic motility and transit . . . . .	65
5.1.4	Colon disorders . . . . .	66
5.2	Functional MRI of the GI tract . . . . .	67
5.2.1	Measuring gastric volume . . . . .	68
5.2.2	Measuring small bowel water content . . . . .	68
<b>6</b>	<b>Methods for measuring physiology of the colon</b>	<b>71</b>
6.1	Introduction . . . . .	71
6.2	Colonic response to an experimental model of human diarrhoeal disease . . . . .	72
6.2.1	Introduction . . . . .	72
6.2.2	Methods . . . . .	73
6.2.3	Results . . . . .	75
6.2.4	Discussion and conclusions . . . . .	80
6.3	Measuring the $T_1$ and $T_2$ of the colonic contents in vitro . . . . .	84
6.3.1	Introduction . . . . .	84
6.3.2	Methods . . . . .	84
6.3.3	Results . . . . .	85
6.3.4	Discussion and conclusion . . . . .	86
6.4	Defining the characteristics of the ascending colon contents . . .	88
6.4.1	Introduction . . . . .	88
6.4.2	Methods . . . . .	88
6.4.3	Results . . . . .	106
6.4.4	Discussion . . . . .	115

<b>7</b>	<b>MRI of pharmacological interventions in the colon</b>	<b>117</b>
7.1	Introduction . . . . .	117
7.2	Novel insights into the mechanisms of action of Metamucil . . .	119
7.2.1	Introduction . . . . .	119
7.2.2	Method . . . . .	119
7.2.3	Results . . . . .	121
7.2.4	Discussion and conclusion . . . . .	122
7.3	Defining the mode of action of loperamide and loperamide plus simethicone using an MRI model of acute diarrhoea . . . . .	128
7.3.1	Introduction . . . . .	128
7.3.2	Method . . . . .	131
7.3.3	Results . . . . .	135
7.3.4	Discussion and conclusion . . . . .	151
<b>8</b>	<b>Using markers to measure GI transit</b>	<b>154</b>
8.1	Fluorine MRI . . . . .	156
8.2	Compounds for human $^{19}\text{F}$ MRI . . . . .	157
8.2.1	Perfluorocarbons . . . . .	158
8.2.2	Potential $^{19}\text{F}$ markers for GI transit . . . . .	162
8.3	In vitro tests of fluorinated compounds . . . . .	173
8.3.1	High resolution MRS . . . . .	173
8.3.2	$T_1$ and $T_2$ of PFOB . . . . .	177
8.3.3	Susceptibility of PFOB . . . . .	178
8.4	$^{19}\text{F}$ coil characterisation . . . . .	180
8.4.1	Methods . . . . .	180
8.4.2	Results . . . . .	181
8.5	Capsules for GI transit studies . . . . .	184
8.5.1	Methods . . . . .	184
8.5.2	Results . . . . .	190
8.5.3	Conclusion . . . . .	193

8.6	GI transit in vivo study with the use of fluorinated markers . . .	194
8.6.1	Introduction . . . . .	194
8.6.2	Method . . . . .	194
8.6.3	Results . . . . .	195
8.6.4	Discussion and conclusion . . . . .	196
8.7	GI transit time using double-labelled markers . . . . .	198
8.7.1	In vitro test: finding the optimal Gd concentration . . .	198
8.7.2	In vivo pilot study . . . . .	200
8.7.3	Discussion . . . . .	204
8.8	Studying the GI transit time using double-labelled markers: mode of action of Moviprep . . . . .	207
8.8.1	Introduction . . . . .	207
8.8.2	Methods . . . . .	208
8.8.3	Results . . . . .	208
8.8.4	Discussion and conclusion . . . . .	214
8.9	Optimisation of the GI transit markers . . . . .	217
8.9.1	Introduction . . . . .	217
8.9.2	Methods . . . . .	217
8.9.3	Results . . . . .	218
8.9.4	Discussion and conclusion . . . . .	219
<b>9</b>	<b>Conclusions</b>	<b>221</b>
<b>A</b>	<b>Standard operating procedure for the capsules manufacture for in vivo studies</b>	<b>224</b>
A.1	Manufacture of the capsules . . . . .	224
A.2	Preparation of the capsules for in vivo studies . . . . .	226
A.3	Leakage test with the spectrophotometer . . . . .	229

**Bibliography**

**230**

# Abstract

The overall aim of this work was to develop MRI methods and techniques to study the physiology and the pathology of the gastrointestinal tract, with particular attention to the colon. Besides, the development of new methods was aimed in order to perform quantitative analysis using proton and fluorine MRI. In particular the first experimental chapter describes the development and the optimisation of imaging protocols for studying colonic function in undisturbed physiologically relevant conditions. In addition a texture analysis method based on Gabor filters is developed and used for the objective assessment of colonic content characteristics. The mechanisms of action of common anti-diarrhoeal and anti-constipation agents are also investigated. The last experimental chapter describes the development of methods for using markers to measure GI transit. Transit time, i.e. the time it takes for a marker to pass through the entire gut, is often affected by functional gastrointestinal disorders, therefore it is of primary importance to develop a non invasive and effective technique for the diagnosis of such gastrointestinal diseases. The use of fluorinated agents and its many advantages compared to other techniques is outlined and the first in vivo studies at high field are presented. The use of gadolinium based compounds as an additional marker is also discussed.

# List of publications

## Articles in journals

“Epid cine acquisition mode for in vivo dosimetry in dynamic arc radiation therapy”

*A. Fidanzio, A. Mameli, **E. Placidi**, F. Greco, G. Stimato, D. Gaudino, S. Ramella, R. D'Angelillo, F. Cellini, L. Trodella, S. Cilla, L. Grimaldi, G. D'Onofrio, L. Azario and A. Piermattei*

Nuclear Instruments and Methods in Physics Research B 266 658–666  
(2008) Impact factor 1.156

“Dynamic conformal arc therapy: Transmitted signal in vivo dosimetry”

*A. Piermattei, G. Stimato, D. Gaudino, S. Ramella, R.M. D'Angelillo, F. Cellini, L. Trodella, G. D'Onofrio, L. Grimaldi, S. Cilla, A. Fidanzio, **E. Placidi**, L. Azario*

MEDICAL PHYSICS 35 Issue: 5 1830–1839 (2008) Impact factor 2.704

“The effects of fasting and refeeding with a 'metabolic preconditioning' drink on substrate reserves and mononuclear cell mitochondrial function”

*S. Awad, M C Stephenson, **E. Placidi**, L. Marciani, D. Constantin-Teodosiu, P. A. Gowland, R C Spiller, K. C. H. Fearon, P. G. Morris, I. A. Macdonald, D. N. Lobo*

Clinical Nutrition, Volume 29, Issue 4, August 2010, Pages 538–544 Impact factor 3.274 P103

“The effects of fasting and refeeding with a ‘metabolic preconditioning’ drink on substrate reserves and mononuclear cell mitochondrial function: potential mechanisms by which preoperative feeding improves insulin sensitivity”

*S. Awad, M.C. Stephenson, E. Placidi, L. Marciani, D. Constantin-Teodosiu, P.A. Gowland, R.C. Spiller, K.C.H. Fearon, P.G. Morris, I.A. Macdonald, D.N. Lobo*

Clinical Nutrition Supplements, Volume 4, Issue 2, 2009, Page 69 Impact factor 3.274 PTH–045

“Effects of an osmotic laxative on the distribution of water between the small and large intestine in humans

*E. Placidi, C. L. Hoad, L. Marciani, P. A. Gowland and R. C. Spiller*

GUT 4, Volume 59, Supplement 1, page A141 (2010) Impact factor 9.357 S1303

“An Experimental Model of Diarrheal Disease: A Magnetic Resonance Imaging Study in Healthy Humans

*E. Placidi, C. L. Hoad, L. Marciani, P. A. Gowland and R. C. Spiller*

Gastroenterology, Volume 138, Issue 5, Supplement 1, May 2010, Pages S–224 Impact factor 12.899

## Articles in peer reviewed conferences

“High resolution imaging of the colonic contents under physio-pathological conditions

*E. Placidi, C.L. Hoad, L. Marciani, E.F. Cox, S. Pritchard, C. Costigan, R.C. Spiller and P.A. Gowland*

British Chapter of ISMRM 2008 3–5 September, Newcastle, UK

“MRI assessment of the water distribution in the ascending colon in health and a model of diarrhoeal disease

*E. Placidi, C.L. Hoad, L. Marciani, E.F. Cox, S. Pritchard, C. Costigan, R.C. Spiller and P.A. Gowland*

ISMRM 2009 17th Annual Scientific Meeting and Exhibition 18–24 April, Honolulu, USA

“A Dynamic Study of Changes in Hepatic and Skeletal Muscle Lipid and Glycogen Levels, Due to 24h Starvation and Re-Feeding: A <sup>1</sup>H and <sup>13</sup>C MRS Study

*M. C. Stephenson, S. Awad, E. Placidi, L. Marciani, K. C. H. Fearon, I. A. Macdonald, R. C. Spiller, P. A. Gowland, P. G. Morris and D. N. Lobo*

ORAL PRESENTATION at the ISMRM 2009 17th Annual Scientific Meeting and Exhibition 18–24 April, Honolulu, USA

“Colonic response to feeding in health and a model of diarrhoeal disease

*E. Placidi, C.L. Hoad, L. Marciani, E.F. Cox, S. Pritchard, C. Costigan, R.C. Spiller and P.A. Gowland*

ORAL PRESENTATION at the British Chapter of ISMRM 2009 2–4 September, Cardiff, UK

“Magnetic resonance imaging assessment of the water distribution in the ascending colon in a model of diarrhoeal disease

*E. Placidi, L. Marciani, C. L. Hoad, E. F. Cox, S. Pritchard, C. Costigan, P. A. Gowland and R. C. Spiller*

GASTRO 2009 21–25 November, London, UK

“Colonic response to an experimental model of human diarrhoeal disease

*E. Placidi, C.L. Hoad, L. Marciani, R.C. Spiller and P.A. Gowland*

ISMRM 2010 18th Annual Scientific Meeting and Exhibition 1–7 May, Stockholm, Sweden

“Characterising a coil/sample system for monitoring GI transit using fluorine markers

*E. Placidi, R.C. Spiller and P.A. Gowland*

ISMRM 2010 18th Annual Scientific Meeting and Exhibition 1–7 May, Stockholm, Sweden

“MRI and MRS monitoring of gastrointestinal distribution, physiological effects and absorption of fat emulsions

*M.O. Hussein, L. Marciani, M.C. Stephenson, C.L. Hoad, E.F. Cox, E. Placidi, S. Pritchard, H. Ribeiro, E. Ciampi, P. Rayment, A. Nandi, N. Hedges, P. Sanderson, I. Kruse, R.C. Spiller and P.A. Gowland*

ISMRM 2010 18th Annual Scientific Meeting and Exhibition 1–7 May, Stockholm, Sweden

“An experimental model of diarrheal disease: a magnetic resonance imaging study in health humans

*E. Placidi, C. L. Hoad, L. Marciani, P. A. Gowland and R. C. Spiller*

DDW ANNUAL MEETING 1–5 May 2010, New Orleans, LA, USA

“Loperamide and loperamide plus simethicone reduce net secretion in a mannitol model of acute diarrhea as shown by magnetic resonance imaging

*E. Placidi, L. Marciani, C.L. Hoad, K. Garsed, S. Pritchard, C. Costigan, R.C. Spiller and P.A. Gowland*

British Chapter of ISMRM 2008 1–3 September, Nottingham, UK

“Loperamide and loperamide plus simethicone reduce net secretion in a mannitol model of acute diarrhea as shown by magnetic resonance imaging

*K. Garsed, E. Placidi, L. Marciani, C. Hoad, S. Pritchard, C. Costigan, P. Gowland, R. Spiller*

ORAL PRESENTATION at the UEGW 23–27 October 2010, Barcelona, Spain

# Acknowledgments

I would like to thank all those who have helped me in the course of my PhD project. In particular my supervisor Prof. Penny Gowland for her invaluable help and support, Dr. Luca Marciani and Dr. Caroline Hoad for their guidance throughout these years and Prof. Robin Spiller for his precious assistance for all my experiments. A big thank you also to Dr Klara Garsed, Dr. Eleanor Cox, Mrs Sue Pritchard and everyone who helped with the projects. Of course, a big thank you to Mr Ian Thexton for being so helpful with the capsules manufacturing. I would like to thank all the volunteers and all my colleagues at the SPMRC. I would also like to acknowledge all my friends in Nottingham and back home and of course my family for their support. Last but not least I thank my husband: this work is dedicated to him.

# Abbreviations

<b>AC</b>	Ascending Colon
<b>ACWC</b>	Ascending Colon Water Content
<b>ANOVA</b>	ANalysis Of VARIance
<b>BMI</b>	Body Mass Index
<b>BOLD</b>	Blood Oxygenation Level Dependent
<b>bTFE</b>	balanced Turbo Field Echo
<b>CPMG</b>	Carr-Purcell Meiboom-Gill
<b>CSF</b>	Cerebral Spin Fluid
<b>CSI</b>	Chemical Shift Imaging
<b>CT</b>	Computed Tomography
<b>CV</b>	Coefficient of Variation
<b>DC</b>	Descending Colon
<b>EPI</b>	Echo planar imaging
<b>ETL</b>	Echo Train Length
<b>FDA</b>	Food and Drug Administration
<b>FFE</b>	Fast Field Echo
<b>FID</b>	Free Induction Decay
<b>FISP</b>	Fast Imaging with Steady Precession
<b>FLASH</b>	Fast Low Angle SHot
<b>FOV</b>	Field Of View
<b>FSE</b>	Fast Spin Echo
<b>FT</b>	Fourier Transform

---

<b>Gd</b>	Gadolinium
<b>GE</b>	Gradient Echo
<b>GI</b>	GastroIntestinal
<b>GLCM</b>	Grey Level Co-occurrence Matrix
<b>GRASS</b>	Gradient Recalled Acquisition in Steady State
<b>HASTE</b>	Half fourier Acquisition Single shot Turbo spin Echo
<b>HFB</b>	HexaFluoroBenzene
<b>IBS</b>	Irritable Bowel Syndrome
<b>ICJ</b>	Ileo-Caecal Junction
<b>IR</b>	Inversion Recovery
<b>LIBSVM</b>	LIBrary for Support Vector Machine
<b>MIP</b>	Maximum Intensity Projection
<b>MRI</b>	Magnetic Resonance Imaging
<b>MRS</b>	Magnetic Resonance Spectroscopy
<b>(N)MR</b>	(Nuclear) Magnetic Resonance
<b>NSA</b>	Number of Signal Averages
<b>PFC(s)</b>	PerFluoroCarbon(s)
<b>PFOB</b>	PerFluoroOctyl Bromide
<b>POM</b>	PolyOxyMethylene
<b>PNS</b>	Peripheral Nerve Stimulation
<b>pO<sub>2</sub></b>	partial oxygen pressure
<b>ppm</b>	parts per million
<b>RARE</b>	Rapid Acquisition with Relaxation Enhancement
<b>RBF</b>	Radial Basis Function
<b>RF</b>	Radio Frequency
<b>ROI</b>	Region Of Interest

<b>SAR</b>	Specific Absorption Rate
<b>SB</b>	Small Bowel
<b>SBWC</b>	Small Bowel Water Content
<b>SE</b>	Spin Echo
<b>SNR</b>	Signal to Noise Ratio
<b>SOP</b>	Standard Operating Procedure
<b>SPGR</b>	SPOiled Gradient Recalled echo
<b>STIR</b>	Short TI Inversion recovery
<b>SVM</b>	Support Vector Machine
<b>TC</b>	Transverse Colon
<b>TMS</b>	TetraMethylSilane
<b>TSE</b>	Turbo Spin Echo

# Chapter 1

## Introduction

Magnetic Resonance Imaging (MRI) has been rapidly expanding since its introduction in the 1970's with the first papers from Mansfield [1] and Lauterbur [2]. Several developments were made in the following years and it is now a well established medical imaging technique which provides a wide range of image contrasts. The main advantage compared to other imaging techniques is the absence of ionizing radiation and its non invasive character.

MRI of the gastrointestinal (GI) tract was initially very limited for various reasons. Firstly, the anatomy of the GI tract presents a very complex three-dimensional structure which is very variable between individuals and it also varies within the same subject according to the fed or fasted state and physical activity. Secondly, respiration and peristaltic movements lead to partial volume artifacts and blurring. With the advent of fast MR imaging, these problems have been overcome [3, 4]. Therefore it is now possible to use this technique for studying the physiology and the pathology of the GI tract. Despite all this, very little work has been published on colonic function. In particular, symptoms of colonic dysfunction such as diarrhoea and constipation are very common in the general population leading to a substantial social and economic impact [5, 6]. Hence, the interest in understanding such mechanisms

and their possible treatment is continuously growing.

## 1.1 Thesis overview

The overall aim of this work was to develop MRI methods and techniques to study the physiology and the pathology of the gastrointestinal tract, with particular attention to the colon. Besides, the development of new methods was aimed in order to perform quantitative analysis using proton and fluorine MRI.

The first chapters introduce the background theory of nuclear magnetic resonance (chapter 2) and magnetic resonance imaging (chapter 3). Definitions of the main terms and the key basic physics concepts are outlined and the principal MRI sequences used in this work are introduced.

Chapter 4 describes the main hardware components of an MR system with particular attention to the equipment used for the experiments performed in this thesis.

An overview of the anatomy and physiology of the gastrointestinal tract is given in chapter 5, in which MRI of the GI tract is also introduced.

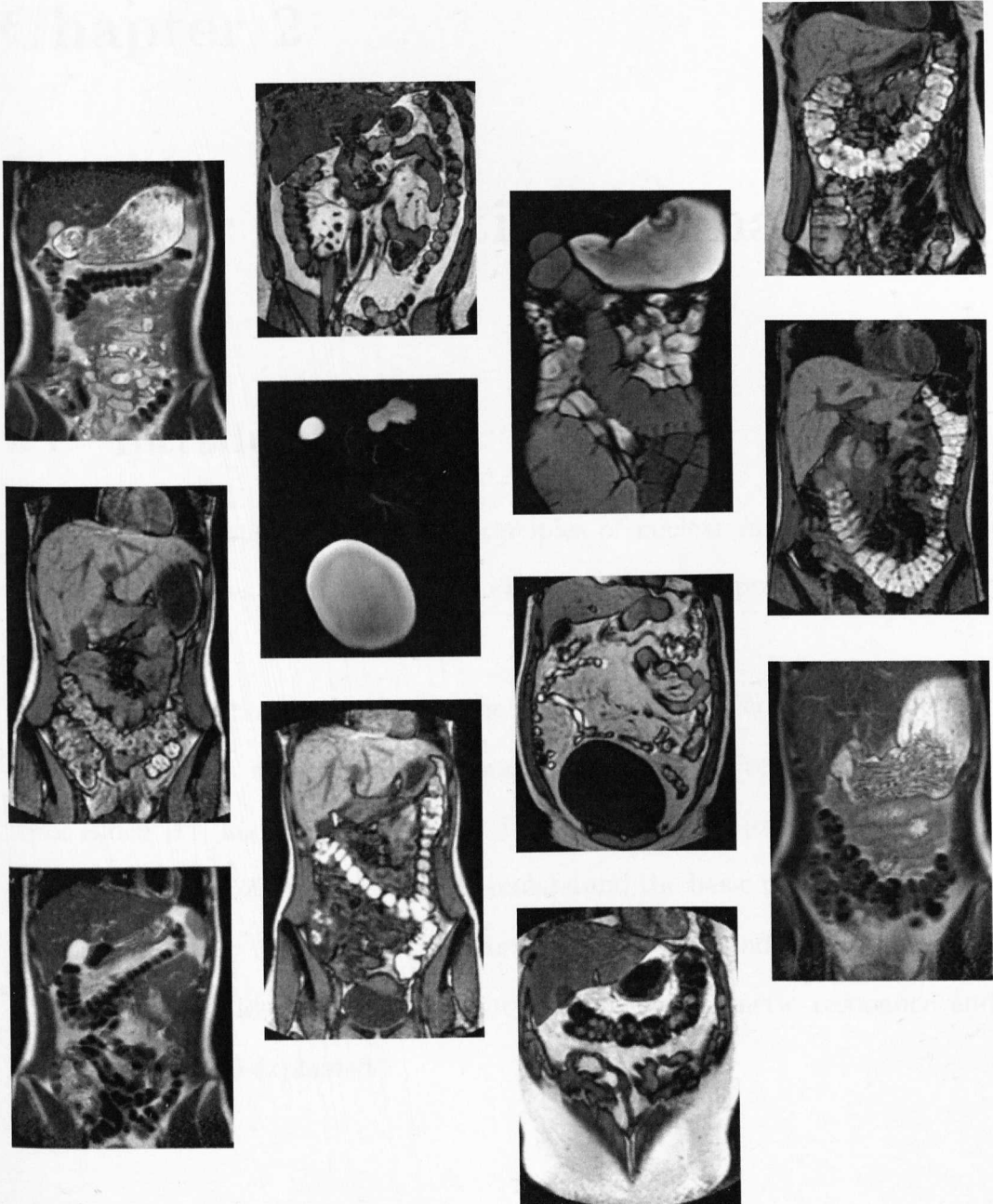
Chapters 6, 7 and 8 are the experimental chapters of this thesis.

Chapter 6 describes the development and the optimisation of imaging protocols for the GI tract and in particular for studying colonic function in undisturbed physiologically relevant conditions. In particular the colonic response to an experimental model of human diarrhoeal disease is presented. The chapter includes the development of a texture analysis method based on Gabor filters, used for the objective assessment of colonic content characteristics.

The methods developed and optimised in chapter 6 are then applied to pharmacological interventions in the colon. In particular, the mechanisms of action of common anti-diarrhoeal and anti-constipation agents are investigated (chapter 7).

The last experimental chapter (chapter 8) describes the development of methods for using markers to measure GI transit. Transit time, i.e. the time it takes for a marker to pass through the entire gut, is often affected by functional gastrointestinal disorders, therefore it is of primary importance to develop a non invasive and effective technique for the diagnosis of such gastrointestinal diseases. The use of fluorinated agents and its many advantages compared to other techniques is outlined and the first in vivo studies at high field are presented. The use of gadolinium based compounds as an additional marker is also discussed.

A general summary of the results of this work together with the future plan are outlined in chapter 9.



# Chapter 2

## Nuclear Magnetic Resonance

### 2.1 Introduction

This chapter outlines the basic principles of nuclear magnetic resonance (NMR) which have been extensively studied and are reported in numerous texts [7–10].

The NMR phenomenon refers to the interaction of nuclei with spin angular momentum with a magnetic field. It was independently discovered in 1946 by Felix Bloch [11] and Edward Purcell [12] and they were jointly awarded the Nobel Prize in 1952. In order to fully understand the basic principles of NMR it is important to understand the properties of atoms and their interaction with magnetic fields. The basic theory of nuclear magnetic resonance and relaxation are also explained.

## 2.2 NMR basic principles

### 2.2.1 Atomic structure and MR active nuclei

The atomic structure includes a central nucleus that contains nucleons (protons and neutrons) and orbiting electrons. The electrons are negatively charged, protons are positively charged while neutrons have no net charge. The electrons, protons and neutrons all also have a quantum mechanical property of spin. The neutrons and protons couple within a nucleus so that a nucleus with an odd number of protons and neutrons has a net spin.

Because of the electromagnetic induction law, charged nuclei that are spinning acquire a magnetic moment. These nuclei have the property of having net spin and being able to align their axis of rotation to an external magnetic field when applied. This alignment can be expressed as a vector sum of all the nuclear magnetic moments and it is specific for each nucleus, thus giving a specific NMR sensitivity.

Table 2.1 gives a selection of MR active nuclei that are commonly used in NMR together with their main properties.

### 2.2.2 Boltzmann statistics

If we consider a real system consisting of an ensemble of nuclear spins as, for example, in a sample of water, the hydrogen nuclei will be randomly oriented and the total magnetic moment of the sample will be zero. When a magnetic field is applied the magnetic moments will align with this magnetic field.

According to the quantum mechanics, hydrogen nuclei have two energy states: the low energy states, where the nuclear magnetic moments align parallel to the magnetic field (spin up) and the high energy states, for which the magnetic moments are antiparallel (spin down). In thermal equilibrium there will be more nuclei in the lower energy state thus meaning that there is a total

Isotope	Nuclear Spin	$\gamma/2\pi$ (rad/s/T)	Natural Abundance (%)
<sup>1</sup> H	1/2	267.52	99.9
<sup>13</sup> C	1/2	67.28	1.1
<sup>14</sup> N	1	19.34	99.6
<sup>23</sup> Na	3/2	70.81	100
<sup>19</sup> F	1/2	251.81	100
<sup>31</sup> P	1/2	108.39	100

Table (2.1): Properties of some nuclear isotopes used for magnetic resonance [7].

net magnetic moment parallel to the external magnetic field (see figure 2.1).

The distribution of the spins between the two different energy levels can be described with the Boltzmann statistics:

$$\frac{N_{\beta}}{N_{\alpha}} = e^{-\frac{\Delta E}{kT}} \quad (2.1)$$

where  $N_{\alpha}$  and  $N_{\beta}$  are the number of nuclei in the lower and higher energy states respectively,  $k$  is the Boltzmann constant ( $1.38 \times 10^{-23}$  J/K) and  $T$  is the temperature. Equation 2.1 implies that the net magnetisation is higher for lower temperature and higher magnetic field strength. Since it is not possible to decrease the temperature of the sample for in vivo studies, the increase of magnetic field strength is desired to increase the signal to noise ratio of NMR experiments.

### 2.2.3 Precession and Larmor frequency

The hydrogen nuclei in the net magnetisation spin on their own axis and when an external magnetic field  $B_0$  is applied the torque on the magnetic

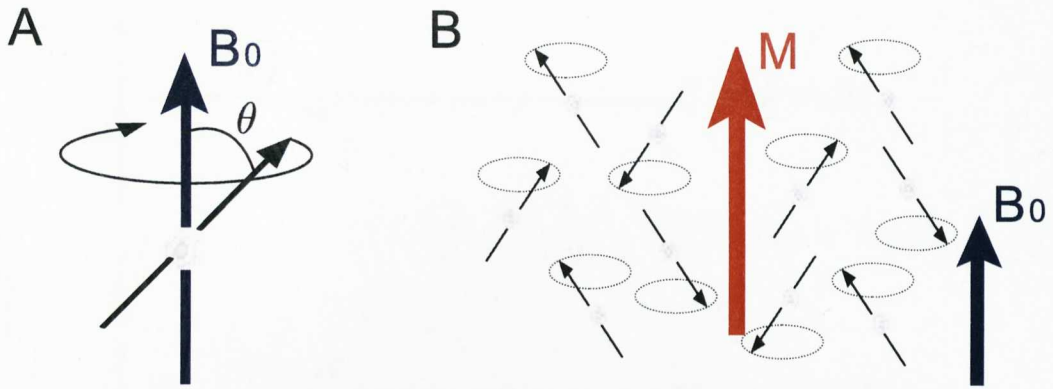


Figure (2.1): Illustration of the spin precession when an external magnetic field  $B_0$  is applied. At thermal equilibrium there is a total net magnetisation parallel to the magnetic field because more nuclei are in the lower energy state. Adapted from [13].

moment causes them to start precessing around the magnetic field axis at a specific frequency called the Larmor frequency, with a specific rotation angle,  $\theta$  that depends on the spin state. This phenomenon is called precession (figure 2.1).

The Larmor frequency,  $\omega_L$ , is given by

$$\omega_L = \gamma B_0 \quad (2.2)$$

where  $\gamma$  is the gyromagnetic ratio, typically described in units of rad/s, and it is a specific property of each nucleus (see table 2.1). The Larmor frequency has a defined sign indicating the direction of the spin precession. Most nuclei have a positive  $\gamma$  which means that the precession is clockwise. As the gyromagnetic ratio is a constant for a given nucleus, the precessional frequency of a nucleus depends on the magnetic field applied.

### 2.2.4 Resonance and MR signal

When a nucleus is exposed to an external perturbation it gains energy and it resonates if the energy is delivered at its precise precessional frequency. The precessional frequency of hydrogen at all field strengths used in clinical MRI

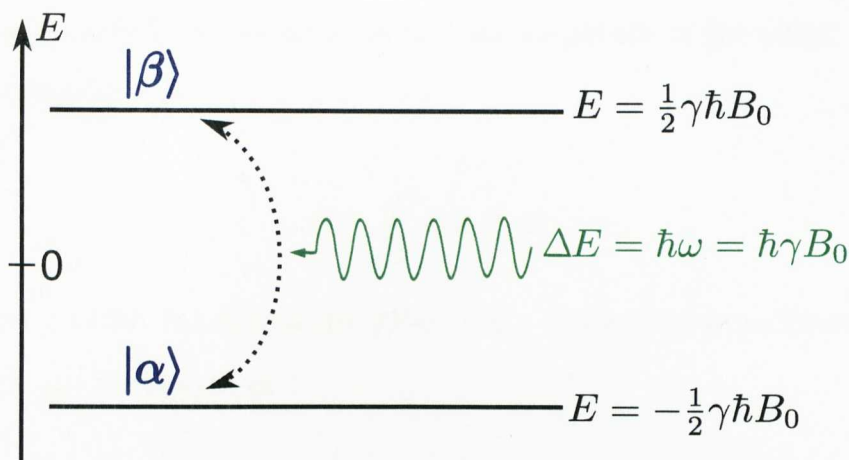


Figure (2.2): Illustration of the Zeeman splitting of the energy levels in the presence of an external magnetic field  $B_0$ . The transition between the two levels only happens when the energy equal to the Zeeman splitting  $\Delta E$  is applied.

correspond to the radiofrequency (RF) region of the electromagnetic spectrum. In order to induce a resonance of hydrogen nuclei in the matter a RF pulse of energy corresponding to the Larmor frequency must be applied. In that case, only hydrogen nuclei will be excited even if other MR active nuclei are aligned with the magnetic field because they have a different Larmor frequency. When the RF is applied, the nuclear spin state can change by the absorption of the energy that matches the Zeeman splitting  $\Delta E$  (figure 2.2), causing the transition to higher energy states.

The photon frequency  $\nu$  required for the transition to happen is given by the following equation

$$\nu = \frac{\Delta E}{h} = \frac{\gamma B_0}{2\pi} \quad (2.3)$$

where  $B_0$  is the static field.

In NMR the nuclei experience two different magnetic fields: the static magnetic field  $B_0$  and the oscillating RF field  $B_1(t)$  which is several orders of magnitude smaller than the static magnetic field. This RF pulse is fundamental in MR because it creates the MR signal: when  $B_1(t)$  is applied the net magnetisation moves out of alignment by an angle called the *flip angle*, whose

magnitude depends on the duration and the amplitude of the pulse. In fact, this equation applies

$$\alpha = \int_0^{\tau} \gamma B_1(t) dt \quad (2.4)$$

where  $\tau$  is the duration of the pulse. For a rectangular pulse envelope the flip angle can be defined as

$$\alpha = \gamma B_1 \tau \quad (2.5)$$

When the magnetisation is given enough energy by the RF pulse to tip through  $90^\circ$ , it is completely transferred into the transverse plane. By convention, "z" is the direction of the static magnetic field while the RF pulse is given in the "x" direction. As a result of resonance, the magnetisation is then flipped by an angle  $\alpha$  and is precessing in phase in the transverse plane. Magnetic moments are in phase when they are in the same place on the precessional path at the same time. The precession of the magnetisation in the transverse plane produces magnetic field fluctuations in that plane, so if a coil is placed in the area of that moving magnetic field, a voltage is induced in the coil as stated by the Faraday's law of induction. This voltage is the MR signal, whose frequency is the same as the Larmor frequency and whose magnitude depends on the amount of magnetisation precessing.

### 2.2.5 Relaxation

Once the RF pulse is turned off, the net magnetisation is still influenced by the static magnetic field  $B_0$ . The process of returning the net magnetisation to be aligned to  $B_0$  is called relaxation. During relaxation, the amount of magnetisation in the longitudinal plane gradually recovers (recovery) while the amount of magnetisation in the transverse plane decreases (decay). In

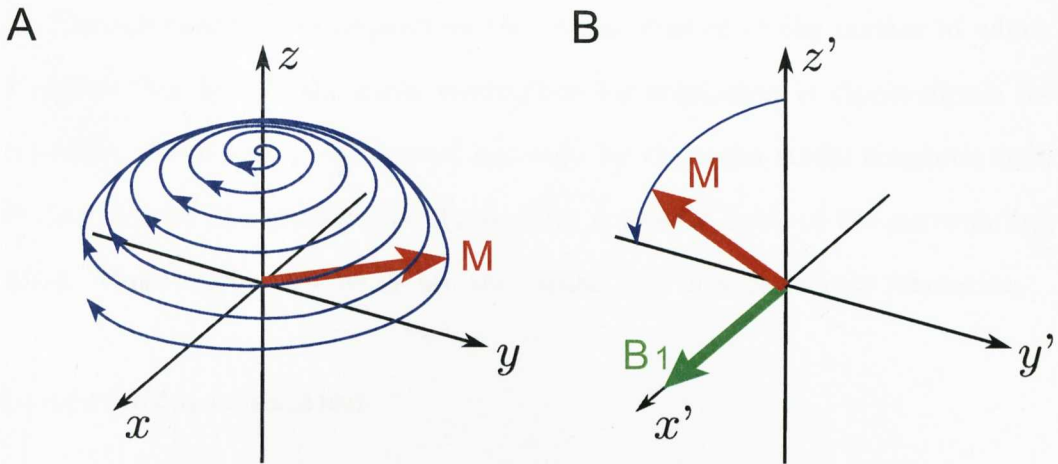


Figure (2.3): Illustration of the behaviour of the net magnetisation  $M$  in two different reference frames, the laboratory reference frame (a) and the rotating reference frame (b). When the RF pulse  $B_1$  is applied in the  $x$  direction, the magnetisation vector  $M$  spirals down to the transverse plane in the static frame, while in the rotating frame it appears as a one dimensional flip to the transverse plane.

order to describe this process it is useful to introduce a rotating reference frame. Since  $B_1$  and the net magnetisation  $M$  both rotate around the  $z$  axis (the direction of the  $B_0$  field) with the angular velocity  $\omega_L$ , a rotating frame will be chosen with the same angular velocity so that the  $B_1$  will appear static in that reference frame. So, by convention, the laboratory reference frame has coordinates  $(x, y, z)$  while the rotating reference frame has coordinates  $(x', y', z')$ .  $z$  and  $z'$  are considered equivalent. Figure 2.3 shows the effect of an RF pulse. While in the static laboratory system the magnetisation relaxes with a spiral motion, in the rotating system it draws a one-dimensional rotation back to the  $z$  direction.

The evolution of the magnetisation is described by the Bloch equation

$$\frac{d\mathbf{M}}{dt} = \gamma(\mathbf{M} \times \mathbf{B}) - \frac{(M_z - M_0)\mathbf{k}}{T_1} - \frac{M_x\mathbf{i} + M_y\mathbf{j}}{T_2} \quad (2.6)$$

where  $\mathbf{B}$  is the total applied magnetic field (superposition of  $B_0$  and  $B_1$  effects),  $T_1$  is the spin-lattice relaxation time describing the recovery of the longitudinal magnetisation and  $T_2$  is the spin-spin relaxation time describing the decay of the transverse magnetisation.

The relaxation rates depend on the characteristics of the matter in which it occurs: for liquids the main mechanism for relaxation is dipole-dipole interaction. Each spin is influenced not only by the main static magnetic field  $B_0$  but also by the microscopic fluctuating magnetic fields of the surrounding spins. These fluctuating fields are very small but they can cause relaxation.

### Longitudinal relaxation

The longitudinal or spin-lattice relaxation describes the mechanism of the spins' alignment returning back to the Boltzmann distribution values ( $M_z = M_0$ ) following the transfer of energy from the spins to the surrounding lattice. The behaviour of  $M_z$  in this process is described by

$$\frac{dM_z}{dt} = \frac{(M_0 - M_z)}{T_1} \quad (2.7)$$

$T_1$  is specific for different kinds of matter and depends on the magnetic field strength ( $B_0$ ): the higher the magnetic field strength the longer the  $T_1$  for the same matter. The most efficient energy transfer occurs from fluctuations of the dipole-dipole magnetic fields at the Larmor frequency. Water and solids do not transfer energy efficiently as they both have characteristic molecular motions with frequencies very different to Larmor frequency. On the contrary hydrogen protons in fat have a natural motion frequency very similar to the Larmor frequency thus giving a very high efficiency of energy transfer and short  $T_1$ . However, it has to be said that the hydrogen protons in the body are normally bound to macromolecules that reduce their motion thus producing a shortening of  $T_1$ . Solving equation 2.7 describing the behaviour of the longitudinal magnetisation from an initial state  $M_z(0)$  it is possible to write the following equation

$$M_z(t) = M_0(1 - e^{-t/T_1}) + M_z(0)e^{-t/T_1} \quad (2.8)$$

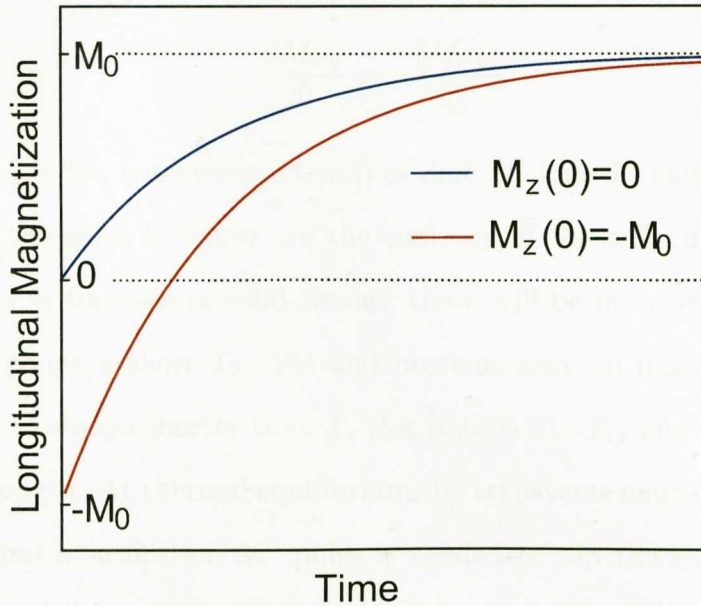


Figure (2.4): Longitudinal relaxation  $M_z(t)$  as a function of time for inversion recovery (red solid line) and saturation recovery (blue solid line) [13].

After a  $180^\circ$  inversion pulse the longitudinal magnetisation is inverted so  $M_z(0) = -M_0$  so the recovery follows an exponential curve given by

$$M_z(t) = M_0(1 - 2e^{-t/T_1}) \quad (2.9)$$

which is illustrated with the red line in figure 2.4.

Following a  $90^\circ$  RF pulse tipping the magnetisation to the x axis, the magnetisation is flipped into the transverse plane and the recovery curve, represented in blue in figure 2.4, is given by the so called saturation recovery curve

$$M_z(t) = M_0(1 - e^{-t/T_1}) \quad (2.10)$$

### Transverse relaxation

Transverse relaxation describes the short-range spin-spin interactions that produce the dephasing of the spins over time. The transverse component of the Bloch equation is given by

$$\frac{dM_{x,y}}{dt} = -\frac{M_{x,y}}{T_2} \quad (2.11)$$

where  $T_2$  is the transverse relaxation time. A long  $T_2$  means that the dephasing of the spins is slower, on the contrary, if the molecules have a rigid structure as in the case of solid tissues, there will be more spin-spin interactions thus giving a short  $T_2$ . Fat and proteins have an intermediate  $T_2$ . In general,  $T_2$  is always shorter than  $T_1$  (for liquids  $T_2=T_1$ ) and depends on the  $B_0$  field strength. At thermal equilibrium the transverse magnetisation is zero ( $M_{x,y}=0$ ) and a saturation  $90^\circ$  pulse is needed to flip the entire magnetisation in the xy plane. The signal decay after the saturation pulse follows the following exponential curve

$$M_{x,y}(t) = M_0(e^{-t/T_2}) \quad (2.12)$$

and is known as Free Induction Decay (FID).

The spin-spin dephasing is also driven by  $B_0$  field inhomogeneities and this effect produces a faster signal decay. In order to take into account this additional contribution, another relaxation time constant is introduced:  $T_2^*$  depends on both the molecular interactions and the  $B_0$  variations and is given by

$$\frac{1}{T_2^*} = \frac{1}{T_2} + \frac{1}{T_2'} \quad (2.13)$$

where  $T_2'$  describes the effect of  $B_0$  inhomogeneities.  $T_2^*$  is always smaller than  $T_2$  and it generally shortens when  $B_0$  increases due to the increased susceptibility effects. The decay of the transverse magnetisation is illustrated in figure 2.5.

As already stated, the transverse magnetisation of the precessing spins produces a detectable electromotive force that is detected by a receiving coil

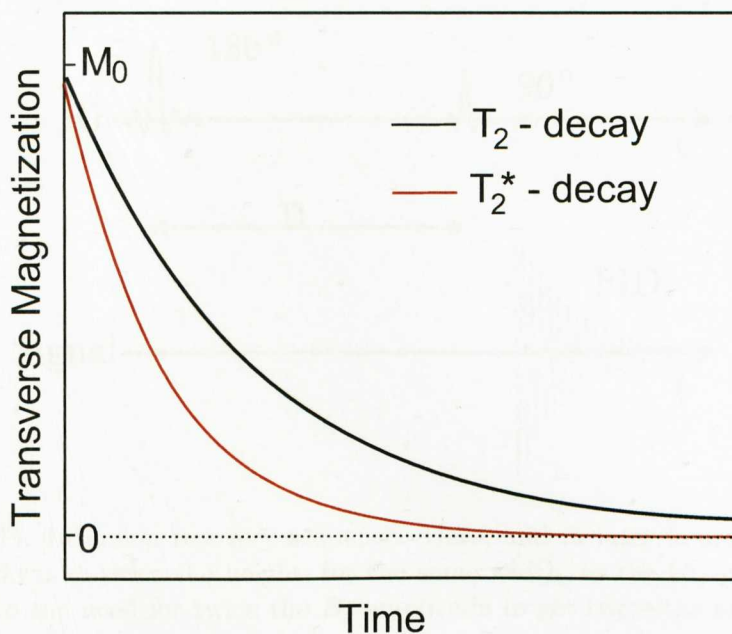


Figure (2.5): Transverse magnetisation decay over time: the combined time constant  $T_2^*$  describes a faster decay as it takes into consideration both the sample interactions and the external magnetic field inhomogeneities.

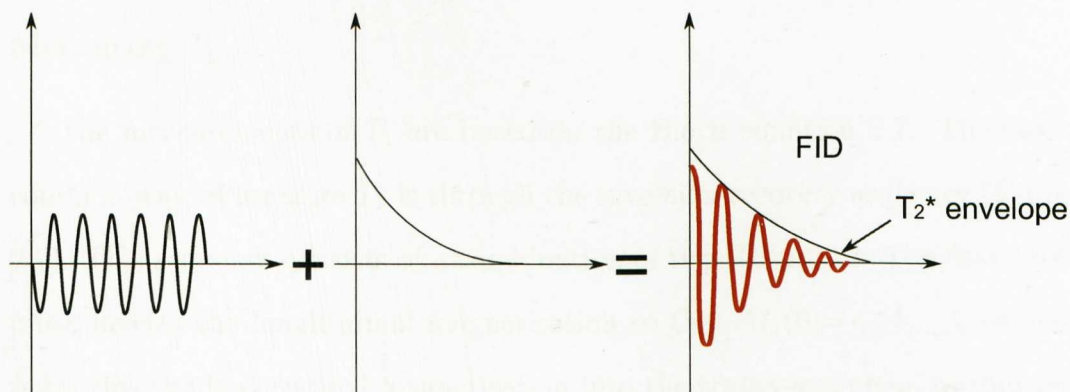


Figure (2.6): Illustration of the FID decay over time showing the  $T_2^*$  effect: the product of a sinusoidal signal and an exponentially decaying signal results in a decaying sinusoidal signal.

in the transverse plane. Once the RF pulse is turned off the spins continue to precess around the  $z$  axis but they start losing their coherence. The received signal is therefore an oscillating, decaying function, as shown in figure 2.6.

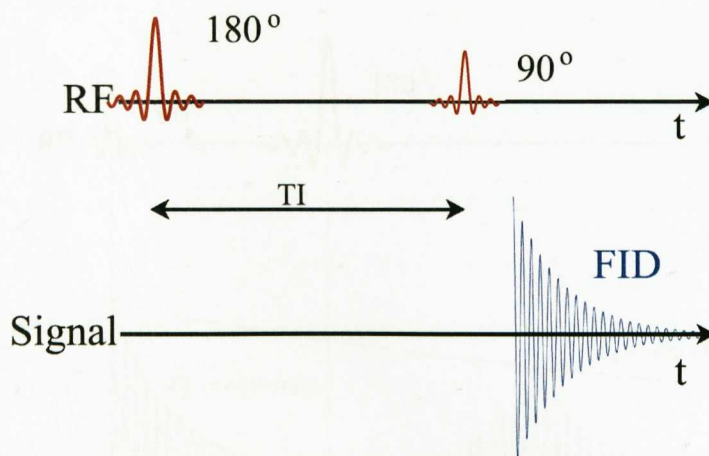


Figure (2.7): Inversion recovery sequence. Here, and in later figures, the  $180^\circ$  pulse is drawn at twice the height, for the same width, as the  $90^\circ$  pulse, corresponding to the need for twice the  $B_1$  amplitude to get twice the angle of spin rotation.

## 2.2.6 Relaxometry

### Measuring $T_1$

The measurements of  $T_1$  are based on the Bloch equation 2.7. The most common way to measure  $T_1$  is through the inversion recovery sequence (figure 2.7). This sequence consists of a combination of two RF pulses. The first  $180^\circ$  pulse inverts the longitudinal magnetisation so that  $M_z(0) = -M_0$ . A second pulse tips the longitudinal magnetisation into the transverse plane so that an FID can be collected. The time between the two pulses is called the inversion time  $T_I$ . The signal as a function of  $T_I$  is given by

$$M_z(t) = M_0(1 - 2e^{-T_I/T_1}) \quad (2.14)$$

which has a zero crossing value for  $T_I = T_1 \ln 2$ . When an inversion recovery sequence is repeated every  $T_R$  (repetition time) seconds, for signal averaging or imaging purposes, the signal equation becomes

$$M_z(t) = M_0(1 - 2e^{-T_I/T_1} + e^{-T_R/T_1}) \quad (2.15)$$

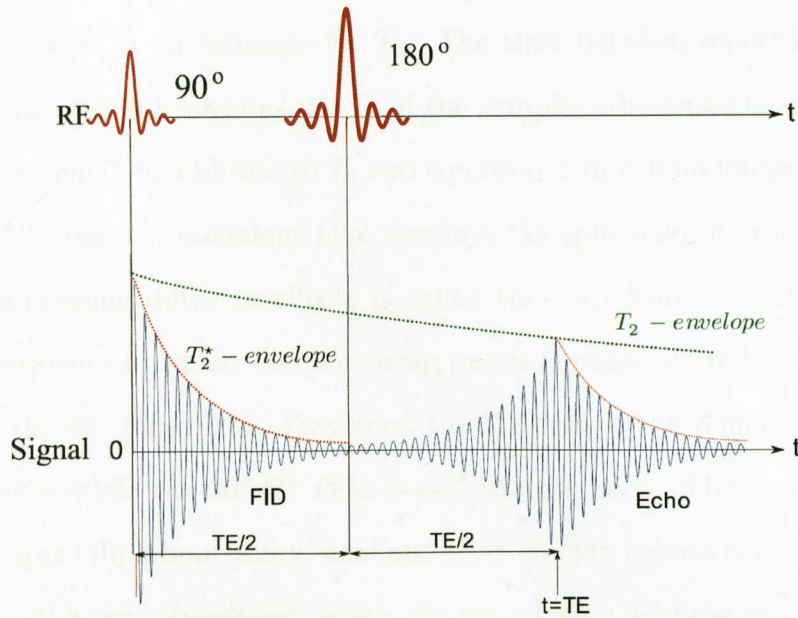


Figure (2.8): Spin echo sequence

### Measuring $T_2$

The transverse relaxation time  $T_2$  can be measured using a spin echo sequence that is able to remove the effects of the magnetic field inhomogeneities (figure 2.8). It is also based on the application of two RF pulses: a  $90^\circ$  pulse applied along the positive x axis that flips the magnetisation into the xy plane and a subsequent  $180^\circ$  pulse applied at a time  $TE/2$  along the positive y axis to invert the phase that the spins have accumulated. The spins continue to precess at the same frequency thus rephasing and producing an echo corresponding to maximum coherence after a further time  $TE/2$ . The magnitude of the magnetisation at the echo will still be limited by the  $T_2$  envelope because the dipole-dipole interactions cannot be refocused.

If the time between the RF pulses is known, the amplitude of the echo measured is related to  $T_2$

$$M_{echo} = M_0 e^{-TE/T_2} \quad (2.16)$$

where  $M_{echo}$  is the peak amplitude of the echo. By repeating the sequence

for different echo times, a series of measurements of  $M_{echo}$  can be collected and fitted to obtain an estimate for  $T_2$ . The time between repetitions, TR, should be more than five times the  $T_1$  of the sample, otherwise the signal will be dependent on  $T_1$  in addition to  $T_2$  and equation 2.16 will no longer be valid.

The most common technique that employs the spin echo in order to measure  $T_2$  suppressing diffusion effects is called the Carr-Purcell Meiboom-Gill (CPMG) sequence in which the refocusing pulses is phase shifted by  $\pi/2$  with respect to the  $90^\circ$  pulse [14]. Therefore, the B1 field of the refocusing pulses aligns along y while the  $90^\circ$  B1 field is still along x' axis. This modification makes the spins flip about the y' axis and thus all spin echoes converge along y' and have the same (positive) phase. By introducing a phase shift between the  $90^\circ$  and  $180^\circ$  pulses the sequence becomes

$$90_x^\circ - \frac{TE}{2} - 180_y^\circ - [TE - 180_y^\circ]_n \quad (2.17)$$

Echoes are formed between successive  $180^\circ$  pulses as the spin refocus and the  $T_2$  can be calculated by fitting the signal amplitude at each echo with the following

$$M_n(t) = M_0 e^{-2nt/T_2} \quad (2.18)$$

With this method there is enough information to obtain the  $T_2$  in a single relaxation curve. This sequence is more tolerant of pulse errors: a refocusing pulse smaller than  $180^\circ$  will cause the first echo to be formed above the x'y' plane but the second echo will rephase back in the x'y' plane. This means that odd-numbered echoes will be formed above the x'y' plane with reduced amplitude. Therefore at least 10 echoes are required with a range of echo times up to three times  $T_2$ .

### 2.2.7 Chemical shift

The magnetic fields experienced by nuclei in the molecule depend on the chemical environment. The electrons in the molecule produce small changes in the magnetic field so nuclei in different position in the molecule will experience a different magnetic field. These differences cause the spins to precess at slightly different frequencies. This shielding effect is known as chemical shift. The measured frequencies are described by the following equation

$$\omega_{meas} = \gamma B_0(1 - \sigma) \quad (2.19)$$

where  $B_0$  is the field applied to the nuclei and  $\sigma$  is the chemical shift shielding constant. Under fully relaxed conditions the ratios of the signals at different frequencies give the number of protons in that particular chemical environment. The chemical shift of a nucleus is usually referred to the shift of a reference peak in parts per million (ppm) and is given by

$$\delta(ppm) = \frac{\omega - \omega_{ref}}{\omega_{ref}} \times 10^6 \quad (2.20)$$

with  $\omega_{ref}$  being the frequency of the reference peak, that is defined as the resonant frequency of the hydrogen nuclei in tetramethylsilane (TMS). In NMR spectroscopy the chemical shift is a useful tool that provides information on the chemical environment of the nuclei and is obtained from a single FID. On the contrary, these chemical shifts lead to artifacts in MRI.

### 2.2.8 Susceptibility

Magnetic susceptibility is a natural property of all substances and is given the symbol  $\chi$ , as depends on the arrangement of the electrons in the material. It is defined as the extent to which any material becomes temporarily magnetised when it is placed in a large magnetic field. There are four regimes of

different magnetic susceptibilities.

- Diamagnetic materials have no unpaired orbital electrons and when they are placed in a magnetic field  $B_0$ , a weak magnetic field is induced in the opposite direction, therefore the effective magnetic field is reduced. The effect on images is, for example, the distortion that occurs at the air-tissue interface. Diamagnetic substances have a small negative magnetic susceptibility  $\chi$  ( $\chi < 0$ ). Most body tissues are diamagnetic, while air and dense bone have almost zero susceptibility.
- Paramagnetic materials have unpaired orbital electrons and they become magnetized when placed in a magnetic field  $B_0$  producing an increase of the effective magnetic field. Therefore they have a small positive susceptibility ( $\chi > 0$ ). In materials containing mobile paramagnetic centres, the dipole-dipole interactions produce a T1 shortening thus giving a bright signal in the T1 weighted images. This is why paramagnetic elements such as gadolinium (Gd) are used as contrast agents (see section 2.2.9). Other examples are deoxy-haemoglobin and met-haemoglobin.
- Superparamagnetic is a term used to describe materials intermediate between paramagnetic and ferromagnetic, with susceptibility values between 100 and 1000. Examples include iron oxide particles (used as MR contrast agents) and ferritin.
- Ferromagnetic materials experience a large force when placed in an external field and become permanently magnetized even when the magnetic field has been turned off. They have a large positive susceptibility. Metal alloys containing iron, nickel and cobalt are often ferromagnetic.

At the boundaries of tissues with different susceptibility there will be slightly different magnetic fields that will produce a perturbation of the static field. The induced magnetisation,  $M_{z,ind}$ , is calculated as

$$M_{z,ind} \approx \frac{\chi}{\mu_0} B_0 \quad (2.21)$$

where  $\mu_0$  is the permeability of the free space. It is then possible to define the effective local magnetic field as

$$B_{eff} \approx (1 + \chi)B_0 \quad (2.22)$$

The perturbations induced in the magnetic field by these susceptibility effects can cause artifacts in magnetic resonance images as will be explained in section 3.12.4. However, these effects can also be used both for functional MRI, where the susceptibility difference between oxygenated and deoxygenated blood allows the visualization of brain activity [15], and for contrast agent studies [16]. In particular, a paramagnetic rare earth element such as gadolinium has been used for this work so it is described more in detail in the following section.

### 2.2.9 Contrast agents

Exogenous contrast agents such as gadolinium have an effect on tissue relaxation times that can be best described using relaxation rates instead of relaxation times. Therefore it is useful to define the following relaxation rates

$$R_1 = \frac{1}{T_1} \quad R_2 = \frac{1}{T_2} \quad R_2^* = \frac{1}{T_2^*} \quad (2.23)$$

that are additive quantities.

For contrast agents it is possible to define a specific relaxivity  $r$  to describe the effect of their concentration on the change in the relaxation rate. For example, the change in relaxation rate of a tissue due to the presence of the contrast agent is given by the following equation

$$R' = R + rC \quad (2.24)$$

where  $C$  is the concentration of the contrast agent. The relaxivity  $r$  may be different for longitudinal and transverse relaxation rates but in the case of gadolinium they are approximately the same (4 and 5  $\text{mmol}^{-1}\text{s}^{-1}$ ).

As already stated in the previous section, gadolinium is strongly paramagnetic because it has seven unpaired electrons in its electronic structure. As a free ion, gadolinium is highly toxic. However, it is generally regarded as safe when administered as a chelated compound, i.e. in chemical structures that chemically shield the gadolinium atom, which eliminate the toxicity preserving the susceptibility characteristics. Different types of gadolinium-containing contrast agents are available. Details concerning the physicochemical properties of some of these agents are given in table 2.2. The first agent developed, gadopentetate dimeglumine (Gd-DTPA, Magnevist<sup>®</sup> by Schering), has a linear structure and is ionic in nature, with a net  $-2$  charge of the gadopentetate chelate [17]. Magnevist was followed initially by gadoterate meglumine (Gd-DOTA, Dotarem<sup>®</sup> by Guerbet) which has a cyclic structure but is again ionic (with a net  $-1$  charge of the gadoterate chelate), and subsequently by Gadoteridol (Gd-HP-DO3A, ProHance by Bracco).

In this work Gadoteridol will be used that has a chemical structure closely related to the two other compounds but showing lower osmolality. ProHance and Dotarem have the highest combined thermodynamic and kinetic stability, reflecting the greater energy and time required to remove the gadolinium ion from the ring structure in which it is held. A comparison of the physicochemical properties of different gadolinium formulations available commercially has been presented recently by Laurent et al. [18].

The strongly paramagnetic behaviour of gadolinium produces a decrease in both  $T_1$  and  $T_2$  relaxation times of the proton nearby. At low concentrations such as those used in normal clinical practice ( $\sim 0.1$  mmol per kilogram) the

	<b>Magnevist</b>	<b>Dotarem</b>	<b>ProHance</b>
Molecular structure	Linear, ionic	Cyclic, ionic	Cyclic, nonionic
Osmolality (Osm/kg)	1.96	1.35	0.63
Viscosity (mPa s at 37°C)	2.9	2.0	1.3
Metal chelate (mg/ml)	469	278.3	279.3

Table (2.2): Physicochemical characteristics of commercially-available, gadolinium-based MR contrast agents, predominantly renally excreted.

major effect is the  $T_1$  shortening, and tissues which take up the agent have an enhanced signal intensity on  $T_1$ -weighted images. At weak concentration, the  $T_2$  effect of gadolinium chelates is negligible compared to the  $T_1$  effects. The  $T_2$  effect predominates and is only visible at high concentrations, for example in the bladder after renal excretion, where a loss of signal occurs.

Perfusion MRI also exploits the magnetic susceptibility effect due to the first intravascular passage of a concentrated bolus of Gd chelate, responsible for a drop in the  $T_2$  and  $T_2^*$  signal.  $T_2^*$  effect is enormous and occurs due to the inhomogeneous distribution of Gd in vessels and around.

While the NMR principles have been explained in this chapter, the next chapters will cover the principles of MR imaging.

# Chapter 3

## Magnetic Resonance Imaging

### 3.1 Introduction

Magnetic resonance imaging (MRI) is an imaging technique discovered independently by Peter Mansfield [1] and Paul Lauterbur [2] in 1973. Several developments followed especially in the group lead by Peter Mansfield including slice selection [19], echo planar imaging (EPI) [20], actively shielded gradients [21] and echo volumar imaging [22]. Peter Mansfield and Paul Lauterbur were jointly awarded the Nobel Prize for medicine in 2003 “*for their discoveries concerning magnetic resonance imaging*” ([www.nobelprize.org](http://www.nobelprize.org)).

This chapter outlines the basic principles of magnetic resonance imaging (MRI). The basic theories on which MRI is based have been extensively described in numerous texts, for example [7, 23].

### 3.2 Gradients

Magnetic field gradients are fundamental for the determination of the spatial information of the NMR signal. A field gradient is an additional small field variation that produces a linearly varying field. The gradient field strength is

measured in millitesla per metre ( $mT/m$ ). In order to create an image from a sample, it is necessary to have one gradient for each of the  $x$ ,  $y$  and  $z$  directions which are called  $G_x$ ,  $G_y$  and  $G_z$  respectively. As the total magnetic field is commonly referred to as along the  $z$  axis, the three orthogonal spatial gradients of  $B_z$  can be expressed as

$$G_x = \frac{dB_z}{dx} \quad (3.1)$$

$$G_y = \frac{dB_z}{dy} \quad (3.2)$$

$$G_z = \frac{dB_z}{dz} \quad (3.3)$$

The three sets of gradients, normally applied for a short time as pulses, give MR its three dimensional capability. The total field gradient is therefore defined as

$$\mathbf{G} = G_x \mathbf{i} + G_y \mathbf{j} + G_z \mathbf{k} \quad (3.4)$$

and the resultant magnetic field at a point  $\mathbf{r}$  can be written as

$$B_z(\mathbf{r}) = B_0 + \mathbf{G} \cdot \mathbf{r} \quad (3.5)$$

where  $\mathbf{r}$  is defined as

$$\mathbf{r} = x\mathbf{i} + y\mathbf{j} + z\mathbf{k} \quad (3.6)$$

As a consequence of the introduction of the field gradients, the Larmor frequency, previously defined in equation 2.2, becomes

$$\omega_L = \gamma(B_0 + xG_x + yG_y + zG_z) \quad (3.7)$$

This means that when the gradients are applied, the protons (spins) will experience a different total field according to their position in the three dimensional space, thus resonating faster or slower. Figure 3.1 shows the effect of field gradient on spins.

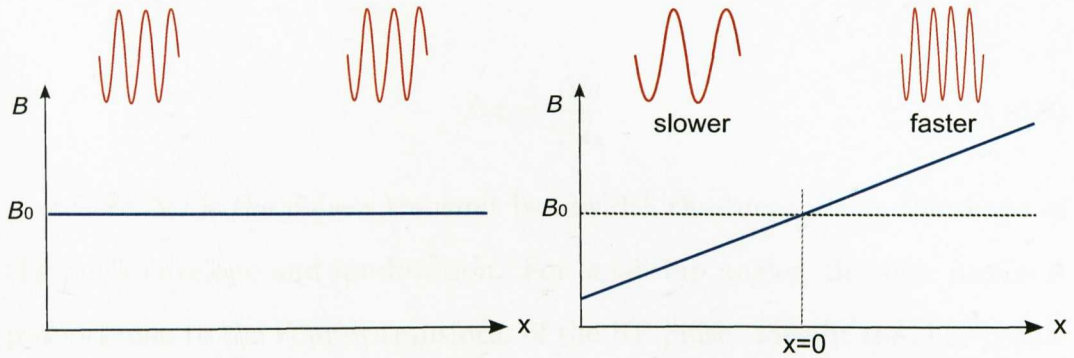


Figure (3.1): Example of the application of field gradients: when only  $B_0$  is applied all nuclei precess at the same frequency (left), when a gradient is applied as for example in the  $x$  direction (right) the spin precession frequency depends on the position and will be slower or faster.

Depending on their function, magnetic field gradients are called slice-select gradient, frequency-encoding gradient or phase-encoding gradient. The following sections will explain these functions in detail.

### 3.3 Slice selection

As shown in figure 3.1 the presence of the gradient causes the resonant frequency to vary according to the position in the gradient direction, being equal to the normal Larmor frequency when  $x=0$  and being higher or lower along the axis. The slice selection occurs when a selective excitation pulse (RF) is applied with a centre frequency  $\omega_0$  and a small range of frequencies  $\Delta\omega$ , the transmit bandwidth. Resonance occurs only when the required frequency is present in the RF pulse's transmit bandwidth. Therefore only spins in a plane with a Larmor frequency corresponding to the range of frequencies contained in the RF pulse will be tipped into the  $xy$  plane. This is called selective excitation. The slice-select gradient field,  $G_z$  introduces a linear variation of

the Larmor frequency in the slice ( $z$ ) direction equal to

$$\omega_{L(z)} = \gamma(B_0 + zG_z) \quad (3.8)$$

The thickness of the slice  $\Delta z$  can be written as

$$\Delta z = \frac{\Delta\omega}{\gamma G_z} \quad (3.9)$$

where  $\Delta\omega$  is the pulse's transmit bandwidth that depends on the shape of the pulse envelope and its duration. For small flip angles, the slice profile is proportional to the Fourier transform of the RF pulse. Ideally, the slice profile should have a rectangular shape, i.e. equal to the maximum inside the slice and equal to zero outside. This would correspond to a sinc<sup>1</sup> shaped RF pulse with an infinite number of lobes. In practice, 3 or 5 lobes are used because a larger number of lobes would increase the minimum echo time (TE) and the repetition time (TR).

From equation 3.8 it can be deduced that the slice thickness can be manipulated by changing the strength of the gradient or bandwidth of the excitation pulse, whilst changing the slice position means changing the centre frequency of the RF pulse, by adding or subtracting a specific frequency offset.

Figure 3.2 shows an example of RF pulse applied together with a gradient  $G_z$ . It has to be underlined that whilst the selective excitation pulse is applied, the signal being generated is also being dephased by the gradient. For most pulses this phase shift is corrected by applying a reversing gradient for half the duration of the pulse.

---

<sup>1</sup>A sinc function is expressed as  $\frac{\sin(x)}{x}$  and consists of adjacent lobes with alternating polarity, with a central high lobe.

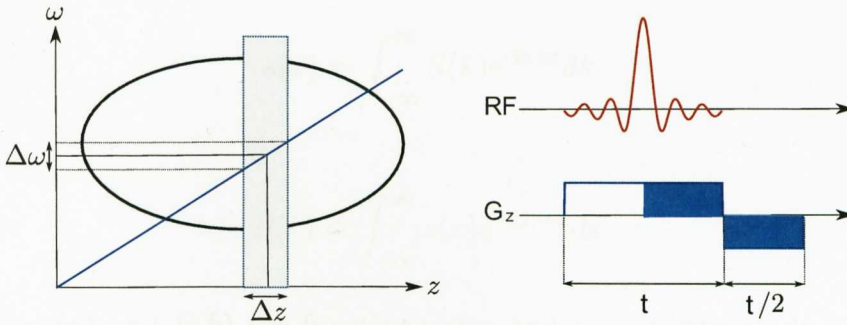


Figure (3.2): The image on the left shows the selection of a slice with a thickness  $\Delta z$  when a linear gradient field  $G_z$  is applied together with an RF pulse with a range of frequencies  $\Delta\omega$ . On the right it can be seen that after the RF pulse, a slice selection gradient with negative polarity is applied for half the duration in order to refocus the dephasing effects induced by the original slice select gradient.

### 3.4 In plane spatial encoding

In order to create an image following the slice selection it is necessary to perform the so called spatial encoding in the two remaining axis. To achieve this, two processes are performed: frequency encoding and phase encoding.

#### 3.4.1 Frequency encoding

The frequency-encoding gradient  $G_x$ , also called the readout gradient, is applied in the  $x$  direction to get spatial information in the  $x$ -direction, influencing only those spins that have already been excited by the slice selection. Because the  $G_x$  gradient is switched on while the NMR signal is being measured, the signal's frequency depends on the position of the material along the  $x$  direction. According to equation 3.7, the spatial location can be measured as both  $B_0$  and  $G_x$  are known. However, the resultant signal is a mixture of many frequency components and a Fourier Transform (FT) analysis is needed to determine the single frequency components.

Fourier analysis is a mathematical tool that reveals the spectral content of a signal. In general, a Fourier transform is defined by the equations

$$s(x) = \int_{-\infty}^{\infty} S(k) e^{i2\pi kx} dk \quad (3.10)$$

$$S(k) = \int_{-\infty}^{\infty} s(x) e^{-i2\pi kx} dx \quad (3.11)$$

where  $s(x)$  and  $S(k)$  are functions of  $x$  and  $k$  respectively. In MRI  $x$  is the spatial domain and  $k$  is the spatial frequency domain. By analogy, a two-dimensional FT is defined as

$$S(k_x, k_y) = \int_x \int_y s(x, y) e^{-i2\pi k_x x} e^{-i2\pi k_y y} dx dy \quad (3.12)$$

and a three-dimensional FT is

$$S(k_x, k_y, k_z) = \int_x \int_y \int_z s(x, y, z) e^{-i2\pi k_x x} e^{-i2\pi k_y y} e^{-i2\pi k_z z} dx dy dz \quad (3.13)$$

The signal received from a point  $\mathbf{r}$  at time  $t$  is proportional to the spin density  $\rho(\mathbf{r})$  and depends on the local Larmor frequency  $\omega_L(\mathbf{r}, t')$

$$S(\mathbf{r}, t) \propto \rho(\mathbf{r}) e^{i \int_0^t \omega_L(\mathbf{r}, t') dt'} \quad (3.14)$$

Therefore we can write the signal received from a three-dimensional region as

$$S(t) \propto \int_V \rho(\mathbf{r}) e^{i \int_0^t \omega_L(\mathbf{r}, t') dt'} dV \quad (3.15)$$

where  $dV = dx dy dz$ . When applying a constant linear field gradient in the  $x$  direction, the precession frequency becomes

$$\omega(x) = \gamma(B_0 + G_x x) \quad (3.16)$$

therefore the demodulated signal (after  $f_0$  removed) can be written as

$$S(t) \propto \int_V \rho(\mathbf{r}) e^{i\gamma x G_x t} dV = \int_V \rho(\mathbf{r}) e^{ixk_x} dV \quad (3.17)$$

where  $k(x)$  refers to k-space which will be explained in section 3.5.

### 3.4.2 Phase encoding

In addition to using the slice-select gradient  $G_z$  and the frequency encoding gradient  $G_x$ , another gradient is needed for localisation along the  $y$  direction. For this a phase encoding gradient  $G_y$  is generally used which produces a linear spatial variation in the phase of the magnetisation. As a result, the spins in the same column will have different phases compared to each other and compared to the spins in the centre of the magnet. The phase-encoding gradient is usually applied right after the RF pulse or just before the readout. The amount of dephasing introduced depends on the magnitude of the gradient applied and on the position in the phase-encoding direction. Therefore

$$\phi(t) = \gamma y \int_0^\tau G_y dt \quad (3.18)$$

where  $\tau$  is the duration of the phase encoding gradient lobe.

If we add the contribution of the phase-encoding gradient to equation 3.17, we can write for the signal

$$S(t) \propto \int \int \rho(\mathbf{r}) e^{i\phi_y + ixk_x} dx dy \quad (3.19)$$

Figure 3.3 shows schematically how the  $G_x$  and the  $G_y$  gradients are applied.

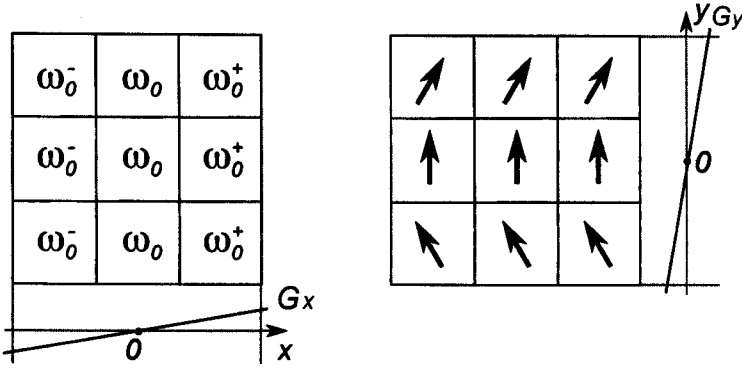


Figure (3.3): The frequency encoding gradient  $G_x$  (on the left) linearly changes the Larmor frequency of the spins along the  $x$  axis. The phase encoding gradient  $G_y$  (on the right) introduces a phase shift along the  $y$  axis.

### 3.5 k-space

The concept of k-space, called “reciprocal space” was introduced into MRI in 1973 by Mansfield and Grannell [1]. K-space can be thought as the raw data matrix which stores the encoded MR signals, being the Fourier space ( $k_x, k_y, k_z$ ) in which images are acquired before being Fourier transformed into the cartesian image space ( $x, y, z$ ). In other terms, it represents the spatial frequency distribution of the MR image: low spatial frequencies are close to the origin and represent the overall brightness or contrast of the image whilst high spatial frequencies, at the outer regions of k-space, give information on the details and the edges.

The k-space description of an image is normally composed of two axes perpendicular to each other, with the horizontal axis related to frequency encoding and the vertical axis to phase encoding axis. Figure 3.4 shows the relationship between k-space and image space.

Immediately after the RF pulse, the signal is at the centre of k-space that corresponds to the sum of the total MR signal of the object. With the application of the frequency encoding and the phase encoding gradients, the sampling position moves to the bottom left corner. During the frequency encoding, data points are recorded at regular intervals along a line of  $k_x$  from left to right. During the phase encoding the trajectory across the k-space is altered

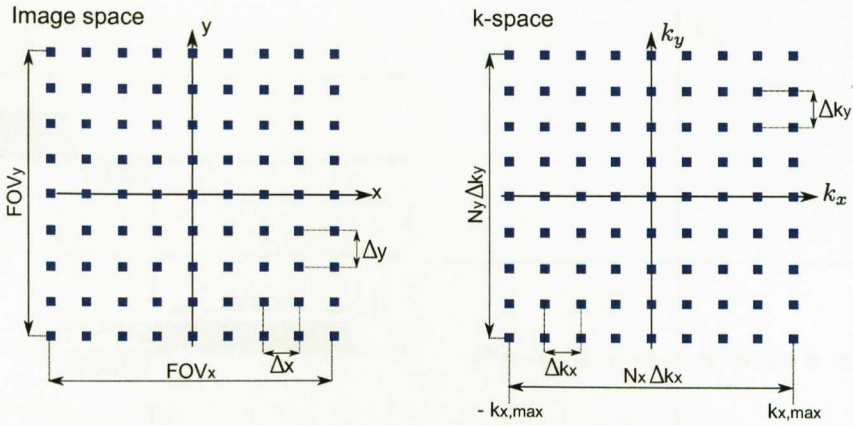


Figure (3.4): Schematic of the image space (left) and k-space (right).

to the second line bottom line. In order to sample the whole image, the four quadrants of the k-space must usually be covered by the readout.

A generalized form for an arbitrarily shaped gradient  $G$ ,  $k$  is defined as

$$k = \gamma \int_0^t G(t) dt \quad (3.20)$$

which defines any k-space trajectory. The Field of View (FOV) is determined by the separation of the  $k_y$  lines and of the samples along each  $k_x$  line

$$FOV_{x,y} = \frac{1}{\Delta k_{x,y}} \quad (3.21)$$

The pixel size is defined by the total length of the k-space axes.

### 3.6 Gradient echo sequence

Figure 3.5 shows the MR pulse sequence diagram for the gradient echo (GE) imaging sequence. In the GE, a frequency selective RF pulse is applied together with a linear slice-selective gradient  $G_z$ , thus allowing the rotation of the magnetisation into the transverse plane. The refocusing component of the z gradient of opposite polarity is used to remove the phase shift across the slice.

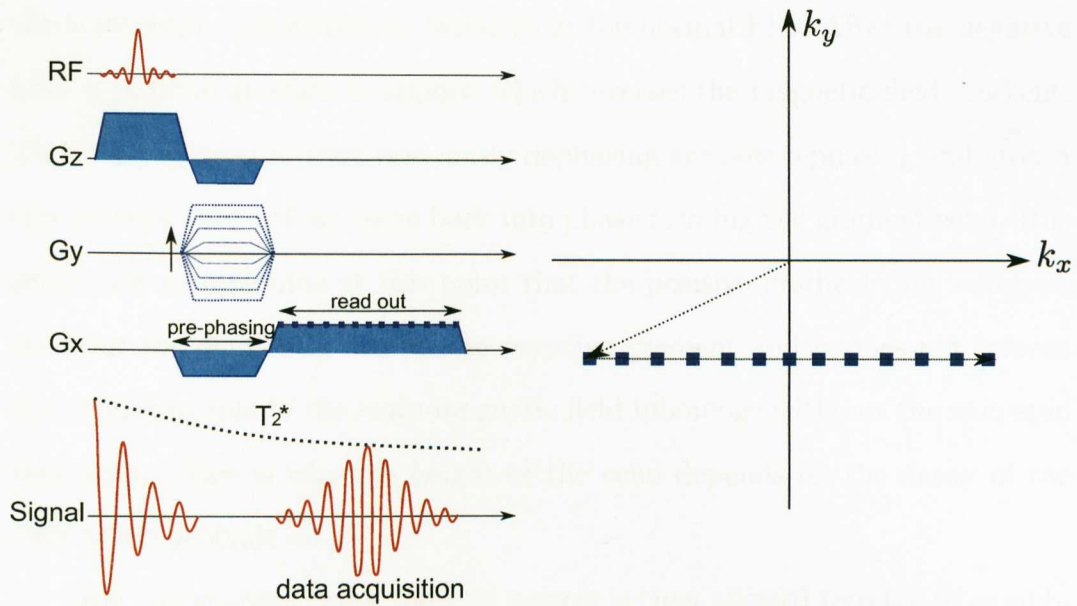


Figure (3.5): Basic gradient echo MR imaging sequence and corresponding sampling in the  $k$  space. The top line shows the RF pulse which is applied simultaneously with a slice selective gradient  $G_z$ , shown in the second line. The third line shows the phase encoding gradient  $G_y$  and the fourth line shows the frequency encoding  $G_x$  with the two lobes. The data acquisition is shown with the blue squares and they correspond to a line in the  $k$  space. It has to be underlined that the rate of decay is given by  $T_2^*$ . See text for more details.

The third line of the diagram shows the phase encoding gradient  $G_y$  which is applied orthogonal to the slice selection. Finally, the frequency encode gradient  $G_x$  is applied in the third orthogonal direction. The frequency encoding gradient consists of two lobes with opposite polarity. The first portion, called dephasing or pre-phasing lobe is applied for a time  $\tau$  and it is used so that the signal is a symmetric echo (rather than FID). When the pre-phasing gradient is applied, the spins have a different phase depending on their position in the gradient field. The second portion of the frequency encoding gradient is the one with opposite polarisation and it is applied for a time  $2\tau$ . When this readout gradient is applied, data are acquired at points along the  $k$  space line, shown in blue squares. The opposite polarity of the two gradients reverses the phases of the spins, therefore producing an echo when the area of the readout lobe equals the one of the pre-phasing lobe. In more detail, in the GE sequence the negative pre-phasing gradient lobe causes rapid dephasing of

the transverse magnetisation, faster than the normal FID. After the negative lobe, a positive gradient is applied which reverses the magnetic field gradient. Therefore, spins that were previously dephasing are now rephasing and after a certain time they will all come back into phase forming the gradient echo. It is important to underline at this point that the positive gradient only compensates for the dephasing due to the negative gradient and it does not refocus the dephasing due to the main magnetic field inhomogeneities or the spin-spin relaxation. This is why the height of the echo depends on the decay of the FID which depends on  $T_2^*$ .

After the gradient echo, the spin system is then allowed to relax to equilibrium before the sequence is repeated to sample a different line in the k space with a different strength of the  $G_y$  gradient, until the 2D k space is complete. The time between the application of two subsequent RF excitation pulses is called the repetition time TR, therefore the total scan time is

$$\text{Scan time} = \text{NSA} \times N_y \times \text{TR} \quad (3.22)$$

where NSA is the number of signal averages and  $N_y$  is the number of phase-encoding steps. NSA is chosen to have a certain signal to noise ratio (SNR) due to the relation  $\text{SNR} \propto \sqrt{\text{NSA}}$  and  $N_y$  is usually used to have a specific resolution, hence the only parameter that can be changed in order to reduce the scan time is the repetition time TR. However, the TR cannot be too short if a  $90^\circ$  RF pulse is applied because in that case the longitudinal magnetisation wouldn't be given enough time to recover to a reasonable value thus causing a reduction in the transverse magnetisation and therefore a reduction in the SNR itself. In order to overcome this problem, a smaller flip angle can be used, as for FLASH sequences (section 3.10.1), thus leading to an incomplete flipping of the longitudinal magnetisation into the x-y plane. In this way, even for small TRs, there will be enough longitudinal magnetisation for the next cycle.

### 3.7 Spin echo

The spin echo (SE) sequence is similar to the gradient echo sequence just explained but the main difference is the way the echo is formed. Figure 3.6 shows a schematic example of the gradient configuration in the case of a spin echo sequence. After the  $90^\circ$  RF pulse, the magnetisation vector  $M_z$  is flipped into the transverse plane. At the beginning all the spins are in phase precessing at the same frequency  $\omega_0$  but they start to dephase due to the  $T_2^*$  effects. Next, a  $180^\circ$  RF pulse is applied to flip the spins about the  $x$  axis as shown in figure 3.7. This pulse doesn't change the precessional frequencies of the spins but it reverses their phase angles. After a time  $\tau$  equal to the delay between the  $90^\circ$  and the  $180^\circ$  pulse, all the spins come back into phase forming the spin echo. We call  $2\tau$ , the echo delay time TE which is the time after the  $90^\circ$  pulse when we get maximum signal again. In this manner, the echo height depends now on  $T_2$  and not on  $T_2^*$  as for the gradient echo. In other words, the decay of the original FID and the decay of each subsequent echo is given by  $e^{-t/T_2^*}$ , whereas the decay of the curve corresponding to the maximum signal reached by each echo is given by  $e^{-t/T_2}$ . However, only static inhomogeneities are eliminated in a SE sequence. The signal decay due to diffusion in inhomogeneous magnetic fields is not recovered in either SE or GE sequences.

### 3.8 Echo planar imaging

Echo planar imaging (EPI) was developed by Sir Peter Mansfield in Nottingham in 1977 [20] and it is the fastest MRI technique available. The basic idea is to fill k-space following a single RF pulse (single-shot EPI) during one  $T_2^*$  decay rather than using multiple RF excitation to sample k-space. A schematic diagram of EPI pulse sequence is shown in figure 3.8. In the gradient echo EPI sequence (GE-EPI), an RF excitation pulse is applied to create a FID (often a  $90^\circ$  pulse to maximise the signal in the transverse plane or

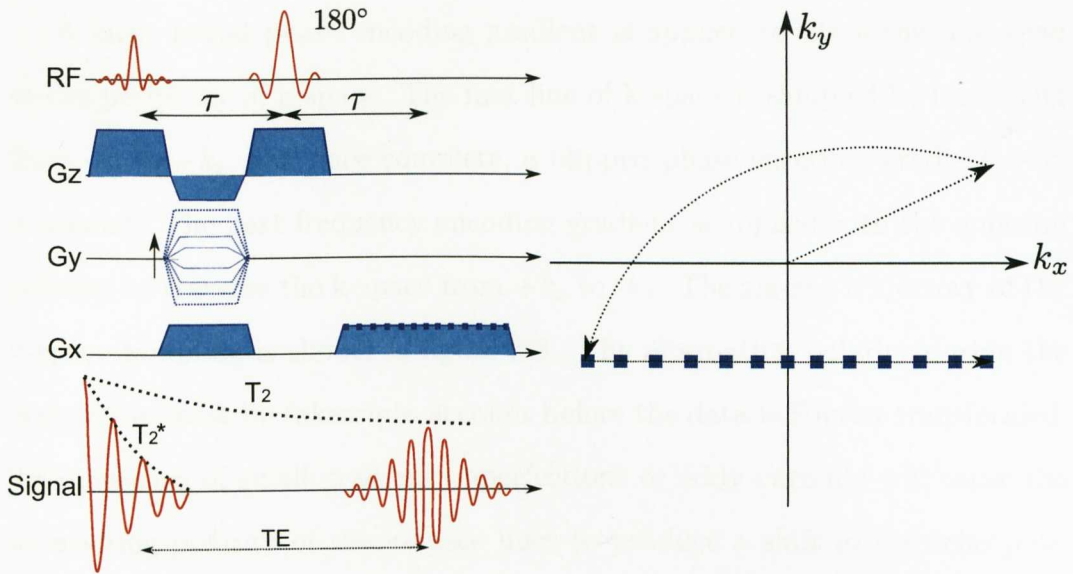


Figure (3.6): Schematic of a simple spin echo sequence and corresponding sampling in the  $k$  space. A  $180^\circ$  pulse is applied at time  $\tau$ , causing the spins to get in phase at time  $2\tau$  (TE), leading to the formation of an echo from the FID. See text for more details.

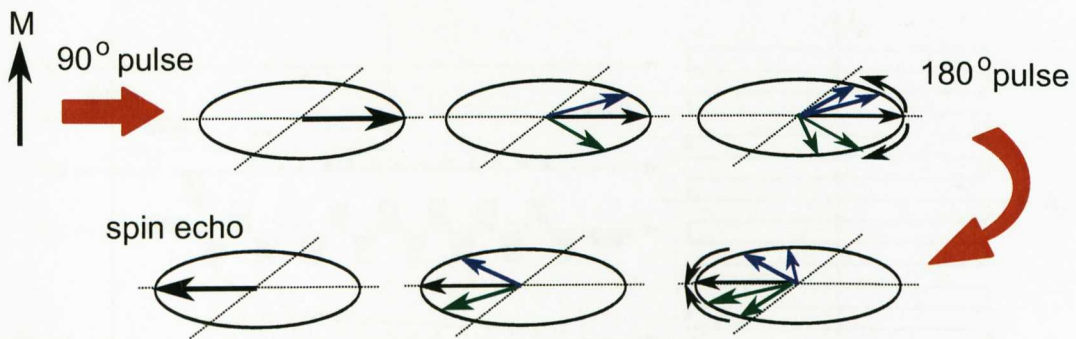


Figure (3.7): Refocusing effect of the spin echo sequence. Spins initially in phase dephase naturally until the  $180^\circ$  pulse is applied. Immediately after their phases are reversed and they start refocusing forming an echo.

long TR). The sampling strategy for EPI consists of using a series of bipolar readout gradients (from  $+G_x$  to  $-G_x$ ) in combination with phase encoding gradients to generate a train of gradient echoes. Each time the frequency gradient is switched, the spins dephase and rephase resulting in a gradient echo. The number of echoes produced following an RF excitation pulse is known as *echo train length* (ETL). In order to allow the rapid on and off switching of the gradients, high performance gradients are required. In general, gradient strengths of over 20 mT/m and gradient rise times of less than 300  $\mu\text{sec}$  are needed.

A large initial phase encoding gradient is applied to place the first echo at the periphery of k-space. The first line of k-space is sampled by traversing from  $-k_x$  to  $+k_x$  and, once complete, a blipped phase encoding gradient  $+G_y$  is applied. The next frequency encoding gradient is applied with the opposite polarity to traverse the k-space from  $+k_x$  to  $-k_x$ . The zig-zag trajectory of the k-space sampling is shown in figure 3.8. The alternating polarity during the acquisition must be taken into account before the data is Fourier transformed. The presence of small gradient imperfections or eddy currents will cause the alternating polarity of the k-space lines to produce a shift in the echo position. In the reconstructed image this shift will appear as an artifact called the Nyquist ghost, a lower intensity ghost of the image seen along the phase encode direction.

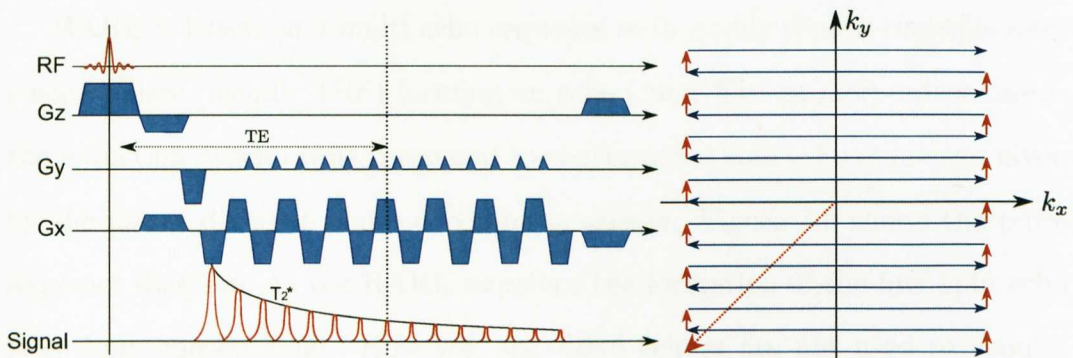


Figure (3.8): Pulse sequence diagram of an EPI (left) and corresponding sampling in the k space (right).

Spin echo EPI (SE-EPI) employs an additional refocusing  $180^\circ$  RF pulse in the transverse plane. In this case, gradient echoes are formed under the envelope of a spin echo, due to the application of refocusing RF pulse before signal acquisition, rather than an FID. For this reason the images are more  $T_2$ -weighted. Another difference of the SE-EPI compared to GE-EPI is that the prephasing gradient lobe  $G_y$  has to be applied before the refocusing pulse with the same polarity of the readout and phase encoding gradients to reduce the TE.

Inversion recovery EPI (IR-EPI) is another version of the EPI based on the

$T_1$  relaxation time which makes use of an inversion recovery module prior to either GE or SE-EPI pulse sequence acquisition. IR-EPI is normally used to attenuate cerebrospinal fluid (CSF), produce  $T_1$ -weighted images or produce  $T_1$  maps.

### 3.9 Fast spin echo

The fast spin echo is a fast imaging sequence that was initially called RARE (rapid acquisition with relaxation enhancement), but different manufacturers have different names for it: fast spin echo (FSE) for GE, Hitachi and Toshiba and turbo spin echo (TSE) for Siemens and Philips. In this thesis this sequence will be called RARE [24].

RARE is based on a multi echo sequence with evenly spaced multiple refocusing pulses (usually  $180^\circ$ ) forming an echo train. The primary advantage is the reduction in scan time compared to conventional spin echo sequences given by the use of different phase encoding gradients. Figure 3.9 shows the pulse sequence diagram. In the RARE sequence the formation of the first spin echo is entirely conventional. However, the extra echoes are not used to acquire images with different TE but to acquire multiple lines of data, i.e. to have different phase encoding for each echo. This is done by using rewinding phase encoding gradients to undo the dephasing of the spins between echoes. To do this a phase encoding step of equal strength but opposite in sign is applied after the completion of the data acquisition. The whole sequence repeats after TR with different phase-encoding steps.

The time between successive echoes, the inter echo spacing, is a fixed value because the RF pulses are all evenly spaced apart in time. As for the conventional spin echo, the ETL is the number of echoes in the spin echo train. Therefore the total scan time is

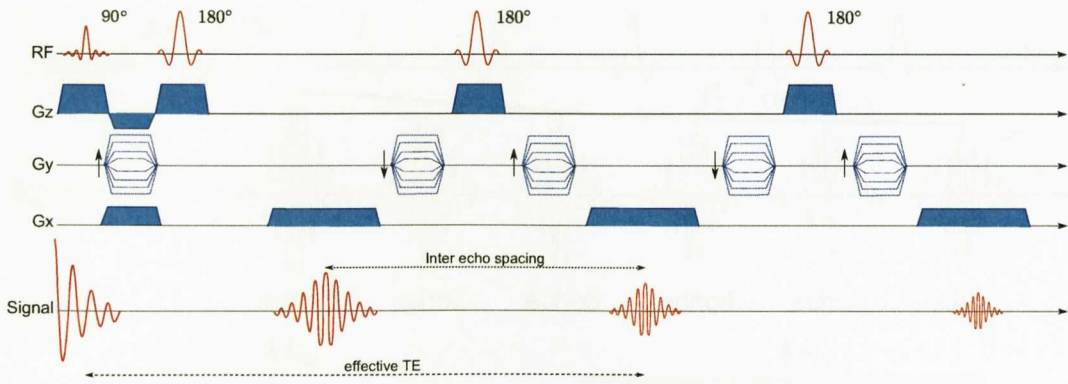


Figure (3.9): Fast spin echo (RARE) sequence with an echo train of three. The effective TE is given by the time from the initial excitation to the second echo.

$$\text{Scan time} = \frac{\text{NSA} \times N_y \times \text{TR}}{\text{ETL}} \quad (3.23)$$

where  $N_y$  is the number of phase encoding steps. This means that a RARE sequence with, for example, 16 echoes, will run 16 times faster than the equivalent spin echo.

In RARE sequences, lines of k-space are acquired from different echoes. The manner in which the k-space is filled is shown in figure 3.10: each echo within the train is phase encoded into a k-space band. Echoes at the same position in the echo train from different acquisitions are assigned the same slab of k-space. The number of phase encoding lines in each slab corresponds to the number of lines required to fill the whole k-space.

The greatest amount of signal comes from the centre of k-space. If we choose an ETL of 3 echoes as in figure 3.9, we will have 3 slabs in the k-space, with each slab having a number of lines equal to the number of shots. Each slab corresponds to a different echo. Because the central slab corresponds to the lowest phase-encoding gradient, it will have the least amount of dephasing. The central slab is assigned to the echo corresponding to the chosen effective TE for which, by definition, there is the maximum signal. The effective TE of the sequence is given by the time between the  $90^\circ$  pulse and the echo obtained with no phase encoding. The signals from the other echoes will be placed in

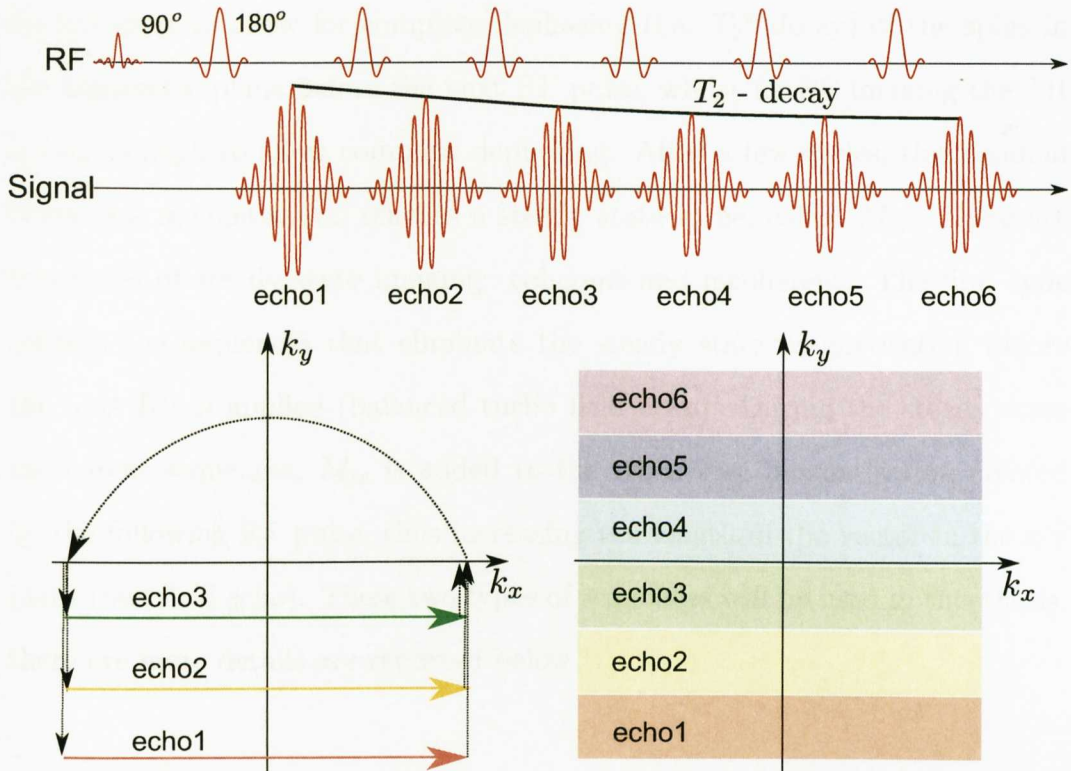


Figure (3.10): Data acquisition (k-space) filling for the RARE sequence. Each echo is phase encoded into a k-space band.

the other slabs so that the echoes that experience progressively greater phase-encoding gradients (therefore less signal) fall into slabs further away from the centre slab, and those experiencing the weakest phase-encoding gradients are placed closer to the centre slab. In other words, by appropriately picking the slabs, we put most of the weight on the echo corresponding to the effective TE. By altering the order by which k-space is sampled, the  $T_2$  contrast can be manipulated. The number of slices that can be sampled is determined by the length of TR.

The main disadvantages of RARE imaging involve higher RF exposure and the reduced coverage (number of slices).

### 3.10 Fast imaging in the steady state

One major difference between GE and SE pulse sequences consists in the transverse magnetisation at the end of the cycle. For GE sequence, TR may

be too short to allow for complete dephasing (i.e.  $T_2^*$  decay) of the spins in the transverse plane before the next RF pulse, whilst for SE imaging the TR is long enough to allow complete dephasing. After a few cycles, this residual transverse magnetisation reaches a steady state value, called  $M_{ss}$ . There are two types of steady state imaging: coherent and incoherent. The first type regards the sequences that eliminate the steady state magnetisation before the next RF is applied (balanced turbo field echo). During the steady state incoherent sequences,  $M_{ss}$  is added to the transverse magnetisation created by the following RF pulse, thus increasing the length of the vector in the x-y plane (fast field echo). These two types of sequences will be used in this thesis, therefore more details are reported below.

### 3.10.1 Fast field echo

The fast field echo (FFE) sequence, also called SPGR (spoiled gradient recalled echo), FLASH (fast low angle shot) or spoiled GRASS (gradient recalled acquisition in steady state), is a gradient echo pulse sequence primarily used for anatomical imaging. This sequence eliminates the steady state transverse magnetisation by applying RF spoiling, by applying variable gradient spoilers or by using a long TR. RF spoiling consists of a phase offset added to each successive RF pulse, which causes a phase shift in successive  $M_{ss}$  vectors. By maintaining a constant relationship between the transmitter and the receiver, successive  $M_{ss}$  vectors cancel each other out. The spoiling achieved by using gradient spoilers consists of the introduction of an additional gradient with variable strength from cycle to cycle. Spoling of  $M_{ss}$  can also be achieved by lengthening TR so that there is enough time to allow complete dephasing of the spins in the transverse plane ( $TR > T_2$ ). This is similar to the SE sequence.

The sequence consists of a train of RF pulses of flip angle  $\alpha$  separated by a time TR, see figure 3.11.

The magnetisation after the first pulse is for the longitudinal and the trans-

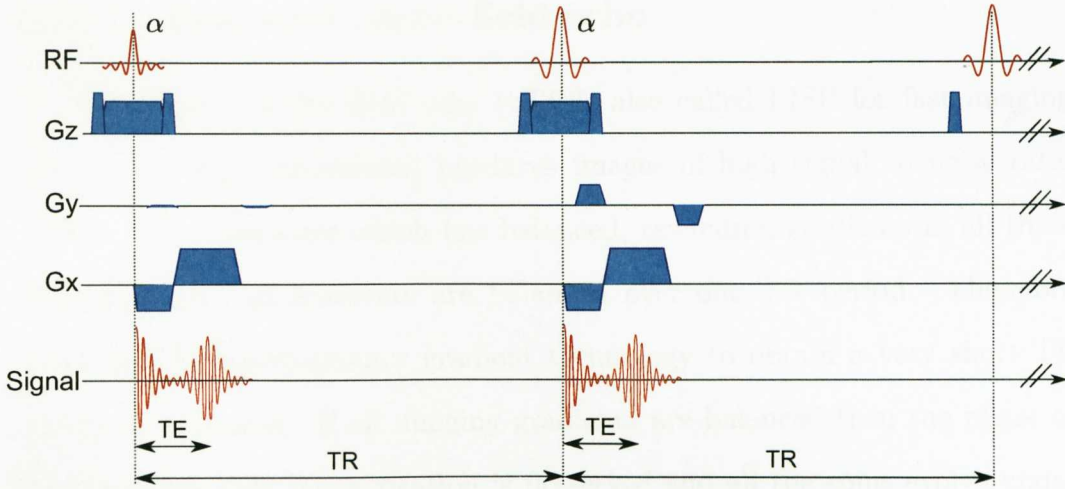


Figure (3.11): FFE pulse sequence diagram.

verse components:

$$M_z = M_0 \cos \alpha \quad (3.24)$$

$$M_{x,y} = M_0 \sin \alpha \quad (3.25)$$

Since the sequence uses flip angles of about  $20^\circ$ – $30^\circ$ , i.e. much less than  $90^\circ$ , a short period for recovery of the longitudinal magnetisation can be used and thus a short repetition time TR. At the same time, the transverse magnetisation is also decaying. The longitudinal magnetisation experiences a series of identical excitation pulses with flip angle  $\alpha$ , evenly spaced in time. When sufficiently repetitions have occurred, the system reaches a steady state so that the same magnetisation values occur after each RF pulse.

The maximum signal can be obtained for a flip angle equal to the Ernst angle  $\alpha_E$

$$\alpha_E = \arccos(e^{-\frac{TR}{T_1}}) \quad (3.26)$$

The Ernst angle lies between  $0$  and  $90^\circ$  and increases with the ratio  $TR/T_1$ .

### 3.10.2 Balanced turbo field echo

The balanced turbo field echo (bTFE, also called FISP for fast imaging with steady state precession) produces images of high signal to noise ratio (SNR). It is a sequence which has balanced, rewinding gradients in all three directions, i.e. all gradients are balanced over one TR period. Therefore it requires high-performance gradient technology to obtain a very short TE and good shimming. If all imaging gradients are balanced then the phase of the transverse spin magnetisation is preserved and all the spins evolve under equivalent free precession conditions over each TR without being affected by the phase and frequency encoding gradients. Figure 3.12 shows the pulse sequence diagram for a bTFE.

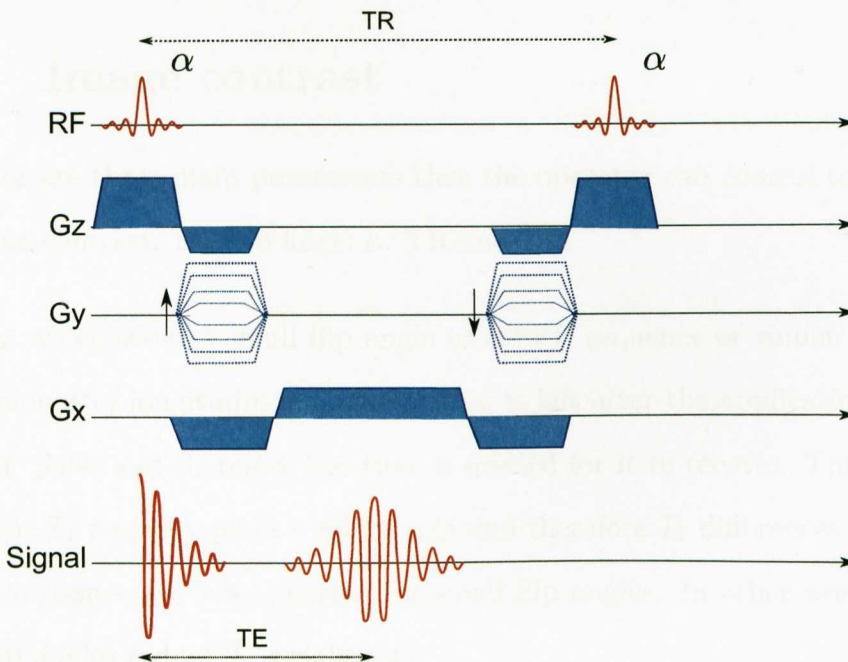


Figure (3.12): bTFE pulse sequence diagram.

Essentially, bTFE is a fast version of the FFE sequence and this allows preparation steps to be added before start of readout. Preparation steps are very useful because in fast GE techniques, the use of ultra-short TR doesn't give an optimal tissue contrast. The preparation step, i.e. before the RF pulse, allows the tissues to develop a certain contrast. If we consider the inversion recovery prepared method, a  $180^\circ$  pulse is applied before the RF

pulse, providing  $T_1$  weighting and allowing the suppression of different tissues. In this work the bTFE has been used for the  $T_2$  quantification. In particular, a  $T_2$ -prep bTFE has been used, consisting of a bTFE preceded by the spin echo preparation step

$$90^\circ \frac{TE}{2} 180^\circ \frac{TE}{2} 90^\circ \quad (3.27)$$

This pulse sequence, similar to SE, provides  $T_2$ -weighted contrast before the RF pulse. The longer the prep time, the more  $T_2$  decay occurs and the more  $T_2$  weighted the tissue contrast becomes. The bTFE sequence is very useful in the abdomen where EPI shows susceptibility artifacts.

### 3.11 Image contrast

There are three main parameters that the operator can control to modify the tissue contrast: the flip angle  $\alpha$ , TR and TE.

$\alpha$  When we consider a small flip angle in a FFE sequence or similar, a large amount of longitudinal magnetisation is left after the application of the RF pulse and therefore less time is needed for it to recover. This means that  $T_1$  recovery plays a minor role and therefore  $T_1$  differences between two tissues are less apparent for small flip angles. In other word, small flip angles reduce  $T_1$  weighting.

From equation 3.25 it can be deduced that the transverse magnetisation is directly proportional to  $M_0$ , therefore the tissue contrast is dominated by the proton density.

On the contrary, a large  $\alpha$  means a better differentiation of the  $T_1$  characteristics, leading to a better  $T_1$  weighting. However, this is true as long as TR is large because otherwise there will not be enough time for  $T_1$  recovery.

**TR** A short TR implies that the transverse magnetisation has not enough time to decay before the next pulse. The residual transverse magnetisation ( $\exp(-TR/T_2^*)$ ) will contribute to the next signal, therefore there will be  $T_2^*$  weighting. Conversely, a long TR will reduce the steady-state component thus reducing  $T_2^*$  weighting and it will also allow more recovery of the  $T_1$  curves. In other words, a longer TR enhances  $T_1$  weighting.

**TE** The role of TE is similar in both GE and SE sequences. A short TE reduces  $T_2^*/T_2$  weighting and increases  $T_1$  and proton density weighting. A long TE will enhance  $T_2^*/T_2$  weighting.

## 3.12 Artifacts

There are many sources of artifacts in MRI. Image processing, patient and gradient related and magnetic susceptibility artifacts are briefly described here.

### 3.12.1 Image acquisition related

**Chemical shift** Protons from different molecules precess at slightly different frequencies as discussed in section 2.2.7 and this chemical shift increases with increased field strength or lower gradient strength. The chemical shift affects the images in particular at water/fat interfaces. The protons in water precess slightly faster than those in fat, with a difference of about 3.5 ppm and frequency separation  $\Delta f$  increases with the static field strength  $B_0$ . In this case, a misregistration of the signal from fatty tissues occurs, since fat and water spins are encoded as if they were in different voxels. This artifact only occurs in the frequency encoding direction and results in the formation of a bright band toward the lower frequencies and a dark band toward the higher frequencies. It is possible to increase the strength of the frequency encoding gradient thus

increasing the bandwidth per pixel so that fat and water are contained in the same voxel. It is also possible to use the so called STIR (Short TI Inversion recovery) sequence. In this case by selecting the TI carefully the signal from fat can be nulled: the appropriate TI depends on the  $T_1$  and should be about 70% of the  $T_1$ . For example, fat has a  $T_1$  of 220 ms at 1.5T, so if the TI is set to be equal to 150 ms then the signal from fat can be suppressed. Fat has a very short  $T_1$  compared to water, white or gray matter therefore it reaches the null point quicker. At the null point for fat, if we draw the  $T_2$  decay curves, fat starts at zero and stays at zero. There will be no transverse magnetization from fat in the x-y plane and water will have the usual  $T_2$  curve. This means that after a  $180^\circ$  inverting pulse, we wait a time  $TI=0.693T_1(\text{fat})$  and we give the  $90^\circ$  pulse. All other tissues will have longitudinal magnetization that will flip into the x-y plane, whilst fat will give no signal in the x-y plane because there is no longitudinal magnetization to flip. Other techniques to eliminate the fat signal include the use of spectrally selective pulses prior to the imaging sequence. A spectrally selective pulse flips only the longitudinal magnetisation of fat into the transverse plane providing that the pulses bandwidth is wide enough to cover the lipid frequencies. The transverse magnetisation of fat is then canceled using spoilers so that the subsequent excitation pulse will flip the longitudinal magnetisation vector of water protons only into the transverse plane. The time between the saturation pulse and readout pulse is usually short to offset the fast recovery of fat magnetisation.

**Nyquist ghost** It is a phase ghost that arises because of imperfections in the rephasing-dephasing cycle of the rapidly switching frequency encoding gradient. The origin of the Nyquist ghost is a mis-positioning of every alternate refocusing of the FID in EPI. Alternate line of k-space are therefore mis-registered. As a result, following the Fourier transform, an

extra periodicity is introduced in the image. Phase correction filters can be derived from a reference scan and can be applied to every line of the image data.

**Aliasing (wraparound)** It consists of some of the anatomy being displaced to the opposite side of the image. This is due to the part of the body which are outside the FOV which are assigned a frequency that is not included in the range of Nyquist frequencies, i.e. the frequencies between the maximum frequency at one end of the FOV and the minimum frequency at the other end. The computer cannot distinguish these frequencies and therefore it will assign lower frequencies. The perceived frequency will be the actual frequency minus twice the Nyquist frequency. This artifact only occurs in the phase encoding direction, since in the frequency encoding direction a low-pass filter is used so that frequencies higher than the Nyquist limit are eliminated. If the aliasing occurs in the phase encoding direction, it is possible to increase the number of phase encoding steps, at the expenses of time.

### 3.12.2 Patient-related

This type of artifacts regard the voluntary or involuntary motion of the patient and are also only in the phase encoding direction. The motion due to blood flow is periodic and will therefore cause a ghost artifact in the AP direction (corresponding to  $G_y$ ). In this case, cardiac gating or flow compensation can be used. Random motion is caused by the patient's voluntary or involuntary movements, including breathing and swallowing. These artifacts are predominant when imaging the abdomen. To reduce these artifacts, the patient can be properly instructed or given sedatives or drugs like glucagon to reduce bowel peristalsis.

Respiratory compensation or breath hold imaging are also useful to over-

come the breathing motion artifacts.

### 3.12.3 Gradient-related

Eddy currents are small electric currents generated when the gradients are rapidly switched on and off. During ramp periods and especially when high slew rates are used, stray parts of the changing gradient fields can pass through the surrounding conducting structures inducing eddy currents. Cryostat and radiation shields in the case of superconducting magnet are the most likely to be affected because they are close to the gradients and their resistance is very low. Because each metal structure has its own resistance and inductance, a voltage  $V$  is induced in these structures according to Faradays law of induction  $V=d\phi/dt$ . This voltage induces eddy currents  $I$  that cause a distortion in the gradient profile which in turn causes artifacts in the image. Also, gradients are not perfectly linear and therefore there can be local magnetic distortions and image artifacts. Spatial distortions can be minimised by reducing the FOV or by decreasing the frequency bandwidth while keeping the gradient field strength constant.

### 3.12.4 Magnetic susceptibility

As previously discussed (section 2.2.8), all substances get magnetised when immersed in a magnetic field to an extent that depends on the magnetic susceptibility. Differences in local tissue susceptibilities, for example at tissue boundaries, produce spatial variations in the magnetic field. Since spatial encoding relies on a homogeneous magnetic field, this inhomogeneity can result in artifacts in MR images. Typically, susceptibility artifacts produce geometric distortions as well as signal loss and image blurring. Because they are caused by inhomogeneities, susceptibility artifacts are generally worse on GE images than SE images and can be also marked in EPI. These artifacts can be

minimised by using a short TE but they cannot be completely removed. The susceptibility artifact can also be advantageous because it can be used to get information on the properties of the tissues. In particular, neural activation can be detected by using the blood oxygenation level dependent (BOLD) contrast based on the local magnetic susceptibility difference between oxygenated and de-oxygenated blood.

This chapter has presented the main principles of MRI. The next chapter will introduce the components of the MR hardware and its safety issues.

# Chapter 4

## Instrumentation

### 4.1 Introduction

This chapter gives an overview of a magnetic resonance imaging system with particular reference to the hardware used for the experiments presented in this work. The following sections will describe the main components of an MRI scanner: the main magnet, the shim coil, the gradients and the RF coil. These components are controlled by a computer station where the user is able to change the parameters for the scanning. Safety regulations are also given at the end of the chapter.

### 4.2 Main magnet

The experiments performed in this thesis were performed on two Philips Achieva scanners (1.5 T and 3.0 T). Figure 4.1 shows a schematic diagram with the principal components of an MR system.

For MRI experiments, the magnetic field produced by the main magnet is required to be highly spatially uniform and to have good temporal stability. Inhomogeneities of the field produce line broadening and image distortions be-

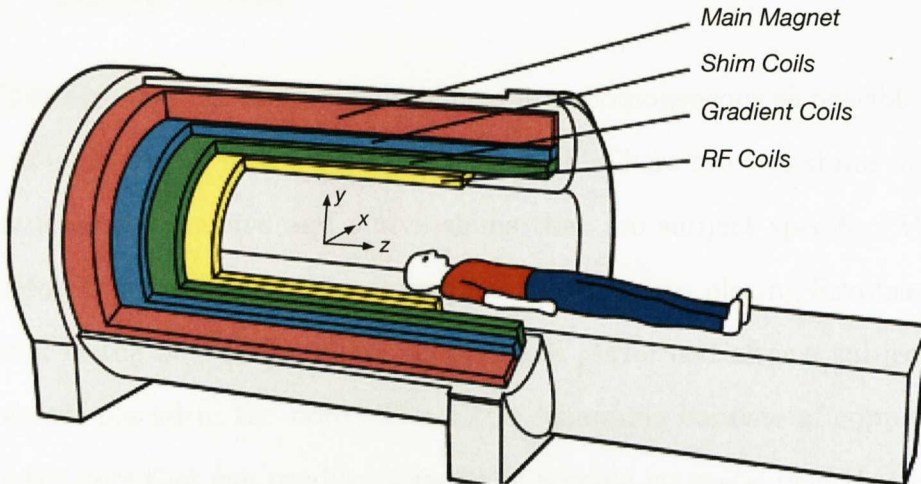


Figure (4.1): Schematic of a whole-body MRI scanner with the principal components. Courtesy of [25].

cause of the varying frequency offset while temporal variations produce image blurring. To produce an intense homogeneous magnetic field, MRI scanners usually use superconducting materials that are able to support large electric currents without requiring an external power supply. For the Philips systems used, the superconducting wires are made of Niobium-Titanium (Nb-Ti) alloy with critical temperature around 10K. In order to maintain the superconductivity a cooling system consisting of liquid helium is used and it is maintained with water and air cooled chillers.

Another characteristic of the main magnet is the field outside the bore (fringe field) and how far it stretches. For safety reasons, access is usually restricted to areas above 0.5 mT for people with particular conditions, such as having pacemakers or metal implants. In order to reduce the fringe field, magnets can be passively or actively shielded. Active shielding involves placing loops of superconducting material to cancel out the fields from primary coils [26]. Passive shielding is used for ultrahigh field systems: large amounts of ferromagnetic material, commonly iron, are placed around the magnet.

### 4.3 Shim coils

To ensure that the main magnetic field is as homogeneous as possible, a set of shim coils are set in the bore of the magnet. There are two shims systems in our magnets: passive and active shims that are subject specific. Passive shimming is used in most clinical magnets and involves placing ferromagnetic material in the bore [27]. Active shimming is performed after a subject or a sample are placed in the bore. The active shimming consists of copper coils inside the bore that can produce a spatially varying magnetic field that can be adjusted for each subject. On the Philips system some automated preparation steps mapping the field homogeneity are included in the pulse sequence set-up process.

### 4.4 Gradient coils

Gradient coils are used to vary the magnetic field homogeneity for frequency and phase encoding and for slice selection. They consist of large resistive, low inductance coils wound on a cylindrical surface and water cooled to prevent overheating. There are several characteristics that define a gradient coil performance such as acoustic noise, peripheral nerve stimulation (PNS), efficiency, resistance and inductance. PNS is caused by the rapid switching of the gradients that induces an electric field in the human body stimulating peripheral nerves (see section 4.6). Gradient coils are also shielded to avoid eddy currents being produced in the bore and in particular in cooled cryostat which has low resistance so eddy currents can persist for very long.

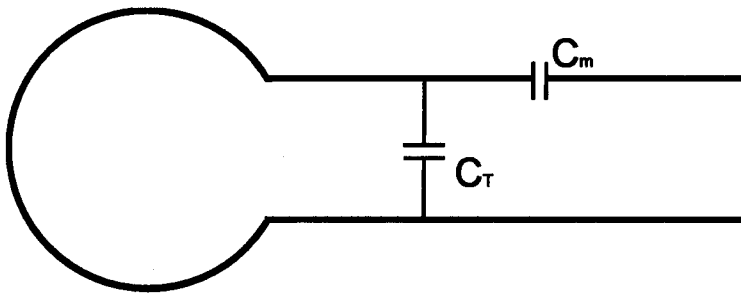


Figure (4.2): Configuration of a basic coil.

## 4.5 RF coils

Radiofrequency coils are used for transmission and reception of RF signals and are positioned closest to the subject. A basic coil consists of a loop of wire with two capacitors (figure 4.2). The value of  $C_T$  enables the coil to be tuned to the Larmor frequency of the nucleus of interest, e.g. 19F. Moreover, the impedance of the RF coil needs to be matched to the impedance of the amplifier so that the reflections are minimised and the signal transmitted and received is maximised. The tuning and matching of the coil are very important because the positioning of a subject or a phantom can influence the 'loading' of the system.

### 4.5.1 Body coil

The body coil is the largest coil associated with the Philips scanners and it is a fixed part of the magnet and can be used for both transmission and reception. Usually, local receive coils are used in order to increase the signal to noise ratio (SNR); since SNR decreases as  $1/r^2$ , the receive coils are positioned as close as possible to the area to be investigated. This is easily done with surface coils as they are usually small and flexible but they do not provide the same large field of view as the body coil. In the work described in this thesis the body coil at 3T has been used to acquire proton imaging in the human body and in conjunction with the fluorine coil. For the proton imaging at 1.5T a SENSE 4-element abdominal body coil has been used, represented in figure

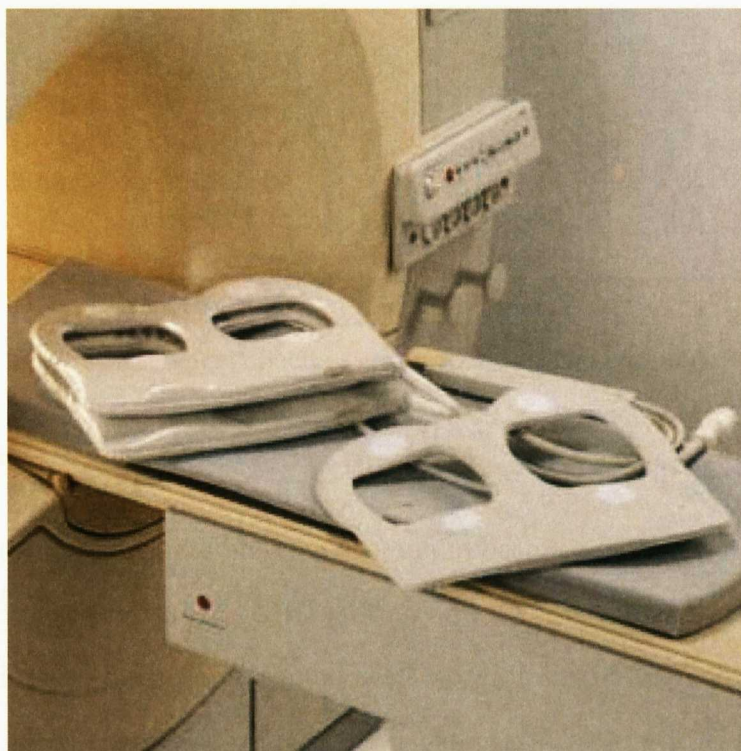


Figure (4.3): The SENSE 4-element abdominal body coil used for proton imaging on the Philips Achieva 1.5T scanner.

4.3.

#### 4.5.2 Fluorine coil

The fluorine coil used is a PulseTeq Flexible 20 cm Surface Coil Pair designed for imaging of the internal organs of the trunk (figure 4.4). It is possible to use the coil pair together, one at the front of the body and the other on the back as shown in the figure 4.5.

It has both transmit and receive capability at fluorine frequency at the field strength of 3T. It is compatible with a transmit body RF coil and it can be left in position whilst low flip angle pilot hydrogen studies are undertaken.

In this work several tests have been performed on this coil in order to characterise its performances. Details are provided in section 8.4.

Coil only length	32 cm
Width	27 cm
Height	2.3 cm
Operating frequency	120.2 MHz
Weight (coil, cable, traps and interfaces)	4.5 kg

Table (4.1): Technical specifications for the PulseTeq fluorine coil.

## 4.6 Safety

MRI is a relatively safe imaging technique because it does not involve ionizing radiation. However, the MRI system and its environment are potentially very hazardous to both patients and staff working in the MRI unit.

The primary hazard associated with the static magnetic field is that of ferromagnetic attraction. When a ferromagnetic object is brought close to the magnet, it will experience a force. If sufficiently close, this can turn the object into a dangerous projectile. People with pacemakers, ferromagnetic foreign bodies or metallic implants should not be allowed to go near to an MRI scanner. As previously stated, the fringe fields can also be a possible

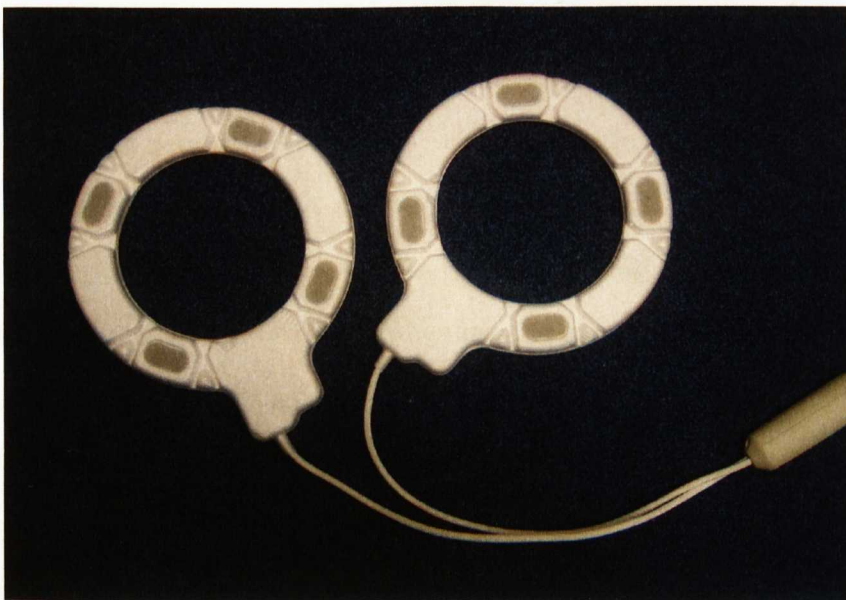


Figure (4.4): PulseTeq Fluorine Coil



Figure (4.5): Position of the fluorine coil on a subject: one coil is on the subject's front and the other coil on the back over the desired imaging area

hazard so a controlled area is defined within the vicinity of the magnet.

The MR scanner is very noisy during operation especially at high field. This is due to the Lorentz force generated by the coils when a current is pulsed through them in the presence of the static magnetic field. Appropriate ear protection must be worn (ear plugs and/or headphones) to reduce the noise level.

The main biological effect of RF is the heating of tissue. The human body has the ability to remove this heat by both conduction and blood flow. Some poorly vascularised structures (lenses) and structures with no pain sensors (brain) can be affected if no control on the RF heating has been done. Therefore there is a restriction on all scanner for the amount of power that can be deposited, the specific absorption rate (SAR). The SAR measures the rate at which the energy is absorbed by the body and it is defined as the power absorbed per mass of tissue (watts per kilogram). In particular SAR is defined as follows

$$SAR = 0.5 \frac{\sigma \pi^2 f^2 r^2 B_1^2 D}{\rho} \quad (4.1)$$

where

$r^2$ : square of conductor loop

$f^2$ : square of Larmor frequency

$B_1^2$ : square of RF field

$\rho$ : mass density

D: duty cycle (=total RF pulse times/TR). Power deposition is manifested as an increase in tissue temperature. A rise of less than 1  $C^\circ$  (corresponding to 2W/kg) is generally acceptable to a normal healthy person. SAR level can be reduced by using quadrature rather than linear coils for transmission, avoiding the whole body coil when other transmission coils can be used, increasing TR, reducing number of slices, reducing echo train length in fast sequences and reducing the RF tipping angle. Tattoos can also lead to overheating because of the presence of ink containing metal.

There is a small risk of patients receiving burns through the coupling of RF energy into wires or cables that are touching the patient. Care must be exercised in ensuring that cables are not formed into loops prior to imaging. There is also the risk of cold burns due to cryogenic liquids.

The switching of the gradients induces electrical currents in conducting tissues according to Faradays induction law. These currents in the tissues may cause peripheral nerve stimulation (PNS) that may result disconcerting to the patient but is not itself hazardous. Theoretically there is also the hazard of stimulating the cardiac muscle. To reduce these risks, there is a dB/dt limitation set by the American and European regulatory agencies.

Contrast agents can be potentially harmful because of their adverse effects. The most common intravenous contrast agents contain gadolinium (see section 2.2.9). They are considered safe if administered intravenously but they are not indicated for patients with renal failure. Restrictions on the use of contrast

agents may apply during pregnancy and to nursing mothers because they can enter the bloodstream.

# Chapter 5

## MRI of the gastrointestinal tract

Over the past years a lot of effort has gone into the development of methods to monitor the GI tract after administration of drugs and the investigation of the anatomical changes due to GI diseases [28]. However the study of normal physiology of the GI tract, including its response to food and functional disorders, is still only investigated with MRI by very few centres.

Imaging the anatomy and the function of the GI tract is challenging for various reasons: firstly its three-dimensional structure is highly variable between individuals, secondly respiration and peristaltic movements cause artifacts and increase partial volume errors between bowel and adjacent tissues and this is worsened by the fact that bowel can assume varying signal intensity including that of normal or abnormal tissues. It also has to be taken into account that two different states, fasted and fed, are normally considered and they vary depending on the physical activity as well.

MRI of the GI tract was initially very limited because of the presence the artifacts mentioned but the advent of fast MR imaging allowed greater anatomic coverage in a single breath hold thus making possible to acquire a

single section in less than 1 second. In comparison with MRI, other methods such as X-rays and CT scans have excellent spatial resolution and are fast and relatively cheap but the delivery of ionising radiation to the subject doesn't allow the study of GI physiology in healthy volunteers. On the other hand, ultrasound could be used because it is a safe and cheap technique but the presence of air and fat in the abdomen makes it difficult to obtain clear images. MRI is therefore an irreplaceable technique for physiological studies of the GI tract, for the lack of ionising radiation delivered to the subject, for the superb contrast and resolution available for the observation of anatomical structures and the possibility of observing the GI tract without any invasive procedure such as enemas and delivery of contrast agents.

This chapter introduces the main features of the gastrointestinal tract and some of the MRI methods that are used in this work to study the function of the GI tract in both healthy and diseased subjects.

## **5.1 The gastrointestinal tract**

### **5.1.1 Anatomy and physiology of the gastrointestinal tract**

The gastrointestinal tract is a muscular tube starting from the oral cavity, where food enters the mouth, continuing through the pharynx, oesophagus, stomach and intestines to the rectum and anus, where food is expelled (figure 5.1). The entire GI tract has a similar basic structure (figure 5.2) even if local variations occur in the different specialised parts. The most internal part is the epithelium which can be simple or stratified, depending on the function, and that is supported by a tissue containing blood vessels, nerves and glands that support the mucosa. The different layers of mucosal muscles allow the contraction of the tube thus changing the shape of the lumen and providing

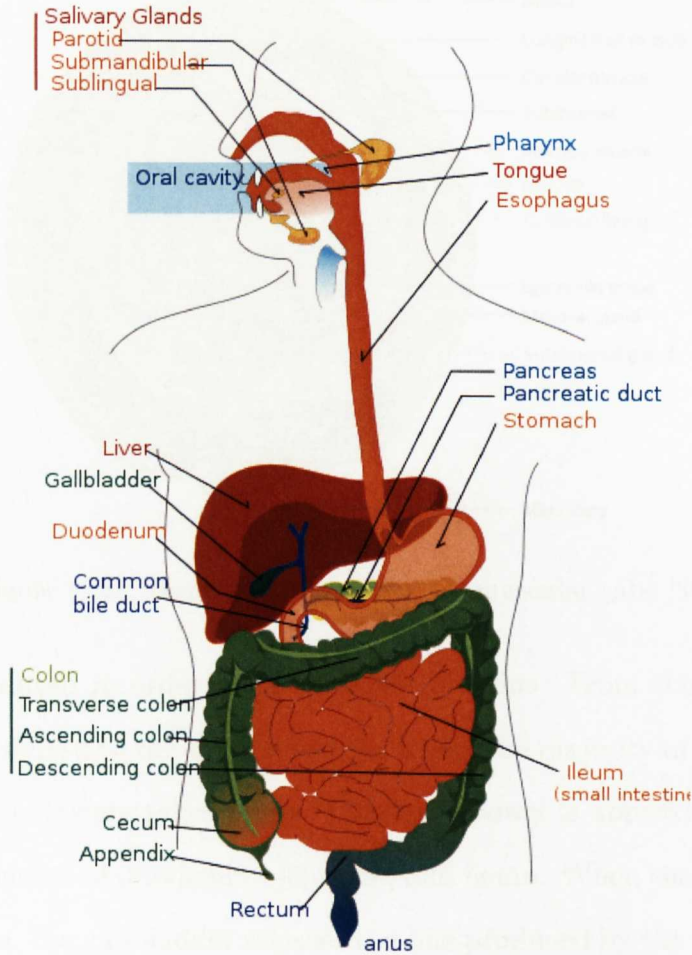


Figure (5.1): The gastrointestinal tract [29].

the peristalsis of the food, which is controlled by specific neural innervations. The outer layer of the GI tract is formed by fat and another layer of epithelial cells called mesothelium.

The main purpose of the gastrointestinal tract is to digest food and absorb the nutrients, to provide energy to the body. A whole set of different organs cooperate to this aim by secreting enzymes: salivary glands, liver, pancreas and gall bladder play an important role.

When food is ingested into the mouth digestion begins both with the mechanical process of chewing and with the softening action of saliva which contains an enzyme called amylase. Following this first processing the food enters the stomach via the oesophagus, where further digestion takes place. The hormone gastrin is secreted on the arrival of food in the stomach and the enzyme

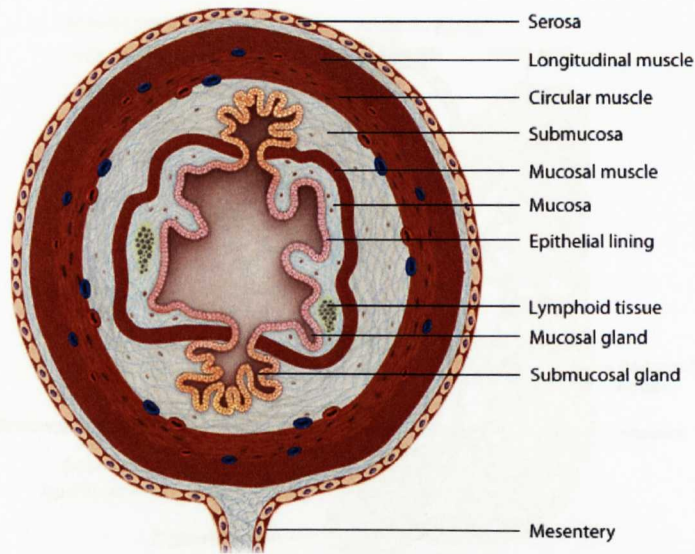


Figure (5.2): Basic structure of the GI muscular tube [30].

pepsin is produced in order to break down proteins. From the stomach the chyme is transferred to the small intestine, where the majority of digestion and absorption of nutrients takes place. The small bowel is approximately 6m in length and consists of duodenum, jejunum, and ileum. When the chyme enters the duodenum, the gallbladder releases the bile produced by the liver, in order to emulsify the fat and neutralise the acid. The jejunum is where the majority of digestion and absorption occurs. The last part of the small intestine, the ileum, is responsible for the absorption of vitamin B12, bile salts and any unabsorbed nutrients. It empties into the caecum at the ileocaecal junction. The caecum is the first part of the large intestine which consists of the appendix, caecum, ascending, transverse, descending and sigmoid colon, and the rectum (figure 5.3). It has a length of approximately 1.5 m and a width of 7.5 cm. The main functions of the large intestine are the reabsorption of water, salts, sugar and vitamins and the accumulation of unabsorbed material to form faeces. Under normal conditions, approximately 90% of salt and water entering the proximal colon (650–800 ml) is absorbed [31]. This happens despite the non-villous structure of the colon which results in a smaller capacity for absorption compared to the small bowel. Therefore, the contact time and the

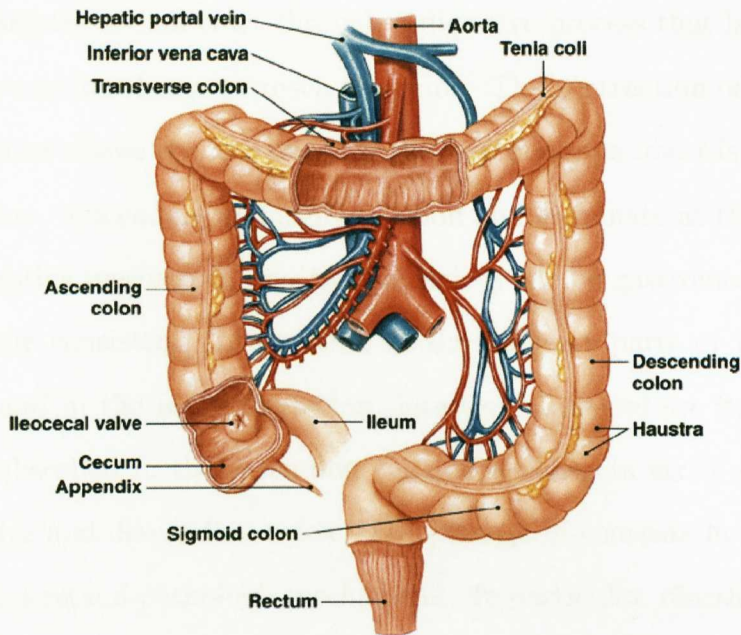


Figure (5.3): The colon [32].

motor activity is an important factor for the fluid transport in the colon. The ability of the colon to remove water from faeces necessitates a tight epithelium and osmotic gradients.

The wall of the colon is made up of several pouches (haustra) that are held under tension by three thick bands of muscle (taenia coli). The mucosal surface is flat with several deep intestinal glands. Colonic contents are far from homogenous with a spatially organised bacterial flora which others have described at a microscopic level [33].

The rectum is the final 15 cm of the large intestine. It expands to hold faecal matter before it passes through the anorectal canal to the anus. Thick bands of muscle, known as sphincters, control the passage of faeces.

Following ingestion of food, a combination of four involuntary movements facilitates the passage of intestinal contents along the gastrointestinal tract toward the rectum. These contractions are defined as pendular, segmental, peristaltic and vermiform. Pendular and segmental movements are responsible for the mixing of the food in the stomach as a result of smooth muscle contraction. Peristaltic movements push the mixed contents from the stomach

along the gastrointestinal tract through a digestive process that lasts approximately three to four hours to reach the colon. The contraction of the colonic smooth muscles allows the movement of the food contents towards the ascending, transverse, descending and sigmoid colon and terminate at the rectum.

The digestive mechanism and the physiology of the gastrointestinal tract determine the consistency of contents in the different parts of the gut. In the cecum and in the ascending colon, intestinal contents are fluid. As the water gets absorbed in the ascending colon, the contents arrive semisolid in the transverse and descending colon. The passage of contents in the colon is crucial to understand pathologic mechanisms. In particular, diarrhoeal disease implies a non efficient absorption of water in the ascending colon, thus entailing a watery and unformed stool. On the contrary, if food passes too slowly through the colon, there will be too much fluid absorbed and the stools result hard and dry, the primary sign of constipation.

The food reaches the rectum after several more hours following ingestion and it causes rectal distention, contraction of muscles and relaxation of the internal anal sphincter and the impulse and decision to defecate. A normal number of bowel movements for adults varies from person to person and may range from three per day to three per week, depending on numerous factors. The diagnosis of bowel disease has to consider this great subjective variability in order to correctly identify significant changes from normal physiology.

### **5.1.2 Definition of colon regions**

In this work, quantitative analysis is performed on the different regions of the GI tract, for instance volume measurement and the anatomical location of ingested capsules within the gut. Some of the analysis has been performed by different operators in order to calculate the inter-observer variability of our methods. For this reason and given the high anatomical variability of the subjects, the exact definition of the different regions in the gut is very

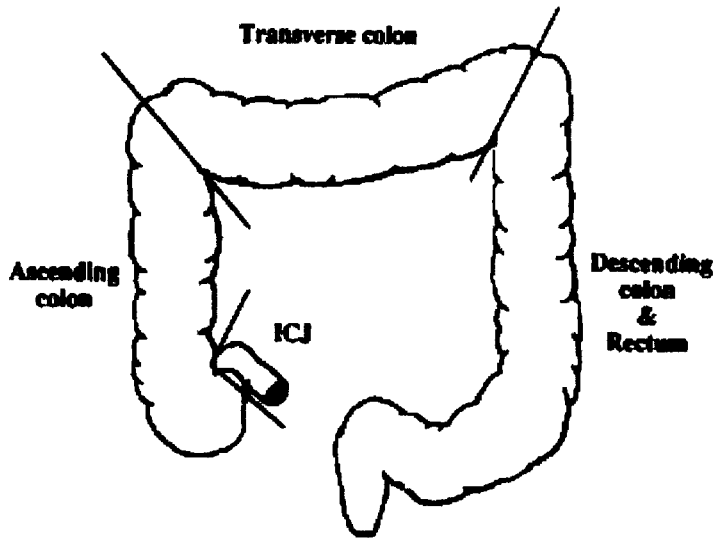


Figure (5.4): The definition of the regions of the colon according to Watts et al [34].

important, especially in the colon. To this aim, we referred to the same criteria used by Watts et al. [34], shown in figure 5.4. If not otherwise stated, the colon images were divided into four regions by simply drawing a diagonal line across the colon on the turning points: the ileo-caecal junction (ICJ), the ascending colon, the transverse colon, and the descending colon/rectum.

### 5.1.3 Colonic motility and transit

In a healthy subject, colonic motility includes two types of motor activity: segmental and propagated contractile events. Segmental activity is the most frequent and regards the low amplitude contractions that allow the optimal absorption of the contents. The contractions are non-propulsive and can be recorded as increases in luminal pressures. Propagated contractile events are occasional propulsive movements (mass movements), which are generally hard to record because they occur rarely. They can happen in both forward and backward directions, on average more than 100 times a day, and are responsible for the transport of fluids within the colon. The high amplitude propagated contractions that precede the defecation are much less frequent, with a large

inter-individual variation [35].

Although much less pronounced than small bowel motility, colonic motility also shows some rhythm, with a strong inhibition during sleep and maximum activity after awakening and after meals. This postprandial increase in colonic activity lasts usually for at least 2 hours, being longer for more fatty meals.

Most information about the colonic contractions have been obtained from balloon catheter measurements of the rectum and distal colonic segments, because of the difficulties of intubation along the entire tract. As an example, Haggart et al [36] described a colonic manometry study where they showed that the intake of a meal increases the motility for both normal and constipated patients. Other techniques include the application of scintigraphic measurements that allow the investigation of the entire gastrointestinal tract. This technique is particularly useful to study the transit of dosage forms in the gut.

Colonic transit is of great relevance when considering *in vivo/in vitro* relationships for oral controlled release dosage forms. The importance of the technology for oral drug delivery is due to the possible increase of efficacy of the drugs with minimised side effects. Even if the colon is not as important as the small bowel in the absorption process, its additional surface for absorption can prolong the time of treatment and it can make the difference when trying to increase the interval between doses. The transit of dosage forms through the colon is therefore of great interest.

#### 5.1.4 Colon disorders

Functional disorders of the bowel most commonly affect the colon and the rectum and the direct cause is frequently unknown. The most common diseases are irritable bowel syndrome (IBS), Crohn's disease and diverticulitis.

IBS is a functional bowel disorder characterized by chronic abdominal pain, discomfort, bloating, and alteration of bowel habits in the absence of any detectable organic cause. Diarrhea or constipation may predominate, or they

may alternate (classified as IBS-D, IBS-C or IBS-A, respectively). Even if the cause is not known, it may begin after an infection or after a stressful event. Even if IBS doesn't lead to more serious conditions, it is still considered to affect the quality of a sufferer's life and it can also be of high economical and social impact.

Crohn's disease is a chronic, inflammatory condition of the intestine that can affect any area of the digestive tract but it is usually confined to the lower end of the small intestine (ileum) and the colon. Even if the cause is not known, Crohn's disease is thought to be linked to a problem with the body's immune system which leads to chronic inflammation. The symptoms include intermittent attacks of diarrhea and abdominal pain, weight loss, and fever. Rarely, the intestine may become blocked or ulcerate.

Diverticulitis results if a diverticulum in the colon becomes inflamed, thus increasing the risk of infection from the bacteria that can spread in the abdominal cavity if the diverticulum bursts open. This can cause a potentially fatal illness (peritonitis). Sometimes inflamed diverticula can cause narrowing of the bowel, leading to an obstruction. Also, in some cases there can even be a break in the colon and stool can flow into other organs.

## 5.2 Functional MRI of the GI tract

MRI of the gastrointestinal tract was limited during the early days of MRI because of the artifacts caused by breathing and peristaltic motion. With the advent of fast MRI sequences these problems were overcome. In particular, EPI allows the imaging of the stomach even at low field thanks to the excellent contrast between water-based liquid meals and the surrounding tissues [4, 37]. No additional contrast agents are necessary. Unfortunately imaging the small intestine and colon with EPI is not suitable because of the susceptibility artifacts especially at higher fields where the artifacts due to the air/water inter-

face worsen. In this case, ultra-fast imaging techniques such as fast spin echo (FSE, RARE or HASTE), balanced turbo field echo (bTFE) and fast field echo (FFE or FLASH) have been optimised and applied for use at both low and high field strength. However, with increased field strength the imaging time also increases because of the increase in RF power deposition, limited by the specific absorption rate (SAR) safety limits. The availability of different ultra-fast sequences on commercial scanners allow the optimisation of imaging techniques suitable for all the different regions of the GI tract.

### 5.2.1 Measuring gastric volume

The evaluation of the gastric emptying plays a key role in the studies involving digestion of food and satiety. The rate of gastric emptying depends on a series of different factors including the physical and chemical state of food but also external factors such as stress or intense pain. The importance of measuring the stomach volume is evident in both physiological and pathological conditions. In this study MRI sequences have been optimised at 1.5 T to allow automatic segmentation. The stomach volumes were measured from a balanced turbo field echo (bTFE) sequence using Analyze<sup>®</sup> software (Mayo Clinic, Rochester, MN, USA) by drawing around the contents of the stomach as regions of interests (ROIs) and then summing all the volumes. The Analyze software available provides an edge-finding tool that can be used to easily identify the definition between stomach contents and air or surrounding tissues, thus improving the accuracy of the measurement.

### 5.2.2 Measuring small bowel water content

The measurement of the small bowel water content (SBWC) is of fundamental importance when studying the gastrointestinal physiology and pathology such as irritable bowel syndrome (IBS) and celiac disease. SBWC depends

on the complex interactions between the liquids absorbed and secreted. The balance between the liquids coming from the stomach and the liquids secreted by the small bowel and also the amount of water absorbed and the progression to the colon determine the SBWC. The intestinal motility also plays a key role on this regard. It is regulated by the central nervous system and it changes between the fed and the fasted state. Fasting intestinal motility is highly episodic with propulsive events occurring every 1–2 hours. The fed state is characterised by constant small movements in order to improve the absorption.

In order to visualise the anatomical details of the small bowel, it is often distended by administering water and preparations that prevent absorption and also by using contrast agents to improve the image quality. These procedures are not ideal when investigating the physiology of the normal gastrointestinal tract because they are highly invasive and they alter the normal balance between the absorption and the secretion of liquids in the gut.

In this work the SBWC has been measured by using a non-invasive method developed by Hoad et al. [38]. It uses a heavily  $T_2$  weighted RARE sequence originally used to study the biliary tract [39], optimised at 1.5 T. The hypothesis is that in the TSE images any pixel with a signal intensity above a given threshold is filled with “free” water. As this technique is based on MR signal intensity rather than measured parameters, the signal must be normalised. Cerebral spin fluid (CSF) is an ideal internal normalising marker because it is present in most slices and it is in the centre of the field of view thus overcoming variations due to the scanner instabilities and repositioning.

After the acquisition, an in-house software written in IDL<sup>®</sup> (Research Systems Inc. Boulder, Colorado, USA) by Dr Caroline Hoad allows the evaluation of the SBWC. The operator selects the centre of the CSF on each slice in which it is visible and then the ROIs can be drawn.

This methods assumes that only pixels with a signal bigger than the thresh-

old contain water, which can lead to an underestimation of the amount of free water because of partial volume effects. Improving the resolution would reduce this problem but it would increase the scanning time therefore introducing other sources of errors such as movement of the water through the bowel. In addition this method has never been validated in the colon, where normally a much smaller amount of water is present. In the next chapters, the extension of this method to the colon is presented, together with the optimisation of other MRI methods to investigate the colonic function in health and diseased subjects.

# Chapter 6

## Methods for measuring physiology of the colon

### 6.1 Introduction

This chapter describes the development of techniques to image colon function under physiological condition with proton MRI. In particular, the processing of the colonic contents is monitored with a multilateral approach: the change in geometric volumes and in the amount of water in the ascending colon is monitored.  $T_1$  and  $T_2$  values are measured in vitro and in vivo. In addition novel methods to characterise the colonic contents are introduced with a texture analysis approach to define the mesoscopic structure of the colonic contents.

## **6.2 Colonic response to an experimental model of human diarrhoeal disease**

### **6.2.1 Introduction**

This study aims at an improved understanding of the water distribution within the ascending colon (AC) both in functional and organic colonic disease conditions. In particular an aim was to determine the approximate time course of the physiological response in the colon to assist in planning future experiments. The MRI techniques used allow the monitoring of colonic function without invasive bowel preparations, which are often used to improve anatomical detail in clinical MRI of the colon. In this work, two contrasting test meals have been used: a readily absorbable glucose drink (the control meal) and a non absorbable mannitol drink, which provides a model of acute diarrhoeal disease. The response of the gut over time to these two different meals was observed. This study also presents some preliminary results regarding motility scans for the observation of peristaltic movements in the AC. The colonic movements are one of the main factors to distinguish the difference between physiologic and pathologic conditions. In particular, diarrhoea is thought to result from colonic hypermotility, while constipation is associated with underactivity of the muscle. However, these phenomena are poorly understood and have only been investigated with invasive techniques as the manometry to measure colonic intraluminal pressures [40,41]. Being able to study the colonic motility with a noninvasive technique is therefore fundamental for future research and clinical applications.

## 6.2.2 Methods

### Volunteer selection

This 2-ways randomized double blinded study was approved by the University of Nottingham Medical School Ethics Committee and all volunteers gave written informed consent before the experiment. Healthy volunteers (n=10; 6 female, 4 male; mean age 26.3 years, age range=20–33) without known contraindications to MR imaging were recruited from the Nottingham University student population to take part in the *in vivo* study. All volunteers had no history of gastrointestinal disease, they were free from medication likely to alter GI motility and they were free from food allergy or intolerance. They were also asked to follow restrictions to diet and lifestyle for the day prior to the study day, including avoid taking foods with high fibre content to avoid excessive residue in the bowel on the study day, avoid spicy food since it can stimulate bowel secretions and avoid caffeine, alcohol and strenuous exercise for 18 hours before the study start time. Volunteers were asked to fast overnight (>12 h) except for a small cup of water on the morning of the study if it was consumed >1 h before arriving at the centre. The first two subjects were used to determine the length of the experiment, being imaged hourly up to 8 hours. The remaining subjects were imaged hourly up to 5 hours.

### Study protocol

All imaging was carried out on a 1.5 T Philips Achieva scanner with a SENSE 4-element abdominal body coil. Volunteers attended on two separate experimental sessions: they were first imaged at the fasted state as a baseline scan; subsequently they were given a drink containing either 5% mannitol or 5% glucose powder in 350 ml of still water (conditions randomized). Mannitol is a common laxative known to stimulate small intestinal secretion and can be used as a model for a range of diarrhoeal diseases, while glucose is known to

be rapidly absorbed. Volunteers were scanned at 60 minutes intervals for three hours after the drink, after which they were fed a large 1000 kcal test meal (400 g macaroni cheese, 100 g cheese cake and 250 ml still water) to elicit the colonic response to feeding. They were then scanned again every hour up to 5 hours after the drink (8 hours for 2 additional pilot subjects), see figure 6.1. A range of MRI sequences were used to image the ascending colon:

- For structural details of colonic contents: high resolution bTFE (TR=3.2 ms, TE=1.58 ms, acquired resolution = 1.50 mm x 1.50 mm, reconstructed resolution = 0.86 mm x 0.86 mm, 8 slices of 5 mm thickness, 0.58 mm gap, 16 seconds duration) acquired sagittally in order to have the whole length in one image;
- For the measurement of colonic geometrical volumes: a dual gradient echo (dual-echo fast field echo, FFE,  $TE_1 = 2.3$ ,  $TE_2 = 4.6$ , TR = 158 ms, acquired resolution = 2.01 mm x 2.87 mm, reconstructed resolution = 1.76 mm x 1.76 mm, 24 slices of 7 mm thickness, 13 seconds duration);
- For free water content measurements: a single shot, fast spin echo sequence (RARE) (TR=8000 ms, TE=320 ms, acquired resolution = 1.56 mm x 2.90 mm, reconstructed resolution = 0.78 mm x 0.78 mm, 24 slices of 7 mm thickness, 24 seconds duration);
- For  $T_2$  measurements: a  $T_2$ -prep bTFE sequence (TR= 3.0 ms, TEprep values (ms): 20, 29, 43, 63, 93, 137, 201, 295, 434, 637, acquired resolution = 2.00 mm x 1.56 mm, reconstructed resolution = 1.56 mm x 1.56 mm, 7 mm thickness, 150 seconds duration);
- For motility measurements: bTFE sequence single slice, sagittal (TR=3.0 ms, TE=1.5 ms, acquired resolution = 1.50 mm x 1.50 mm, reconstructed resolution = 0.86 mm x 0.86 mm, 15 mm thickness, acquired every 2.5 secs for 2 mins).

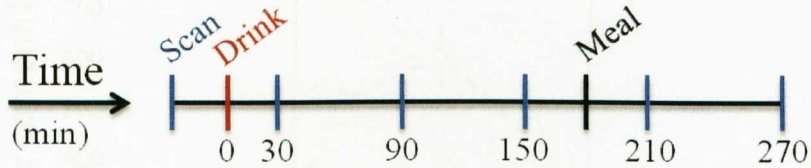


Figure (6.1): Protocol of the study for each occasion. The subjects were scanned fasted and immediately after the drink (mannitol or glucose) and then hourly for up to 5 hours after the drink. Details of the drinks and the meal are given in the text.

With the exception of the motility sequence, each image set was acquired on an expiration breath-hold with a duration between 13 and 24 seconds depending on the sequence. Including set-up and imaging the volunteers spent approximately 10 min inside the magnet for every time point, spending the rest of the time sitting upright in an adjacent room. The sequence for the motility measurement was set to be of 2 minutes because of time constraints of the complete study.

### 6.2.3 Results

All volunteers tolerated the experiment well, with no side effects experienced.

Figure 6.2 and 6.3 show the variation in the water content for the whole bowel and the AC averaged over the 10 volunteers, quantified from the RARE sequence: very little free water was seen in the small bowel and in the AC after the control drink, while a large amount of free water was visible in both regions after the mannitol drink.

Following the glucose drink the volume of free mobile water in the whole bowel did not vary significantly from the fasting baseline being  $124 \pm 24$  versus  $112 \pm 27$  ml at 90 min,  $p < 0.9$ . Conversely, after the mannitol drink, the water in the whole bowel rose from baseline  $109 \pm 36$  ml to  $590 \pm 73$  ml at 90 min,  $p < 0.008$ . The difference in the amount of free water that reached the AC at 90 min was particularly marked being  $2 \pm 1$  ml after the glucose drink and

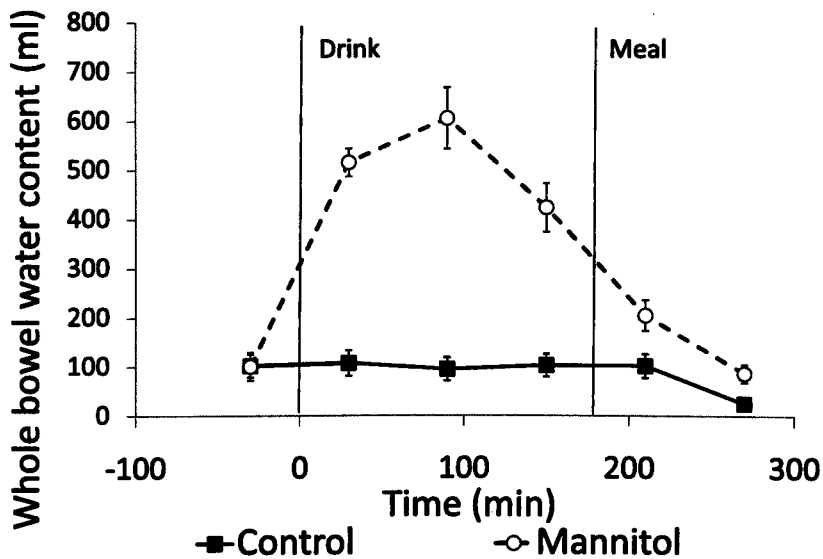


Figure (6.2): (Mean  $\pm$  STD) Total water content of the whole bowel measured using a RARE sequence showing a larger quantity of fluid after the mannitol drink compared to after the control drink.

73 $\pm$ 20 ml after the mannitol drink,  $p < 0.008$ . The water that arrived in the AC readily mixed with the colonic contents and caused distension of the AC.

The second larger meal was followed by a significant fall in total bowel water content from 396 $\pm$ 58 ml at time 150 min to 198 $\pm$ 37 ml at time 210 min with the mannitol drink ( $p < 0.0011$ ), whilst no corresponding change was observed for the glucose drink ( $p < 0.7$ ). The same trend was reflected in the total volume of the AC (figure 6.4). Its total (geometric) volume at 90 min was 146 $\pm$ 17 ml for glucose and 230 $\pm$ 18 ml for mannitol,  $p < 0.0004$ .

The  $T_2$  values calculated from the  $T_2$ -prep bTFE sequence showed an overall increase in the values for the mannitol case, while constant values around 50 ms were found for the control at all time points. Figure 6.5 shows the average values for all the volunteers including the two pilots that were imaged up to 450 minutes. This longer time scale allows to see the full change of the  $T_2$  values, increasing up to a maximum of 160 ms at 210 minutes and slowly decreasing toward normal physiologic values of around 50 ms at 450 minutes.

Further analysis was performed for the two pilots on the  $T_2$  in the ascending colon. The  $T_2$  were calculated in 3 different regions of the ascending colon in

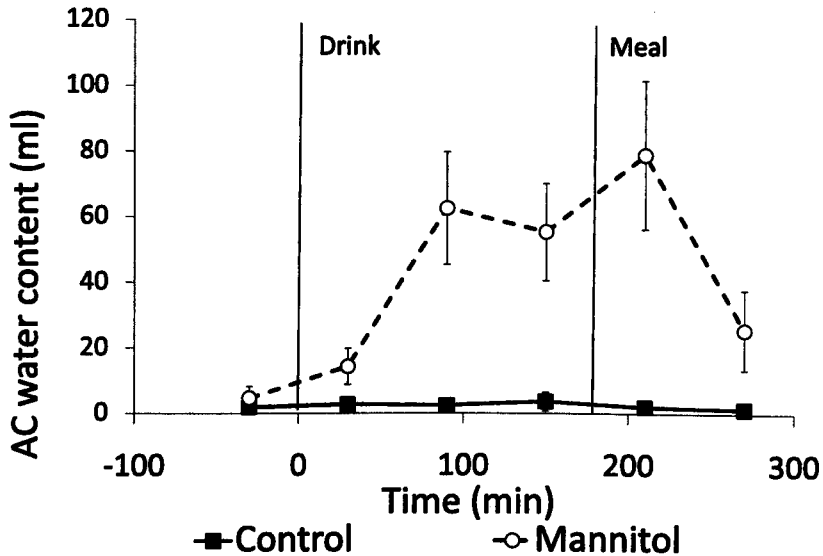


Figure (6.3): (Mean  $\pm$  STD) Ascending colon water content of the whole bowel measured using a RARE sequence showing a larger quantity of fluid after the mannitol drink compared to after the control drink.

order to evaluate any eventual difference in contents along the AC. Figure 6.6 shows an example for the ROIs defined as cranial, middle and caudal. The corresponding  $T_2$  values are shown in figure 6.7: a higher variability in  $T_2$  values between the regions is found from 180 to 270 minutes thus implying a greater heterogeneity of the colonic contents on the arrival of the fluids. No specific characteristics were found on the regions depending on their position, i.e. higher or lower in the AC. The average of values of the 3 regions shows higher values for the mannitol case compared to control, thus reflecting the same overall trend of figure 6.5.

The motility scans tended to show more peristaltic movements in the AC for the mannitol case compared to the control. However, the events over two minutes resulted to be very rare and equal to zero for most cases, thus leading to very small numbers as reported in figure 6.8. Therefore no statistical analysis was performed. It was not possible to scan for longer than two minutes for time reasons. The number of peristaltic movements in the AC is highly subject dependent and a two minutes observation may not be efficient to fully describe physiologic changes. Nevertheless, the MRI motility sequence was

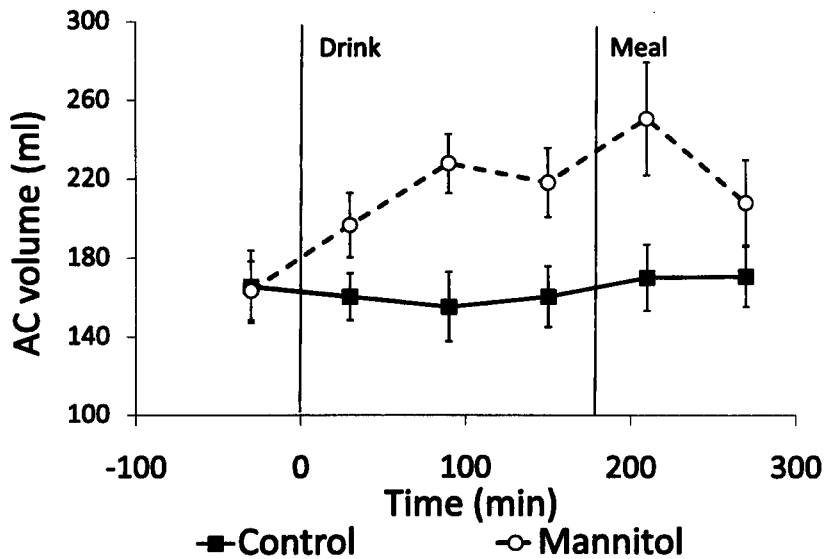


Figure (6.4): (Mean  $\pm$  STD) AC geometric volumes calculated from the dual echo FFE sequences.

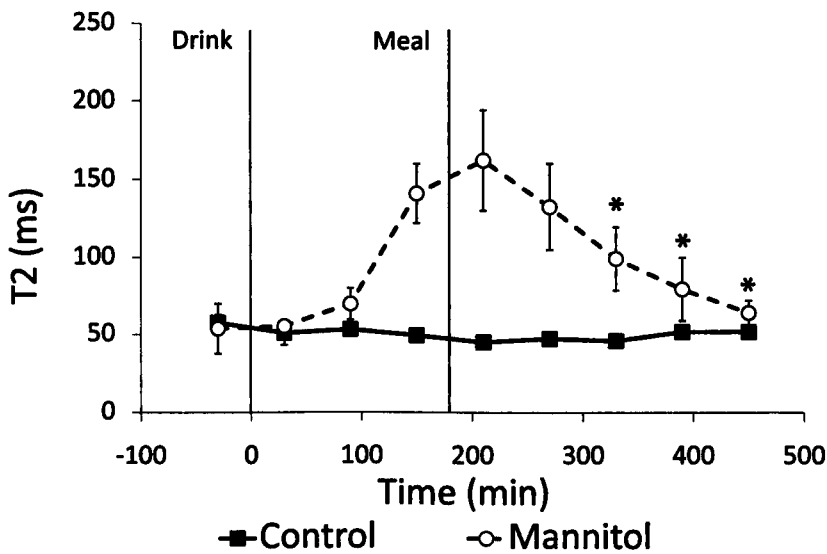


Figure (6.5): (Mean  $\pm$  STD)  $T_2$  values in ms calculated in the ascending colon from the  $T_2$ -prep bTFE sequence. The values obtained after the mannitol case are significantly higher than the control case, reaching a maximum averaged value of 160 ms at 210 minutes. For the control, the  $T_2$  of the contents stayed constant at a value of about 50 ms at all time points. The last points, marked with the asterisk, refer only to the data corresponding to the two pilots, who were imaged for longer.

optimised to study colonic function in undisturbed, physiologically relevant conditions and was able to detect any eventual movement in the AC.

The high resolution bTFE images clearly showed the colonic response to feeding over time for both conditions (figure 6.9). After the mannitol drink the

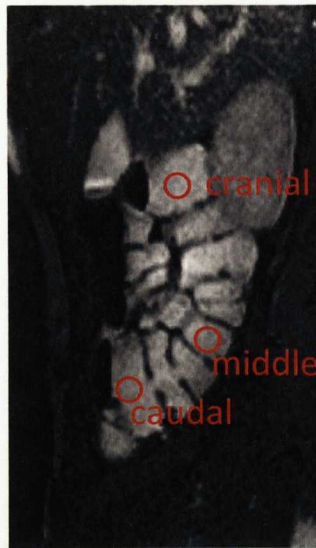


Figure (6.6): Example of the ROIs drawn in the cranial, middle and caudal regions of the ascending colon. The image corresponds to the  $T_2$ -prep sagittal image described in the section.

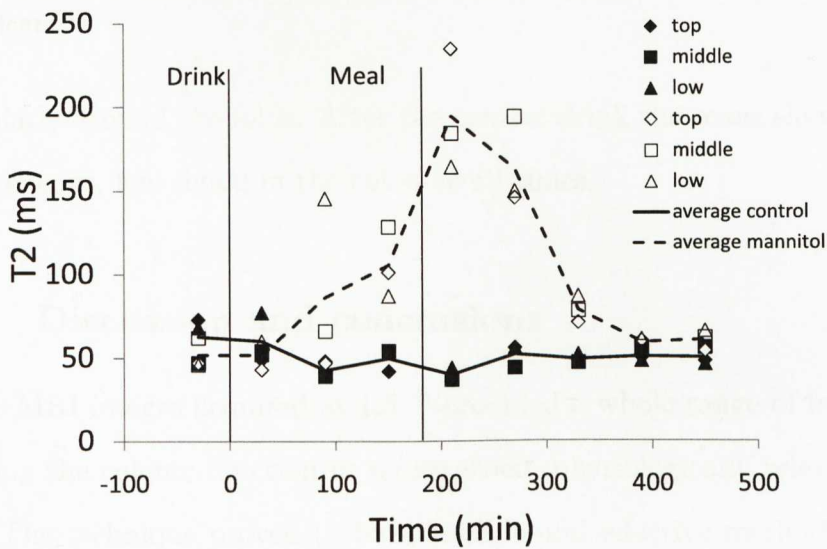


Figure (6.7):  $T_2$  values and average in ms calculated in the 3 regions of the ascending colon: a higher variability in  $T_2$  values between the regions is found from 180 to 270 minutes thus implying a greater heterogeneity of the colonic contents on the arrival of the fluids. The average shows higher values for the mannitol compared to the control, as shown previously for the overall trend  $T_2$  of all the volunteers.

arrival of water in the AC was observed at 90 minutes, which readily mixed with the colonic contents and caused distension of the colon. At 150 minutes it was possible to observe a bright, homogeneous signal in the AC. The following scans showed that as the water signal was declining darker material appeared

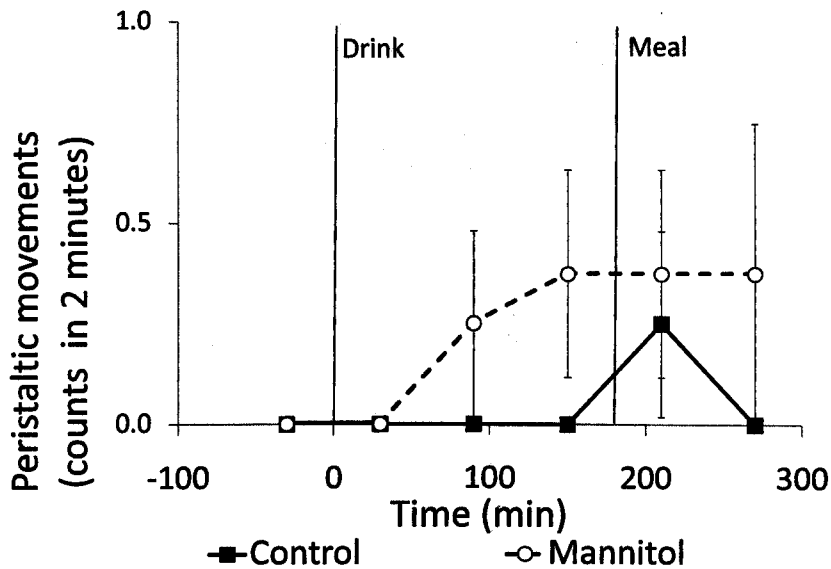


Figure (6.8): (Mean  $\pm$  STD) Number of peristaltic movements counted during the 2 minutes scan averaged for all the volunteers. A higher number of peristaltic movements is found for the mannitol case but the differences are not statistically significant.

particularly around the folds. After the control drink the scans showed a very heterogeneous, low signal in the colon at all times.

#### 6.2.4 Discussion and conclusions

The MRI images acquired at 1.5 T provided a whole range of information regarding the colonic function in undisturbed, physiologically relevant conditions. The technique proved to be a feasible and effective method to obtain multiple parameters of the gastrointestinal function. The unabsorbable, osmotically active mannitol solution causes secretion in the small bowel causing a great amount of fluids drawn in the gut, with a peak value of about 600 ml at 90 minutes after the drink. After that, the small bowel water content starts to fall within two hours.

The arrival of fluids in the ascending colon is shown to be at 90 minutes after the drink: when the secretions arrive in the colon they distribute heterogeneously. Figure 6.3 and 6.4 show that the water carried into the colon by the mannitol was a small fraction of the total colonic contents which was oth-

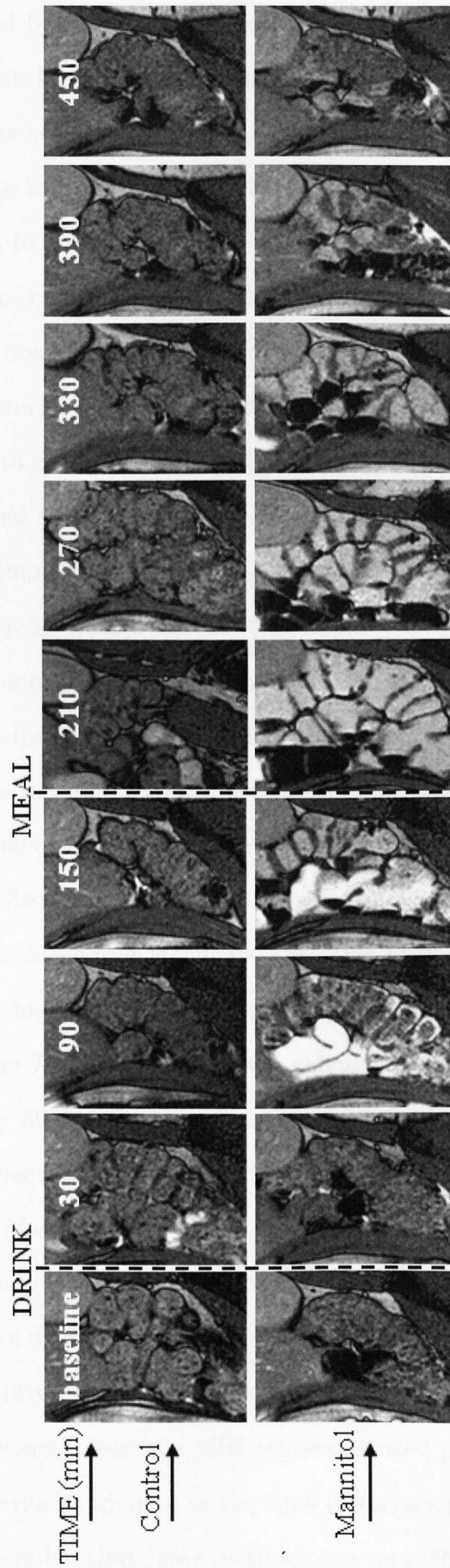


Figure (6.9): High resolution bTFE sagittal images of the AC after the glucose and the mannitol drink for the same volunteer.

erwise dominated by solid material and gas. The change in total AC volume with mannitol can largely be explained by the increase in free water content, although this was not true at the last time point, possibly due to the increase in the mass of the bacterial biofilm, where intracellular water will give reduced signal compared to free water in the colon. In the colon mannitol is rapidly fermented to short chain fatty acids which are known to be co-transported with sodium causing associated water absorption. The mannitol metabolism will also increase bacterial mass which will incorporate water intracellularly where it would appear to give a low signal. The high resolution images of the ascending colon reported in figure 6.9 showed varying signal characteristics, with a definite more homogeneous bright region for the mannitol case compared to the more heterogeneous and darker area of the control case. The images of the ascending colon at 390 and 450 minutes for the mannitol case show how the water gradually gets absorbed thus leaving the colonic contents dark and heterogeneous as in the control. The characteristics of the colonic contents have also been investigated with the  $T_2$  calculation. The  $T_2$  values for the mannitol case reflect the fact that the mannitol drink draws a great amount of fluids into the ascending colon, because the  $T_2$  values, in various regions of the colon, are higher than the control and can reach values of hundreds of milliseconds. The  $T_2$  in the control was calculated to be constant at a value of approximately 50 ms. This technique is potentially very useful for future clinical studies, because the different  $T_2$  values can lead to a completely non-invasive diagnosis of eventual gastrointestinal disease. First attempts were also performed to study gut motility. Some peristaltic movements were recorded after the mannitol drink while for the control drink almost no movements were found. Gut motility is highly subject dependent and in the fasted state it is also very rare. Nonetheless, the MRI sequences used proved to be efficient to record all the events happening in the time of the scan.

It can be concluded that these methods are very efficient, non invasive and

well tolerated by the subjects, thus proving to be a very useful tool for the investigation of the gastrointestinal diseases. This technique has been used to evaluate mechanisms of diarrhoea and drug intervention as described in the following chapter and it can be further implemented for clinical studies.

## 6.3 Measuring the $T_1$ and $T_2$ of the colonic contents in vitro

### 6.3.1 Introduction

The determination of  $T_1$  and  $T_2$  is fundamental to understand the inherent properties of the contents of the colon and tissues and also measure changes due to disease. However  $T_1$  and  $T_2$  of colonic contents are very short and reasons for this are not clear. Some hypothesis would see the cause due to the presence of iron or the low free water fraction.

This section presents in vitro work performed with faecal samples. The samples are imaged at intervals before and after lyophilization because of the hypothesis that the water is normally included in bacterial macromolecules. The addition of water after lyophilization should give a different water distribution.

### 6.3.2 Methods

A single stool sample from a healthy subject was collected and imaged in a 1.5 T Philips Achieva system according to the schedule in figure 6.10. After a baseline scan it was centrifuged to separate the water from solid materials. At this point the sample was weighted and imaged again. Successively it was freeze dried overnight and imaged again the next morning. Distilled water was then added in order to reconstitute the initial weight and another scan was performed on the suspension straight after mixing and after 15 minutes. A final centrifuge was undertaken to be sure that all particulate matter had been removed and a final scan was performed on the liquid fraction.

At each time point a series of scans was performed:

- For structural details: high resolution bTFE (TR=3.2 ms, TE=1.58 ms,

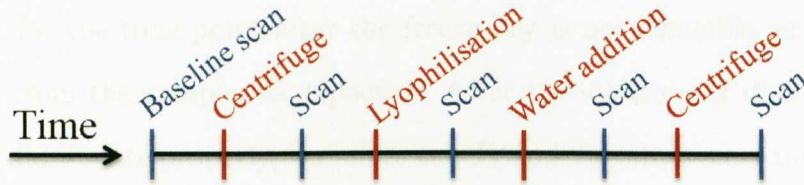


Figure (6.10): Schedule for the in vitro study of faecal samples.

acquired resolution = 1.50 mm x 1.50 mm, reconstructed resolution = 0.86 mm x 0.86 mm, 8 slices of 5 mm thickness, 0.58 mm gap);

- For  $T_2$  measurements: a  $T_2$ -prep bTFE sequence (TR/TE = 3.0/1.5 ms, TEprep values (ms): 20, 29, 43, 63, 93, 137, 201, 295, 434, 637, acquired resolution = 2.00 mm x 1.56 mm, reconstructed resolution = 1.56 mm x 1.56 mm, 7 mm thickness);
- For  $T_1$  measurements: a IR-bTFE sequence (TR/TE = 3.0/1.5 ms, TI values (ms): 0.025, 0.175, 0.425, 0.925, 1.425, 1.925, 2.925 and 4.925, acquired resolution = 2.00 mm x 1.56 mm, slice thickness 7 mm);

$T_2$  data sets were processed drawing a region of interest and then using the mean signal of this region at all the different echo times to calculate the  $T_2$  of the tissue using a program in-house which modelled the effect of the  $T_2$ -prepared scheme and subsequent imaging sequence for the  $T_2$ -prepared bTFE sequence [42].  $T_1$ s were also obtained by fitting the data with the appropriate TI values.

### 6.3.3 Results

Good SNR was obtained for the high resolution images at all time points. The lyophilization process resulted in loss of water equal to the 70% of the total weight. Adding the water after freeze dry resulted in a different distribution of water with the stool being separate from water even after centrifugation.

Table 6.1 summarizes the results for the  $T_1$  and  $T_2$  for this in vitro study. The data for the time point after the freeze dry is not available as there was no signal from the sample, as expected. After the addition of distilled water the stool didn't mix properly, therefore the  $T_1$  and  $T_2$  values were measured in two different areas, shown in figure 6.11.

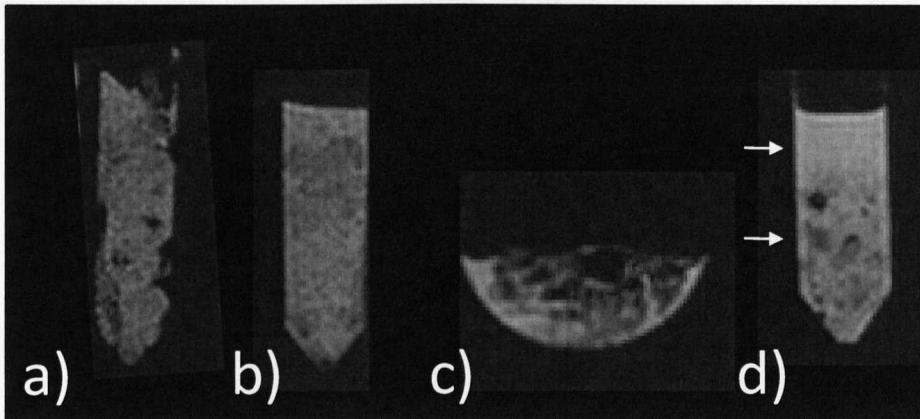


Figure (6.11): High resolution images for the in vitro sample at the different time points: (a) baseline, (b) after first centrifuge, (c) after the water addition of distilled water and (d) after the last centrifuge. Figure (d) shows how the faecal matter stays separate from water. In this case the  $T_1$  and  $T_2$  values were measured in the two areas separately, shown by the arrows (top arrow for watery ROI and lower for the sample ROI).

	Baseline	Centrifuge	Lyophilization	Water addition	Centrifuge
$T_1$	118	101	na	96	95 <sup>†</sup> , 59 <sup>‡</sup>
$T_2$	7	6	na	17	8 <sup>†</sup> , 6 <sup>‡</sup>

Table (6.1):  $T_1$  and  $T_2$  values in ms at the different time points. <sup>†</sup> for the watery ROI, <sup>‡</sup> for the sample ROI shown in figure 6.11.

### 6.3.4 Discussion and conclusion

This in vitro experiment showed particular characteristic of the faecal matter which are helpful for the understanding of the colon MRI scans. One first interesting result is that the faecal matter used here contains a small amount of water which leads to very short  $T_1$  and  $T_2$  values for the baseline condition and the water is not bound in cells. The persistence of very short  $T_1$  and  $T_2$

values after water addition may imply that the quenching of the signal is due to ferrous ions present in faecal matter. However it has to be considered that this experiment has been performed at room temperature, which is much lower than body temperature and this may have affected the  $T_1$  and  $T_2$ . In addition, this study only involved a single sample, therefore no conclusion may be assessed on the variability and  $T_1$  and  $T_2$  may be considered only as estimates.

## 6.4 Defining the characteristics of the ascending colon contents

### 6.4.1 Introduction

$T_1$  and  $T_2$  can assess water content of colon and can be measured on an ROI or on a voxel basis but heterogeneity is a particular feature of the MR scans of colonic contents. This section aims to develop a method to assess the heterogeneity of the colonic contents and its microscopic structure.

The first approach is to use a subjective method based on the visual assessment of the composition of the AC contents. Following this, two automated methods for the objective assessment are compared.

These methods have been validated on the data sets presented in section 6.2, corresponding to the study of colonic response to the model of human diarrhoeal disease.

### 6.4.2 Methods

#### Subjective assessment

In order to take into account the inter-observer variability in the AC contents subjective assessment, two observers (myself and Dr. C.L. Hoad), with substantial experience in studying MRI images, independently graded the high resolution bTFE images from 8 different data sets (single score per time point covering all 8 slices), between 1 (all dark) and 5 (all bright) with 3 having a mixture of dark and bright patches (fig 6.12). To calculate the intra-observer variability of the AC contents assessment, I measured the same 8 data sets on two different occasions, separated by one month gap to avoid any partiality. The inter-observer and intra-observer variability for the subjective measurements were assessed by calculating the weighted kappa from the subjective

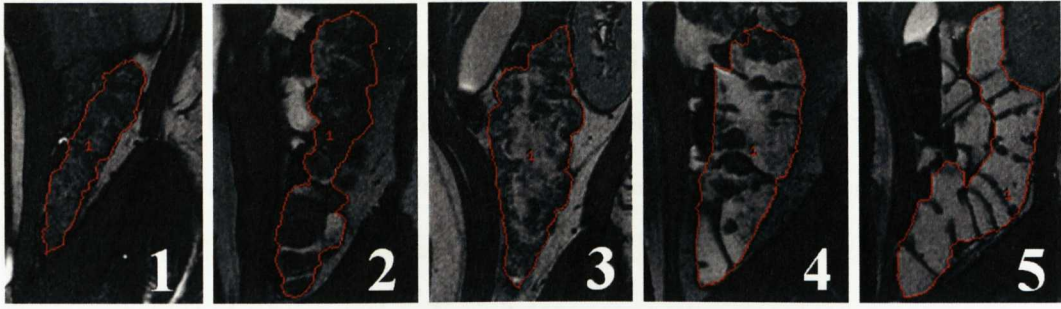


Figure (6.12): Examples of the 5 scores given to the AC contents, between 1 (all dark) and 5 (all bright) with 3 having a mixture of dark and bright patches. The AC is contoured in red.

data according to the Bland-Altman method [43–45].

### First automated method: histogram and Bi-Gaussian fit

ROIs of the AC were manually drawn using Analyze<sup>®</sup> software (as in figure 6.12) and the data were normalized by the mean intensity of the kidney where a small ROI was drawn. The histogram of the signal intensity in the ROI over the AC was fitted to the following Gaussian equation using Matlab:

$$y_{fit} = a_1 \cdot e^{-\frac{(x-b_1)^2}{2c_1^2}} + a_2 \cdot e^{-\frac{(x-b_2)^2}{2c_2^2}} \quad (6.1)$$

where  $c_1$  and  $c_2$  were constrained  $\geq 0.1$  (10 times bigger than one bin) and  $a_2$  was constrained  $\geq 0$ . The ratio  $a_2/a_1$  was used to assess AC content composition, as a measure of the ratio of dark to bright signal fractions.

### Second automated method: feature extraction using Gabor filters

Gabor filtering is a useful signal processing technique that can extract local spatial frequencies of an image, by representing signals as a combination of elementary functions [46]. Spatial frequencies and their orientation characterise the texture of an image. Methods like Fourier analysis have long been used for the spectral decomposition in signal processing but the main problem is that the spectral features from different parts of an image are mixed

together. Gabor filters make it possible to have this spatial information and to obtain localised features of an image [47, 48].

A complex Gabor filter can be viewed as a sinusoidal plane of particular frequency and orientation, modulated by a Gaussian envelope. Figure 6.13 shows how a Gabor filter is obtained for a 2D case, while figure 6.14 shows some examples of filters with different frequency and orientation.

It is possible to write the function describing a Gabor filter in 2D as

$$g(x, y, \theta, \phi) = e^{-\frac{x^2+y^2}{\sigma^2}} \cdot e^{2\pi i(x\cos\phi+y\sin\phi)} \tag{6.2}$$

where  $\theta$  is the spatial frequency,  $\phi$  the orientation and  $\sigma$  the standard deviation of the Gaussian kernel which depends on the spatial frequency and it is chosen to take into account all the range of frequencies.

If we have an image  $I(x, y)$ , we can obtain the Gabor feature  $G(x, y, \theta, \phi)$  by convolving the Gabor filter and the image as follows

$$G(x, y, \theta, \phi) = \int \int I(p, q)g(x - p, y - q, \theta, \phi)dpdq \tag{6.3}$$

Gabor filters have been used as an automated method to extract features from images of the colon. The 5 grades of typical colonic contents, described in the previous sections and displayed in figure 6.12, present a variety of pat-

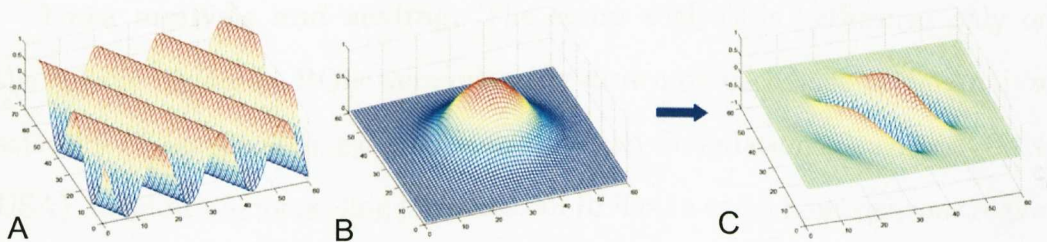


Figure (6.13): A complex Gabor filter as in (C) can be viewed as a sinusoidal plane of particular frequency and orientation (A) modulated by a Gaussian envelope (B).

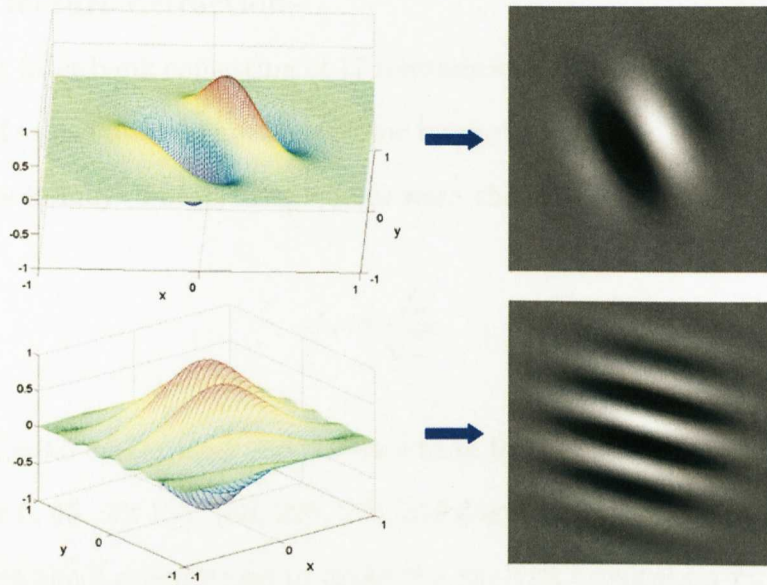


Figure (6.14): Examples of different Gabor filters.

terns which depend on a variety of factors such as brightness, wall thickness, homogeneity, contrast etc. These features can be extracted as image textures and the images can be then classified according to that texture.

The entire process of this automated method for the definition of the characteristics of the ascending colon is embedded in a Matlab code<sup>1</sup> and consists of 4 main parts: the data analysis and scaling, the Gabor feature extraction, the co-occurrence matrix feature computation and a support vector machine (SVM) discrimination analysis. Texture analysis for a whole data set for one subject (consisting of about 6 sets) takes less than 3 minutes and it is fully automated.

**Data analysis and scaling:** The entire analysis is performed only on the colonic region so, ROIs were manually drawn on each slice using Analyze software (Biomedical Imaging Resource, Mayo Foundation, Rochester, MN, USA). In addition, for scaling purposes, an ROI on a small homogeneous region of the kidney is also drawn. The kidney has been chosen since it has been recognized as the most homogenous region across all the subjects. The input of the Matlab code consists of the two ROIs and the images in Analyze format.

<sup>1</sup>The Matlab code has been written in collaboration with Dr. A. Napolitano.

**Gabor feature extraction:**

A Gabor filter bank consisting of 17 frequencies and 8 orientations is applied on the set of scaled images, i.e. the colonic images normalised with the intensity signal of the kidney. The 17 frequencies were chosen based on the equation

$$f_n = \frac{f_0}{\sqrt{2}^n} \quad (6.4)$$

where  $f_0=0.5$  cycle/pixel and  $n$  varies from 0 to 16 [49]. The chosen orientations were 0, 45, 90, 135, 180, 225, 270, 315 degrees so that the images are averaged across the 8 orientations to make the analysis orientation-independent. In addition, the images are reconstructed by cumulatively summing the images from the lower frequencies to the higher ones. The choice of the summing order is based on the fact that the colonic content is more visible at lower frequencies than higher ones where, conversely, the colon edges and wall are more visible. Therefore, by summing the reconstructed images from the lower to the higher frequencies, the contribution from the walls is minimised.

The flow chart reported in figure 6.15 represents the main steps of the Gabor feature extraction program. The reconstruction of the images by cumulatively summing on the frequencies is reported as an example in figure 6.16. The mean signal of the reconstructed images up to the 17th frequency is also calculated and will be called “mean Gabor signal”.

**Co-occurrence matrix feature computation:** The third part of this automated method computes the main features on the set of images obtained from the Gabor texture analysis.

Before computation of the co-occurrence matrix, the images previously normalised to the kidney mean signal are scaled to lie in the range 0–10 by using maximum and minimum values calculated on the whole set of data. These images will be called “binned images”.

The co-occurrence matrix (also called gray levels co-occurrence matrix,

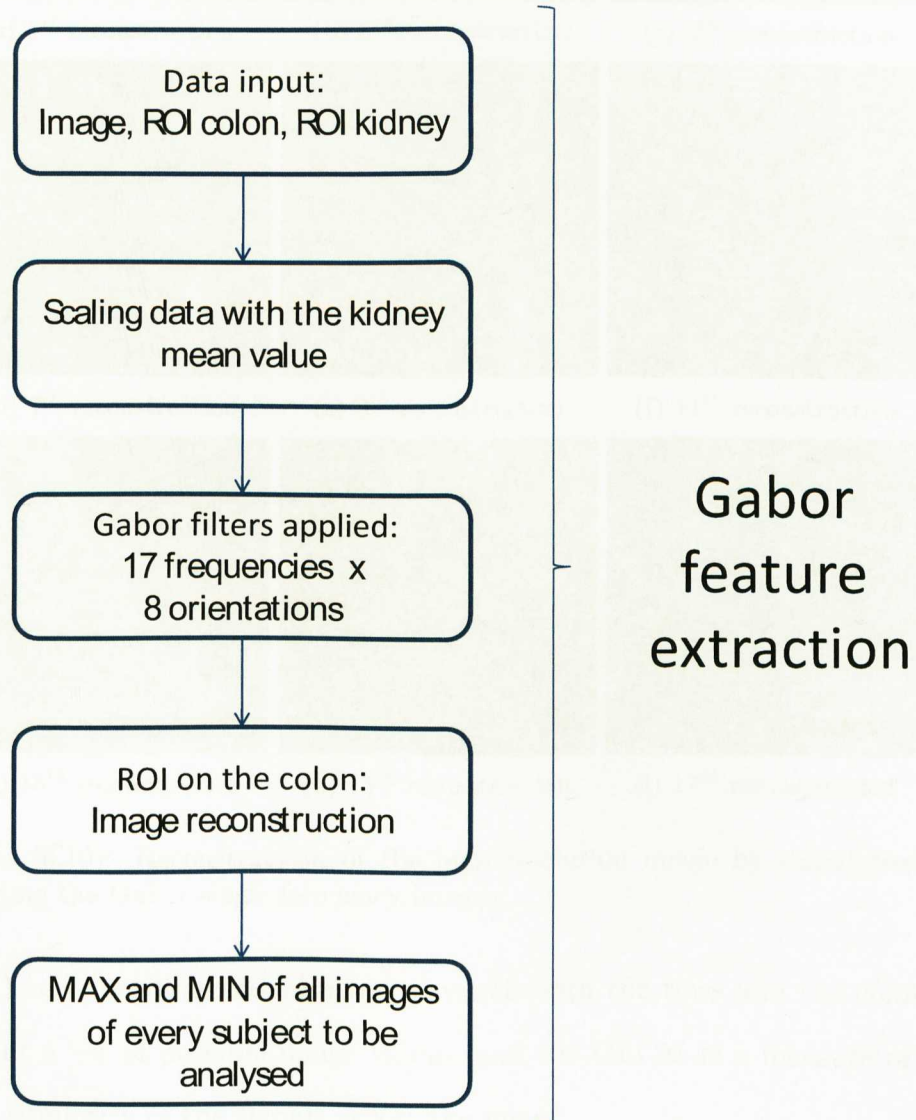


Figure (6.15): Schematic diagram of the Gabor feature extraction program.

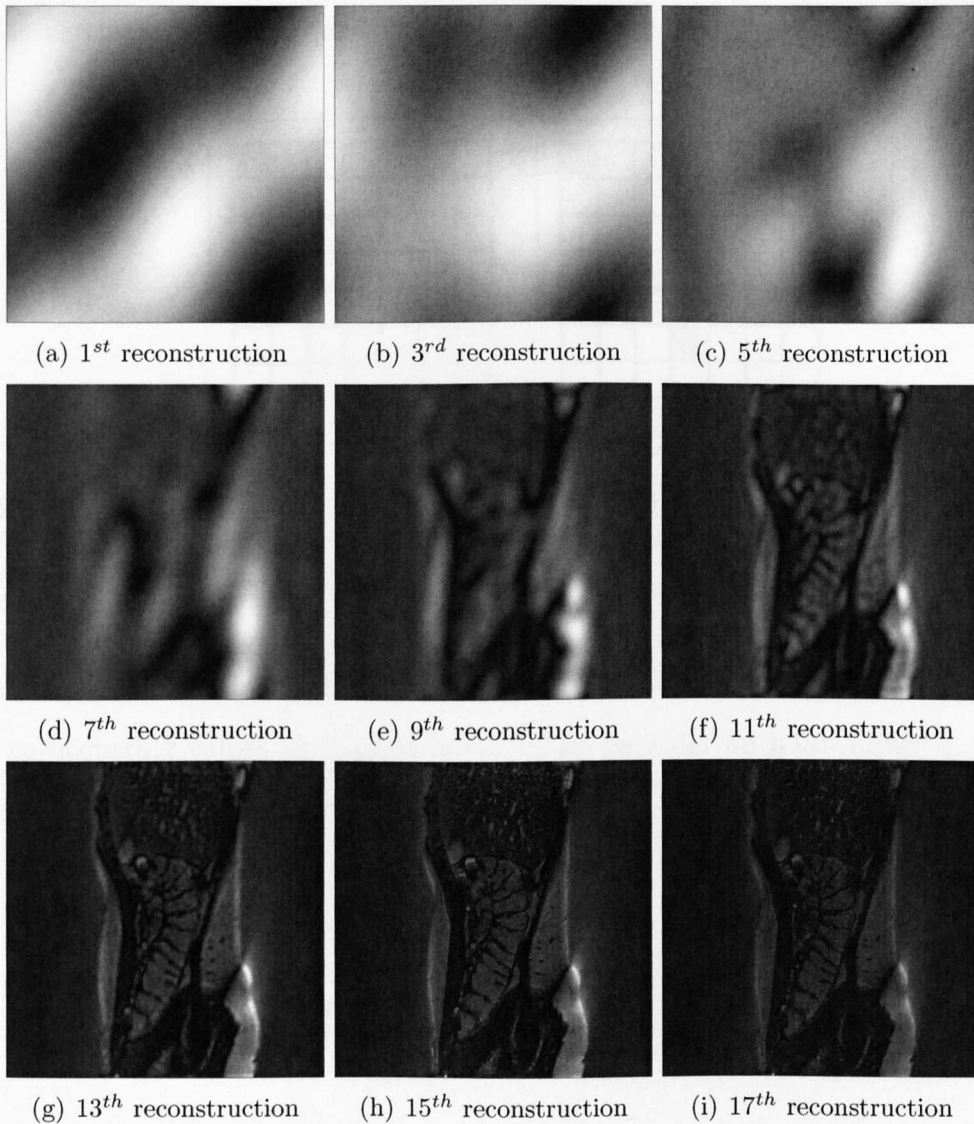


Figure (6.16): Reconstruction of the high resolution image by cumulatively summing the Gabor single frequency images.

GLCM) is a two-dimensional array in which both the rows and the columns represent a set of possible image values, and the GLCM is a measure of the spatial similarity of the signals across the image.

A GLCM of a binned image is defined by first specifying a displacement vector  $(\Delta x, \Delta y)$  and counting all pairs of pixels separated by  $(\Delta x, \Delta y)$  having gray levels  $i$  and  $j$ . The displacing vector will be referred to as offset. Figure 6.17 shows a schematic for 2 binned images where two pixels are compared: the low offset (1,1) takes into account more local effects whilst the high offset (5,3) considers longer distances, thus reducing the effect of the the medium

scale vertical oscillation due to the presence of the colonic walls.

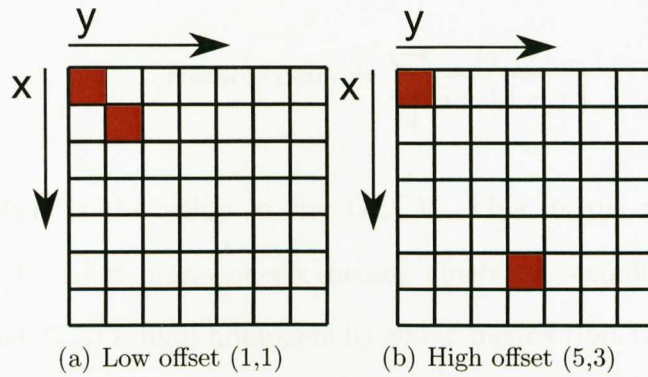


Figure (6.17): Example for the different offsets used: (1,1) to take into account local effects, while (5,3) considers the longer distances in the ascending colon in the vertical direction as for the AC shape.

The GLCM is therefore defined over a binned image to be the distribution of co-occurring values at a given offset. If we consider an  $n \times m$  image  $I$ , then we can write the co-occurrence matrix  $C$  as

$$C_{\Delta x, \Delta y}(i, j) = \sum_{p=1}^n \sum_{q=1}^m \begin{cases} 1 & \text{if } I(p, q) = i \text{ and } I(p + \Delta x, q + \Delta y) = j \\ 0 & \text{otherwise} \end{cases} \quad (6.5)$$

The GLCM has dimension  $l \times l$ , where  $l$  is the number of gray levels in the image, 10 in our case. It can be noted that the GLCM is not symmetric, since the number of pairs of pixels having gray levels  $(i, j)$  does not necessarily equal the number of pixel pairs having gray levels  $(j, i)$ . Figure 6.18 shows an example of the creation of a GLCM from a binned image with an offset of (1,1).

Gray level co-occurrence matrices contain properties of texture but they are not directly useful for further analysis, such as the comparison of two textures. Instead, numeric features are computed from the co-occurrence matrix. Among all the possible features, the following have been considered as important:

- Homogeneity, which is a measure of the closeness of the distribution of elements in the GLCM to the GLCM diagonal, i.e. homogeneity=1 for

a diagonal GLCM. It can be written as

$$\text{Homogeneity} = \sum_{i,j} \frac{p(i,j)}{1 + |i - j|} \quad (6.6)$$

where  $p(i,j)$  is the value in the GLCM. This means that for the low offset (1,1), high homogeneity means clustered signals, whilst for the high offset (5,3) a high homogeneity value means that the signals repeat at distances. A heterogeneous image will result in an even spread of  $p(i,j)$  and a low homogeneity value.

- Contrast: it is a measure of the local variations present in an image and it is 0 for a constant image.

$$\text{Contrast} = \sum_{i,j} |i - j|^2 p(i,j) \quad (6.7)$$

If there is a large amount of variation in an image the  $p(i,j)$  values will be concentrated away from the main diagonal and contrast will be high.

- Entropy: as the term comes from thermodynamics to define the quantity of energy that is permanently lost to heat, in the context of texture analysis entropy represents a measure of disorder, i.e. the randomness of intensity distribution. The equation is

$$\text{Entropy} = \sum_{i,j}^{N-1} p(i,j)(-\ln p(i,j)) \quad (6.8)$$

Entropy is highest when all  $p(i,j)$  are of similar magnitude, and small when  $p(i,j)$  values are very different.

- Correlation: it returns a measure of how correlated a pixel is to its neighbor over the whole image. Correlation is 1 or  $-1$  for a perfectly positively

or negatively correlated image. Correlation is NaN for a constant image.

$$\text{Correlation} = \sum_{i,j} \frac{(i - \mu_i)(j - \mu_j)p(i, j)}{\sigma_i \sigma_j} \quad (6.9)$$

where

$$\mu = \sum i p(i, j) \text{ and } \sigma = \sum i^2 p(i, j) - \mu^2 \quad (6.10)$$

Correlation will be high if an image contains a considerable amount of linear structures.

- **Energy:** it is the sum of squared elements in the GLCM and it is 1 for a constant image.

$$\text{Energy} = \sum_{i,j} p(i, j)^2 \quad (6.11)$$

Figure 6.19 shows some examples of binned images with the features calculated for an offset of (1,1). Among all these features, homogeneity and contrast were chosen as they were more representative for our data. For these two features, the cumulative integrals were performed over different ranges of Gabor frequency values, for different offsets.

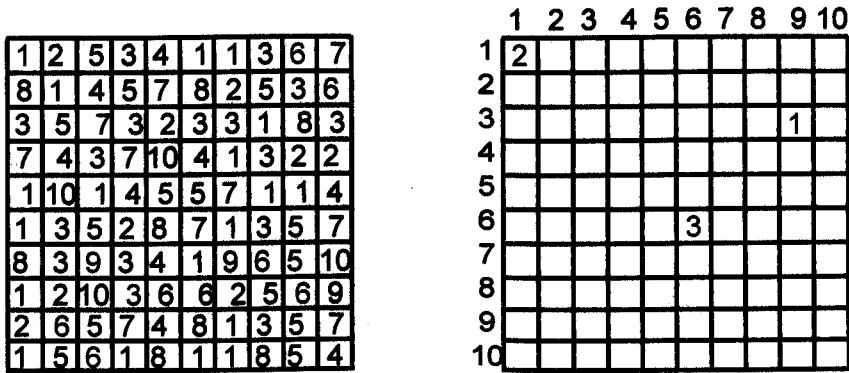
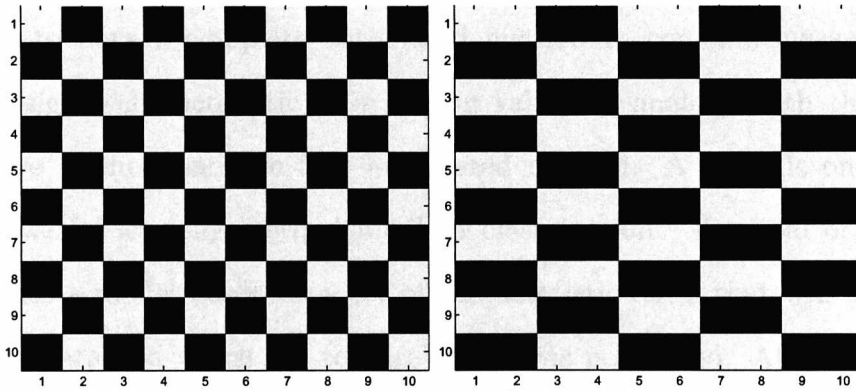
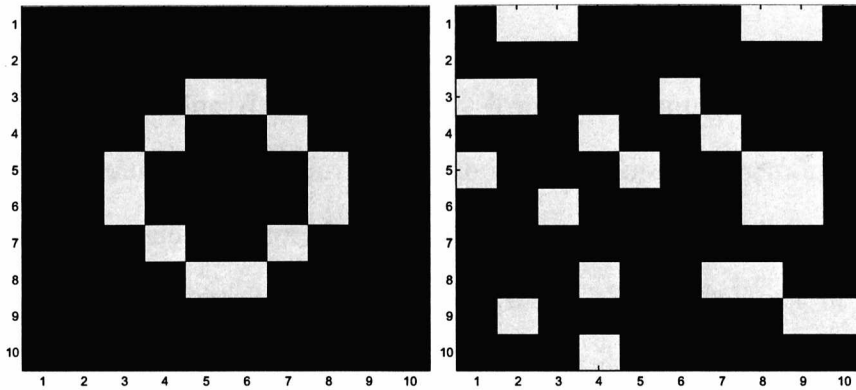


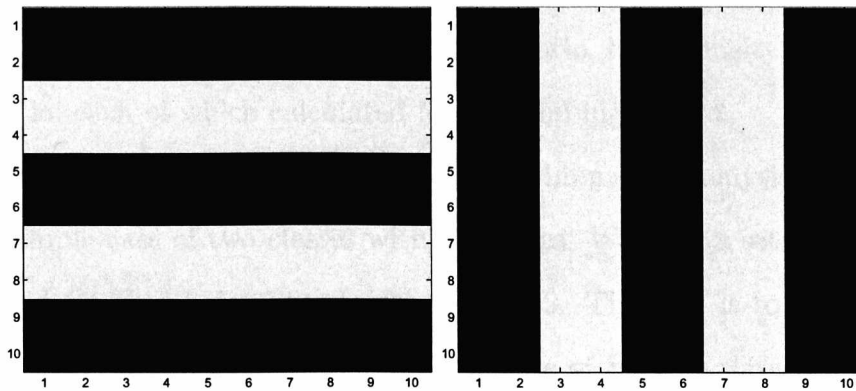
Figure (6.18): Schematic diagram of the creation of a GLCM (right) from a binned image (left), with an offset of (1,1). For each pixel in the binned image on the left the neighbor is considered and their values (e.g. 9 and 3 in green) count as a 1 in the co-occurrence matrix. This is done for each pixel in the binned image with the chosen offset.



(a) Contrast: 0. Correlation: 1. Energy: 0.5. Entropy: 0.7. Homogeneity: 1. (b) Contrast: 45. Correlation:  $-0.1$ . Energy: 0.2. Entropy: 1.4. Homogeneity: 0.5.



(c) Contrast: 16. Correlation: 0.2. Energy: 0.6. Entropy: 0.8. Homogeneity: 0.8. (d) Contrast: 28. Correlation: 0.04. Energy: 0.4. Entropy: 1.1. Homogeneity: 0.7.



(e) Contrast: 36. Correlation: 0.1. Energy: 0.2. Entropy: 1.4. Homogeneity: 0.6. (f) Contrast: 36. Correlation: 0.1. Energy: 0.2. Entropy: 1.4. Homogeneity: 0.6.

Figure (6.19): Example binned images with correspondent texture parameters calculated with an offset of (1,1).

**Support Vector Machine discrimination analysis:**

The support vector machine (SVM) discrimination analysis was performed in order to have a complete automated method to combine measurements of MRI signal characteristic into scoring values in analogy with the visual subjective method and the first automated method. A SVM is one of the most powerful learning method for data classification. The goal of SVM is to produce a model based on a set of characteristic data, that will be called "training data" on which the texture analysis is performed. All the features obtained on this set of training data are then used to build a model. Afterwards this model can be used to classify any set of data available which will be called "testing data".

The set of training data was chosen from the mannitol data presented previously (section 6.2). In particular the images chosen corresponded to the ones that were visually scored the same value by the two observers in the subjective method (myself and Dr. C.L. Hoad). The whole set of training data included: 7 images for score 1, 6 images for score 2, 6 images for score 3, 17 images for score 4 and 12 images for score 5, for a total of 48. For this data the following features were considered for the classification: mean, CV, contrast, entropy, contrast homogeneity ratio, homogeneity, homogeneity mean ratio, each of which calculated for low and high offset.

However, in order to explain the SVM discrimination analysis, we can consider a simple case of two classes with  $l$  features. We have a set of given data points which either belong to class 1 or class 2. The goal is to decide which class a new data point will belong. In the case of SVM, a data point is considered to be a  $n$ -dimensional vector  $\mathbf{x}_i$ , with  $i=1,\dots,l$ , where the elements of the vector correspond to different features of the data point (eg. homogeneity, contrast, mean, etc). We can then consider an indicator vector  $y_i$  which is equal to either 1 or  $-1$ , so that if  $\mathbf{x}_i$  is in class 1 then  $y_i$  is 1 and if  $\mathbf{x}_i$  is in class 2 then  $y_i$  is  $-1$ . In order to distinguish the two classes, one option is

to choose a hyperplane that represents the largest separation between the two classes (see figure 6.20). A general hyperplane can be written as the set of points satisfying the following equation

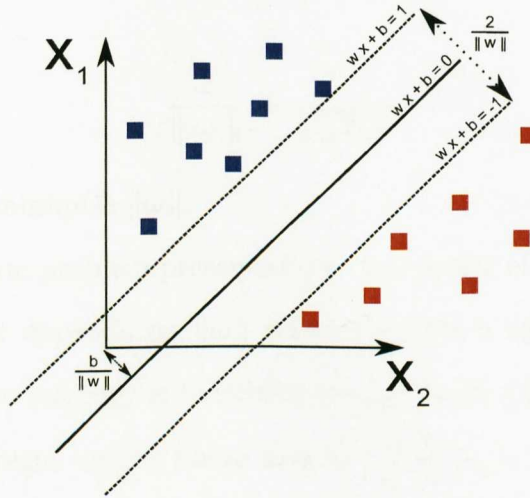


Figure (6.20): Schematic diagram of the hyperplane and margins for an SVM trained with samples from two classes.

$$\boldsymbol{\omega}^T \cdot \mathbf{x} + b = 0 \tag{6.12}$$

where  $\cdot$  denotes the dot product,  $\boldsymbol{\omega}$  is the normal vector to the hyperplane and  $b/\|\boldsymbol{\omega}\|$  being the offset of the hyperplane from the origin along the normal vector  $\boldsymbol{\omega}$ . We want to choose  $\boldsymbol{\omega}$  and  $b$  to maximize the distance between two parallel hyperplanes that are as far apart as possible and separate the data. These hyperplanes can be described by the equations

$$\boldsymbol{\omega}^T \cdot \mathbf{x} + b = 1 \tag{6.13}$$

and

$$\boldsymbol{\omega}^T \cdot \mathbf{x} + b = -1 \tag{6.14}$$

such that

$$\boldsymbol{\omega}^T \cdot \mathbf{x}_i + b \geq 1 \text{ if } \mathbf{x}_i \text{ is in class 1} \tag{6.15}$$

and

$$\omega^T \cdot \mathbf{x}_i + b \leq -1 \text{ if } \mathbf{x}_i \text{ is in class 2} \quad (6.16)$$

The distance between  $\omega^T \cdot \mathbf{x}_i + b = 1$  and  $\omega^T \cdot \mathbf{x}_i + b = -1$  is defined as

$$\frac{2}{\|\omega\|} = \frac{2}{\sqrt{\omega^T \omega}} \quad (6.17)$$

so we want to minimize  $\|\omega\|$ .

The optimization problem presented, i.e. the choice of  $\omega$  and  $b$ , is not easy to solve because it depends on  $\|\omega\|$  which involves a square root (equation 6.17). One common strategy is to substitute  $\|\omega\|$  with  $\frac{1}{2} \|\omega\|^2$  without changing the solution (same values for  $\omega$  and  $b$ ). The factor  $\frac{1}{2}$  is introduced for calculation convenience. Therefore we have a quadratic optimization problem as the following [50, 51].

$$\min_{\omega, b} \frac{1}{2} \omega^T \omega \quad (6.18)$$

subject to

$$y_i(\omega^T \cdot \mathbf{x}_i + b) \geq 1 \text{ with } i = 1, \dots, l \quad (6.19)$$

where  $y_i$  is the indicator vector equal to 1 or  $-1$  already introduced.

At this point it becomes necessary to take into account possible class mixing in the training set. This would imply that there is no hyperplane that can exactly split the data in either one class or the other. Therefore another term in the optimization can be introduced with this form

$$\min_{\omega, b, \xi} \frac{1}{2} \omega^T \omega + C \sum_{i=1}^l \xi_i \quad (6.20)$$

where  $C > 0$  is an additional constraint and  $\xi > 0$  measures the degree of misclassification of the data.

Up to this point we have considered a linear classification. However, it may be necessary to introduce the function  $\phi$  to map the vectors  $\mathbf{x}_i$  into a transformed space, see figure 6.21, in which the classes can be separated by a hyperplane [50, 52].

Since guessing the  $\phi$  function is not a trivial task, a “kernel trick” [52] is introduced: the kernel function  $K(\mathbf{x}_i; \mathbf{x}_j) = \phi(\mathbf{x}_i)^T \phi(\mathbf{x}_j)$  is defined to help with the calculation. From this point onward the kernel structure in terms of  $\phi$  is replaced by studying the possible structures of the kernel. This allows the algorithm to fit the hyperplane in a transformed feature space. The transformation may be nonlinear and the transformed space high dimensional.

Many possible kernel functions are found in literature<sup>2</sup>, but in this work the radial based function (RBF) kernel has been chosen for its fewer numerical difficulties. An RBF kernel is defined as

$$K(\mathbf{x}_i, \mathbf{x}_j) = e^{-\gamma \|\mathbf{x}_i - \mathbf{x}_j\|^2} \quad (6.21)$$

where  $\gamma > 0$  is a kernel parameter.

A matlab library for support vector machines (LIBSVM) from Chang et al. [53]<sup>3</sup> has been used for the prediction of information of a data set based on the set of training data. LIBSVM basically compares the data to different pairs of classification in turn. If  $k$  is the number of classes, then  $k(k-1)/2$  classifiers are constructed. Each binary classification is considered to be a voting so that at the end a point is chosen to be in a class with the maximum number of votes. The testing data were then classified according to the resulting model

<sup>2</sup>Four main basic forms for the kernel functions are found in literature:

- Linear;  $K(x_i; x_j) = x_i^T x_j$ .
- Polynomial;  $K(x_i; x_j) = (\gamma x_i^T x_j + r)^d$ ,  $\gamma > 0$ .
- Radial basis function (RBF);  $K(x_i; x_j) = \exp(-\gamma \|x_i - x_j\|^2)$ ,  $\gamma > 0$ .
- Sigmoid;  $K(x_i; x_j) = \tanh(\gamma x_i^T x_j + r)$

where  $\gamma$ ,  $r$  and  $d$  are kernel parameters.

<sup>3</sup>Software available at <http://www.csie.ntu.edu.tw/~cjlin/libsvm>

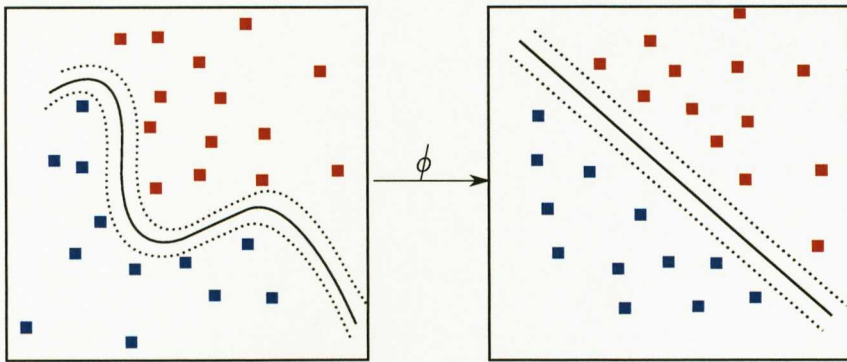


Figure (6.21): Schematic of a non linear transformation.

and both final predicted classification (scoring), and underlying probabilities of belonging to one of the classes (scores) were reported. Also a probability weighted score was computed in order to associate each data to a continue rather than discrete level. In our case, with the 5 scores as different classes, the sum of the 5 probabilities is equal to 1.

#### **Accuracy for ROI drawing and reproducibility:**

Further analysis was performed to optimise the method and the time needed for the analysis. In particular, the required accuracy of drawing ROIs was tested, being the most time consuming step. Even if some software packages provide tools to assist the recognising of the edges in an image, the accuracy in drawing the ROIs still influences the analysis time. For this study the ROIs were defined precisely around the walls of the colon. Therefore a comparison between a coarse and a precise type of contouring was performed. In particular, a set of 3 subjects was analysed by two observers and in the two different contouring approaches, as in figure 6.22. The results for the scoring from the classification analysis for the precise and coarse ROIs were subtracted and their difference was considered to quantify the accuracy.

The reproducibility of the ROI contouring was also similarly tested, by two observers (the author and Dr. Caroline Hoad) on two different subject sets.

### 6.4.3 Results

#### Subjective assessment

For the more coarse segmentation, 75% of the selected regions were drawn manually. The remaining 25% were drawn automatically. The accuracy of the automatic drawing was 1.00, which is a very good agreement. For the more precise segmentation, 75% of the selected values were also drawn manually and 25% were drawn automatically. The accuracy of the automatic drawing was 0.97, which is a very good agreement.

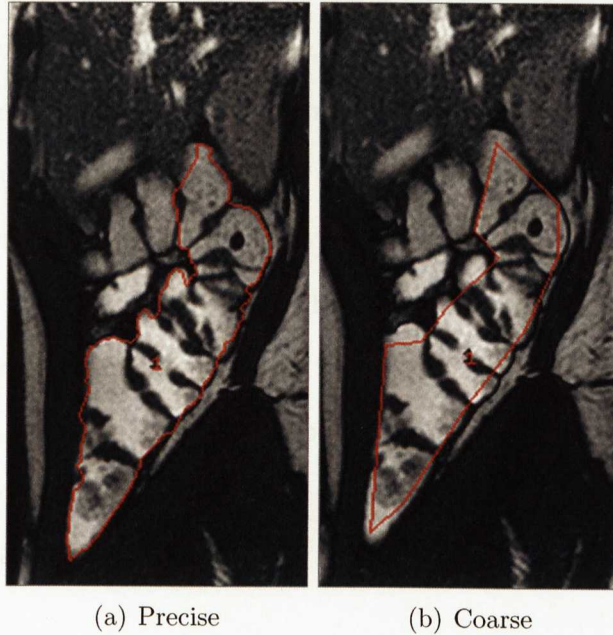


Figure (6.22): Example for the difference accuracy of drawing the regions.

### 6.4.3 Results

#### Subjective assessment

For the intra-observer reproducibility, 75% of the scored values were identical and 25% were 1 bin different, thus having a weighted kappa for the intra-observer of 0.84 which indicates a very good agreement. For the inter-observer variability, 75% of the scored values were also the same, 24% were 1 bin different and 1% was 2 bins different, and the calculated weighted kappa was equal to 0.82 which also indicates a very good agreement.

Figure 6.23 shows the average scores for the 8 volunteers in the 2 conditions, scored by E.P. For the mannitol case, the colonic contents are given much higher scores, in agreement with the results of brightness and homogeneity presented in the previous chapter, due to the arrival of water in the AC after the mannitol. In particular this is shown in figure 6.24 which shows the scores and the ACWC together versus time: the higher scores for the mannitol case mirror the bigger amount of free water in the AC, while for the control a more heterogeneous and dark signal correspond to the low amount of free water. The similarity in the trend shows that the scoring system is robust.

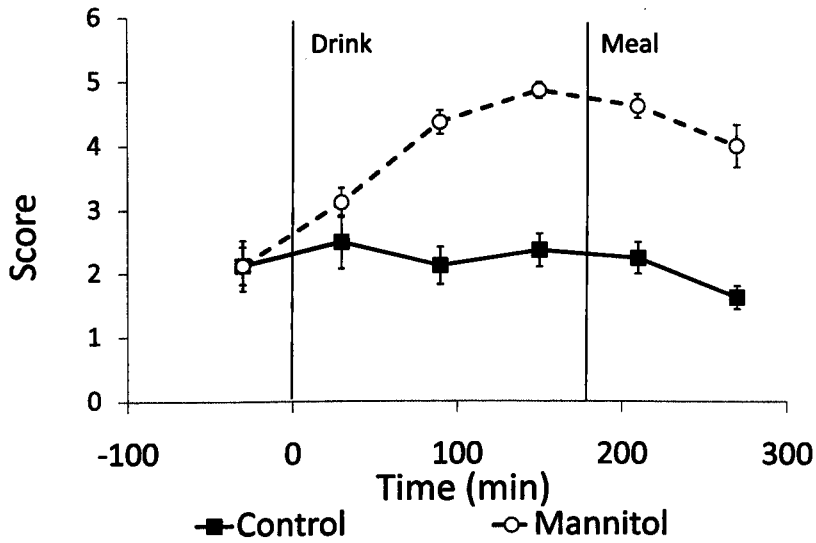


Figure (6.23): (Mean  $\pm$  STD) Average scores versus time for the 8 volunteers scored by E.P. For the Mannitol case the scores result to be much higher for all the volunteers compared to the control: the AC contents were more homogeneous and bright for the Mannitol case.

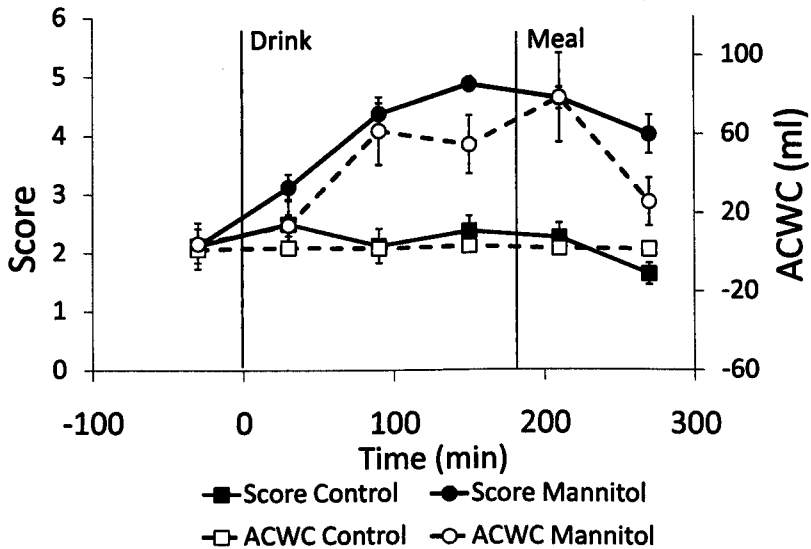


Figure (6.24): (Mean  $\pm$  STD) Average scores by E.P. (primary axis) and ACWC in ml (secondary axis) versus time for the 8 volunteers. The higher scores for the mannitol case mirror the bigger amount of free water in the AC, while for the control a more heterogeneous and dark signal correspond to the low amount of free water.

**First automated method: histogram and Bi-Gaussian fit**

Figure 6.25 shows the histograms and the fits of the images shown in figure 6.12 as an example of this method (histogram in grey, 2 gaussians plotted as blue and light blue and the total fit in red).

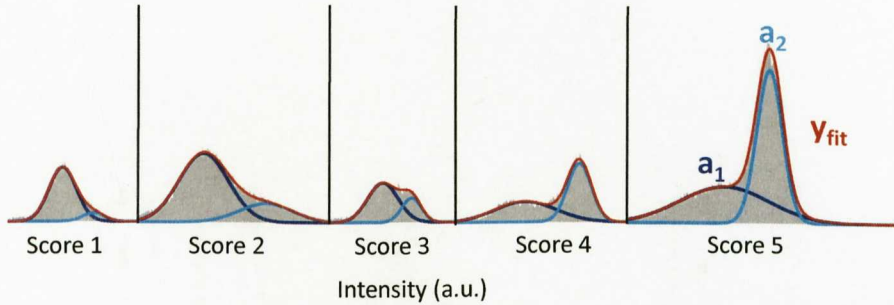


Figure (6.25): Histograms for colonic ROIs from the 5 images in figure 6.12 with the  $a_2/a_1$  values calculated on 5 sets of images for each score. The five graphs are plotted in the same horizontal axis for convenience.

Table 6.2 summarises the results for the  $a_2/a_1$  ratios calculated on 5 sets for each score from different subjects. The  $a_2/a_1$  values are sensitive to the different grades except for score 1 and 2 that give similar values.

Figure 6.26 shows the results for one subject for the mannitol case compared to subjective scores, showing a very good accordance and a more smooth transition between dark and bright compared to the scores. The high resolution images used for this analysis are reported in figure 6.9.

Scores	$a_2/a_1$ (mean $\pm$ STD)
1	$0.1 \pm 0.1$
2	$0.2 \pm 0.1$
3	$0.5 \pm 0.1$
4	$1.9 \pm 0.8$
5	$3.5 \pm 0.5$

Table (6.2): Results for the analysis with the histogram and Bi-Gaussian method.  $a_2/a_1$  values calculated on 5 sets of images for each score.

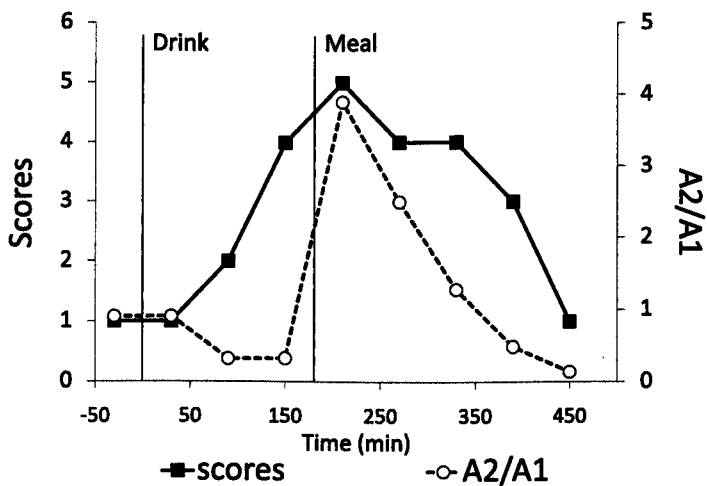
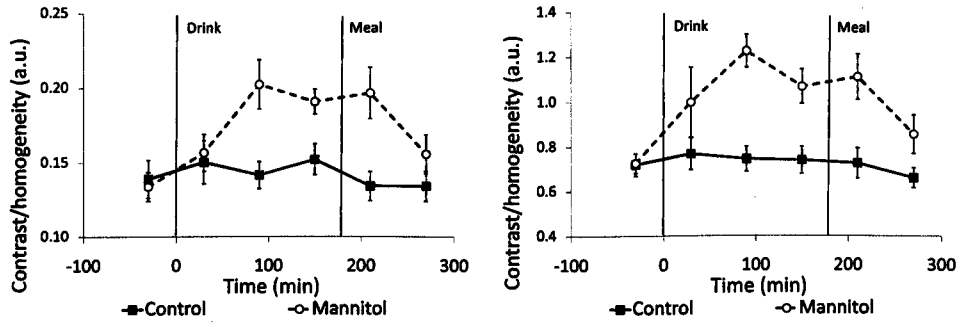


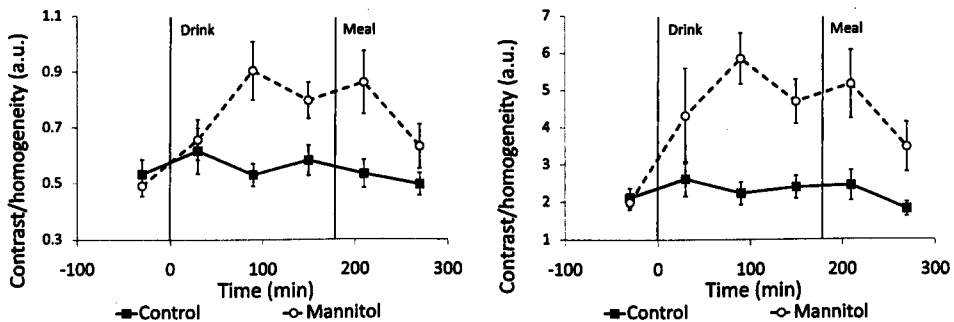
Figure (6.26): Visual subjective scores (primary axis) and  $a_2/a_1$  values versus time for one subject for the mannitol case. The high resolution images are reported in figure 6.9.

**Second automated method: feature extraction using Gabor filters**

For the texture analysis, the ratio between contrast and homogeneity is reported in figure 6.27 for the two different offsets in order to take into account also long range effect and integrated up to either the 11th or the 17th frequency. The sum up to the 17th frequency shows more evident differences between the texture features of the two arms of the study.



(a) Low offset, summed up to the 11th frequency. (b) Low offset, summed up to the 17th frequency.



(c) High offset, summed up to the 11th frequency. (d) High offset, summed up to the 17th frequency.

Figure (6.27): (Mean  $\pm$  STD) Contrast/homogeneity ratio averaged on the 8 subjects and plotted as a function of time for the control and the mannitol cases.

Figure 6.28 gives an example of the texture analysis for four different colonic contents. The mean signal calculated is higher for more homogeneous regions (figure 6.28(b)). The cumulative integral of the contrast homogeneity ratio calculated with the high offset is plotted as a function of frequency in figure 6.28(c): the difference in intensity increases with the frequencies, with the more heterogeneous area having less intensity.

Figure 6.29 shows the results for the weighted scores calculated with the

SVM classification, while figure 6.30 shows the mean Gabor signal. The average on the 8 subjects is plotted with the standard deviation as a function of time.

The cross validation in case of the training data showed an accuracy of 95.3%. For the testing data, corresponding to the study of control and manitol cases, the cross validation showed an accuracy of 92.4%.

### **Reproducibility:**

Figure 6.31 represents the difference of weighted scores computed on the basis of ROIs drawn by the same observer twice on two different subjects. This intra-observer variability proved to be reliable as the difference in scores was about 7%.

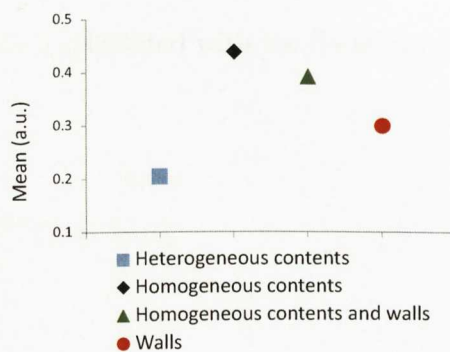
The inter-observer variability was also performed on two sets of data. Figure 6.32 reports the difference in scores for subject 1 and subject 2, averaged on the two observers' results. As the previous case, the inter-observer variability was less than 10%, which implies that the same score is given on the same set of data if two different operators perform the analysis.

### **Accuracy of drawing the regions:**

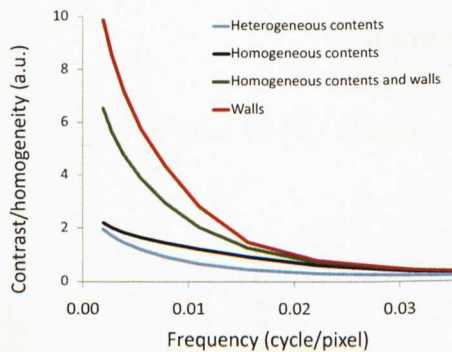
The results for the scoring for the 3 sets of data analysed with a coarse and a precise ROI were subtracted and plotted according to the two experimental conditions. In both cases, the difference in scores is less than 5%, figure 6.33.



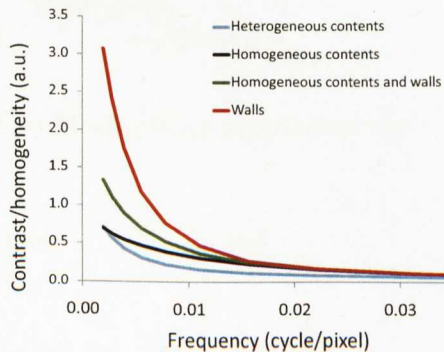
(a) Examples for the four different areas taken into account for the Gabor texture analysis: walls (red), walls and contents together (green), homogeneous contents (black) and heterogeneous contents (blue).



(b) Mean of the signal for the 4 regions.



(c) Cumulative integral (high offset) for the contrast homogeneity ratio as a function of frequency.



(d) Cumulative integral (low offset) for the contrast homogeneity ratio as a function of frequency.

Figure (6.28): Feature analysis for different AC regions.

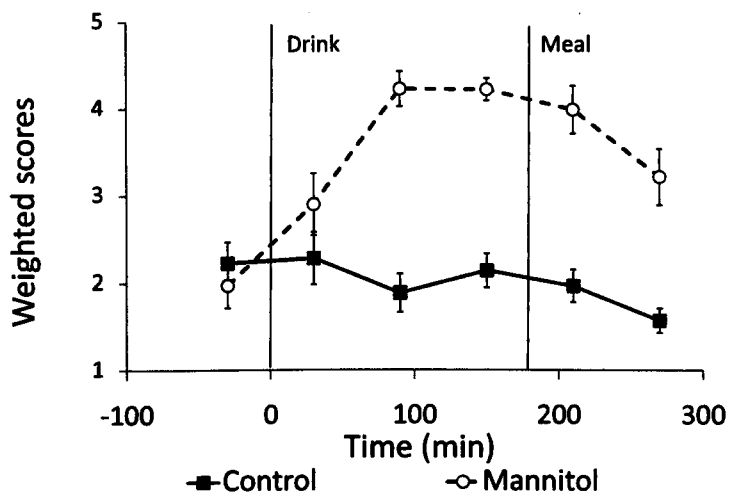


Figure (6.29): (Mean ± STD) Weighted scores calculated with the SVM classification.

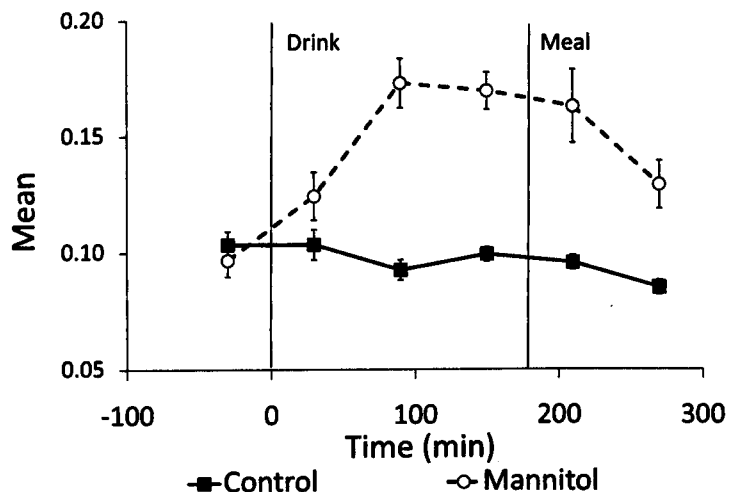


Figure (6.30): (Mean ± STD) Mean Gabor signal over time.

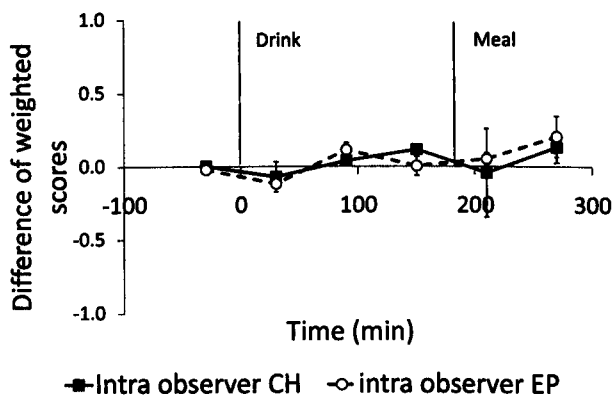


Figure (6.31): Intra-observer variability calculated on two sets of different subjects. The scores difference is about 7% meaning that the variability doesn't imply a change in the score.

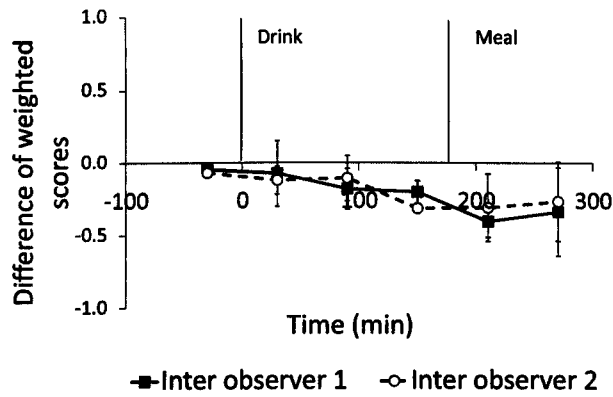


Figure (6.32): Inter-observer variability calculated on two sets of data. The difference is less than 10%, which implies that the same score is given on the same set of data if two different operators perform the analysis.

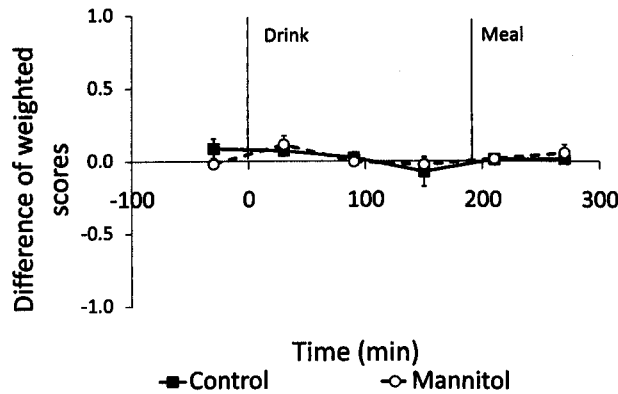


Figure (6.33): Difference in scores for the two types of accuracy in drawing ROIs. For both control and mannitol cases, the difference between precise and coarse is less than 5%, meaning that the same score is given in every condition.

#### 6.4.4 Discussion

The subjective scoring system proved to be robust and both the intra-observer and the inter-observer resulted in a good accordance (75 % for both cases). However, being a subjective method, the observer needs to be properly trained and it also relies on the person's judgment. In addition, the observer scores the images while looking at all the slices available together, thus leading to possible biases.

The Bi-Gaussian fit and the Gabor texture analysis methods provide an improved objective assessment of the AC contents compared to the subjective scoring, providing continuous values for the different AC characteristics. The Bi-Gaussian fit method requires the input from the operator to verify the accuracy of the fit. For that reason no discrimination was performed with this method but the method was only reported for completeness.

The feature analysis proved to be reliable, with an inter- and intra-observer variability much smaller than the subjective method (more than 90%). The only inputs required are the ROIs of the AC and of a small region in the kidney thus providing a very efficient objective method. The computation time is very short as it allows the analysis of a whole set of data in a few minutes. The scores and the mean were found to be higher in time and for the mannitol case compared to the control (figure 6.29 and 6.30), thus reflecting the results obtained previously with the water content in the ascending colon, see figure 6.3. These results reflect the scoring performed subjectively (figure 6.23) but they have the advantage of being obtained without any operator intervention.

This method has also been used for the calculation of features that can be applied to any sets of data. In particular, chapter 7 will present the results of the features of the colonic contents under pharmacological intervention.

Further improvements may include the possibility of drawing the ROIs in Matlab as it was proven that a coarse definition of the region is sufficient, thus avoiding the use of other licensed softwares.

The feature analysis method was a preliminary attempt to solve the complex and time consuming problem of characterising colonic contents. More work needs to be done to optimise such method. Firstly, a systematic study of the role of the filters must be undertaken in order to consider the importance of each frequency for the feature discrimination. Secondly, a deeper study of the features needed for the discrimination needs to be performed so that only dominant features are considered. In addition a more detailed comparison between different offsets can be performed in order to further investigate the role of the colonic walls contribution in the features results.

This will not only potentially simplify the analysis but also provide new information about changes in colonic content over time.

# Chapter 7

## MRI of pharmacological interventions in the colon

### 7.1 Introduction

Symptoms of colonic dysfunction such as diarrhoea and constipation are very common in the general population; both symptoms may coexist and can have a major impact on the quality of life [5, 6]. However, they are often embarrassing and underreported thus leading to poor diagnosis of eventual underlying pathologies.

Acute diarrhoea is a disorder that occurs in a majority of adults at least once a year [54]. There is a number of causes for acute diarrhoea including food intolerance, psychological stress and adverse reactions to medications. In most cases diarrhoea is due to infections caused by viruses and bacteria but it can also be non-infectious. Many patients report symptoms associated with their diarrhoeal illness including abdominal pain, bloating, flatulence, nausea and vomiting. Diarrhoeal diseases usually resolve spontaneously within 3–5 days occasionally aided by over the counter medication; however, being such a common illness, diarrhoea can have a substantial social and economic impact.

Constipation is a common heterogeneous condition that affects more than 15% of the population in the western world [55]. It is defined by several symptom criteria (ROME III<sup>1</sup>) determined by the association with abdominal discomfort or pain. The frequency of constipation is higher in the elderly, in non-whites and in subjects of lower socioeconomic status [57], thus suggesting the influence of environmental factors. Constipation is poorly understood because of the difficulties of access to the small and large bowel. The majority of cases can be treated with dietary changes or mild medications but there is a group of patients in whom the symptoms are more acute and persistent and are thought to be due to impaired colonic transit and/or to obstructed defecation [58].

Advances in understanding the pathophysiology of the colon as a guide to treatment of patients with constipation and diarrhoea is a continuing important goal. Imaging has therefore become fundamental to this aim and to investigate the mode of action of treatments. In this work, novel MRI techniques have been developed that allow imaging in great detail the characteristics of the small bowel and the colon non invasively, to study the physiology of the undisturbed state.

This chapter presents the application of these MRI techniques developed and explained in the previous chapters to the pharmacological interventions in the colon.

---

<sup>1</sup>The Rome criteria is a system developed to classify the functional gastrointestinal disorders, in which symptoms cannot be explained by the presence of structural or tissue abnormality, based on clinical symptoms. Rome criteria apply not only to constipation but also to irritable bowel syndrome, functional dyspepsia and functional heartburn [56].

## 7.2 Novel insights into the mechanisms of action of Metamucil

### 7.2.1 Introduction

Metamucil® (Procter and Gamble, USA) is a bulking agent for the treatment of constipation which is also used as a dietary fibre supplement as it doesn't contain any chemical stimulants. The active ingredient, psyllium, is the husk of the seed of *Plantago ovata* or *P. psyllium* characterised by a high mucilage content. Mucilages are clear colourless gel forming materials obtained by milling the outer layers of the seed which bind water, increasing in volume of 10 fold or more when added to water. Metamucil has been used together with Gd-DOTA (Dotarem) as an orally administered contrast agent in MRI studies for the imaging of the small bowel [59] and for the measurement of the small bowel flow rate measurement [60] but its mechanism of action has never been studied with MRI.

This pilot study investigates whether it is possible to visualise the effects of Metamucil on the colon and in particular to assess the effects of Metamucil on small bowel water content, colonic water content and ascending colon motility. Variations of such parameters would give information regarding the mode of action of the product thus providing useful information for possible future developments of technology. This pilot study has been funded by Procter and Gamble for visualisation of the product in three subjects only.

### 7.2.2 Method

This study was approved by the University of Nottingham Medical School Ethics Committee and all volunteers gave written informed consent. For this pilot study we recruited volunteers who attended the imaging centre twice (at

least one week apart), having fasted overnight on each occasion. 3 healthy female volunteers, without known contraindications to MRI imaging (e.g. metal implants in their body), participated in the study. They had normal BMI and were aged 22–39 years. All images were acquired with a 1.5 T Philips Achieva system using a range of MRI sequences including:

- A balanced gradient echo (bTFE) sequence (TR = 2.4 ms, TE = 1.19 ms, acquired resolution of 2.50 mm x 1.56 mm and slice thickness of 10 mm, scan duration 11 seconds) to measure the gastric volumes.
- A high resolution bTFE to image the contents of the ascending colon (AC) (TR = 3.2 ms, TE=1.58 ms, acquired resolution = 1.50 mm x 1.50 mm, 8 slices 5 mm thick, 0.58 mm gap, scan duration 16 seconds).
- A thicker slice bTFE used to identify the peristaltic movements in the AC (TR = 3.0 ms, TE = 1.49 ms, acquired resolution = 1.50 mm x 1.50 mm, 15 mm thick acquired every second for 3 minutes). No longer scans were possible for timing restrictions.
- A single shot, fast spin echo sequence (RARE) to acquire in a single breath-hold 24 coronal images with in-plane resolution interpolated to 0.78 mm x 0.78 mm and a slice thickness of 7 mm, with no gap between slices (TR = 8000 ms, TE = 320 ms, acquired voxel size = 1.56 mm x 2.90 mm, scan duration 24 seconds). This sequence yields high intensity signals from areas with liquid fluid and little signal from body tissues and is used for the small bowel and colon water content estimation.

With the exception of the motility sequence, each image set was acquired on an expiration breath-hold with a duration between 13 and 24 seconds depending on the sequence. Including set-up and imaging the volunteers spent approximately 10 min inside the magnet for every time point, spending the rest of the time sitting upright in an adjacent room. The volunteers underwent a baseline



Figure (7.1): Protocol of the study for each occasion. The subjects were scanned fasted and immediately after the drink (Metamucil or placebo) and then hourly for 7 hours. A single data point at 24 hours was also acquired. Details of the drinks and the meal are given in the text.

scan before being administered Metamucil (one rounded teaspoon in 227 ml still water) or placebo (6.9 g glucose in 227 ml still water to match calories and water volume of active). They were then scanned immediately after this and then hourly for 7 hours (8 hours in total). The subjects were imaged again the following morning to acquire a single data point at 24 hours after dosing.

On the first study day the subjects also received a breakfast meal comprising a standard rice pudding meal used in previous studies [61]. It consisted of:

- 220 g Sainsbury's creamed rice pudding
- 15 g coarse wheat bran (Holland and Barratt)
- 34 g Sainsbury's seedless raspberry jam
- 100 ml Sainsbury's pure orange juice from concentrate

The total caloric content for this meal was 362 kcal.

The subjects were dosed again with the active or the placebo twice according to the schedule reported in figure 7.1 and to the product instructions.

### 7.2.3 Results

All volunteers tolerated well the Metamucil and the placebo drinks and the study procedures. There were no adverse events reported in this study. No statistical analysis was performed on the sets of data, given the number

of subjects. However these data could be used to plan and to calculate the power for future studies. The results are shown below as mean and standard deviation.

Gastric emptying showed no significant difference between the two conditions (figure 7.2). The Metamucil and placebo drinks emptied rapidly as shown by the data from the third dosing of the day. The first two dosings overlap with the emptying of the solid meal. The behaviour of intra gastric volume of air is not different between conditions, figure 7.2(b).

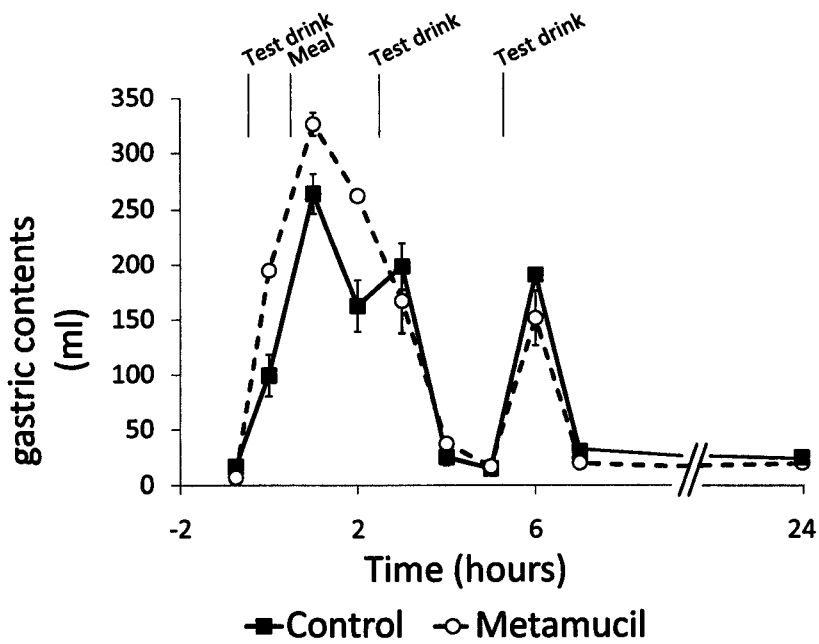
The small bowel water content showed characteristic drop after feeding but no difference between the two conditions was observed in the small bowel free mobile water content as measured from the RARE images, figure 7.3. At later times it was possible to visualise the arrival and persistence of a bright bolus of material in the colon of all three volunteers. The graphs showing the total colon contents over time is shown in figure 7.4(a). After the Metamucil drink a big amount of fluid arrives in the colon, whilst the total colonic water contents stays low for the control. Figure 7.4(b) reports the area under the curve of the total colon water content over time, showing an evident increase of about 900%.

In particular, two volunteers showed the arrival and the persistence in the ascending colon between 2h and 5h post dosing, showed in figure 7.5. An example of the arrival of fluid in the transverse colon is given in figure 7.6.

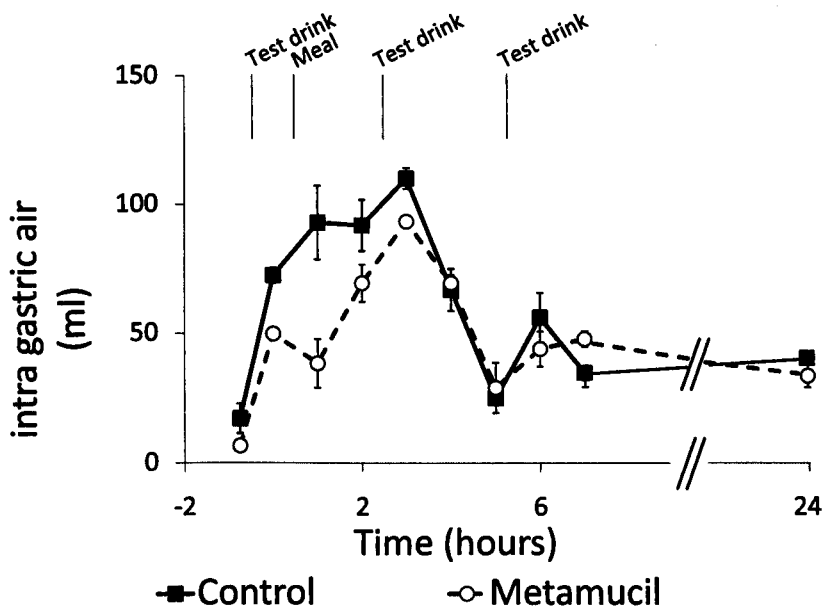
At every time point a dynamic MRI scan of the ascending colon was acquired to visualise ascending colon walls movements. These movies showed very little motility on either arm of the study. However ascending colon motion was observed in the presence of the Metamucil bolus in the first volunteer.

#### **7.2.4 Discussion and conclusion**

This pilot study showed that it was possible to visualise the arrival and persistence of a bright watery bolus in the colon of all 3 volunteers after dosing



(a) (Mean  $\pm$  STD) Stomach contents excluding air over time averaged over all subjects.



(b) (Mean  $\pm$  STD) Intra gastric air over time averaged over all subjects.

Figure (7.2): Average values for the gastric contents and air over time.

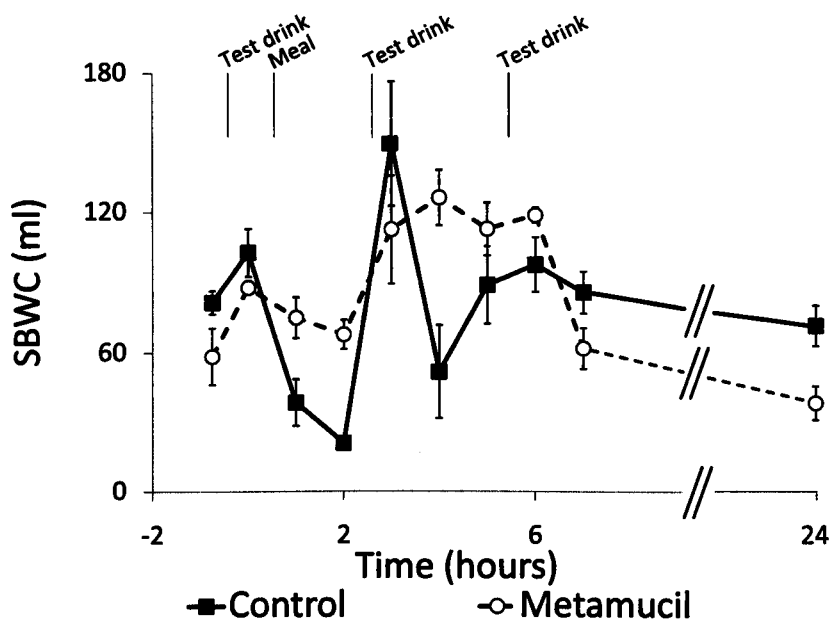
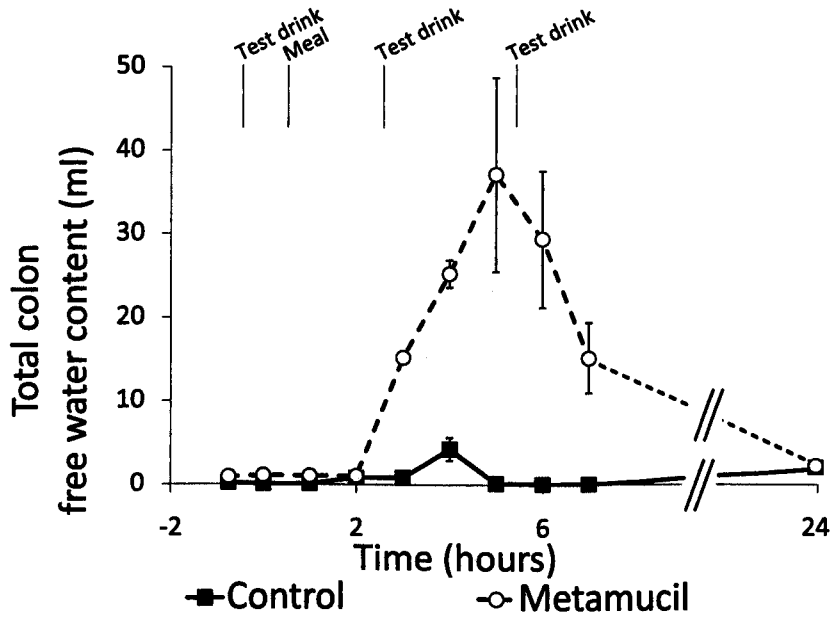
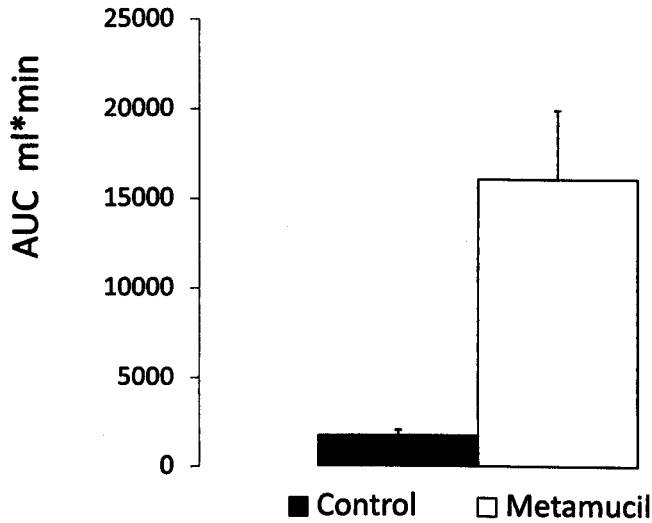


Figure (7.3): (Mean  $\pm$  STD) Average values for the small bowel water contents over time.

with Metamucil using MRI. No such bright mass was seen on the placebo condition. We can infer that changes in the appearance and time to peak and time of persistence of the active bolus in the colon, in addition to the assessment of gastric emptying and small bowel water content would relate to the product mode of action of metamucil. The MRI visualisation could also provide unique non-invasive insights and novel information regarding the mode of action of different products thus potentially aiding future pharmacological developments.

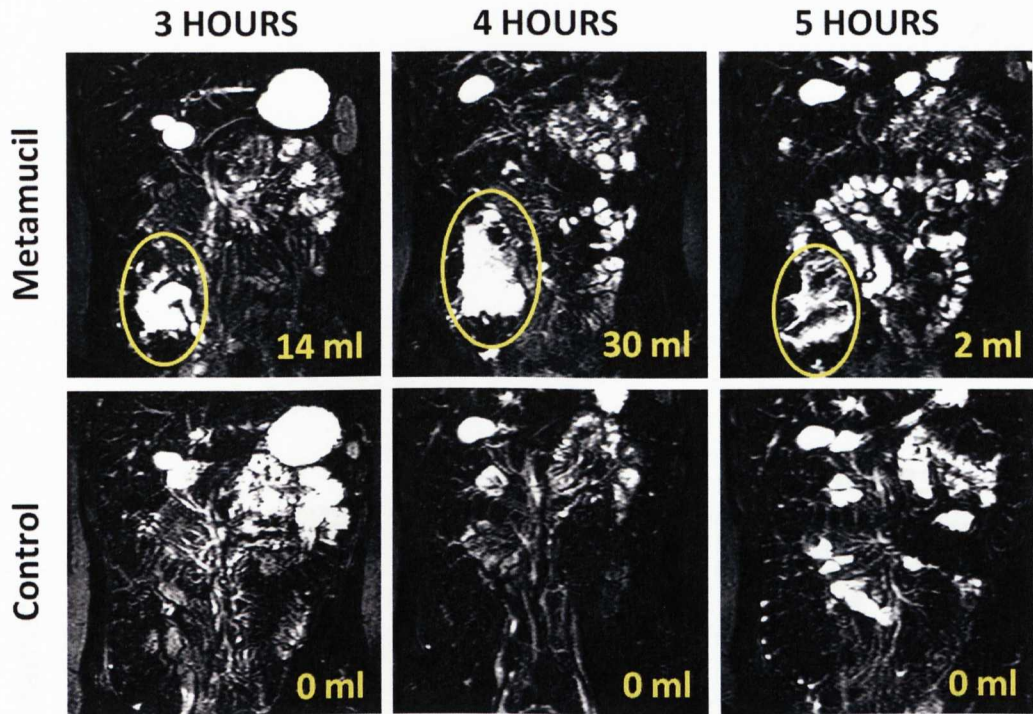


(a) Average values for the total colon (ascending + transverse) water contents over time.

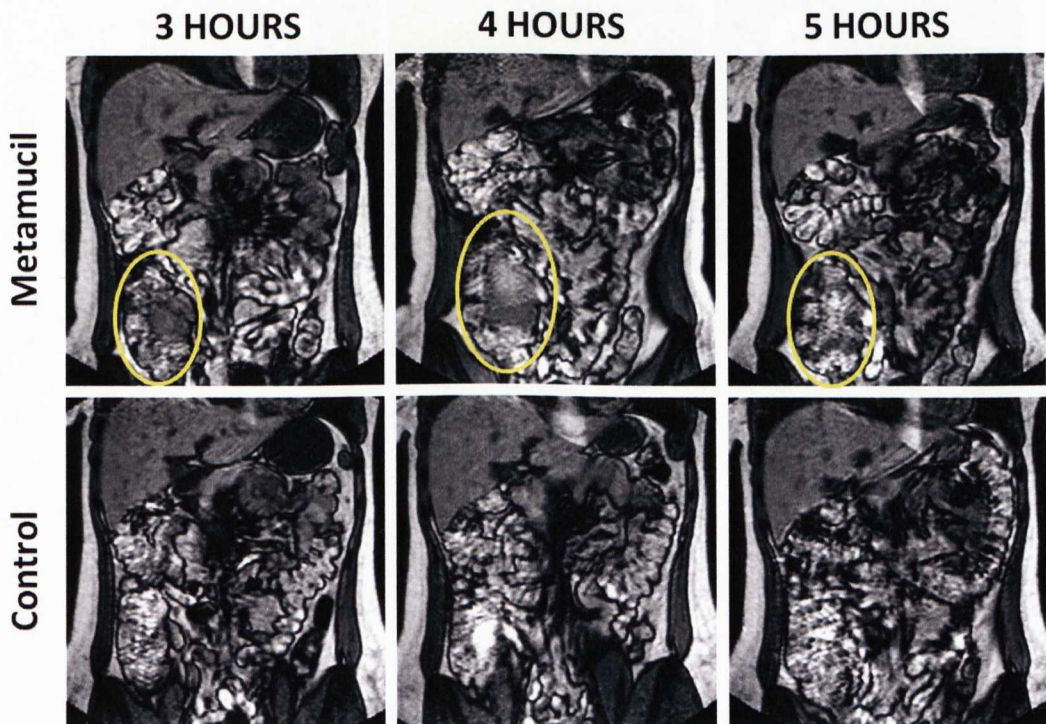


(b) AUC (ml\*min) for the total colon (ascending + transverse) water contents.

Figure (7.4): Average value for the water contents in the lower gut.



(a) Coronal RARE single slice images of the arrival and persistence of a bright bolus of material in the ascending colon of the second volunteer after drinking Metamucil at different time points. The corresponding images after the placebo (glucose) drink underneath showed no such filling.



(b) Corresponding dual echo fast field echo coronal anatomical roadmaps of the ascending colon.

Figure (7.5): An example from the second volunteer's ascending colon.

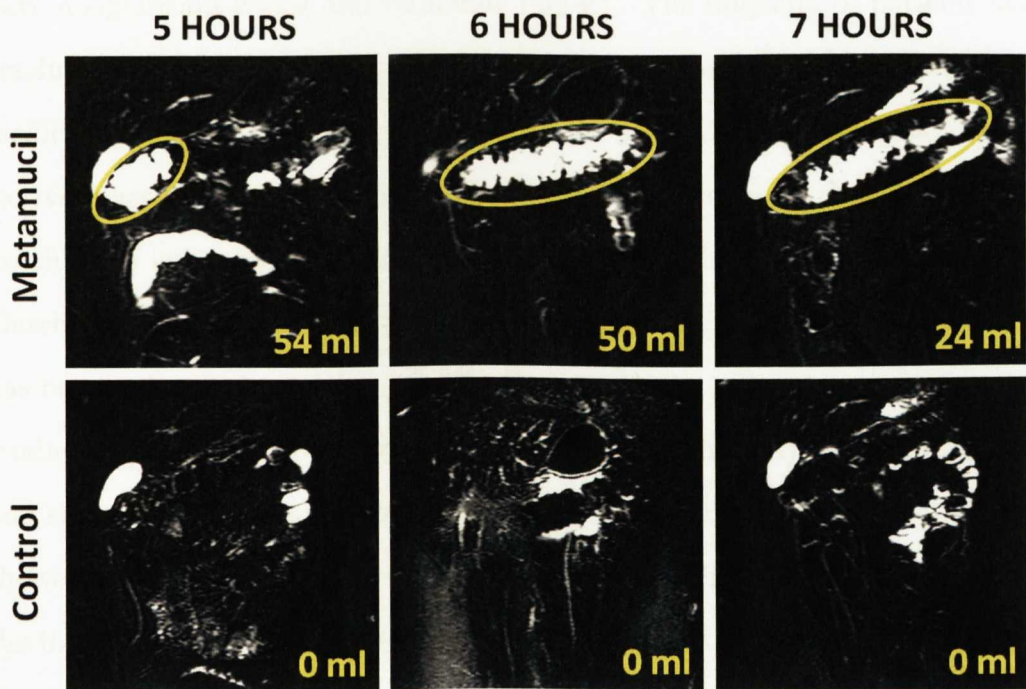


Figure (7.6): Coronal RARE single slice images of the arrival and persistence of a bright bolus of material in the transverse colon of the third volunteer after drinking Metamucil at different time points. The corresponding images after the placebo (glucose) drink underneath showed no such filling.

## **7.3 Defining the mode of action of loperamide and loperamide plus simethicone using an MRI model of acute diarrhoea**

### **7.3.1 Introduction**

As previously stated, acute diarrhoea is a very common disorder that can have a significant social and economic impact. The majority of patients successfully obtain symptomatic relief of acute diarrhoea with over-the-counter medication; however, until now there is no single medication that can effectively act on both diarrhoea and gas-related discomfort. Loperamide hydrochloride is a widely used anti-diarrhoeal agent shown to be efficacious in diarrhoea of both infectious and non infectious origin. Its mechanism of action has been extensively studied [62, 63]. Early works in humans and more recent studies in animals show that loperamide reduces the peristaltic movements and slows the gastrointestinal transit. In particular, Schiller et al. [64] in 1984 showed that loperamide is responsible for a change in the motor function of the intestine. They studied this mechanism during experimental diarrhea produced by the rapid intragastric infusion of electrolyte solution. They suggested that this change in the motor function results in a delay in the passage of fluids through the intestine thus implying that this delaying mechanism, rather than a change in rate of absorption by intestinal mucosal cells, is responsible for the antidiarrheal effect of loperamide.

Sandhu et al. in 1981 [65] and then in 1983 [66] suggested from animal studies that loperamide may also have an anti-secretory effect, and concluding that this process is mediated via opiate receptors.

More recent studies include the work from Szilagyi et al. [67] investigating the influence of loperamide on lactose handling and oral-caecal transit time.

They showed that the main effect of loperamide appears to be an increase in oral-caecal transit time of 30–50%. Similar studies using 0.1 mg/kg by mouth in pigs showed this was able to reverse the strong secretory effect of hypertonic mannitol and enhance colonic water absorption [68]. Human studies using jejunal, ileal and colonic perfusion showed that 12 mg of loperamide by mouth increased the frequency of migrating motor complexes, decreased irregular motor activity and increased jejunal but not ileal transit time [69].

Simethicone is a silicone polymer which acts as a surfactant: it has a very low surface tension and it forms a thin film. For this reason it is often used as an antifatulent in gas and bloating conditions. Loperamide and simethicone combination would therefore provide a better relief from the diarrhoeal symptoms. A study from Kaplan et al. [63] demonstrated that the combination of loperamide and simethicone improved not only the relief of symptoms but it also improved the control of diarrhoea itself, thus increasing the efficacy speeding onset of action. The reason for faster onset of action is unclear but scintigraphic studies suggest a more even spread throughout the bowel which might enhance its action which is largely local since very little is absorbed systemically [70]. It has also been suggested that the interaction between loperamide and simethicone may induce a different distribution of loperamide, leading to a prolonged action of the drug locally in the GI mucosa.

Based on these assumptions, it was hypothesized that the predominant effect of loperamide in treating acute secretory diarrhoea originating in the small bowel will be to delay transfer of fluid from small bowel to the colon. It was also hypothesized that it is the rapid transfer of fluid to the ascending colon which causes propulsive motor patterns in the colon and hence urgent bowel movements.

Until recently proving such hypotheses involved arduous intubation experiments, which were highly unphysiological since as it has been recently showed, intestinal intubation alters gut motility, accelerating transit [61]. This thesis

presents the development of an MRI technique to investigate the colon non-invasively and non-ionising, based on the work recently validated on the small bowel water content [38] to demonstrate the marked secretory effects of mannitol with increase in small bowel water content and delivery of free water to the colon [61].

In this study a model of acute diarrhoea has been used in which marked small bowel secretion occurs. Loperamide is thought to cause pooling of fluid in the small bowel and to reduce the amount of free water transferred to the ascending colon thereby preventing diarrhoea. Loperamide and loperamide plus simethicone are compared in order to determine if this greater coating of the small bowel causes faster onset of action in the small bowel and whether it reduces total water reaching the colon.

A range of different MRI sequences have been optimised in order to characterise the ascending colon. Movements of the colonic walls are also observed with a motility scan over 3 minutes. The ascending colon contents are described by means of their  $T_2$  values: this is important because knowledge of the composition of the colonic contents would avoid other more invasive diagnostic techniques to assess eventual disease progression. In addition, the texture analysis described in section 6.4 was performed in order to have an objective information regarding the ascending colon content.

## **Aim**

The aim of this study is to assess the effect of loperamide and of loperamide plus simethicone in prolonging small intestinal transit, delaying time to peak of total colon water content and reducing peak and integrated total colon water content.

## **Power of the study and dosing**

Using our mannitol MRI model of acute diarrhoea [61] we have previously found (section 6.2) in 10 healthy subjects a marked rise in total small bowel free water content with time. Small bowel water content at its peak was  $398 \pm 198$  ml (mean  $\pm$  standard deviation) so if we aim to detect an increase of 33% i.e. 130 ml this would require  $n=12$ . We planned to recruit up to 18 healthy volunteers to increase power for other outcomes. Similar previous studies in pigs showed loperamide 0.1 mg/kg, equivalent to 7 mg in a 70 kg man, could completely block the effect of mannitol [68] while studies in man suggest 12 mg will delay small bowel transit by 50% [71]. We suggested that we use 12 mg dose which is well tolerated to ensure we would get a clear effect. The loperamide and simethicone capsules were reencapsulated by Nottingham University Hospitals QMC Pharmacy who also provided the placebo. The Pharmacy dispensed the study drugs according to a randomisation schedule provided by our Clinical Trials Unit. This was an Investigator Initiated Study which was funded by a research grant from McNeil Consumer Healthcare.

### **7.3.2 Method**

#### **Study design and population**

This was a randomised, double blind, placebo controlled, 3-ways, crossover study in healthy adult volunteers.

18 healthy subjects (11 female and 7 male, age range 20–45 years) without known contraindications to MRI imaging and normal BMI participated in the study. All volunteers had no history of gastrointestinal disease, they were free from medication likely to alter gastrointestinal motility and they were free from food allergy or intolerance. This study was approved by the University of Nottingham Medical School Ethics Committee and all volunteers gave written informed consent.

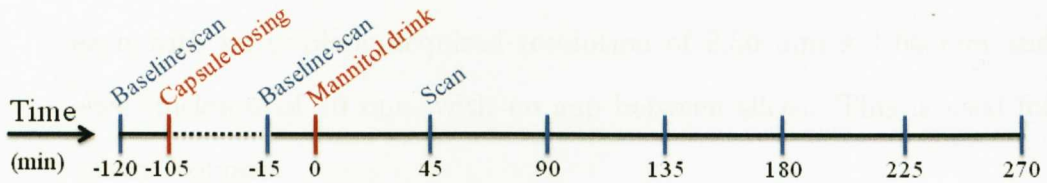


Figure (7.7): Protocol of the study for each occasion. Schedule of the experiment: a first baseline scan is performed after an overnight fast; a second baseline after dosing and following scans every 45 min after the mannitol drink.

## Study protocol

The volunteers were asked to follow restrictions to diet and lifestyle for the day prior to the study day, including avoid taking foods with high fibre content to avoid excessive residue in the bowel on the study day, avoid spicy food since it can stimulate bowel secretions and avoid caffeine, alcohol and strenuous exercise for 18 hours before the study start time. Volunteers were asked to fast overnight (from 8 pm the night before) except for a small cup of water on waking on the morning of the study.

All imaging was carried out on a 1.5T Philips Achieva scanner with a SENSE 4-element abdominal body coil.

Volunteers attended on three separate experimental sessions: they were first imaged in the fasted state as a baseline scan; subsequently they ingested capsules containing placebo or 12 mg loperamide or 12 mg loperamide + 125 mg simethicone. The timelines of the study day are summarised in figure 7.7.

100 minutes later they underwent a second baseline scan and 15 minutes after that they received a drink containing containing 5% mannitol in 350 ml of water. Mannitol is a common laxative known to stimulate small intestinal secretion and can be used as a model for a range of diarrhoeal diseases and we used it in the same dose previously [61]. The subjects then underwent serial imaging at 45 minutes intervals for 4.5 hours after the drink.

A range of MRI sequences were used to image the abdomen including:

- A balanced gradient echo (called balanced turbo field echo, bTFE) se-

quence (TR = 2.4 ms, TE = 1.19 ms) to acquire 25 transverse images each with an in-plane acquired resolution of 2.50 mm x 1.56 mm and slice thickness of 10 mm, with no gap between slices. This is used for gastric volumes.

- A high resolution bTFE to image the contents of the ascending colon (AC) (TR = 3.2 ms, TE = 1.58 ms, acquired resolution = 1.50 mm x 1.50 mm, 8 slices 5 mm thick, 0.58 mm gap). These images were used for the texture analysis.
- Motility bTFE used to identify the peristaltic movements in the AC (TR = 3.0 ms, TE = 1.50 ms, acquired resolution = 1.50 mm x 1.50 mm, single slice 15 mm thick acquired every second for 3 minutes).
- A single shot, fast spin echo sequence (RARE) to acquire in a single breath-hold 24 coronal images with in-plane resolution interpolated to 0.78 mm x 0.78 mm and a slice thickness of 7 mm, with no gap between slices (TR = 8000 ms, TE = 320 ms, acquired resolution = 1.56 mm x 2.90 mm). This sequence yields high intensity signals from areas with liquid fluid and little signal from body tissues and is used for small bowel water content.
- A dual gradient echo (dual-echo fast field echo, FFE,  $TE_1 = 2.3$ ,  $TE_2 = 4.6$ , TR = 158 ms) imaging sequence was used to visualise the anatomy acquiring 24 coronal images with in-plane acquired resolution 2.01 mm x 2.87 mm and a slice thickness of 7 mm, with no gap between slices.
- A  $T_2$ -prep bTFE sequence (TR = 3.0 ms, TE values (ms): 20, 29, 43, 63, 93, 137, 201, 295, 434, 637, acquired resolution 2.00 mm x 1.56 mm and a slice thickness of 7 mm) to measure the  $T_2$  values in the ascending colon [42].

With the exception of the motility sequence, each image set was acquired

on an expiration breath-hold with a duration between 13 and 24 seconds depending on the sequence. Including set-up and imaging the volunteers spent approximately 10 min inside the magnet for every time point, spending the rest of the time sitting upright in an adjacent room.

## **Analysis**

Measurements of the gastric contents and AC volumes have been carried out by manually tracing the region of interest on each slice using Analyze<sup>®</sup> software (Biomedical Imaging Resource, Mayo Foundation, Rochester, MN, USA) and summing across all the slices to determine the total volume at each time point. In particular the gastric volumes were analysed distinguishing the contents and the gas, with the gas being the dark area in the stomach. The total gastric volume is the sum of the contents and the gas. The manual tracing of an entire stomach or colon takes approximately 1 minute.

The volume of freely mobile water content, in both the small bowel and ascending colon, was calculated for each volunteer using methods validated by duodenal infusion intubation studies [38, 61]. At each time point, the volume of all image pixels above a threshold was integrated, after exclusion of signal from regions other than bowel.

The Gabor texture analysis introduced in section 6.4 was performed on the high resolution images of the colon for every subject with the exception of one because the volunteer had an ectopic kidney which meant that no kidney was visible in the slices and therefore no normalization was possible and the subject had to be excluded from the analysis. For the other 17 subjects the texture analysis was performed as described previously (section 6.4.2) and spot checks were carried out to check the accuracy of the classification in comparison with the visual scoring procedure.

$T_2$  data sets were processed, firstly using Analyze<sup>®</sup> software to generate a region of interest in the ascending colon chyme avoiding small 'pockets' of free

water (high intensity signal) if present. Then using the mean of this region at all the different echo times to calculate the  $T_2$  of the tissue using a program in-house which modelled the effect of the  $T_2$ -prepared scheme and subsequent imaging sequence for the  $T_2$ -prepared bTFE sequence [42].

Net secretion was assessed by subtracting the ingested 350 ml and the baseline values for the fluids in the bowel from the sum of stomach contents, small bowel water contents and ascending colon water contents. Previous work with mannitol showed that gastric emptying is rapid and effectively complete by 135 minutes [61]. Therefore, the total observation time (from 0 to 270 min) was divided into the “early phase” 0 to 135 min when the small bowel water content is strongly influenced by gastric emptying and “late phase” 135 to 270 min when the SBWC depends more on absorption and rate of transit into the colon.

### Statistical analysis

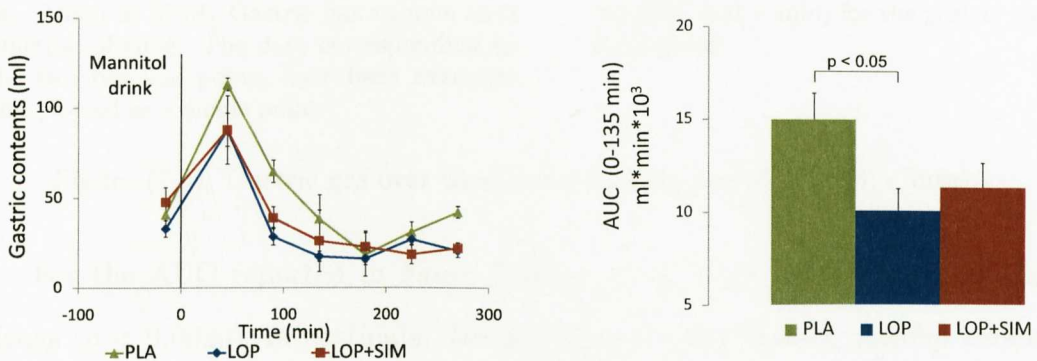
Statistical analysis was carried out using Prism 4 (GraphPad Software Inc.). All data was tested for normality using the Shapiro-Wilk’s Test. Two-way analysis of variance (ANOVA) was used to assess the significance of differences over time, followed by post-hoc tests corrected for multiple-comparison. Paired comparisons were performed using two-tailed Student’s t test for normal, and two-tailed Wilcoxon’s test for non-normal data. A p-value < 0.05 was considered to be statistically significant.

### 7.3.3 Results

All volunteers tolerated the experimental procedures well. One of the 18 volunteers experienced an acute diarrhoea episode that lasted for less than 2 hours but did not withdraw from the study.

## Gastric emptying (figures 7.8, 7.9 and 7.10)

As expected gastric emptying was rapid and effectively complete by 135 minutes. Loperamide and loperamide + simethicone accelerated the emptying of the gastric contents by 17% and significantly reduced the overall area under the curves (AUCs) of the gastric contents in the early phase (0–135 mins),  $p < 0.03$ .



(a) (Mean  $\pm$  SEM) Gastric contents volume as a function of time. The data corresponding to the two baseline points have been averaged and plotted as a single point.

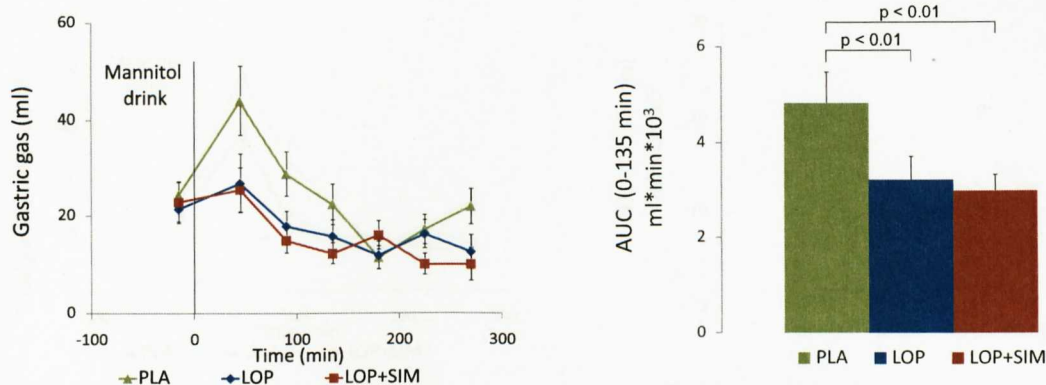
(b) AUC (ml  $\times$  min) for the gastric contents in the early phase.

Figure (7.8): Gastric volumes over time and corresponding AUC (ml  $\times$  min).

Both combinations of drugs also reduced the amount of gas in the stomach by 40%. In particular in the early phase as can be seen in figure 7.9(a) the drugs had an effect on the intra gastric air ( $p < 0.01$ ), reducing the amount of gas by 33%.

For the overall AUC there is a significant difference for the drugs compared to the placebo ( $p = 0.004$ ). Post tests showed a significant difference of both loperamide and loperamide + simethicone versus placebo, both  $p < 0.01$ .

Figure 7.10(a) shows the total gastric volume over time. The individual data are normally distributed and show a significant effect of the drug proved with a 2-ways ANOVA test,  $p < 0.0001$ . Post test show a significant effect of the drugs at 45 min and 90 min (loperamide versus placebo  $p < 0.01$  for both time points and loperamide + simethicone versus placebo  $p < 0.01$  and  $p < 0.05$  respectively).



(a) (Mean  $\pm$  SEM) Gastric gas volume as a function of time. The data corresponding to the two baseline points have been averaged and plotted as a single point.

(b) AUC (ml  $\times$  min) for the gastric gas in the early phase.

Figure (7.9): Gastric gas over time and corresponding AUC (ml  $\times$  min).

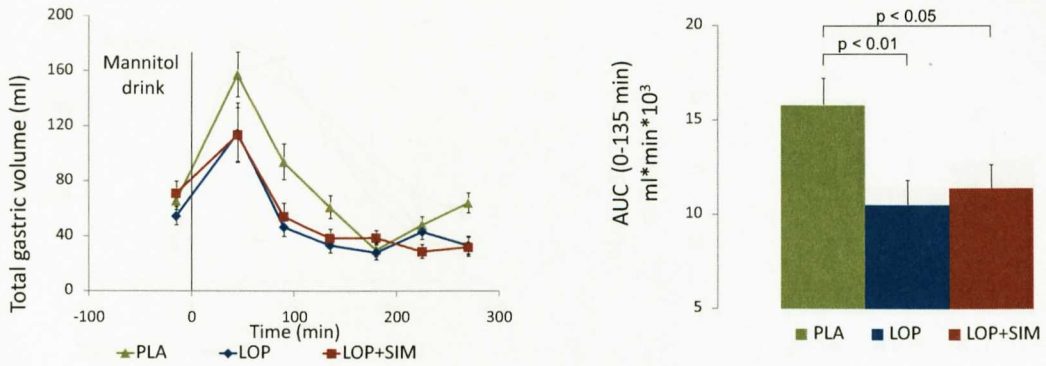
For the AUC reported in figure 7.10(b), there is an overall effect of the drugs ( $p < 0.0026$ ), in particular Dunnett's post tests showed placebo versus loperamide  $p < 0.01$  and placebo versus loperamide + simethicone  $p < 0.01$ .

During the early phase loperamide and loperamide + simethicone significantly reduced the AUCs of the total gastric volume ( $p < 0.0094$ ). The Dunnetts comparison post tests showed a significant difference of loperamide + simethicone versus placebo,  $p < 0.05$ , and also a significant difference for loperamide versus placebo,  $p < 0.01$ .

During the late phase there is also a significant difference between loperamide and placebo  $p < 0.01$  and between loperamide + simethicone versus placebo,  $p < 0.01$ .

### Small bowel water content (fig 7.11)

As expected from the accelerated gastric emptying, the peak of the small bowel water content which occurred during the early phase was slightly higher with loperamide and loperamide + simethicone being  $578 \pm 32$  ml and  $600 \pm 30$  ml respectively but the differences were not statistically different (repeated measures ANOVA  $p < 0.2$ ) compared to placebo  $564 \pm 38$  ml. No post tests were carried out.



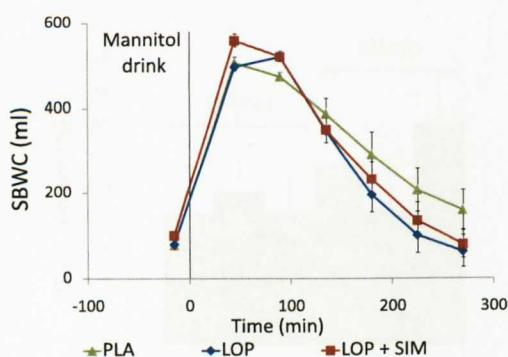
(a) (Mean  $\pm$  SEM) Total gastric volume as a function of time. The data corresponding to the two baseline points have been averaged and plotted as a single point.

(b) AUC (ml  $\times$  min) for the total gastric volume in the early phase.

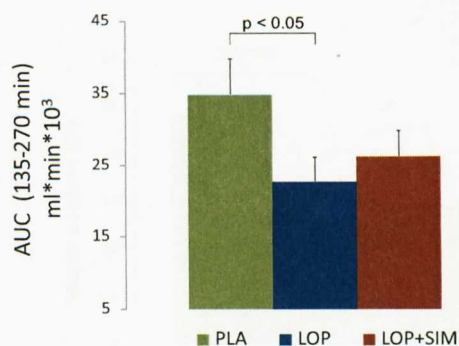
Figure (7.10): Total gastric volume over time and corresponding AUC (ml  $\times$  min).

The graph representing the SBWC over time shows an initial increase of the water content for the loperamide + simethicone compared to placebo. This is explained by the faster gastric emptying. However, even if the amount of water in the small bowel is higher for loperamide and loperamide + simethicone at 45 and 90 mins, it is significantly reduced at a later phase (135–270 min). This means that the drugs act on either accelerating the absorption of fluids or on inhibiting the secretions in the small bowel. Loperamide and loperamide + simethicone reduced the overall AUCs of the small bowel water content volumes from 0 min to 270 min compared to placebo (not shown). The differences were just outside the statistically significant threshold (repeated measures ANOVA  $p < 0.07$ ), so no post tests were carried out. Figure 7.11(b) shows that during the late phase loperamide and loperamide + simethicone markedly reduced the area under the curves (AUCs) of the small bowel water content volumes from 135 min to 270 min, which result significantly lower than placebo values, Friedman's  $p < 0.009$ . Dunn's multiple comparison post tests showed a significant difference of loperamide versus placebo,  $p < 0.05$ , whilst loperamide + simethicone versus placebo was not significantly different,  $p > 0.05$ .

Further analysis has been performed considering four areas in the small bowel: upper left and right, lower left and right. Figure 7.12 shows the areas



(a) (Mean  $\pm$  SEM) Small bowel water content over time. The data corresponding to the two baseline points have been averaged and plotted as a single point.



(b) AUC (ml  $\times$  min) for the SBWC in the late phase.

Figure (7.11): Small bowel water content over time and corresponding AUC (ml  $\times$  min).

under the curves for 180 minutes and 225 minutes.

### Ascending colon water content and geometrical volume (figures 7.13, 7.14 and 7.15)

The change in total volume and in water contents for the ascending colon show how the drugs delay the arrival of fluids in the AC, figures 7.13 and 7.14(a) respectively.

The drugs reduced the amount of free water in the AC,  $p < 0.04$ , shown by the overall AUC from 0 min to 270 min, figure 7.14(b). Figure 7.15 shows the AUC for the early and late phases. During the early phase (time 0 to 135 min) loperamide and loperamide + simethicone significantly reduced the AUCs of the ascending colon water content volumes by more than 40%,  $p < 0.004$ . The Dunnett's comparison post tests showed a significant difference of loperamide + simethicone versus placebo,  $p < 0.05$ , and also a significant difference for loperamide versus placebo,  $p < 0.01$ .

During the late phase (time 135 to 270 min), there was no significant difference between loperamide and placebo, but there was a significant reduction due to loperamide and simethicone,  $p < 0.04$ , figure 7.15(b).

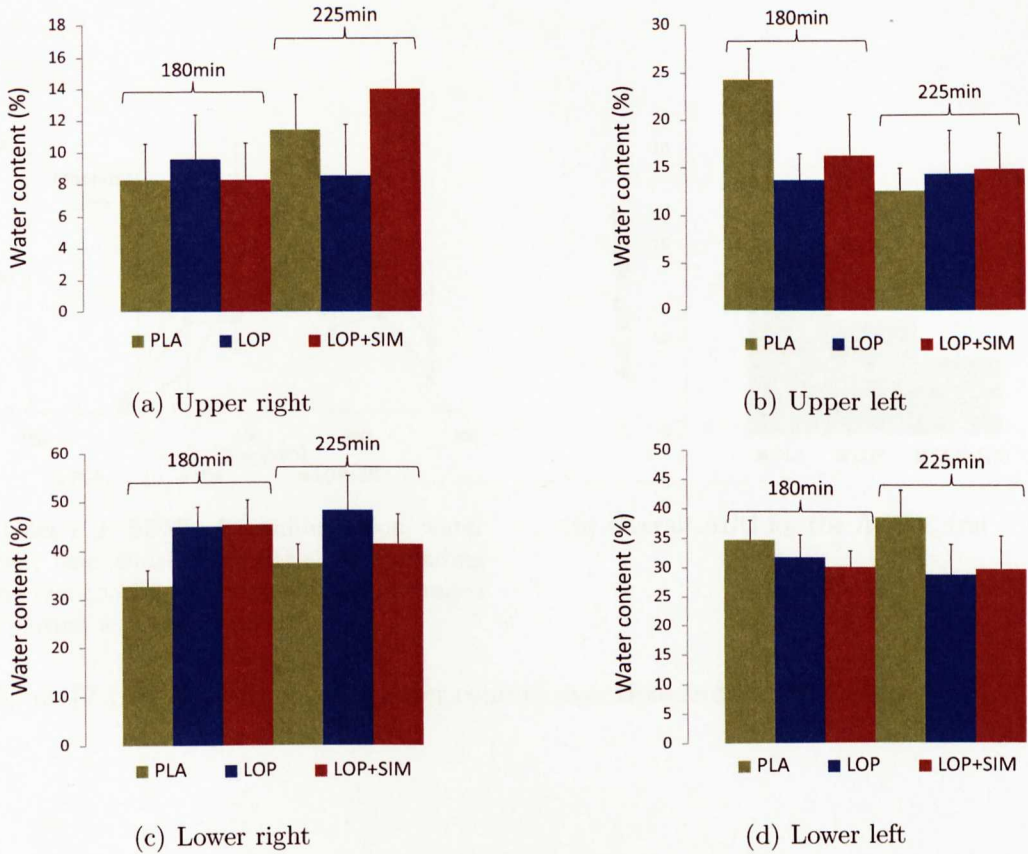


Figure (7.12): AUC (ml × min) for the SBWC in the four areas for 180 minutes and 225 minutes.

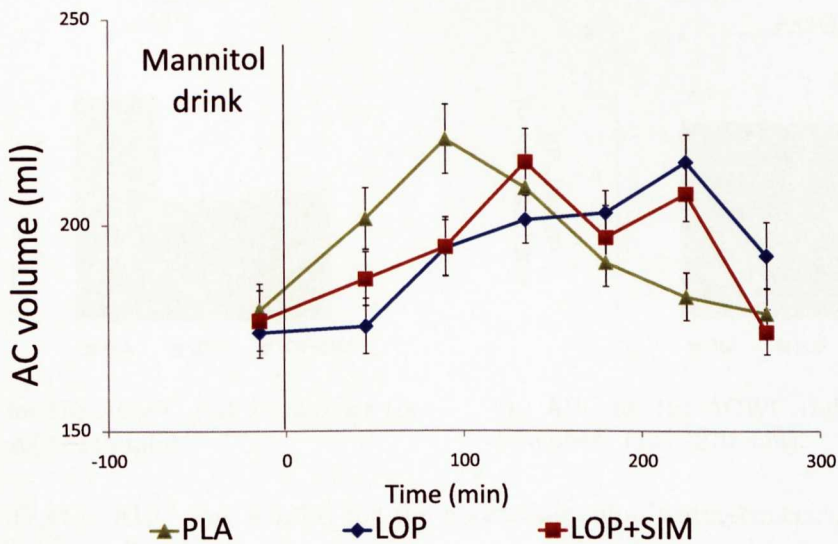
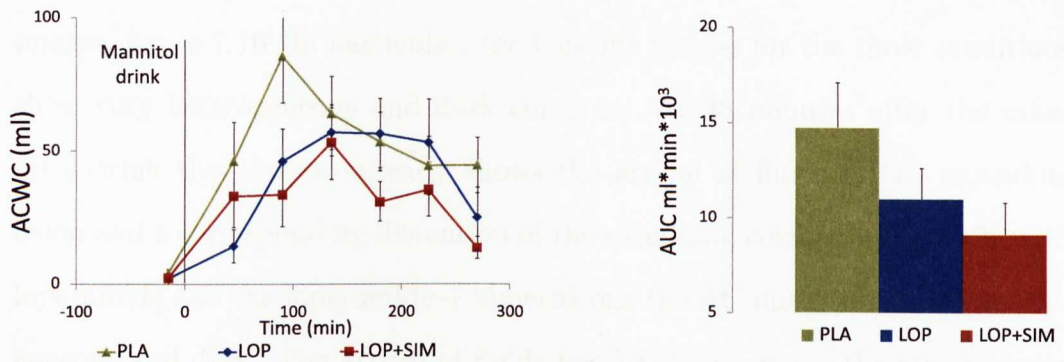


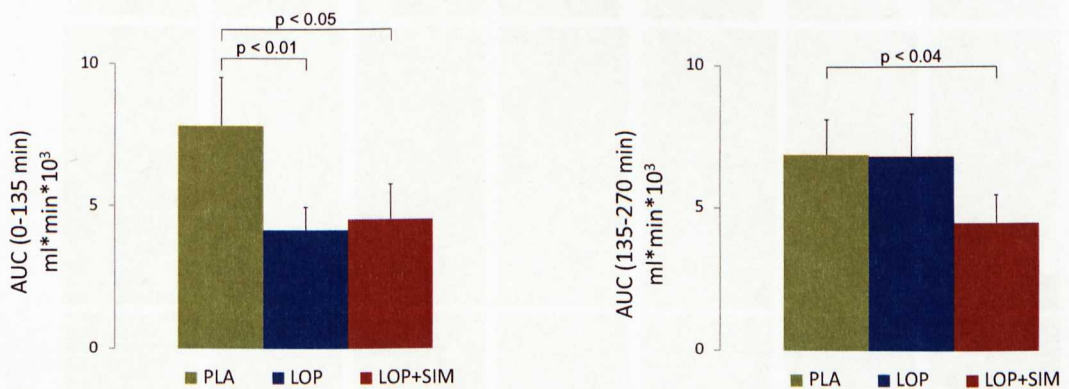
Figure (7.13): Ascending colon geometric total volume versus time. The AC volume after loperamide and loperamide + simethicone increases in a late phase showing the delay of fluid arrival in the AC.



(a) (Mean  $\pm$  SEM) Ascending colon water content over time. The data corresponding to the two baseline points have been averaged and plotted as a single point.

(b) Overall AUC for the ACWC (ml  $\times$  min).

Figure (7.14): Ascending colon water content over time and corresponding AUC.



(a) AUC for the ACWC (ml  $\times$  min) for the early phase (0–135 min).

(b) AUC for the ACWC (ml  $\times$  min) for the late phase (135–270 min).

Figure (7.15): AUC (ml  $\times$  min) for the ascending colon water content, represented in figure 7.14(a).

**High resolution sagittal images of the ascending colon (figure 7.16)**

The high resolution sagittal bTFE images provided detailed anatomical images, figure 7.16. In particular, the baseline images for the three conditions show very heterogeneous and dark contents. At 45 minutes after the mannitol drink the placebo already shows the arrival of fluids in the ascending colon and a corresponding distention of the ascending colon volume while with loperamide and the loperamide + simethicone the AC image remained heterogeneous and dark. The arrival of fluids for the drug arms of the study occurs at 90 minutes and the ascending colon remains bright and homogeneous for the following hours, gradually decreasing in volume and brightness.

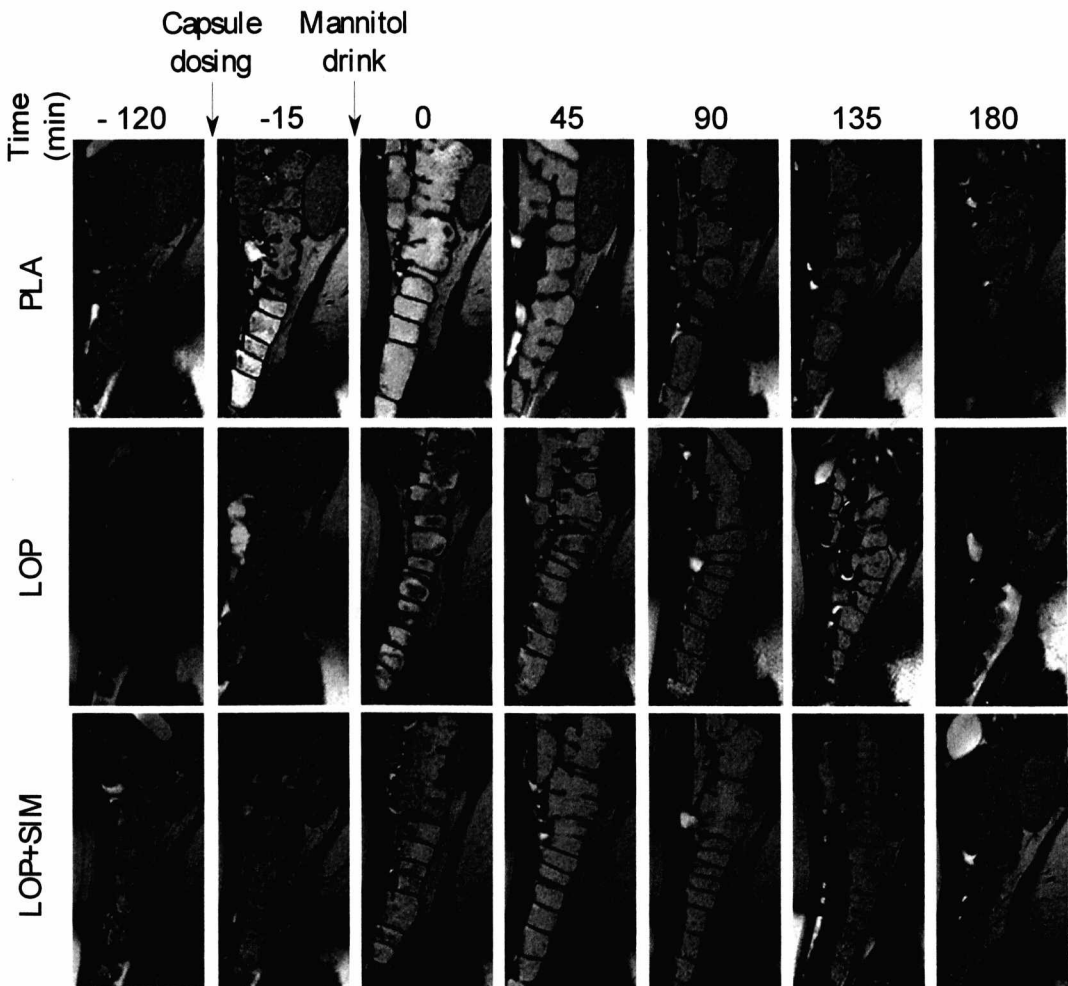


Figure (7.16): High resolution bTFE sagittal images of the AC for the same volunteer.

## Texture analysis on the high resolution colonic images (figures from 7.17 to 7.21)

The spot checks conducted on the data showed a similar accuracy as for the glucose versus mannitol study (section 6.4.3): out of the 20 colon images checked, 18 were in accordance with the visual scoring procedure and the 2 remaining were just one score different.

Figure 7.17 shows the mean signal from the texture analysis up to the 17<sup>th</sup> frequency for all subjects as a function of time: even if a general increase in mean signal is visible, there is no significant difference between the drugs and the placebo.

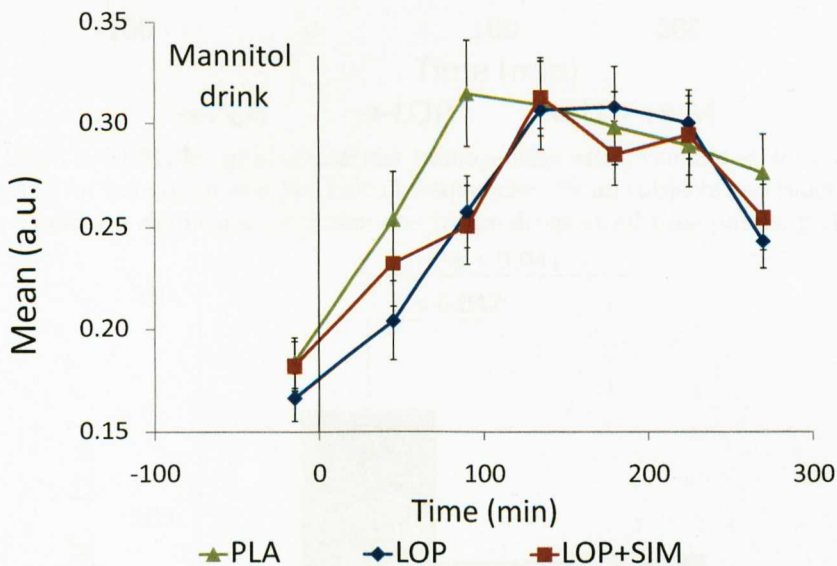
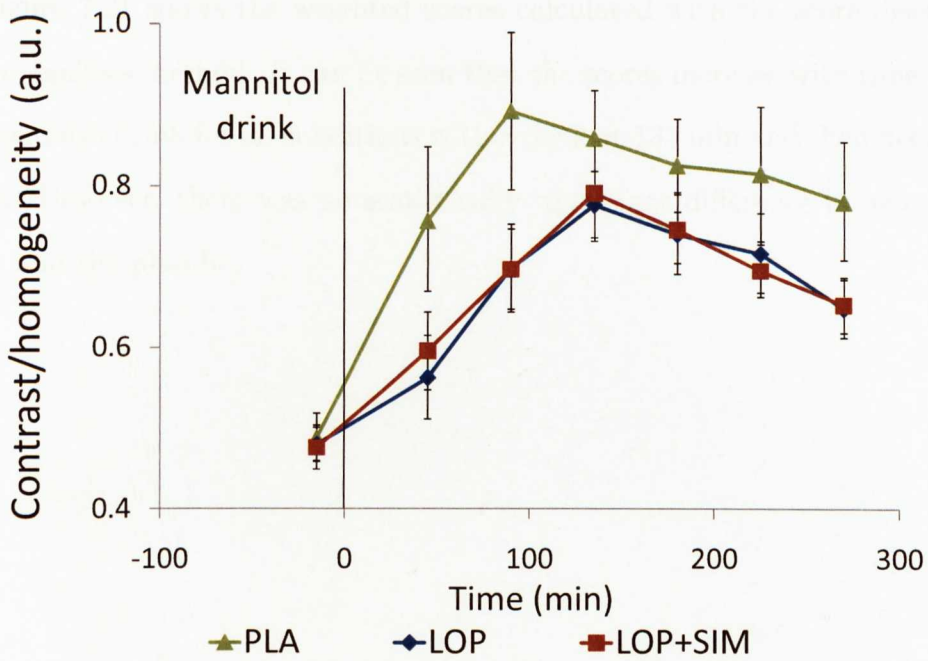


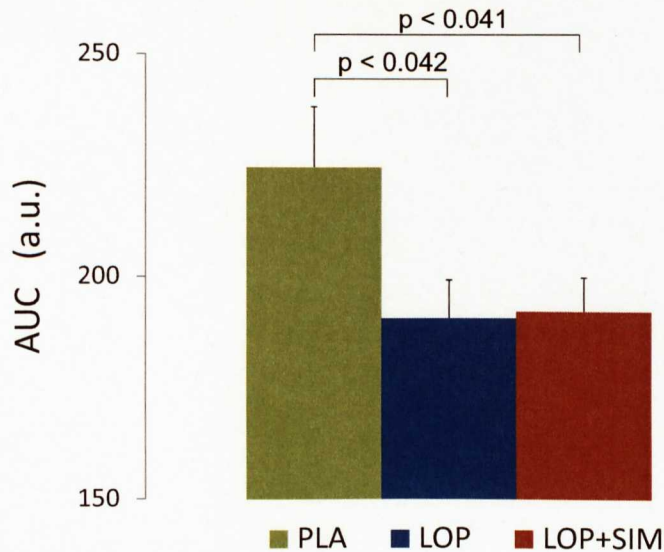
Figure (7.17): (Mean  $\pm$  SEM) Cumulative integral of the mean signal up to the 17<sup>th</sup> frequency.

However, the results of the texture analysis alone showed that the contrast homogeneity ratio was significantly higher for the placebo than for the drugs at all time points, ANOVA repeated measurements  $p < 0.034$ , for the high offset case integrated over the first 11 frequencies (figure 7.18(a)). In addition, post hoc tests showed a significant difference between loperamide and placebo ( $p < 0.041$ ) and loperamide+simethicone and placebo ( $p < 0.042$ ), figure 7.18.

Figures 7.19 and 7.20 show the results of the texture analysis for the subject



(a) (Mean  $\pm$  SEM) Integral of contrast homogeneity ratio, calculated with a high offset and for integrated over the first 11 frequencies, for all subjects as a function of time, showing a significant reduction due to the drugs at all time points,  $p < 0.034$ .

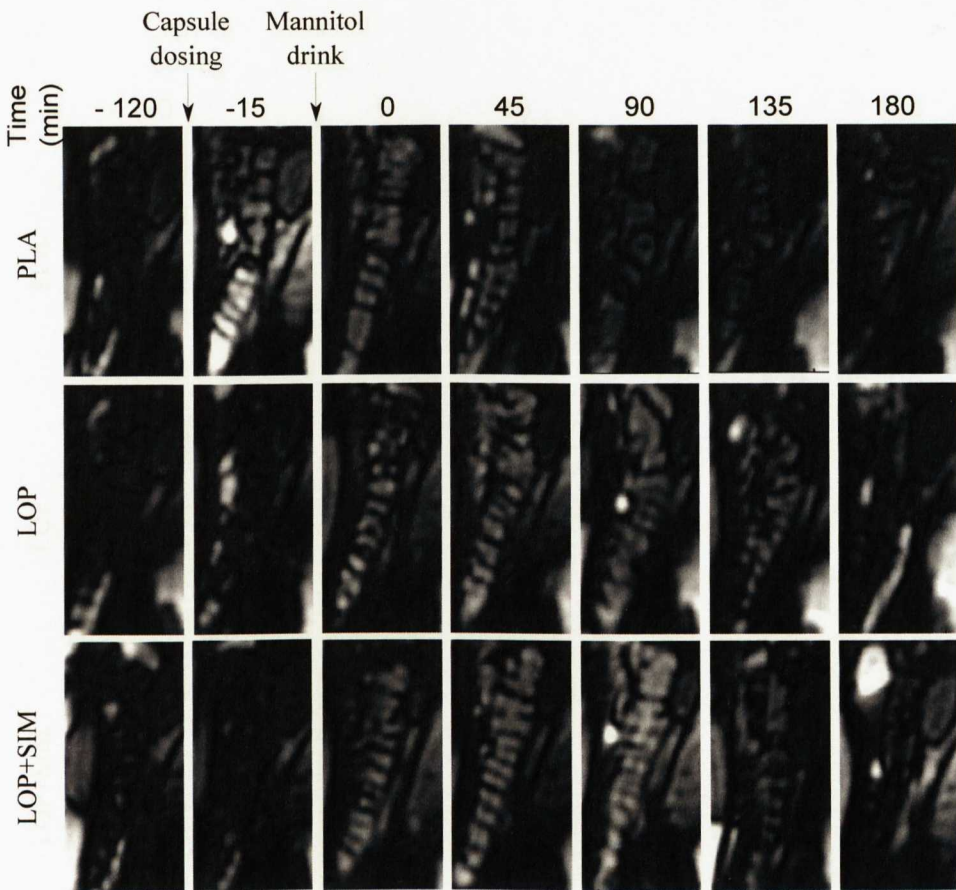


(b) AUC for the contrast homogeneity ratio, represented in figure 7.18(a).

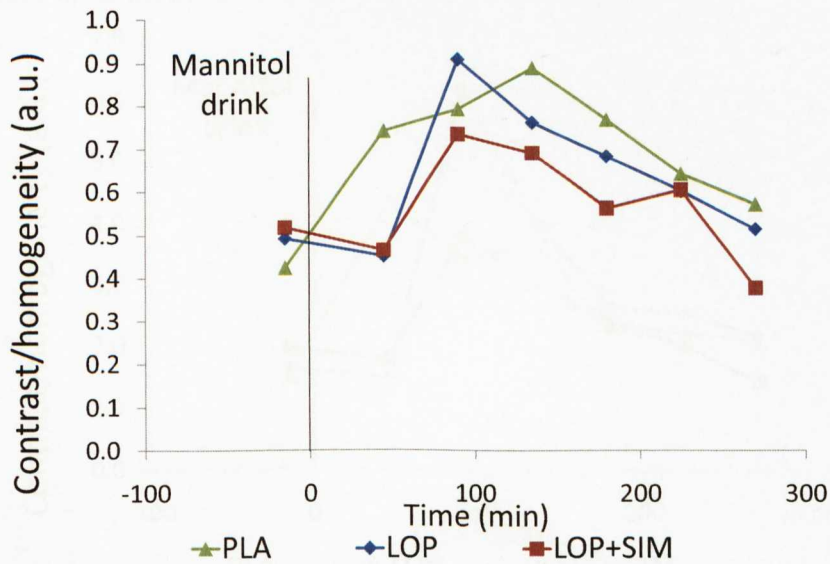
Figure (7.18): Integral of contrast homogeneity ratio (high offset integrated over the 11 frequencies) for all subjects: a significant reduction was found for the drug cases,  $p < 0.034$ .

represented in figure 7.16, with both the Gabor reconstructed images and the contrast homogeneity ratio.

Figure 7.21 shows the weighted scores calculated with the score discrimination analysis method. It can be seen that the scores increase with time after the mannitol drink for all conditions with a peak at 135 min and then decrease slowly. However, there was no statistically significant difference between the drugs and the placebo.

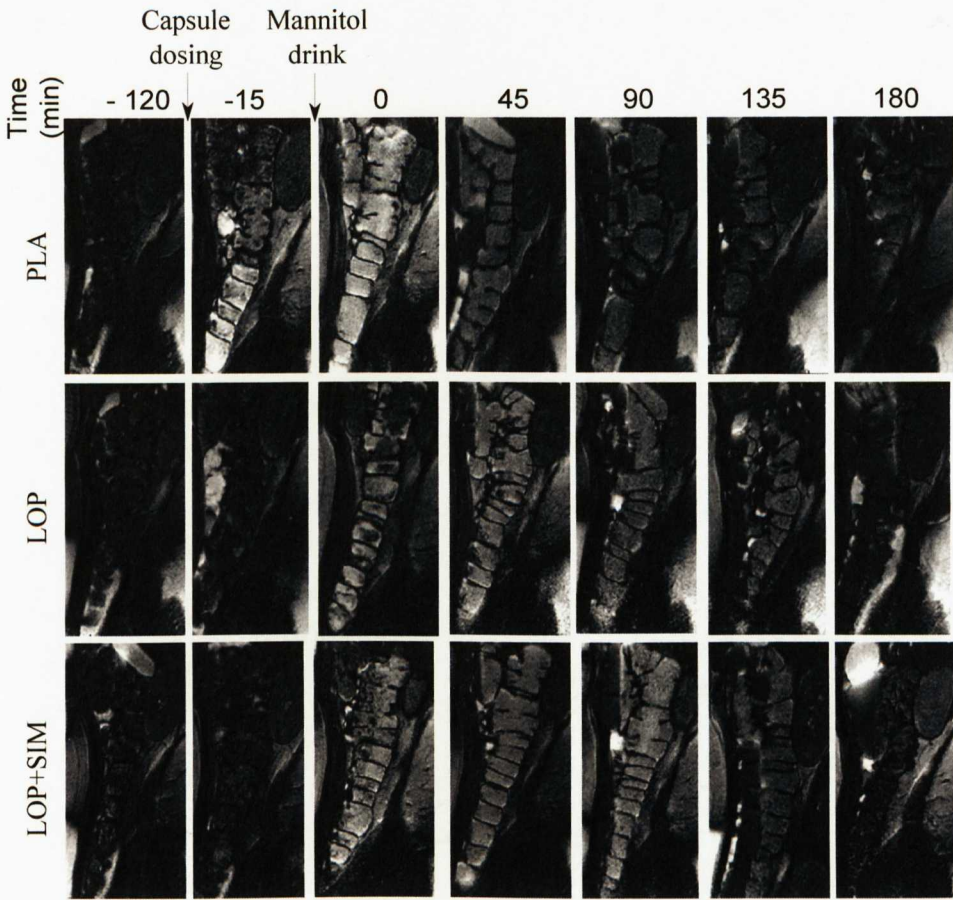


(a) Gabor reconstruction of the high resolution images of the AC for the same volunteer up to the 11<sup>th</sup>.

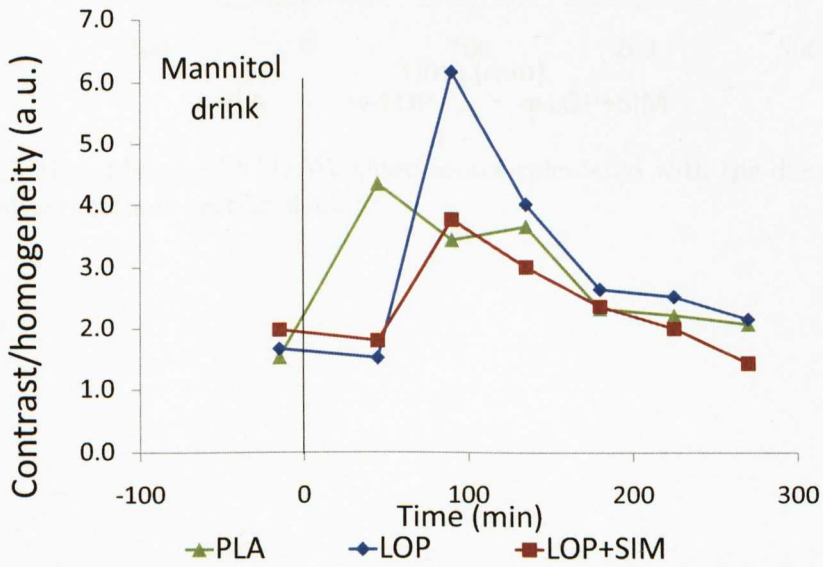


(b) Integral of contrast homogeneity ratio for subject represented in figure 7.16, calculated with a high offset and integrated over the first 11 frequencies.

Figure (7.19): Texture analysis for one subject, with high offset and integrated up to the 11<sup>th</sup> frequency.



(a) Gabor reconstruction of the high resolution images of the AC for the same volunteer up to the 17<sup>th</sup>.



(b) Integral of contrast homogeneity ratio for subject represented in figure 7.16, calculated with a high offset and integrated over the 17 frequencies.

Figure (7.20): Texture analysis for one subject, with high offset and integrated up to the 17<sup>th</sup> frequency.

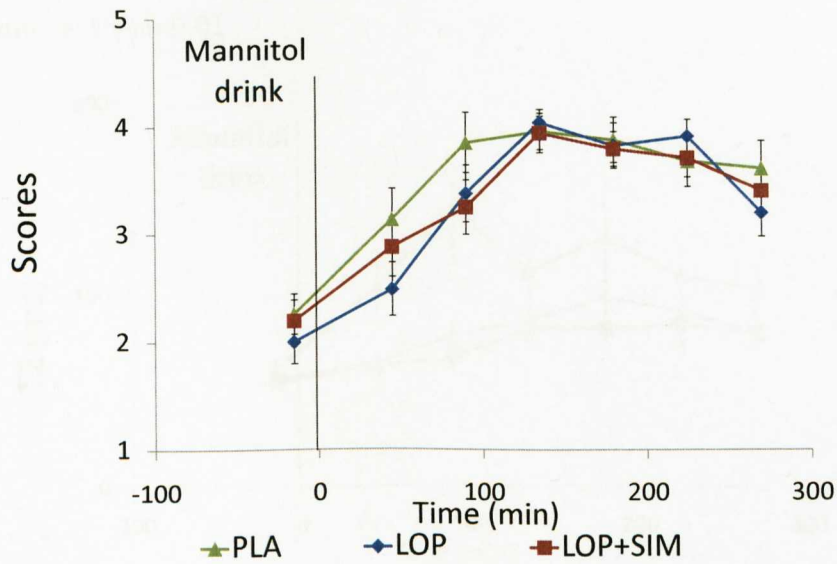


Figure (7.21): (Mean  $\pm$  SEM) Weighted scores calculated with the discrimination analysis method, section 6.4.2.

**$T_2$  in the ascending colon (fig 7.22)**

Longer  $T_2$  values reflect a greater amount of unbound water in the AC. Both loperamide and loperamide + simethicone reduced the  $T_2$  measured in the ascending colon compared to placebo with a significant overall effect ( $p < 0.0001$  calculated on the data normalized by log transformation), figure 7.22. Post hoc tests showed a significant difference at 90 minutes, with the placebo having a  $T_2$  of  $144 \pm 28$  ms versus  $79 \pm 4$  ms for the loperamide and  $67 \pm 6$  ms for the loperamide + simethicone (both  $p = 0.001$ ). Loperamide + simethicone also showed a statistically significant reduction of  $T_2$  from  $130 \pm 22$  ms to  $82 \pm 6$  ms at 180 min, with  $p = 0.01$ .

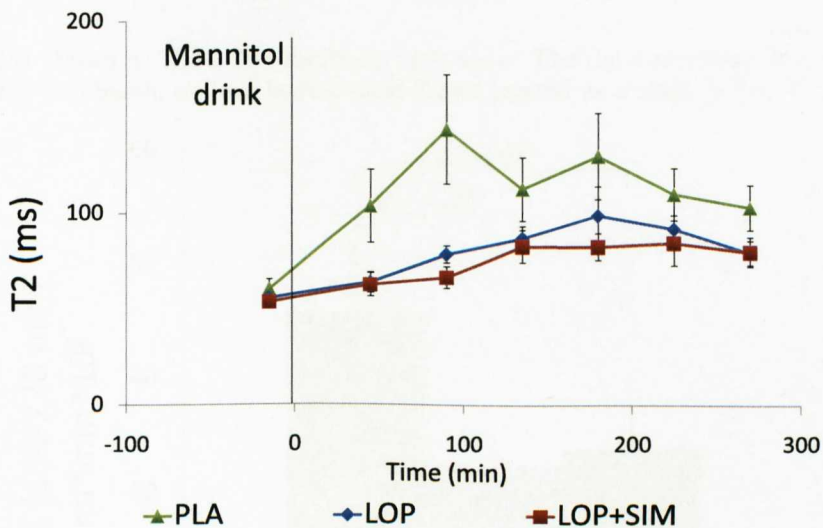
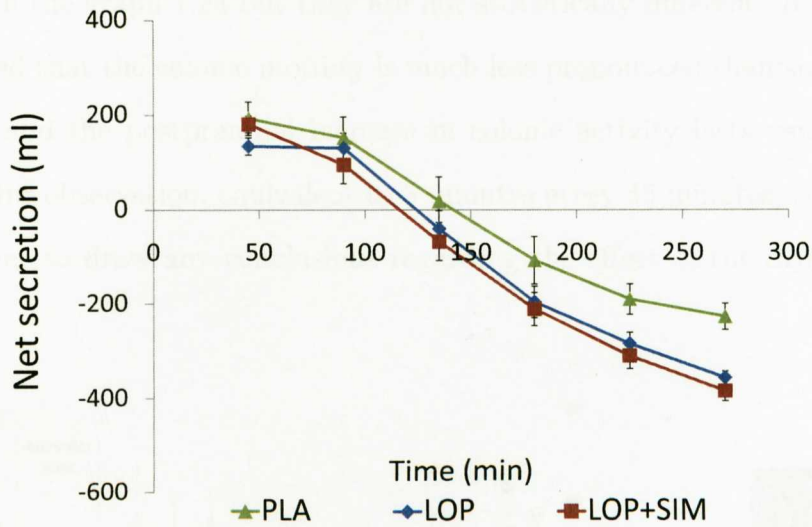


Figure (7.22): (Mean  $\pm$  SEM)  $T_2$  values measured in the ascending colon as a function of time. The data corresponding to the two baselines have been averaged and plotted as a single point.

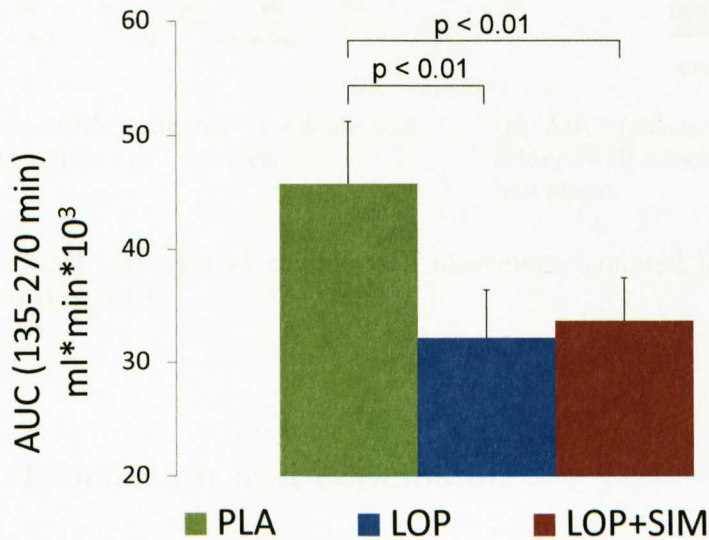
**Net secretion (figure 7.23)**

Net secretion was assessed by the formula: Net secretion = total gut water (gastric + SBWC + ACWC) - (ingested + basal). Figure 7.23(a) represents the data over time: it clearly shows that there is an overall effect of the drugs in reducing net secretion in the gut ( $p < 0.004$ ). This reduction was most obvious during the late phase, see figure 7.23(b), both for loperamide ( $p < 0.01$ )

and loperamide + simethicone ( $p < 0.01$ ) which decreased the amount of net secretion in the gut by more than 25%.



(a) (Mean  $\pm$  SEM) Net secretion over time. The data corresponding to the two baselines have been averaged and plotted as a single point.



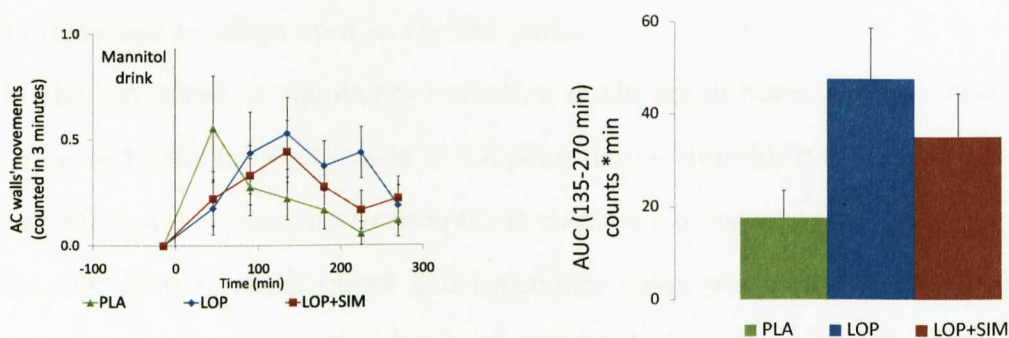
(b) AUC (ml $\times$ min) for the net secretion in the late phase.

Figure (7.23): Net secretion in the gut over time and corresponding AUC in the late phase (ml $\times$ min).

### Motility scans to monitor the wall movements in the AC

The number of colonic wall movements counted in the 3 minute motility scan increased after the mannitol drink for both the placebo and the drug arms

of the study. However, a bigger number of events was found in the loperamide and loperamide + simethicone cases in the later phase. These differences are evident in the graph 7.24 but they are not statistically different. It has to be considered that the colonic motility is much less pronounced than small bowel motility and the postprandial increase in colonic activity lasts usually for 2 hours. Our observation, equivalent to 3 minutes every 45 minutes, is therefore insufficient to draw any conclusions regarding the effect of the drugs on the motility.



(a) (Mean  $\pm$  SEM) Number of colonic wall movements counted in 3 minutes.

(b) AUC (counts $\times$ min) for the number of colonic wall movements in 3 minutes in the late phase.

Figure (7.24): Number of colonic wall movements counted in 3 minutes and corresponding AUC.

### 7.3.4 Discussion and conclusion

The study showed that the optimized MRI protocol constitutes a powerful and well tolerated method for studying the gastrointestinal tract response to pharmacological agents. The unabsorbable mannitol solution caused secretion in the small bowel and provided a model of secretory diarrhoea which proved to be effective and highly accepted by the volunteers compared to other techniques [64]. This is a second study with too short a time for measuring peristaltic movements.

Both drug combinations significantly increased the gastric emptying rate

of the non-nutrient meal, possibly because loperamide increases the frequency of migrating motor complexes [69]. The increase in gastric emptying rate led to a higher amount of water in the small bowel for the loperamide and loperamide + simethicone in the early phase as for the aims of the study. This mechanism may also be the reason why no significant delay in the time to peak of the small bowel water content was found, as initially hypothesised. The reduction in gastric air content suggests an increased tone in the wall of the stomach. A paper from Cann et al [72] showed that loperamide accelerated gastric emptying of a test meal as confirmed by Yeoh et al. [73] suggesting that loperamide has an effect even in the fed state.

In the late phase, a significant reduction in the small bowel water content was observed both for loperamide and loperamide + simethicone. One advantage of MRI over intubation techniques is that we can assess total gut water. Combining gastric, small bowel and ascending colon water and subtracting the basal water and ingested volume we could calculate a net secretion. This showed that mannitol does induce a net secretion of several hundred milliliters for the first few hours and that loperamide shortens this phase. This could be due to either stimulation of absorption or inhibition of secretion, which is more important, could only be determined by measuring flux of labeled water or ions.

It was also shown that loperamide and loperamide + simethicone delayed the arrival in the ascending colon, thus increasing the orocolonic transit time in agreement with previous studies in animals [68]. The drugs also reduced the area under the curve of total colon water content as assessed by MRI.

Both drugs reduced the  $T_2$  of the chyme in the ascending colon. Although the ACWC indicated a significant difference between drugs at the late phase, this difference between drugs however was not reflected in the  $T_2$  values at corresponding times. This was the case for two reasons, firstly the  $T_2$  data was acquired for a single slice only and so may have missed the 'pockets' of free

water, and secondly, if 'pockets' of free water were visible on the images these were avoided as we were more interested in the properties of the chyme, hence the 2 techniques measure two different parameters of the AC .

The high resolution images reflect the characteristics of the colonic contents, with great detail. The texture analysis performed on the data showed a significant reduction in contrast homogeneity ratio due to drugs at all time points. The weighted scores calculated with the discrimination analysis showed a variation in time for all cases but that change was not statistically significant. The texture analysis proved to be robust and reliable for the objective assessment of colonic content structure. Compared to the  $T_2$  analysis, the texture analysis method has the main advantage of considering the whole colon giving information on the mixing of the contents, while for the  $T_2$  calculation only a small more homogeneous region is taken into account.

Motility scans have also been performed but no conclusions can be drawn because of the small time interval of observation. The duration of the scan couldn't be increased because of time constraints of the complete study.

In conclusion, the optimised MRI sequences and analysis methods provided a non invasive method of monitoring a number of different parameters that provide novel insights that are likely to be useful in defining the mode of action of new drugs coming on to market with both pro- and anti-secretory / motility effects. In particular, this study allowed the quantification of the gut total free water content, thus showing that loperamide and loperamide + simethicone reduced the net secretion after a mannitol challenge and prolonged upper GI tract transit.

# Chapter 8

## Using markers to measure GI transit

Many achievements have been made in the use of MRI for monitoring gastrointestinal physiology but directly monitoring transit through the gut remains an unsolved problem in MRI. Transit time, i.e. the time it takes for a marker to pass through the entire gut, is often affected by functional gastrointestinal disorders, therefore being able to measure the transit is a very valuable tool for diagnosis of gastrointestinal diseases. A number of techniques have been used in the past since the first experiment performed by Hertz et al with bismuth [74]. Some methods use single doses of a coloured marker [75], others use radiopaque markers [76] or non-absorbable markers [77] calculating the transit time on the basis of the appearance of the marker in the x-ray or in the stools. Scintigraphy [78] and manometry [79] are also used. The main disadvantage of these techniques is the use of radiation, thus limiting the potential use because of the exposure. In addition, some of these approaches measure the transit through the gut using the analysis of a single stool [80], thus limiting the estimate of the real transit time. Another important method which has been recently developed is the use of a device called Smartpill<sup>®</sup> (SmartPill

Corporation, Buffalo, NY), a wireless motility capsule able to measure pH, temperature and pressure. This device has been shown to be effective for the investigation of colonic and whole-gut transit [81] but it has to be considered that it is a very expensive technique and is subject to electrical faults.

Transit measurement with MRI would simplify patient management and speed up patient throughput since it could be combined with other MR measurements of GI function in a single examination.

Fluorinated agents have particular advantages in this application: there is a negligible amount of fluorine in biologic tissues so no background noise is present,  $^{19}\text{F}$  is the only naturally occurring isotope of fluorine and it has the highest MR sensitivity after proton. Finally if the marker is designed to be absorbed, then since it has a large range of chemical shifts, metabolic changes are easily resolved *in vivo*. Fluorinated agents would ideally be given as an emulsion that would mix with a meal in order to show the transit of the meal. However, given the toxicity of fluorine compounds, the more realistic use of encapsulated  $^{19}\text{F}$  will be investigated. In particular, during the course of this work, some studies on this regard have been presented. Hahn et al. presented some initial work on the visualization and quantification of intestinal transit by means of real-time tracking of labelled capsules in humans [82].

This chapter provides an introduction to  $^{19}\text{F}$  MRI and it describes the development of methods to use  $^{19}\text{F}$  MRI to study the GI transit times. The studies presented in this chapter have already been accepted on peer-reviewed conferences [83, 84]. The use of gadolinium based compounds as an additional marker will also be described. The main advantage of gadolinium compared to fluorine markers is that it does not necessitate a dedicated coil, thus improving the cost effectiveness of the method and also facilitating its translation to standard scanners. The last sections will compare the efficacy of the two markers.

## 8.1 Fluorine MRI

$^{19}\text{F}$  MRI and MRS of exogenously administered agents have been used largely in biomedical application and this is because of the particular properties of the fluorinated agents as *in vivo* MR probes.

The sensitivity of  $^{19}\text{F}$  is 83% that of protons, at the same magnetic field strength and molar concentration, so its MR signal is comparable to the most sensitive nucleus. This has also a very useful practical consequence: since  $^1\text{H}$  and  $^{19}\text{F}$  have very similar gyromagnetic ratios ( $\gamma(^{19}\text{F})=0.94\gamma(^1\text{H})$ ) their resonance frequencies are also very close.

Naturally occurring fluorine exists entirely in one stable isotope ( $^{19}\text{F}$ ), thus preventing any signal loss per mole of fluorine.

A particularly interesting feature of fluorine is the lack of endogenous fluorine-containing metabolites in the soft tissues, so that the signal obtained can be assigned exclusively to the contrast agent administered exogenously. The intensity of the  $^{19}\text{F}$  MR signal will then be proportional to the amount of contrast agent present in the GI tract. By monitoring the change in the intensity level, it is possible to track the movement of the contrast agent inside the gut noninvasively.

Another aspect to take into account is that a fluorine nucleus in a molecule is on average surrounded by 9 electrons, rather than a single electron as is the case with hydrogen: this implies that the range of fluorine chemical shifts is much higher for fluorine than hydrogen. For example, a protein in which all tryptophan residues have been replaced by a fluorinated tryptophan analog will typically exhibit a resolved signal in its fluorine NMR spectrum for each tryptophan position of the sequence, while the proton spectrum of the same tryptophan residues in the native protein will be appreciably overlapped. In other words, while the chemical shift for proton is up to 20 ppm, the range for fluorine may exceed 300 ppm [85]. Therefore, metabolic changes are likely to produce large chemical shift changes that can be easily resolved *in vivo*.

However this can also cause of severe chemical shift artifacts that may be overcome by exciting only a narrow chemical shift range containing one or a small group of resonances [86]. Even if this approach is effective, it is necessary to consider that it suppresses the signal available from the fluorine atoms in the molecule.

Despite their excellent properties as contrast agents, fluorinated compounds have not been widely used for human studies. This is primarily due to the difficulties related to finding an efficient and safe agent for human use.

An overview of the properties of fluorine containing compounds is given in the following section.

## 8.2 Compounds for human $^{19}\text{F}$ MRI

Fluorine containing chemicals have excellent characteristics for the use as contrast agents in MRI but there are several aspects to consider in particular regarding safety. As the most electronegative of all elements, fluorine has very special properties [87]. It forms compounds with other elements very easily and it is very toxic in the gas state. Therefore a stable fluorinated molecule must be used as a contrast agent. In order to get a good NMR signal the density of the fluorine atoms should be as high as possible and the chemical groups containing fluorine should be chemically equivalent, i.e. the fluorine atoms should have an identical microscopic environment so to have only one peak in the NMR spectrum.

The most common fluorine compounds for in vivo use are called perfluorocarbons (PFCs) because they are composed of carbon and fluorine atoms only. PFCs can be arranged in linear, cyclic or polycyclic shape and can change their properties depending on the functional group attached.

The physicochemical and biologic aspects of the PFCs are presented in detail in the following sections.

## 8.2.1 Perfluorocarbons

### Physicochemical aspects

Fluorine is a relatively small atom but is significantly larger than hydrogen (van der Waals radius 1.47 Å vs 1.20 Å). This has two main consequences: firstly, the perfluoroalkyl (F-alkyl) chains ( $C_nF_{2n+1}$ ) are more bulky than the hydrogenated ones (cross sections: 30 Å<sup>2</sup> vs 20 Å<sup>2</sup>), secondly, there is the greater stiffness of perfluorinated chains. Besides, because there is the overlapping of the orbitals, the C-F bond is the most stable single bond found in organic chemistry ( $\sim 485 \text{ kJ mol}^{-1}$  as compared to  $\sim 425 \text{ kJ mol}^{-1}$  for a standard C-H bond). The bond strength further increases with increasing fluorine substitution. As a consequence, fluorocarbons are thermally and chemically very stable. They are also biologically inert. Another characteristic is that the dense electron cloud of the fluorine atoms results in a repellent sheath that protects the perfluorinated chain against the approach of reagents.

Fluorine is also very difficult to polarize and for this reason there are low van der Waals interactions between fluorinated chains and low cohesive energy densities in liquid fluorocarbons. The most valuable properties of fluorocarbons are consequences of these low interactions. These properties are: very low surface tensions, excellent spreading properties, high fluidity, low dielectric constant, high vapor pressure, high compressibilities and high gas solubilities. The effective fluidity and the spreading properties allow PFCs' molecules to spread evenly over a surface. This can be used, for example, to form a barrier in the lungs thus preventing further growth of a malignant disorder [88].

There are also other fluorocarbon's properties which are important in the biomedical field: high density, antifriction properties and magnetic susceptibility values close to that of water.

The typical high hydrophobicity of the fluorine atoms is due to the combined effect of the larger surface of the fluorinated chains (the hydrophobic

effect of the chain is roughly proportional to its area in contact with water) and the low polarizability of the fluorine atoms. Perfluorinated chains have two contradictory properties: they are extremely hydrophobic but also lipophobic and this means that they repel water and fat at the same time. The low water solubility of PFCs leads to their slow diffusion and a long stay at the target site in their natural form. This can be of obstacle for their medical applications and their preparation as water emulsions has been proposed [89].

One of fluorinated compounds most important properties is their oxygen affinity, discovered in the 1960s when mice and cats were shown to survive complete immersion in oxygenated PFCs, followed by long-term survival without apparent ill-effects [90]. However, it was not until the 1980s that the chemical inertness of PFCs and, more specifically, their inability to be metabolized were fully documented.

### **Biological aspects**

The biocompatibility of liquid fluorocarbons is well documented as a result of the intensive efforts that are being devoted to developing materials for liquid ventilation, oxygen delivery and imaging [91, 92]. Fluorocarbons intended for biomedical uses can be linear or cyclic, and may contain hydrogen, halogen, or nitrogen atoms. Although several hundreds of such compounds have been screened over the past twenty years, very few were found to meet the appropriate physicochemical and biological criteria for *in vivo* oxygen delivery. These criteria include high purity, rapid excretion, ability to form stable emulsions, absence of clinically significant side-effects, and at large scale, cost-effective industrial feasibility. Even at large doses, most fluorocarbons appear to be innocuous and physiologically inactive [93]. One exception is the volatile perfluoroisobutylene,  $(CF_3)_2CF = CF_2$ , which is extremely reactive and toxic. In particular, fluorocarbons do not show any of the side effects that have been reported for hemoglobin-based oxygen carriers and their pharmacology is sim-

pler and better understood. It is essential for fluorocarbons for biomedical uses to be thoroughly purified in order to remove any toxic impurities. There is no evidence of metabolism for fluorocarbons. Also, for intravascular use, fluorocarbons need to be excreted rapidly. The fluorocarbon emulsion droplets are cleared from the circulation by macrophages, and the fluorocarbon is temporarily stored in the liver, spleen and bone marrow. The fluorocarbon is then slowly reintroduced into the circulation in dissolved form by lipid carriers, at a rate that depends primarily on molecular weight and lipophilicity, eventually released through the pulmonary capillary bed and excreted unchanged as a vapor with the expired air.

### **The potential of highly fluorinated molecular materials in medicine and biology**

PFCs find many applications in medicine and biology thanks to the properties just discussed. For example, oxygen delivery can be enhanced using a fluorocarbon emulsion and that is of vital importance when a patient's hemoglobin level is declining. Such emulsions are expected, when combined with blood transfusion strategies, to play a major role in surgery by increasing safety at low hematocrits and avoiding or reducing donor blood transfusions. Fluorocarbon-based oxygen carriers should also prove beneficial in trauma situations, especially during the prehospital "golden hour" period which has a large impact on outcome for the patient and during which blood is usually not available, or during which transfused blood has not yet reached its full effectiveness.

Fluorocarbon-in-water oxygen-delivering emulsions also have potential for the treatment of conditions of restricted blood flow such as those which occur in myocardial infarction or stroke; for the prevention of ischemia during the coronary angioplasty procedure; to protect the heart during cardiopulmonary bypass surgery; during extracorporeal circulation; to improve oxygen deliv-

ery to certain tumors, making the tumor more responsive to radiation and chemotherapy; and for organ and tissue preservation. Diverse gaseous microbubbles, generated or stabilized by fluorocarbons, are in advanced stages of development as contrast agents for ultrasound imaging.

In addition to the so-called "blood substitutes", a neat fluorocarbon may also be used for the treatment of the respiratory distress syndrome by liquid ventilation. In particular, perfluorooctyl bromide (PFOB,  $C_8F_{17}Br$ , also called Perflubron) has been investigated for the treatment of this severe condition with high mortality for which no satisfactory treatment is available yet [87]. In comparison with ventilation with a gas, liquid ventilation eliminates the gas-liquid interface, thus reducing the alveolar surface tension and leading to improved lung compliance and lung oxygenation in patients with severe respiratory failure. Due to its low surface tension, PFOB is uniformly distributed and reaches gas exchange regions at low insufflation pressures, which is particularly valuable in case of insufficiency. A detailed description of PFOB will be presented in section 8.2.2.

### Drugs for absorption

The measurement of drug concentrations in an organ for evaluation of distribution volumes was previously only feasible in animals because it requires biopsy. NMR has been shown to provide a method to estimate local concentrations of some compounds in humans in vivo, in a repeatable non invasive manner. Fluorine magnetic resonance spectroscopy (MRS) has been applied to estimate the characteristics of some drugs which have fluorine atoms in their active form in humans in vivo [94].

Compared to a simple aqueous solution, the relaxation properties of a drug/compound in vivo will be influenced by the biophysical and chemical makeup of the microenvironment within which it resides. Many fundamental biological processes, including cell signaling and enzyme action, are acutely

sensitive to the biophysical state of the microenvironment. There is, therefore, a considerable incentive in developing methodologies that could non-invasively assess such biophysical processes in vivo.

### 8.2.2 Potential $^{19}\text{F}$ markers for GI transit

Biocompatibility and non-toxicity are the most important considerations in choosing a fluorine agent for imaging the gastrointestinal tract in humans. It is also necessary to maximize the NMR signal by choosing molecules with high density of fluorine atoms and possibly a single resonant peak.

Most PFCs are very inert and safe. However in the multiplicity of PFCs available, not many of them can be used for biological studies. The main reasons for this is because of some inconveniences like instability, split  $^{19}\text{F}$  signals and excessive retention times of the agents within the organs [95]. Furthermore even if most PFCs are innocuous and inert, the main concern about using them for biological applications is the potential presence of impurities which need to be checked for non-toxicity. This implies a very expensive and time consuming process to both perform toxicology tests and to obtain the permission to use those compounds in humans.

An overview of the potential  $^{19}\text{F}$  markers to be used in vivo is given below.

#### 1. *Perfluorooctyl-bromide*

As with other PFCs, perfluorooctylbromide (also called perflubron or PFOB) has no hydrogen atoms, is chemically inert and has a low surface tension. It can easily be emulsified with egg yolk phospholipids and is rapidly excreted from the body, especially because of the presence of the single bromine atom on the terminal carbon which provides a very high lipophilicity, see figure 8.1. The retention half-time is about 4 days [96]. Even if PFOB is immiscible with aqueous systems, including blood, it can be safely injected into the bloodstream as an emulsion. This is

why it is used as temporary, intravascular respiratory gas-carrier and tissue oxygenating fluid ("blood substitutes"). In particular, a commercial perflubron-based formulation, *Oxygent*<sup>TM</sup> <sup>1</sup> has been widely used and it has been approved for clinical use, but unfortunately it is no longer produced.

PFOB shows a complex <sup>19</sup>F MR spectrum because of nonequivalent chemical environments for the individual fluorine atoms within the molecular configuration. Therefore a chemically selective imaging method that excites only one of those peaks is needed, thus degrading the SNR. Lee et al. [86] developed a reduced-bandwidth imaging method for two main aims: firstly, in order to simplify the misregistration problems due to the complicated spectrum by reducing the receiver bandwidth and secondly to improve the SNR increasing the data acquisition time.

PFOB is a clear, inert liquid with no taste and no odour and has no side effects when ingested orally. It has also been used as negative contrast agent for proton MRI in the gastrointestinal tract [97–99]. Since it lacks hydrogen, PFOB creates no proton MR signal, therefore like air it creates a signal void both in  $T_1$ - and  $T_2$ -weighted proton images. This mechanism is expected to be equally effective at all field strengths and with all pulse sequences. These studies in rats and in man show that PFOB has great potential for use as oral MR contrast agent. Since it is immiscible with water, it layers out in water and so it never mixes with the bowel contents. Besides, because it has a magnetic susceptibility similar to that of tissues, it does not influence the relaxation properties of bowel or adjacent tissue protons.

Mattrey et al. [97] in 1987 presented a human study where two volunteers were given up to 525 ml of PFOB to swallow, thus achieving the

---

<sup>1</sup>*Oxygent*<sup>TM</sup> is developed by the Alliance Pharmaceutical Corporation in San Diego. It is an intravascular oxygen carrier in clinical development as a temporary "blood substitute" to reduce or eliminate the need for donor blood transfusions during surgery.

complete filling of the small bowel. In the stomach, the PFOB allowed the identification of the gastric wall. PFOB was very well tolerated: one subject had an oily sensation in the mouth and neither of the volunteers had any gastrointestinal symptoms. PFOB was then excreted in liquid form in the stool within 18 hours of ingestion. Therefore, PFOB proved to be safe and effective.

Another paper from Mattrey et al. [100] shows the assessment of PFOB MR imaging of the abdomen in a multicenter trial. A total of 127 subjects were imaged before and after the ingestion of PFOB, showing that it increased the bowel darkening in over 92% of subjects with different sequences and field strengths. Also in this study, PFOB proved to be safe and its efficacy was unaffected by pulse sequences or magnetic field strengths. The subjects were given up to 1,000 ml of perflubron which was mostly eliminated in the first few hours with no side effects.

The use of perflubron as a gastrointestinal agent for MR imaging of patients with Crohn disease was the object of a study presented by Anderson et al. [98]. 12 subjects were imaged before and after the ingestion of 600 ml of perflubron without bowel preparation or fasting instructions. PFOB was shown to effectively mark the bowel in patients with Crohn disease and to improve the clarity of bowel wall visualization when used in conjunction with glucagon. However, there was no significant increase in the detection of bowel wall abnormalities related to Crohn disease.

Among various applications of PFOB for clinical imaging, Pisani et al. [101] showed the characterization of polymeric nano/microcapsules filled with a single core of liquid PFCs such as PFOB. These could be used to increase the stability of ultrasound contrast agents in order to enable the qualitative and quantitative evaluation of blood flow. It would also be possible to use ultrasound to trigger the drug release from contrast agents encapsulating a drug, thus opening a great potential for targeted

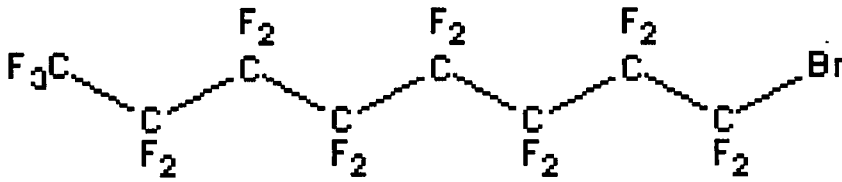


Figure (8.1): Chemical structure of perfluorooctyl bromide (PFOB,  $C_8F_{17}Br$ ).

treatment.

The use of PFOB emulsions as delivery media for hyperpolarized xenon has also been investigated [102], showing its potential in animal models for in vivo magnetic resonance applications.

Sotak et al. [103] measured the  $T_1$  and  $T_2$  relaxation times of PFOB:  $T_1$  varied approximately between 1.1 and 1.2 s, while  $T_2$  shows a strong dependence on the molecular location of the fluorine atoms, see figure 8.1. For PFOB, the terminal  $-CF_2Br$  and  $-CF_3$  groups display considerably longer  $T_2$  relaxation times than the  $-CF_2-$  groups in the chain.

In conclusion, PFOB has several advantages over competing gastrointestinal contrast agents. Its low viscosity results in rapid bowel transit even in the absence of active peristalsis. It is immiscible with water and therefore resistant to concentration-dependent signal changes. The intraluminal signal void produced by perflubron causes no artifact increase and it also produces little or no appreciable magnetic susceptibility artifact.

More importantly, PFOB has been approved for clinical use by the U.S. Food and Drug Administration.

Therefore our interest regarding its use has been increasing and it has been used for a wide range of in vitro and in vivo experiments. The certification for a complete absence of impurities still remains as a major concern and for this reason efforts have been focused on finding a safe way to encapsulate the PFOB for delivery to subjects.

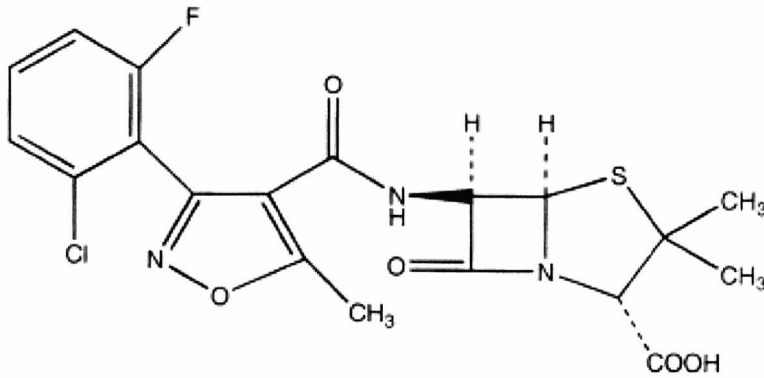


Figure (8.2): Chemical structure of flucloxacillin ( $C_{19}H_{16}ClFN_3NaO_5S$ ) [104].

## 2. Flucloxacillin

Flucloxacillin belongs to a group of antibiotics called penicillins and it is used to treat infections caused by bacteria. Flucloxacillin works by interfering with the ability of bacteria to form cell walls, which are vital for their survival. They keep unwanted substances from entering their cells and stop the contents of their cells from leaking out. Flucloxacillin impairs the bonds that hold the bacterial cell wall together. This allows holes to appear in the cell walls and kills the bacteria. Flucloxacillin differs from other penicillin antibiotics and is used primarily to treat infections caused by bacteria that are resistant to other penicillin antibiotics. It is a useful fluorine compound because it can be easily dissolved in water and used for MRI and MRS.

Interesting work has been done by Dzik-Jurasz et al. in 2004 [104] in order to examine microenvironmental factors likely to influence the longitudinal relaxation time of MR visible drugs or compound in vivo at 1.5 T. In particular the influence of paramagnetic MR contrast agent on the longitudinal relaxation time of flucloxacillin using  $^{19}F$  MRS was assessed.

The chemical structure of flucloxacillin is showed in figure 8.2. It has

to be said that the fluorine concentration in the drug is very low, especially compared to other compounds like perfluoro-compound FC-43 and PFOB (figures 8.2, 8.3 and 8.1 respectively) and this is the main reason why flucloxacillin cannot be used in vivo with whole body scanners.

### 3. Perfluorotributylamine, FC-43

This fluorine compound has been used for in vitro tests because of its high NMR signal. Since it is toxic, it can just be used for animal studies or in humans if safely encapsulated. The molecular structure is given in figure 8.3.

### 4. Perfluorononane

The use of perfluorononane as a contrast agent in vivo has been presented from Schwarz et al. [105, 106]. In their work  $^{19}\text{F}$  MR images of the GI tract of mice and man have been acquired in combination with  $^1\text{H}$  MR images, which provided anatomical information. Perfluorononane, structurally similar to PFOB, was in one case ingested [106] and in the other case [105] included in capsules for transit studies in man. In both studies Perfluorononane with a nominal purity of 97% was purchased from Aldrich Chemical Co. (Switzerland). Perfluorononane,  $\text{C}_9\text{F}_{20}$  see

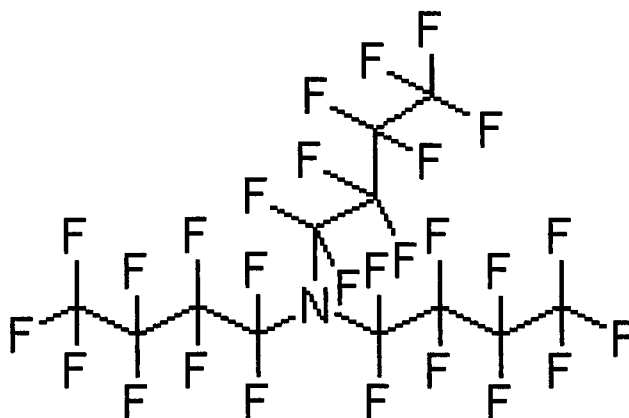


Figure (8.3): Chemical structure of perfluorotributylamine FC-43 ( $\text{C}_{12}\text{F}_{27}\text{N}$ ).

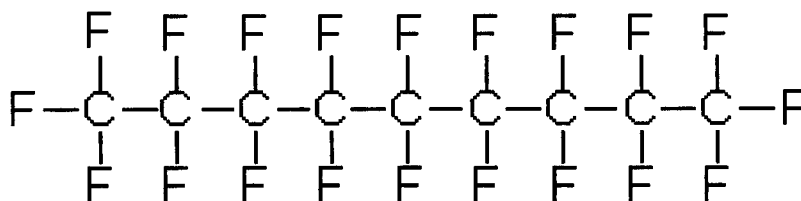


Figure (8.4): Chemical structure of perfluorononane ( $C_9F_{20}$ ).

figure 8.4, is a perfluorinated linear alkane with a molecular weight of 488 Da. It is a colorless, odorless liquid with low surface tension and high specific density. It has a magnetic susceptibility approaching that of biological tissues. Since perfluorononane is immiscible with water, no dilution and accompanying signal loss occur even when the contrast agent is in contact with the intraluminal contents of the GI tract. It is neither resorbed nor metabolized and being nontoxic it can also be used for the localization of pharmaceutical capsule disintegration to be evaluated in situ. Furthermore, perfluorononane exhibits long  $T_1$  and  $T_2$  relaxation times in vitro, which are comparable to those of water in biological tissue. Since perfluorononane has a low viscosity and surface tension, it passes through the gut faster than the contents: on one hand this is useful to assess morphologic and pathologic details but this also limits its use as a marker for the transit. This could be overcome controlling the intestinal movements by means of anesthesia or lack of food input. Since perfluorononane is neither resorbed nor metabolized, the only way it can leave the body is by excretion thus making it an ideal marker for the GI tract. The main concern about using it for biological application is therefore the presence of toxic impurities.

##### 5. Hexafluorobenzene

The main advantage of hexafluorobenzene (HFB) is that the fluorine atoms are all magnetically equivalent and thus a single resonance is observed providing optimal sensitivity and avoiding the need for selec-

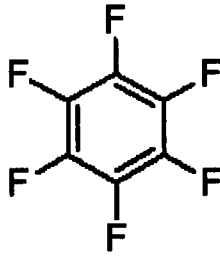


Figure (8.5): Chemical structure of hexafluorobenzene ( $C_6F_6$ ).

tive excitation-observation regimens associated with  $^{19}F$  MRI of others PFCs. Because it is highly volatile, it clears from the body rapidly, with a complete clearance from the body within 24 hours. This has to be considered if quantitative measurements are needed. Mason et al. [107] used HFB as a sensitive  $^{19}F$  NMR indicator of tumor oxygenation based on direct intratumor injection in animals. This approach was based on the linear relationship existing between the  $^{19}F$  spin-lattice relaxation rate ( $R_1=1/T_1$ ) of perfluorocarbons and partial oxygen pressure ( $pO_2$ ), described by Parhami and Fung in 1983 [108]. The determination of a tumor  $pO_2$  by means of non invasive method is very important because it is a fundamental parameter for the effectiveness of various therapies. HFB proved to be considerably more sensitive to changes in  $pO_2$  than other molecules used and it also has the lowest sensitivity to changes in temperature. The proton and the fluorine MR images were compared to indicate the distribution of the fluorine compound in the tumor.

Although known to be toxic, HFB was used in sealed minicapsules for the investigation in a rat model by Christmann et al. [109]. The simultaneous visualization of HFB-labelled microcapsules and anatomical structures of the GI tract in rats was investigated. In proton MRI, fluorine labelled capsules are dark while the GI contents are bright. On the contrary, on the fluorine MRI only the fluorine filled capsule is displayed. The superimposition of the two images gives an explicit localization of the oral dosage forms even in the distal parts of the GI tract.

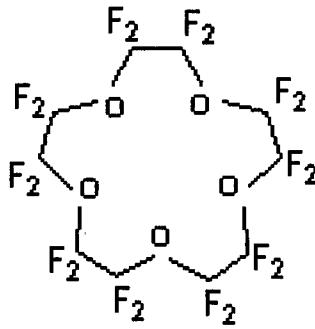


Figure (8.6): Chemical structure of Perfluoro-15-crown-5-ether (15C5).

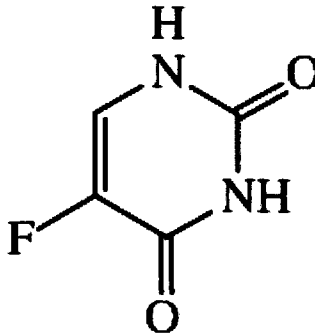


Figure (8.7): Chemical structure of 5-Fluorouracil (5FU).

#### 6. *Perfluoro-15-crown-5-ether (15C5)*

Perfluoro-15-crown-5-ether (15C5), figure 8.6, is an excellent contrast agent for MRI because its NMR spectrum has a single narrow resonance and since it has a large number of equivalent fluorine atoms per molecule, it has a very high sensitivity. 15C5 has been used by Ahrens et al. [110] to track cells in vivo. The fluorine-labelled cells were injected intravenously or into tissue in mice and then tracked using  $^{19}\text{F}$ -MRI.

Previously, encapsulated 15C5 has also been used for MRI to measure the partial pressure of oxygen in tissue [111].

Unfortunately, despite the successful studies on animals, 15C5 cannot be used in humans because of its high clearance rate from the body, which is presumed to be through the liver, spleen and lungs.

#### 7. *5-Fluorouracil (5FU)*

5-Fluorouracil (5FU), figure 8.7, after several decades of use, is still one

of the most widely used agents for the treatment of several cancers especially of the gastrointestinal tract, breast and ovary. The metabolism of 5FU has been extensively studied and monitored in in vivo studies with MR [112].

Dzik-Jurasz et al. [113] investigated with  $^{19}\text{F}$  MRS the distribution of hepatobiliary fluorine signals arising from the catabolism of 5-fluorouracil (5FU) in nine patients.

More recently, McIntyre et al. [114] examined a total of 32 subjects with colorectal cancer undergoing 5FU treatment in a 1.5 T MRI scanner. They showed how MRS can distinguish the parent drug from its active and inactive metabolites in vivo, with a good time resolution for the analysis of the drug metabolism.

Table 8.1 summarizes the names and references for the potential compounds to be used in vivo. In this work, in vitro tests have been performed with PFOB, flucloxacillin and FC-43. However for the in vivo experiments PFOB has been chosen because of its favorable properties, having a high density fluorine atoms and possibly a single peak. In particular, PFOB will be encapsulated for GI transit measurements.

19F compound	Molecular formula	Molecular weight [g/u]	Reference(s)
Perfluorooctyl-bromide (PFOB)	$C_8F_{17}Br$ , Figure 8.1	498.96	[86, 96–103, 115]
Flucloxacillin	$C_{19}H_{16}ClFN_3NaO_5S$ , Figure 8.2	453.87	[104]
Perfluorotributylamine FC-43	$C_{12}F_{27}N$ , Figure 8.3	671.09	[116]
Perfluorononane	$C_9F_{20}$ , Figure 8.4	488.06	[105, 106]
Hexafluorobenzene (HFB)	$C_6F_6$ , Figure 8.5	186.05	[107, 109]
Perfluoro-15-crown-5-ether (15C5)	$C_{10}F_{20}O_5$ , Figure 8.6	580.07	[110, 111]
5-Fluorouracil (5FU)	$C_4H_3FN_2O_2$ , Figure 8.7	130.08	[112–114]

Table (8.1): Comparison of potential 19F compounds for in vivo use. See section 8.2.2 for a more detailed description.

## 8.3 In vitro tests of fluorinated compounds

### 8.3.1 High resolution MRS

Preliminary in vitro tests of fluorinated compounds were carried out with a Bruker AV(II) 600 NMR spectrometer operating at a fluorine detection frequency of 564 MHz. Different samples have been prepared with the compounds presented in section 8.2.1:

- *Flucloxacillin sodium*

This compound has been purchased in powder for solution for injection so it has been very easy to prepare a solution where the drug was completely dissolved. In our case a test bottle was filled with 20 ml of distilled water in which 20 mg of drug has been dissolved: about 570  $\mu\text{l}$  of this solution was put in a test tube suitable to be inserted in the spectrometer.

- *Perfluorooctyl bromide (PFOB)*

PFOB was purchased from Apollo Scientific and tested neat in an organic solvent ( $\text{CDCl}_3$ , deuterated chloroform) and in an aqueous emulsion<sup>2</sup> for which 10 ml of PFOB were dispersed in 100 ml of deionized water. The PFOB was tested as an emulsion in this first in vitro test because the first aim was to try and verify if the PFOB could be diluted and used for ingestion. In this case, PFOB would have provided an easy way of measuring the transit of meals in the gastrointestinal tract. For this reason, in order to stabilize the emulsion, 1 g of surfactant (Tween 20, Sigma-Aldrich) has been added. An Ultraturrax emulsifier was used for 10 minutes in order to get a droplet size of 8  $\mu\text{m}$ . The spectra of PFOB

---

<sup>2</sup>An emulsion is a mixture of two immiscible substances: one substance (the dispersed phase) is dispersed in the other (the continuous phase). Whether an emulsion turns into a water-in-oil emulsion or an oil-in-water emulsion depends on the volume fraction of both phases and on the type of emulsifier. The emulsifier is a substance which stabilizes an emulsion, frequently a surfactant.

in CDCl<sub>3</sub> and in aqueous emulsion are reported in figure 8.9 with the assignments of the peaks according to Shukla et al. [117].

- *FC-43*

A 1 ml test tube containing neat perfluoro-compound FC-43 (Acros Organics) was inserted in the spectrometer in order to acquire the spectrum of the compound (the chemical structure is shown in figure 8.3).

High resolution spectra have been acquired for these fluorine compounds in order to compare the relative chemical shifts and the signal amplitudes. Figure 8.8 shows the spectra obtained: the signal to noise ratio is very high because of the use of the high resolution spectrometer. The spectrum obtained for flucloxacillin sodium is from -100 and -120 ppm and it shows a very sharp single line at about -110 ppm. This result in particular has been very interesting because it states that the compound is very pure and the neat spectrum could be very useful for future possible applications even if the density of fluorine atoms is very low, thus limiting its use in humans because the amount needed would be unsafe. The spectra of the tri-fluoroacetic acid and of the sodium fluoride have been added as a reference. Trifluoroacetate is often used as a chemical shift reference, but <sup>19</sup>F NMR doesn't have a single generally accepted reference compound. For in vivo applications, the reference is inevitably an external reference compound with the associated problems of magnetic susceptibility differences between sample and reference. This can lead to errors of several ppm, making in vivo assignments of resonances difficult. Although the total chemical shift range spans more than 300 ppm, spectral overlap is a significant problem as many relevant compounds have almost identical chemical environments (and almost the same chemical shift).

Fluorine MRS of these compounds with a high resolution spectrometer has been very useful to see the characteristics of each spectrum, hence helping to choose the optimal compound to be used in vivo. Flucloxacillin proved to

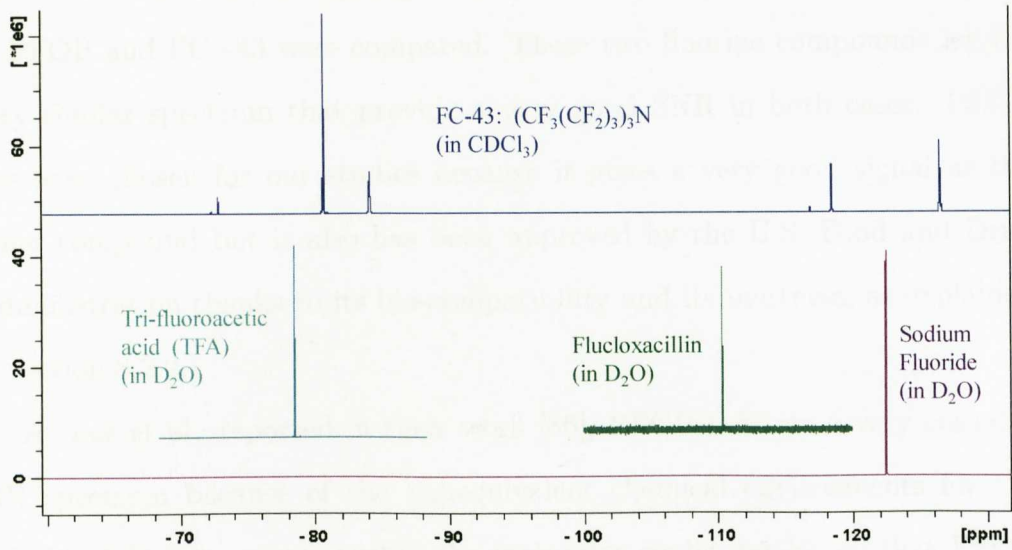


Figure (8.8): Illustration of range of  $^{19}\text{F}$  NMR chemical shifts obtained with a Bruker spectrometer operating at a frequency of 564 MHz. The spectra are showed together in order to compare the range of ppm they occupy, the amplitudes are not referred to the y axis showed. The spectra of the Tri-fluoroacetic acid and of the Sodium Fluoride have been added as a reference.

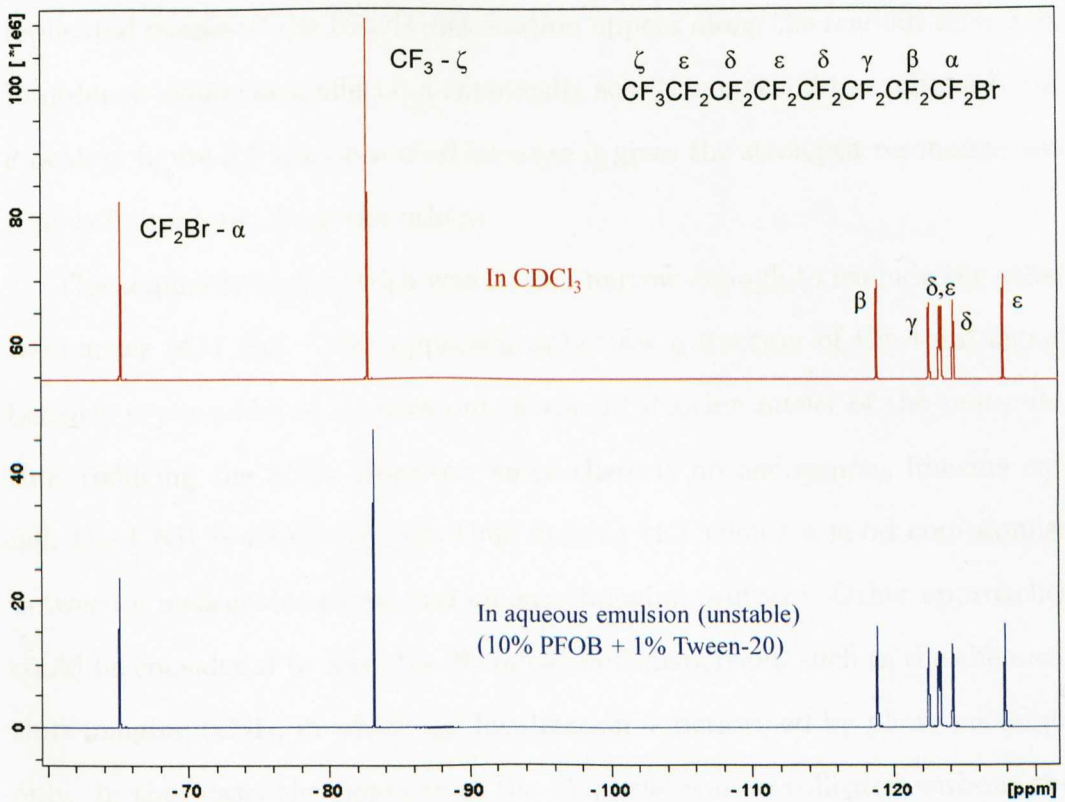


Figure (8.9): Spectrum of the PFOB at acquired with a Bruker spectrometer operating at a frequency of 564 MHz in an organic solvent,  $\text{CDCl}_3$  (top) and in aqueous emulsion (bottom). Peaks have been assigned according to Shukla et al. [117].

be unable to provide enough signal on the Philips 3T scanner so the spectra of PFOB and FC-43 were compared. These two fluorine compounds have a very similar spectrum that provide a very good SNR in both cases. PFOB has been chosen for our studies because it gives a very good signal as the other compound but it also has been approved by the U.S. Food and Drug Administration thanks to its bio-compatibility and its inertness, as explained in section 8.2.2.

As Lee et al. reported in their work [86], PFOB exhibits a very complex MR spectrum because of the nonequivalent chemical environments for the individual fluorine atoms within the molecular configuration, so that PFOB has multiple spectral peaks, as shown in figure 8.9. This complicated spectrum has the obvious disadvantage of producing chemical shift artifacts that lead to misregistration in MRI. In particular, because of this chemical shift dispersion, replicated images of the PFOB distribution appear along the readout direction. In order to avoid these effects, a chemically selective method to excite only the  $\theta$  peak in figure 8.9 has been used because it gives the strongest resonance and it is well separated from the others.

The acquisition bandwidth was chosen narrow enough to exclude the other resonances (434 Hz). This approach only uses a fraction of the total signal because it considers only three out of the 17 fluorine nuclei of the molecule, thus reducing the SNR. However, since there is no endogenous fluorine signal, the CNR is relatively high thus making this choice a good compromise between a measurable signal and an easy imaging protocol. Other approaches could be considered to solve the chemical shift dispersion, such as the chemical shift imaging (CSI), in which the localization is performed by phase encoding only. In that case, the signal from the 17 nuclei can be collected without the appearance of replicated images thus increasing the SNR but it would require a longer acquisition time and the use of strong gradients to reduce the artifact from the two resonant groups  $CF_2$  and  $CF_2Br$ .

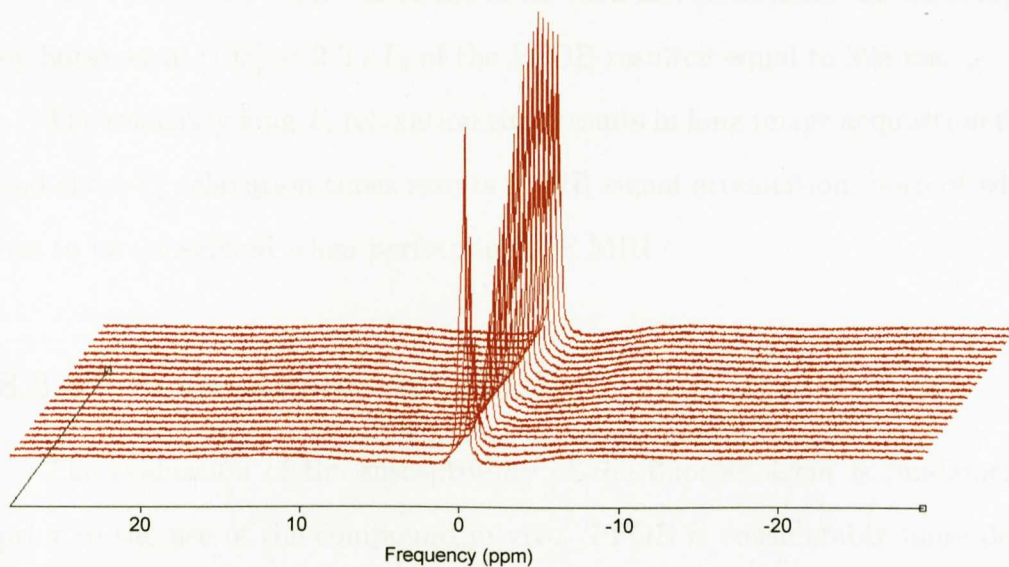


Figure (8.10): Spectra of the PFOB at 3T for the calculation of  $T_1$ . The trifluoromethyl  $CF_3$  group has been arbitrarily assigned at 0 ppm on spectrum. The data were acquired by incrementing the TE value from 100 ms to 4850 ms in 250 ms steps for a total of 20 TIs.

### 8.3.2 $T_1$ and $T_2$ of PFOB

The relaxation times of PFOB have been measured using two PRESS sequences, based on the largest peak of the spectrum i.e. with the trifluoromethyl  $CF_3$  group assigned at 0 ppm. The measurements were performed at room temperature ( $20^\circ\text{C}$ ), run overnight to acquire a great number of averages.

For the  $T_1$  measurement of PFOB, the data were acquired by incrementing the TI value from 100 ms to 4850 ms in 250 ms steps for a total of 20 TIs (figure 8.10). The TR was set at 10000 ms and TE equal to 28 ms. The number of averages was set at 128.

$T_2$  was measured acquiring spectra with different TEs, with a starting value of 50 ms and spacing 50 ms for a total of 10 spectra. The NSA was set at 512, TR = 3000 ms and TE = 50 ms.

The analysis of the spectra was performed with jMRUI software: the areas of the peaks were plotted versus the TIs and TEs respectively for the  $T_1$  and the  $T_2$  calculation and the curves were fitted according to equations 2.14 and 2.16.

The  $T_1$  for the PFOB was found to be 1278 ms, confirming the value found by Sotak et al [103] at 2 T.  $T_2$  of the PFOB resulted equal to 398 ms.

The relatively long  $T_1$  relaxation time results in long image acquisition time and short  $T_2$  relaxation times results in MR signal attenuation, both of which has to be considered when performing 19F MRI.

### 8.3.3 Susceptibility of PFOB

The evaluation of the susceptibility of the fluorine agent is fundamental prior to the use of the compound in vivo. PFOB is considerably more dense than water (1.93 g/ml). In particular, if PFOB has to be encapsulated for transit studies in the GI tract it is important that its susceptibility is not too different from water or it will cause large field gradients and the signal from the agent may be dephased. In order to measure the susceptibility of PFOB, the sample was placed in a medium-walled NMR tube of 20 mm diameter, which was inserted in a collar on the top of a 500 ml spherical flask full of water. This phantom was placed in the centre of the bore with the long axis of the tube perpendicular to the main magnetic field. An FFE sequence was used to acquire phase images in the coronal plane (TR=100 ms, rec. res. = 0.48 mm x 0.48 mm, 10 slices of 1 mm thickness), for TE =10, 25 and 50 ms in order to calculate the field shift from the relation  $\phi = \gamma \Delta B \Delta T$ . A second phase map was acquired after replacing the sample with water without moving the phantom by using a cannula and a syringe to pull the PFOB out and then pouring the water. The difference between the two phase maps is due to the difference in susceptibility between PFOB and water, and susceptibility can be calculated from:

$$\Delta B = B_0 \frac{\Delta \chi}{2} \left[ \frac{R}{r} \right]^2 \cos(2\theta) \quad (8.1)$$

where  $R$  is the radius of the tube,  $r$  is the distance from the centre of the

tube,  $\theta$  is the angle around the coronal plane (defined relatively to  $B_0$ ) and  $\Delta\chi$  is the susceptibility difference between the PFOB and the water.

Figure 8.11 shows the images used to calculate the susceptibility of the PFOB which was found to be  $7.0 \pm 0.3 \cdot 10^{-7}$ , units relative to water. The images of the phantom also show that for higher TEs, the artefacts near the test tube worsens, due to the presence of the glass.

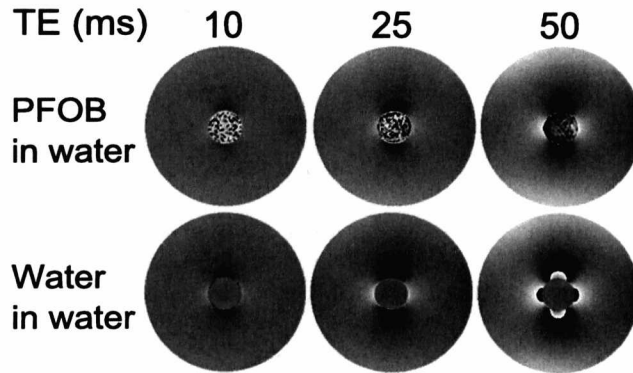


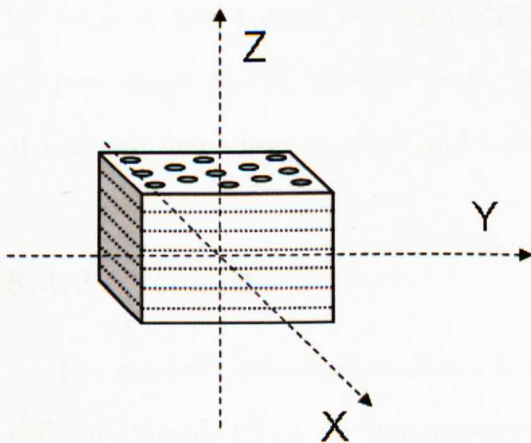
Figure (8.11): Phase images for PFOB and water at different TEs

## 8.4 19F coil characterisation

This section reports a series of tests performed on the 19F coil presented in chapter 4 prior to its use in vivo. These tests include a heating test of the coil, the compatibility of the 19F coil with the 1H body coil, maps for the B1 and the sensitivity of the coil and also a test to verify the loading of the coil in in vivo conditions.

### 8.4.1 Methods

Different phantoms have been imaged on a 3T Philips Achieva scanner, using the body coil and the 19F coil for the proton and the fluorine images respectively. A standard FFE sequence (TR=1000 ms, 2.4 mm x 2.4 mm voxel size, 1 slice of 50 mm thickness) was used to acquire images of the PFOB. Figure 8.12 shows the 2 experimental setups for the tests: the phantom 8.12(a) has been used for the sensitivity map of 19F while the cylindrical water phantom 8.12(b) has been used for the other tests.



(a) Schematic illustration of the grid used for the sensitivity map. 2 ml balls have been filled with PFOB.



(b) 20 cm diameter water test object designed for surface coils with curved surface.

Figure (8.12): Phantoms used for the 19F coil tests.

For the heating test a gradient echo sequence was repeated operating at 100% of the allowed body SAR for 5.5 minutes to test if any RF coupling

between the body coil and the 19F coil would cause any heating. The specification is that surfaces that could be touched must not heat above 41°C, however the aim should be to see minimal temperature rise, i.e. smaller than 5 degrees. An optical temperature sensor (courtesy of PulseTeq) was used to measure the temperature change.

The spatial distribution of the B1 field has been tested for homogeneity. Since large volumes of PFOB were not available, a 20 cm NMR tube was scanned in 3 different positions in the FOV. The FFE sequence was acquired at multiple flip angles  $\alpha$  ( $\alpha = 40^\circ, 70^\circ, 90^\circ, 110^\circ, 130^\circ$  and  $150^\circ$ ) and the images have been analyzed by a Matlab program which performs the fit of the experimental data to the theoretical equation

$$S = S_0(\sin\alpha) \quad (8.2)$$

where  $S$  is the signal obtained and  $\alpha$  is the flip angle which, together with  $S_0$ , is the parameter of the fitting.

The effect of loading the coil with a human being has also been investigated by using a test tube filled with PFOB positioned between the legs of the subject, inside the 3T scanner bore. The two surface coils were positioned one at top and one below the legs and secured with straps.

## 8.4.2 Results

The gradient echo images shown in figure 8.13 show that the presence of the 19F coil doesn't affect the image quality: the image SNR and uniformity close to the copper tracks of the 19F coil were not visibly changed by the presence of the 19F coil, which was plugged in and in position during the proton scan with the body coil.

The high SAR scans showed no detectable heating in the coil and a change less than 2°C on the cable foam, which is acceptable.

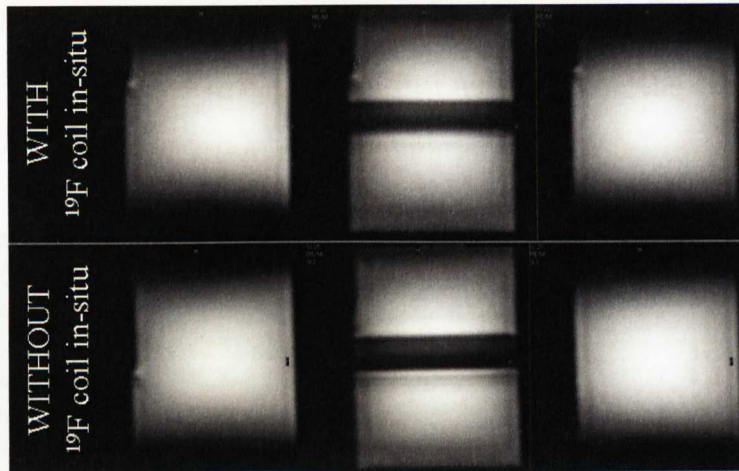


Figure (8.13): Gradient echo images of a water phantom positioned between the two  $^{19}\text{F}$  coils, acquired with the body coil. The  $^{19}\text{F}$  coil doesn't affect the quality of the  $^1\text{H}$  images.

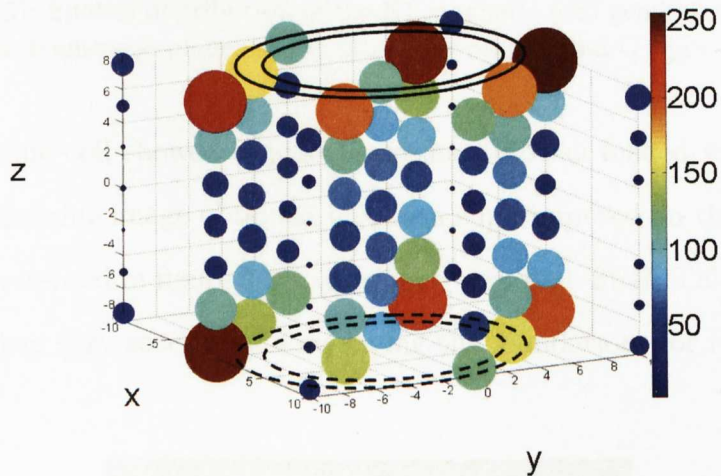


Figure (8.14): Three-dimensional illustration of the grid used for the sensitivity map. The size and the colour of the balls represent the sensitivity according to the legend.

The results for the sensitivity test are shown in figure 8.14 which represents the signal obtained from each sample in the corresponding position in the FOV shown in figure 8.12(a). The size of the circle scales with the signal and the colour corresponds to the intensity level. From the figure we can deduce that with our coil we can get good signal from a depth of up to 12.5 cm, which is sufficient for most subjects considering that the two coils are positioned one at the front of the body and the other on the back as shown in the figure 4.5.

Figure 8.15 shows the results for the B1 map in the three positions in the

FOV. The B1 fields are homogeneous over the full volume of the sample even if it has to be considered that a 20 cm distance between the two coils is not always in accordance with the in vivo conditions.

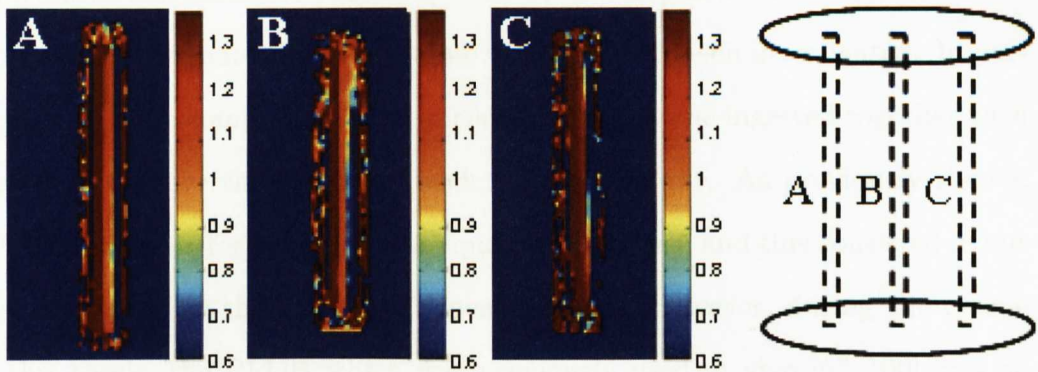


Figure (8.15): Spatial distribution of the B1 magnetic field generated by the RF pulse on the transverse plane: A left lateral, B central and C right lateral.

The fluorine coil showed a good performance when loaded with a human being. The fluorine image obtained has been superimposed on the proton one and it is represented in figure 8.16, showing a very high SNR. This first in vivo result has been very successful, thus laying the foundations for future studies in the gut.

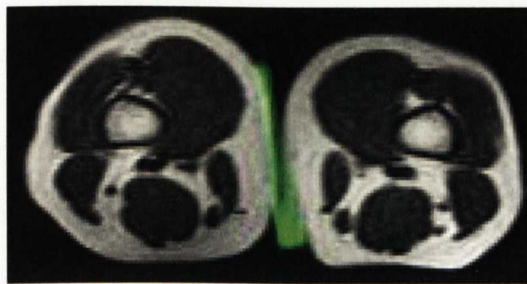


Figure (8.16): Overlay of the proton and the fluorine images in vivo: the  $^{19}\text{F}$  intensity of the PFOB is displayed in green and the  $^1\text{H}$  images are shown in gray scale.

## 8.5 Capsules for GI transit studies

As previously mentioned, the measurement of transit time of markers through the gastrointestinal tract would be very useful for the diagnosis of functional gastrointestinal diseases. For this reason the development of a safe noninvasive technique to estimate the transit time in the gut has been investigated. In particular, fluorine compounds were initially thought to be ingested together with meals to measure the transit of such meal in the gut. As previously shown, PFOB is suitable for being used in aqueous emulsions, and this consisted in our first approach for the gut transit measurement. However, during the course of this thesis, the PFOB which was previously used *in vivo* [97, 100] was no longer available on the market. The only available source of PFOB consisted in chemical industries as Apollo Scientific, which don't guarantee the use of compounds for human use. For this reason, even if PFOB is FDA approved, the encapsulation of the compound was considered. In particular, different types of capsules have been tested for safety and effectiveness. The development of the whole system for GI transit times measurement using labelled capsules is described.

### 8.5.1 Methods

Different types of capsules have been prepared and tested for *in vivo* use. In particular, gelatine capsules and plastic capsules were tested for stability in acidic environment and for leakage.

#### Gelatine capsules

Some batches of 0 sized gelatine capsules were dip-coated in Eudragit S100, a pH-sensitive coating polymer commonly used for delivery of drug molecules to colon for the treatment of colon cancer. A 200 ml solution of Eudragit S100 was made up from 26 g of Eudragit S100 (Degussa, Röhm Pharma Polymers)

powder, provided by the Medical Physics Department, Queens Medical Centre, Nottingham, dissolved in 80 ml of Acetone and 120 ml of Isopropanol at 37° Celsius, according to the Medical Physics Department Clinical Procedures Manual. Since Eudragit S100 is designed for delivery in the colon, i.e. it dissolves at pH=7.0, it has been necessary to perform multiple coatings, from 1 to 30 layers, in order to avoid dissolution in the whole GI tract.

### Plastic capsules

Plastic capsules have been manufactured in our mechanical workshop with the same shape as the 0 sized gelatine capsules. The material was Polyoxymethylene (commonly referred to as POM and also known as polyacetal or polyformaldehyde), chosen because of its favorable properties: its chemical stability and inertness towards biological material is comparable to Teflon but it is far more rigid and thus easier to machine at high precision. It is commonly known under DuPont's trade name Delrin.

The capsules were made from a plastic rod that was lathed and milled into the shape of a conventional size 0 gelatine capsule, with a final length of 22 mm and a diameter of 8 mm. Detailed measures are given in table 8.2 and in figure 8.17(b).

Material	Delrin
Length	22 mm
Width	8 mm
Weight (empty)	1.0 g
Weight (full of PFOB)	2.5 g
Density (full)	1.7 g/cm <sup>3</sup>
Internal volume	0.8 ml

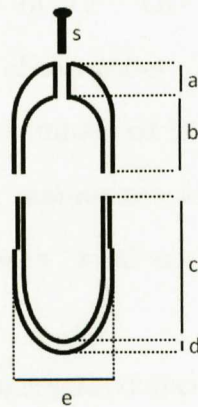
Table (8.2): Characteristics of the capsules.

In analogy with the gelatine capsules, our capsules consisted of two half-shells with a cuff that allowed the two pieces to be fitted together, see figure

8.17. A little hole was drilled on top so that liquid compounds could be poured in with a needle avoiding air bubbles. A little plastic screw was then inserted and glued with superglue (Loctite) in the hole to prevent leakage from the hole. The standard operating procedure (SOP) for manufacturing the capsules are given in appendix A. The manufacture of these capsules aimed at their use in vivo, for the tracking in the gastrointestinal tract in healthy and diseased human subjects. Therefore the main effort in the production is the safety of the capsules and the prevention of the leakage.



(a) This figure presents a picture of the used custom manufactured Derlin capsule.



(b) This figure provide exact geometric data of the used capsules.  $a=3$  mm,  $b=8$  mm,  $c=15.5$  mm,  $d=1.5$  mm,  $e=8$  mm.  $s$  is the screw.

Figure (8.17): Example of a custom manufactured capsule.

### pH test

In order to check the chemical stability and the biological inertness of the capsules, pH tests were performed with both types of capsules using three buffer solutions to simulate in vivo behaviour. Simulated gastric fluid was made up from 2 g of sodium chloride, NaCl, dissolved in 7 ml of concentrated hydrochloric acid, HCl, diluted and made up to 1 litre with distilled water. The final pH range estimated on the basis of an average of several batches was

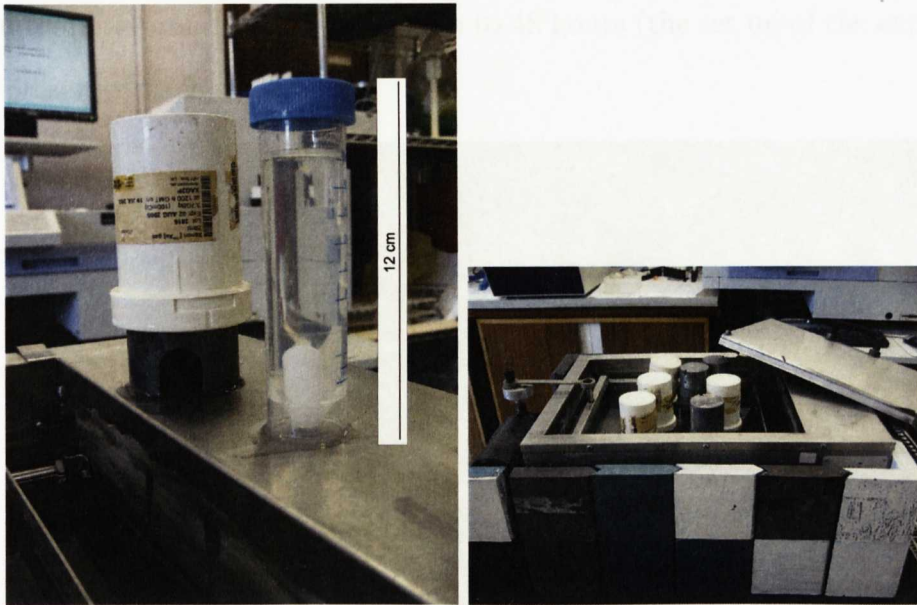
1.0–1.3. Buffer solutions of pH 4, 7 and 10 were also used so that the whole range of pHs in the GI tract could be simulated. A pre-calibrated pH meter Corning 240 was used to measure the pH of all solutions used. In order to simulate the in vivo condition, the capsules were left in the simulated gastric fluid up to 8 hours and they were examined hourly for integrity.

### Leakage test with radiolabels

The plastic capsules were tested for leakage using radiolabels. 7 capsules were filled with 0.5 ml of PFOB and 0.25 ml of  $\text{Tc}^{99m}\text{O}_4^-$  of activity 250 MBq and then individually immersed in 45 ml of tap water. The 6 test tubes were subsequently shielded for radioactivity and immersed in a water bath at 37° Celsius, figure 8.18, where they have been maintained at constant body temperature and in movement for up to 48 hours. 1 ml samples were taken from the water every 4 hours.

A 3 inch well-type sodium iodide scintillation crystal detector, PerkinElmer WALLAC Wizard 3", 1480 Automatic gamma counter was used to establish the amount of activity released into the beaker. The gamma counter was used to measure the activity of samples, withdrawn from the beaker at specified time intervals.

It has to be underlined that the use of radioactives has implied extra care and specific training in order to perform the tests safely. For example, the filling of the capsule with 0.25 ml of  $\text{Tc}^{99m}\text{O}_4^-$  of activity 250 MBq is extremely dangerous for the very high activity of the compound. Also, the capsule with the  $\text{Tc}^{99m}\text{O}_4^-$  was to be held with the hand while pouring the PFOB in and this procedure is also very dangerous. The risk of spilling the radioactive while closing the capsule is also quite high especially because the procedure has to be undertaken as quickly as possible in order to avoid any unnecessary exposition to the radioactive. Given the technical difficulties associated with the use of radioactives, another testing method has been take into account and



(a) Illustration of the capsule filled with 0.5 ml of PFOB and 0.25 ml of  $\text{Tc}^{99m}\text{O}_4^-$  of activity 250 MBq, individually immersed in 45 ml of tap water. On the left the shield used for each test tube is presented.

(b) The 6 shielded test tubes are immersed in a water bath at  $37^\circ\text{C}$ . The capsules have been maintained at constant body temperature and in movement in the water bath for 48 hours. 1 ml samples were taken every 4 hours during the day.

Figure (8.18): Equipment for the leakage test of the capsules with radioactive materials.

it is explained below.

### Leakage test with a VIS spectrophotometer

An alternative leakage test would use an optical marker, using a spectrophotometer in the range of the visible light. The preparation of the capsules followed the standard procedure explained in appendix A, including the use of superglue to seal the capsules and a glue approved for human use (Blue Histoacryl<sup>®</sup> by Brown) for an additional coating layer. 10 capsules were filled with 0.8 ml of blue food colour using a needle through the hole on top. The screw was then inserted and glued. They were left to dry for a day and then they were individually immersed in 45 ml of tap water in a water bath at  $37^\circ\text{C}$ . The capsules have been maintained at constant body temperature in a water bath equipped with a motor system to keep the samples in motion with

1 ml samples taken every 3 hours up to 48 hours (the set up of the experiment is presented in figure 8.19).



Figure (8.19): Experimental setup for the leakage test: the capsules have been filled with blue dye and then glued. They have then been maintained at constant body temperature and in movement in a water bath. 1 ml samples have been taken every 3 hours up to 48 hours.

A UV/VIS Jenway Model 6105 spectrophotometer was used to establish the presence of colour in the samples. After choosing the blue complimentary colour, the precise analytical wavelength was selected by scanning in 5 nm steps until a maximum absorbance value was reached, corresponding to a wavelength value of 400 nm.

Blank and sample calibration of the instrument was carried out at the beginning and at the end of every sample batch.

The linearity (i.e. concentration vs reading) of the methodology at the selected wavelength  $\lambda$  has been verified by preparing samples at different concentrations. The absorbance is defined as

$$Abs_{\lambda} = \log_{10} \frac{I_0}{I} \quad (8.3)$$

where  $I$  is the intensity of light at the wavelength  $\lambda$  that has passed through

the sample and  $I_0$  is the incident light intensity.

## 8.5.2 Results

### Gelatine capsules

The gelatine capsules which successfully stayed intact at pH 1 up to 8 hours were the ones with more than 15 layers and these have been then inserted in a solution with higher pH. 25 and 30 layers were found to be necessary to guarantee the integrity of the capsules in basic solution up to 48 hours. It might be concluded that 30 layers would be enough for guaranteeing the total absence of leakage in the GI tract but it has to be said that at this stage no mechanical strain has been applied to the capsules and they were kept at room temperature, which is lower than the body temperature. Also, the manufacture of the capsules with 30 coating layers is time consuming and not effective.

Given these results the use of gelatine capsules was abandoned and the leakage test was not performed.

### Plastic capsules

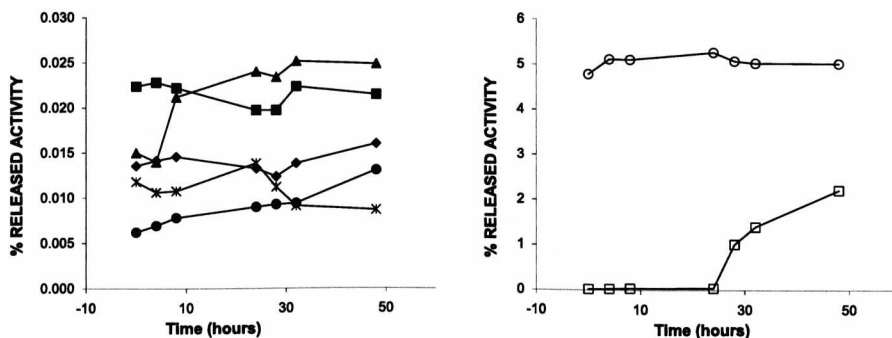
The plastic capsules proved to be insoluble and stable in water, in 0.1 M hydrochloric acid and in buffer solutions of pH 4.0, 7.0 and 10.0. Therefore they were also tested for leakage as described below.

### Leakage test with radiolabels

Gamma counter data is presented as a percentage loss of activity from the capsule and a percentage increase in the activity of the solution. Decay corrections were done over the time span of detection.

As can be seen in figure 8.20(a), the released activity appears to level off at a value below 0.025 % for five out of seven capsules. These values were

then constant for 24 hours, meaning that the leak is due to the initial closing procedure, when it could be expected that some of the  $\text{Tc}^{99m}\text{O}_4^-$  may remain attached superficially to the surface of the capsules. A much bigger release, up to 5 %, has been found for two capsules, figure 8.20(b). These data suggest that there is a possibility that  $\text{Tc}^{99m}\text{O}_4^-$  does in fact slowly diffuse out of capsules. This might also be due to the initial procedure of closure of the capsule and might be overcome by careful preparation. It is worth noting that working with radioactives required quick handling of the beads thus providing considerable opportunities for error in the closing procedure.



(a) Five out of seven capsules showed a small leakage equal to a released activity of maximum 0.025%. (b) Two out of seven capsules showed a much bigger leakage reaching the 5% in one case probably due to inaccuracy during the preparation of the capsule.

Figure (8.20): Results from the leakage test of the 7 capsules with radioactives.

In addition, a leakage test using a radioactive must take account of the time needed for the capsule to dry after being glued which would noticeably increase the amount of radioactive needed, thus raising many further safety issues.

### Leakage test with a VIS spectrophotometer

Figure 8.21 reports the values of the absorbance versus the concentration of the blue colour in water: it shows the linear dependence of the concentration with the absorbance. The resolution of the instrument for the absorbance is 0.001 thus meaning a resolution in concentration of less than 1 part in 10000.

This technique has been adopted as standard procedure to test the leakage of the capsules.

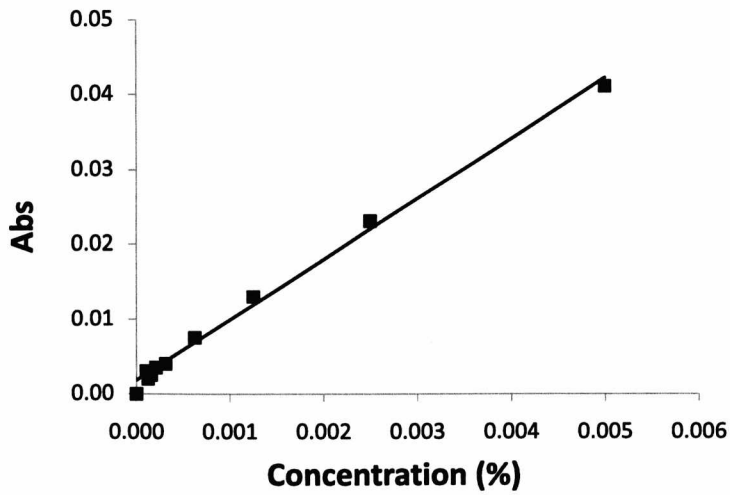


Figure (8.21): Linearity tests showing the absorbance value versus the concentration.

Figure 8.22 shows the mean values of the absorbance for the 10 capsules tested for up to 48 hours. The values obtained are within the resolution of the instrument, meaning that no leakage was found.

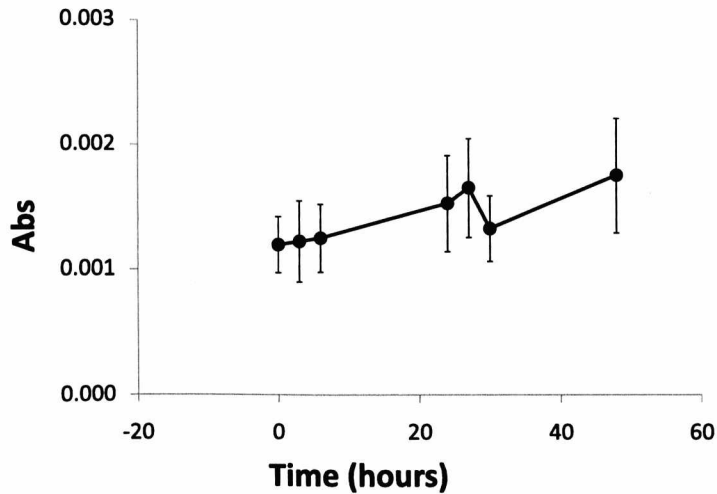


Figure (8.22): (Mean  $\pm$  STD). Results for the leakage test with the VIS spectrophotometer: the mean values of absorbance for the 10 capsules used for the test for up to 48 hours. The values obtained are considered not significant because they lie within the instrument resolution, i.e. less than 1 part in 10000.

### **8.5.3 Conclusion**

The tests performed on the different capsules showed that the in house manufactured plastic capsules are safe for in vivo use. The leakage test carried out with the VIS spectrometer proved to be safe and easy to perform. It also showed better results, i.e. no leakage from the capsules, as it allows a more careful and efficient preparation of the capsules. The in vivo experiment presented in the following sections have been performed on the basis of these in vitro results, therefore preparing and testing the capsules according to the procedure just described.

## 8.6 GI transit in vivo study with the use of fluorinated markers

### 8.6.1 Introduction

The purpose of this pilot study is to develop a protocol of measuring gut transit times using capsules labelled with a fluorine compound as described above. As discussed in section 8.2.2, PFOB proved to be a safe and effective contrast agent to be encapsulated for gastrointestinal MR, so it has been used to label the home made capsules described in section 8.5.1.

### 8.6.2 Method

This study was approved by the University of Nottingham Medical School Ethics Committee and all volunteers gave written informed consent. For this pilot study we recruited 2 healthy volunteers who attended the MRI centre on 4 consecutive days having fasted overnight on the first occasion. All images were acquired with a 3T Philips Achieva system using a range of MRI sequences for both proton and fluorine scans. The volunteers received a breakfast meal comprising a standard rice pudding meal and pure orange juice from concentrate used in previous studies [61]. Then they underwent a baseline scan before consuming 4 capsules filled with 0.8 ml PFOB and prepared as explained in section 8.5.1 with water ad libitum. PFOB with a nominal purity of 99.0% was purchased from Apollo Scientific. However this has not been testified as safe for human consumption and therefore the PFOB was encapsulated securely as described above. Subjects were then scanned immediately after swallowing the capsules and then blocks of subsequent fluorine and proton MRI were routinely acquired every 30 min for 7 hours. The subjects were imaged again the following days to acquire a single data point at 24, 48 and

72 hours after dosing. Coronal images were acquired in order to use the same geometrical orientation as other imaging techniques such as X-ray. A range of MRI sequences were used to image the stomach, bowels and the colon:

- Proton images were acquired with a dual echo FFE sequence ( $TE_1 = 2.3$ ,  $TE_2 = 4.6$ , rec. res = 1.56 mm x 1.56 mm). The data matrix consisted of  $256^2$  pixels over a field of view of 400 x 400  $cm^2$ . 15 contiguous slices with a slice thickness of 10 mm were acquired for a total scan time of 20 seconds, i.e. within a single breath hold.
- The fluorine images were acquired without moving the volunteer as the fluorine coil was already in place when the proton images were acquired with the whole body coil. An FFE sequence was used ( $TE=3.0$  ms, acq. res = 2.3 mm x 2.3 mm, TR 350 ms, FOV(AP, FH, RL)=300x230x300, flip angle  $70^\circ$ , NAV 1) to acquire 3 slices 100 mm thick, for a total scan duration of 22 seconds. A narrow acquisition bandwidth (434 Hz) was used to overcome the chemical shifts artifacts as discussed in section 8.3.

In vivo proton and fluorine images of the abdominal region were superimposed using a code written in Matlab to correctly locate the position of the capsules within the GI tract (figure 8.23).

### 8.6.3 Results

The two volunteers tolerated the capsules and the study procedures well although one of the volunteers found it difficult to swallow the capsules at first because of their rigid structure. There were no adverse events in this study.

Images of the first volunteer showed all the capsules in the stomach up to 2 hours after ingestion. At 24 hours one of the capsules was visible in the ascending colon and at 48 hours the fluorine images showed one capsule in the rectum (see figure 8.24). Nothing was found at 72 hours; the volunteer confirmed that the capsules had all been evacuated.

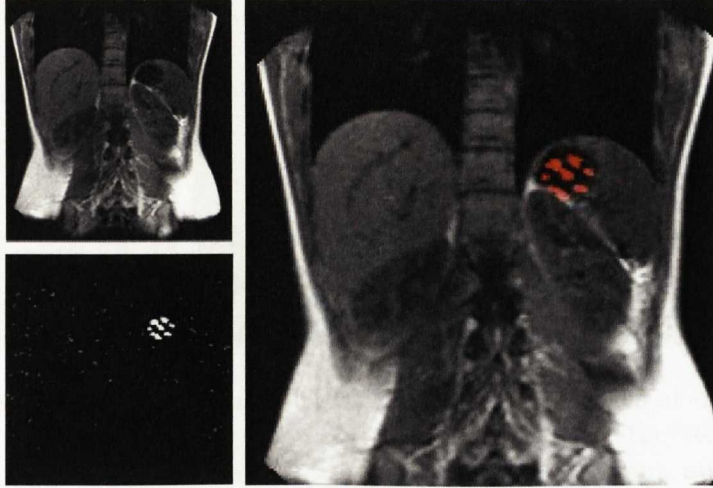


Figure (8.23): Example of proton and fluorine images (left) and their superimposition (right), see section 8.6.2 for details. This image was taken for one subject immediately after swallowing the capsules.

Similar results were obtained for the second volunteer (see figure 8.25): the capsules were visualized in the stomach at 45 minutes and then in the small bowel at 2 hours after ingestion. At 24 hours one capsule was detected in the rectum. Nothing was found at 48 and 72 hours.



Figure (8.24): Superimposition of proton and fluorine images at different time points for the first volunteer: at 2 hours the capsules are all in the stomach (left), at 24 hours one capsule was found in the ascending colon (middle) and at 48 hours one capsule was found in the rectum.

#### 8.6.4 Discussion and conclusion

This first pilot study was successful. The method proved to be well tolerated by the volunteers and the capsules were visualized and correctly located



Figure (8.25): Superimposition of proton and fluorine images at different time points for the first volunteer: a capsule was visualised in the stomach at 45 minutes (left), and another one in the small bowel at 2 hours after ingestion (middle). At 24 hours one capsule was detected in the rectum.

in the GI tract for the 2 volunteers. The capsules were all evacuated by 72 hours for both volunteers.

However, some issues have been raised; for example, the capsules are quite large making them quite challenging for healthy volunteers to consume and hence possibly not suitable for patients. However, it has to be pointed out that the size of the capsules is similar to the Smartpill (© 2009 SmartPill Corporation) capsules normally used for clinical practice [118–120].

The detection of the capsules with the fluorine coil proved to be very difficult most of the time because the sensitive volume of the coil was not big enough to cover the entire GI tract. In order to overcome this problem, it was often necessary to reposition the coil. This is of course a major issue because the method needs to be implemented and used with patients and needs to be reproducible, quick and easy to use. In this regard double labelling of the capsules with gadolinium based contrast agent and fluorine has been considered allowing an easy visualization of the capsules on T1-weighted proton images, followed by a fluorine scan to allow the confirmation of the presence of a capsule in the surrounding anatomical structures.

This has been implemented in a second study that is reported in the following section.

## 8.7 GI transit time using double-labelled markers

A chelated form of the rare earth element gadolinium (Gd) has been used as a water phase marker together with the fluorine compound PFOB described in the previous section. The contrast agent that we used is Gadoteridol (Gd-HP-DO3A, Prohance® ; Bracco-Altana, Konstanz, Germany) that is a non-ionic, extracellular, water-soluble contrast material for MRI. It has paramagnetic properties with Gd concentration of 0.5 M. Each millilitre of Prohance contains 279.3 mg of Gadoteridol [121]. Gadoteridol is usually applied intravenously: the safety and benefit of intravenous Gadoteridol injection have been demonstrated in various MRI studies [122, 123]. However we enclosed this contrast agent in the capsules to be administered orally. It has also been shown that the Gd molecule does not dissociate in the acidic gastric environment [16, 124, 125]. The safety of the capsules, proven by means of the leakage tests described in the previous sections, guarantees the safe use of Gadoteridol itself.

In order to find the optimal concentration of gadolinium and the minimum amount of solution to be put in the capsules, some preliminary tests were performed.

### 8.7.1 In vitro test: finding the optimal Gd concentration

As explained in section 2.2.9, the effect of the contrast agents on the relaxation times depends on their concentration (see equation 2.24). Therefore an in vitro test has been performed using sequences optimised to be used in vivo, acquired in one or two breath holds.

Eleven solutions of Gadoteridol in water at different concentration ranging from 0.25  $\mu\text{M}$  to 25  $\mu\text{M}$  were prepared at room temperature.

The test tubes were then imaged in a water phantom with the following sequences:

- A  $T_1$ -weighted TFE sequence (TR=4.6ms, TE=2.3ms, rec. res. 1.14 x 1.14 x 3 mm<sup>3</sup>). This has been used because the signal from the Gd is very bright due to the  $T_1$  shortening of the contrast agent and it will be helpful to locate the capsules for the in vivo study.
- A HASTE sequence (TSE) with parameters TR=1670ms, TE=65ms, acq. res. 5 x 5 x 10 mm<sup>3</sup>. This is a  $T_2$ -weighted sequence and therefore the signal from the gadolinium is completely lost because of the  $T_2$  shortening. However, the images showing a signal drop corresponding to the gadolinium presence can be useful in order to provide additional details when distinguishing the capsules from other anatomical structures in vivo.
- $T_2$ -weighted FFE sequence (TR=100 ms, TE=25 ms and acq. res. of 1 x 1 x 1 mm<sup>3</sup>). This sequence is not optimised on the basis of the Gd concentration but it provides good anatomical details, thus helping for the exact localisation of the capsules in the gastrointestinal tract.

Figure 8.26 shows the results for the in vitro test.

In particular, figure 8.26A shows the  $T_1$ -weighted TFE sequence for the 11 samples, showing the change in signal according to the Gd concentration. The signal obtained from this image has been plotted in logarithmic scale as a function of the concentration in order to find the optimal concentration to be used for the capsules, see graph 8.27. It can be seen that there is a biphasic relationship, due to the competing effects of  $T_1$  and  $T_2$ , between the concentration of Gd-HP-DO3A and the MRI signal intensity which has a log-linear dependency between 2 and 10  $\mu\text{M}$ . From the graph 8.27 it is possible to conclude that for this sequence the concentration that maximises the signal is equal to 15  $\mu\text{M}$ . This concentration will be used to prepare the capsules for the in vivo study.

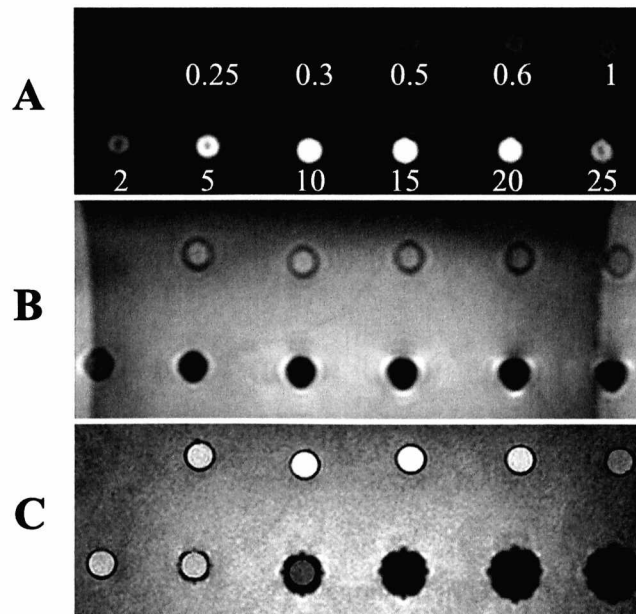


Figure (8.26): A shows how the signal changes according to the concentration of gadolinium in the sample in the T1 weighted TFE image. B shows how for a different sequence, the TSE, the MRI signal is completely lost because of the presence of Gd. C shows a T2 weighted FFE sequence acquired just for argument sake in order to demonstrate that the presence of Gd may create susceptibility artifacts and signal loss if the concentration is not optimised.

Figure 8.26B shows the results for the HASTE sequence, confirming the signal loss due to the contrast agent, also dependent on the concentration value. Figure 8.26C shows the results for the different concentrations acquired with a  $T_2$ -weighted FFE sequence: this has been acquired in order to demonstrate that the presence of Gd may create susceptibility artifacts at high concentration. In conclusion, a concentration of  $15 \mu\text{M}$  will be used together with a  $T_1$  weighted TFE sequence for the in vivo studies described below.

## 8.7.2 In vivo pilot study

### Methods

This study was approved by the University of Nottingham Medical School Ethics Committee and all volunteers gave written informed consent. In analogy with the first study, we recruited 2 healthy volunteers that attended the MRI centre on 4 consecutive days having fasted overnight on the first occasion.

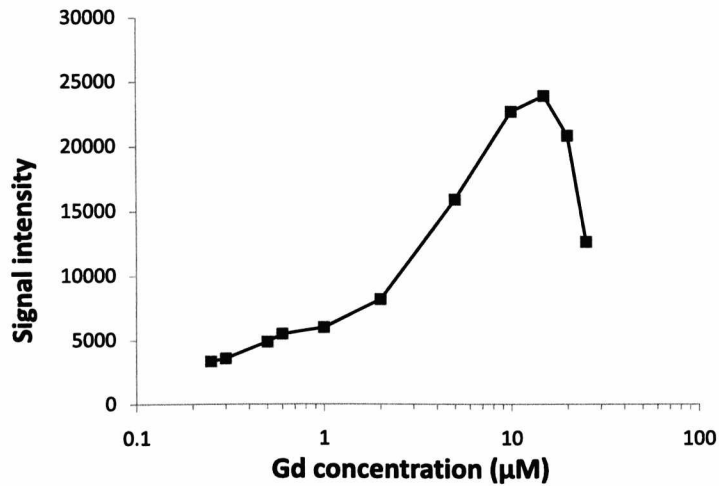


Figure (8.27): Signal intensity versus concentration of gadolinium in water, calculated using a T1-weighted TFE sequence (TR=4.6ms, TE=2.3ms). The MRI signal response decreases at both high and low concentrations, although there is a log-linear relationship between 2 and 10  $\mu\text{M}$ .

All images were acquired with a 3T Philips Achieva system using a range of MRI sequences for both proton and fluorine scans. The volunteers received a breakfast comprising a standard rice pudding and pure orange juice from concentrate used in previous studies [61]. They underwent a baseline scan before swallowing 4 capsules with water ad libitum, filled with 0.2 ml of Gd 15  $\mu\text{M}$  solution and 0.6 ml of PFOB and prepared as explained in section 8.5.1. PFOB with a nominal purity of 99.0% was purchased from Apollo Scientific. They were then scanned immediately after this and then blocks of subsequent fluorine and proton MRI were routinely acquired every hour for 7 hours. The subjects were imaged again the following days to acquire a single data point at 24, 48 and 72 hours after dosing. A range of MRI sequences were used to image the stomach, bowels and the colon. For the proton images three different sequences have been used:

- A heavily  $T_1$ -weighted TFE sequence (TR=4.6 ms, TE=2.3 ms, acq. res. = 3.03 mm x 3.01 mm, rec. res. = 1.14 mm x 1.14 mm, thickness 3 mm) The total number of slices is 40 with no gap and the total duration is 25 s, performed with 2 breath holds. This sequence has been optimised in

vitro (details in the previous section) and it shows a very bright signal from the Gd, providing a very efficient tool to find the capsules in the gut. On the contrary, the PFOB produces a signal void.

- Haste sequence (TSE) with parameters TR=1667 ms, TE=65 ms, acq. res. = 5.00 mm x 5.05 mm, rec. res. = 1.56 mm x 1.55 mm and thickness 10 mm for a total number of 10 slices with no gap. This is a  $T_2$  weighted sequence therefore the Gd is displayed very dark but it can be useful, together with the other images, when distinguishing the capsules from the other anatomical structures. Being a proton scan, the PFOB is also displayed dark.
- Dual echo FFE sequence (TR/TE1/TE2 (ms) = 126 / 2.3 / 5.8, acq. res. 2.00 mm x 2.50 mm, rec. res. = 1.56 mm x 1.56 mm) to acquire proton images with good anatomical images for the exact localisation of the capsules in the gastrointestinal tract. The data matrix consisted of  $256^2$  pixels that represented a field of view of 400 x 400  $cm^2$ . 30 contiguous slices with a slice thickness of 5 mm were acquired for a total scan time of 40 seconds, two breath holds.

The fluorine images were acquired without moving the volunteer as the fluorine coil was already in place when the proton images were acquired with the whole body coil. An FFE sequence was used (TR=350 ms, TE=3.0 ms, acquired resolution = 2.34 mm x 2.34 mm, FOV (AP, FH, RL)=300x230x300, flip angle 70°, NAV 1) to acquire 3 slices 100 mm thick, for a total scan duration of 22 seconds. A low bandwidth was used to overcome the chemical shifts artifacts exposed in section 8.3.

In vivo proton and fluorine images of the abdominal region were superimposed to correctly locate the position of the capsules within the GI tract.

## Results

The two volunteers tolerated the capsules and the study procedures well and there were no adverse events in this study. The capsules were detected in the gut for both volunteers at all time points until evacuation. Figure 8.28 summarises the results for this study. At 2 hours, the 4 capsules were visible in the stomach for both volunteers. From 2 to 5 hours the capsules were seen in the small bowel for both subjects. At 24 hours, for subject 1 two capsules were found in the transverse colon and 2 in the rectum, whilst for subject 2, 1 capsule was found in the descending colon and 2 in rectum. At 48 and 72 hours no capsules were found for both volunteers.

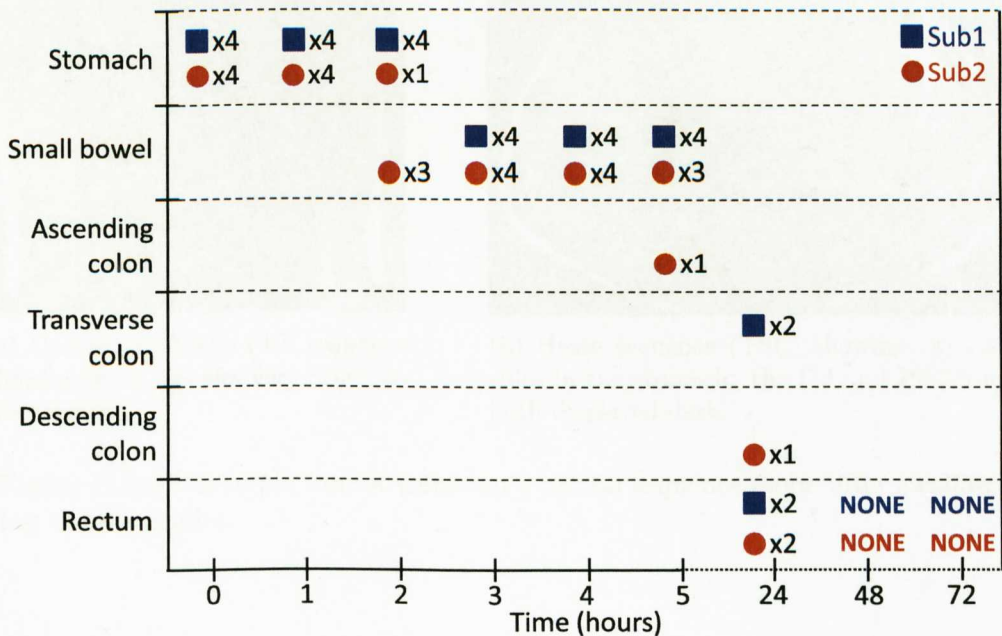


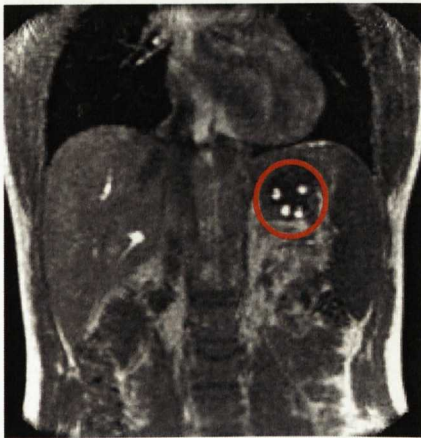
Figure (8.28): Position of the capsules for the 2 subjects over time. The capsules were detected in the gut for both volunteers at all time points until evacuation.

Figure 8.29 and 8.30 show examples of the different images acquired for this experiment. In particular, figure 8.29(a) shows the dual echo FFE and figure 8.29(b) shows the haste sequence which display the gadolinium very bright and very dark respectively. The presence of the capsules, together with their position, is very easy to locate in both cases. Figure 8.30 shows the

images (MIP) acquired with the  $T_1$ -weighted TFE sequence for volunteer 1 at 24 hours: 2 capsules are found in the transverse colon and 2 in the rectum.

The fluorine images confirm the presence of the capsules especially in those cases where other bright anatomical structures such as vessels are evident.

However it has to be underlined that the slice thickness of the fluorine images is much bigger (100 mm for the fluorine sequence compared with 3 mm of the proton  $T_1$ -weighted TFE sequence), thus the fluorine slice covers a region that is displayed in multiple slices in the proton images. An example is given in figure 8.31.



(a) Coronal dual echo FFE sequence showing the 4 capsules very bright in the stomach.



(b) Haste sequence (TSE) showing the capsules in the stomach: the Gd and PFOB are both displayed dark.

Figure (8.29): Example from a volunteer's proton sequences soon after swallowing the 4 capsules.

### 8.7.3 Discussion

The use of double-labelled markers has proved successful because all the capsules were easily detected in the gut for both volunteers at all time points until evacuation. By using the range of sequences available one can easily differentiate the bright signal of the gadolinium in the capsules from the vessels nearby and the fluorine image gives double confirmation of their position. However, in most cases the fluorine coil had to be repositioned after the exact

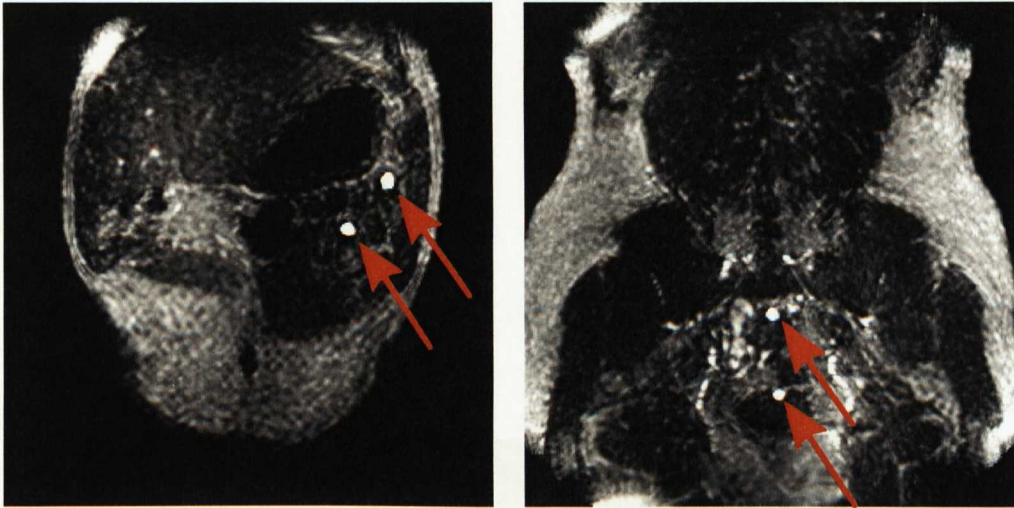


Figure (8.30): MIPs of the  $T_1$ -weighted TFE sequence for volunteer 1 at 24 hours. Two capsules are easily visible in the transverse colon (left) and two are in the rectum (right).

location of the capsules was established by the proton images because the fluorine coil sensitivity doesn't cover the entire GI tract.

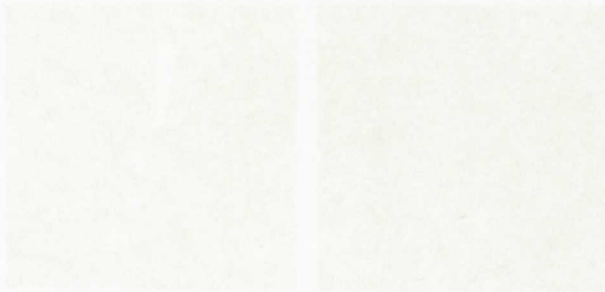
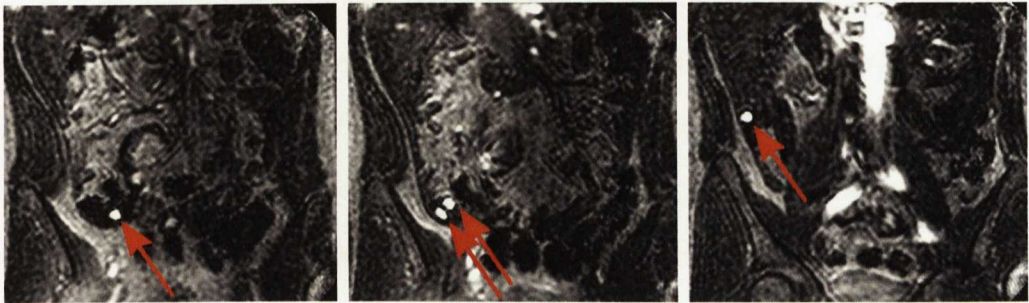


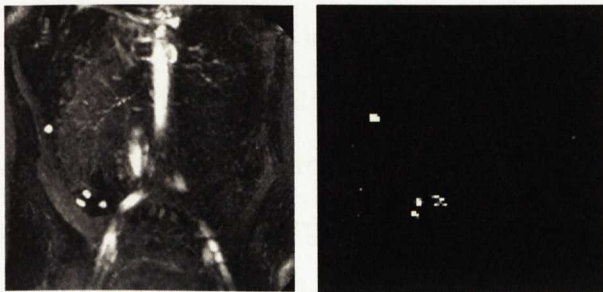
Figure (8.31): MIPs of the proton MRI sequence for volunteer 1 at 24 hours. The locations of the capsules are not clearly visible in these images.

## 8.5 Studying the GI transit time using double-labelled markers: mode of action of Moviprep

### 8.5.1 Introduction



(a) Proton  $T_1$ -weighted TFE images for the second volunteer at 24 hours showing the presence of 3 capsules in the last part of the SB and one capsule in the AC.



(b) MIP of the Proton  $T_1$ -weighted TFE images (left) and fluorine FFE image (right). The fluorine image is a single slice showing the 4 capsules all together because the slice thickness is much higher compared to the proton images.

Figure (8.31): Proton and fluorine images for the second volunteer at 24 hours.

## 8.8 Studying the GI transit time using double-labelled markers: mode of action of Moviprep

### 8.8.1 Introduction

Moviprep is an osmotic laxative commonly used in the clinical practice for the bowel preparation carried out before a colonoscopy. When fully made up as 1 litre of Moviprep, it provides 100 grams of polyethylene glycol, a nonnutrient substance which is not absorbed and therefore rapidly leaves the stomach and generates a substantial inflow of fluid in the upper small intestine. Water flows down the osmotic gradient markedly increasing the small intestinal water content compared with fasting. We have shown in section 6.2 that the arrival of small bowel fluid induced by mannitol produces a radical change in the heterogeneous structure of the ascending colon. The rate of recovery after purgation with polyethylene glycol is said to be normally rapid but slower in certain patient groups though data is still very limited [126]. It has been reported that patients find an improvement in bowel function after colonic lavage thus suggesting that the reconstituted microbiota may be different, though this has not been scientifically proven.

In this study the colonic transit after purgation with polyethylene glycol is investigated by means of the double-labelled markers developed. In particular, two different cases will be compared: the intake of Moviprep in a single 2 litre dose or in a split dose of 1 litre per day as it has been previously shown that Moviprep is more effective and better tolerated in a split dose [127]. The changes in colonic transit in these two arms of the study will be investigated.

### 8.8.2 Methods

This study was approved by the University of Nottingham Medical School Ethics Committee and all volunteers gave written informed consent. For this study 24 healthy volunteers (12 females) were recruited. They had normal BMI and mean age of  $25.7 \pm 9.9$ . The volunteers were split into two groups. Group 1 received a split dose of Moviprep, i.e. 1 litre on Day 1 and 1 litre on Day 2. Group 2 had the 2 litre dose of Moviprep in one day. In order to prevent nutritional bias of colonic transit all volunteers were asked to follow a dietary plan, avoiding alcohol for at least 24 hours before the study day.

The transit scans were carried out at 3 time points throughout the study: 7 days before dosing, 14 days after dosing and 28 days after dosing, to see the extended effect of purging the bowel on the colon. For each of these occasions volunteers swallowed 3 capsules, with as much water as they desired, 24 hours before the scan under the supervision of one of the study investigators. On the study day the volunteers attended the study centre having fasted overnight and a 30 min scan was performed. A series of images, in analogy with the pilot study described in section 8.7.2, were acquired to localize the position of the capsules in the gut.

The transit was assessed by scoring the position of the capsules according to the scores represented in figure 8.32. The geometric centre of the 3 capsules was calculated to give a single final score.

### 8.8.3 Results

All volunteers attended every session and completed the study. The experiment procedures were well tolerated and all the capsules were easily swallowed. None of the capsules were found in the upper part of the GI tract, confirming the time scales found in the pilot study. For the majority of the subjects the detection of the capsules with the gadolinium sequences was straightforward

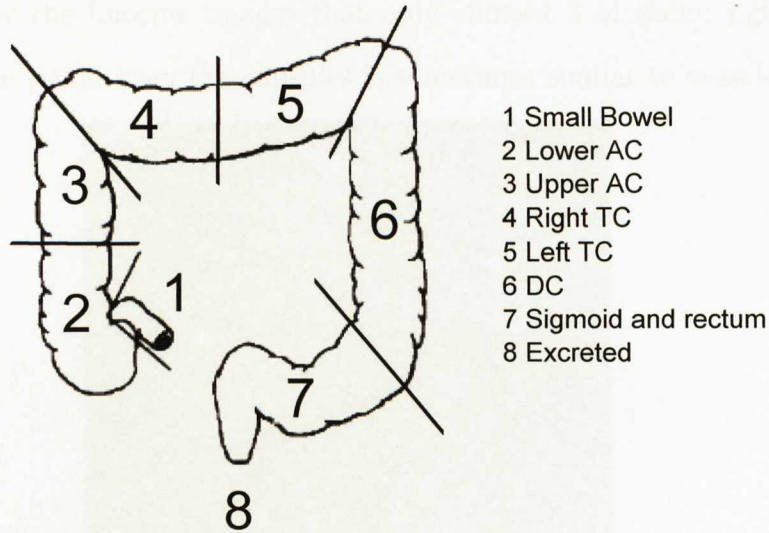


Figure (8.32): Illustration of the scores associated with each region of the gut. In order to give a comparable score for the transit of the capsules in the gut, the bowels were divided in 8 sections, and the geometric centre was calculated as a final score.

and quick, with a few cases having visible capsule in the survey scans (figure 8.33).

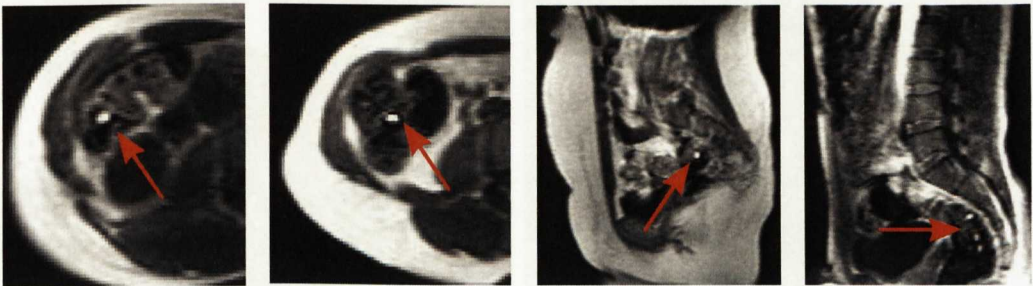


Figure (8.33): Examples to show the evidence of the position of the capsules from the survey scans. These images correspond to different subjects at different time points.

For the fluorine scans it was often necessary to reposition the coil after the survey scan, in order to get a good coverage of the area to image and a good signal from the PFOB. However, the scan time didn't normally exceed 20 minutes duration.

The fluorine images confirm the presence of the capsules especially in those cases where other bright anatomical structures are evident. Some examples are given in figures 8.34 and 8.35: in figure 8.34 the presence of a fourth capsule

was denied by the fluorine images that only showed 3 of them; figure 8.35 shows how the signal from the capsules is sometimes similar to vessels.

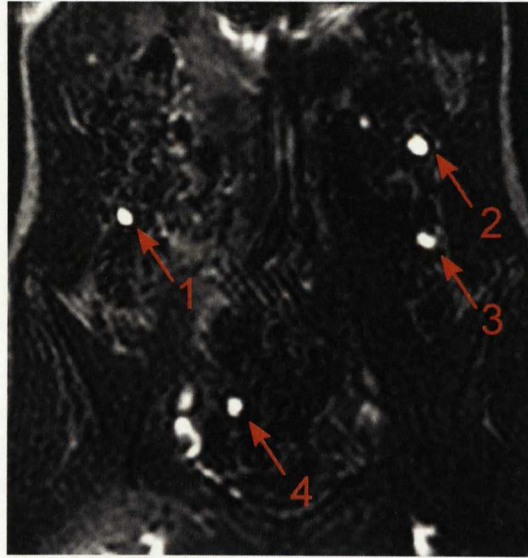


Figure (8.34): Example of anatomical structure similar in shape to the capsules. The fluorine images showed signal only from 1, 2 and 4, therefore number 3 is not a capsule.

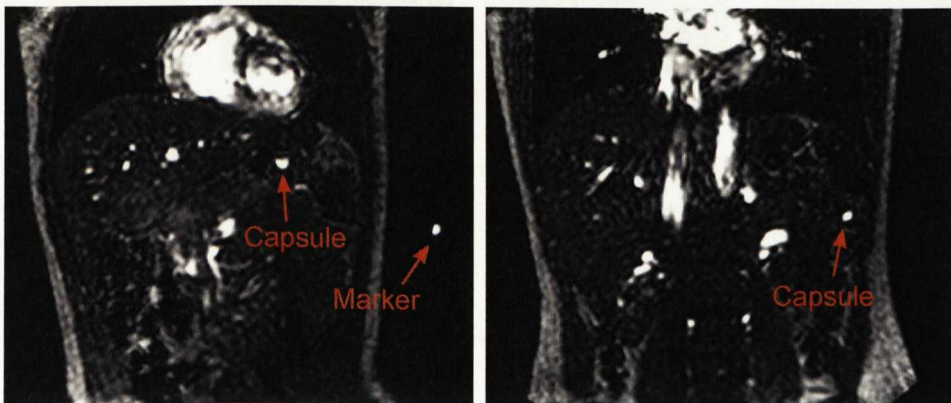


Figure (8.35): Example of capsules that can be confounded as vessels. In both cases the fluorine images confirmed their presence.

Figure 8.36 shows two examples of the MIPs (maximum intensity projections) of the  $T_1$ -weighted TFE sequence (left) and of the dual echo FFE sequence (right) for the same volunteer. The capsules are easy to see in the ascending and descending colon in both images.

A whole set of images acquired with the sequences optimised during the pilot study is represented in figure 8.37, showing an example of 3 capsules in the rectum for one of the subjects.

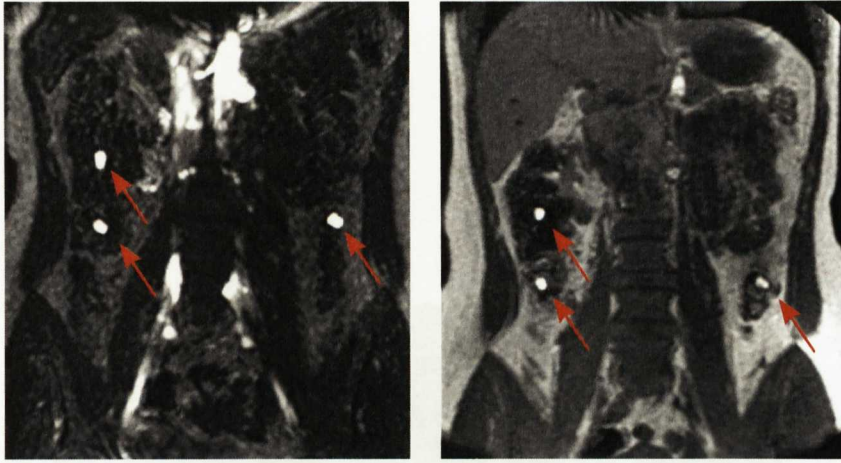


Figure (8.36): Example of MIPs from a volunteer's proton images 24 hours after swallowing the 3 capsules: T1-weighted TFE sequence (left) and dual echo FFE sequence (right). Both images clearly show the position of the capsules within the gut, in this case two in the ascending colon and 1 in the descending.

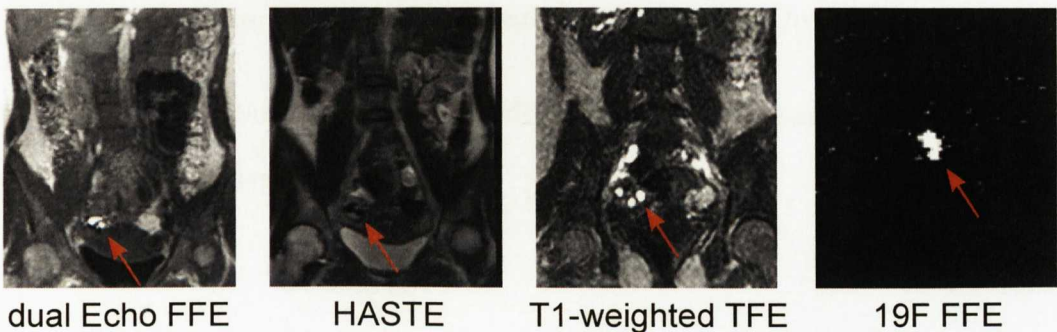


Figure (8.37): Example of MIPs from a volunteer's whole set of sequences 24 hours after swallowing the 3 capsules. The position of the 3 capsules in the rectum is evident in all images.

The geometric centres did not show a significant trend of transit change across the three scans for the two groups. Figure 8.38 reports the mean results for all volunteers on the 3 days.

For Group 1 each visit has a mean centre around the value 6 corresponding to the descending colon. The overall change in the three visit is not statistically different. The differences for the three visits in Group 2 are slightly more significant, indicating a slowing down of transit at visit 2 and a faster transit at visit 3 although this change is not statistically significant ( $p < 0.25$ ). The data from single individuals show a great variability: transit increased in some subjects whilst for others it stayed constant, with the largest changes in Group

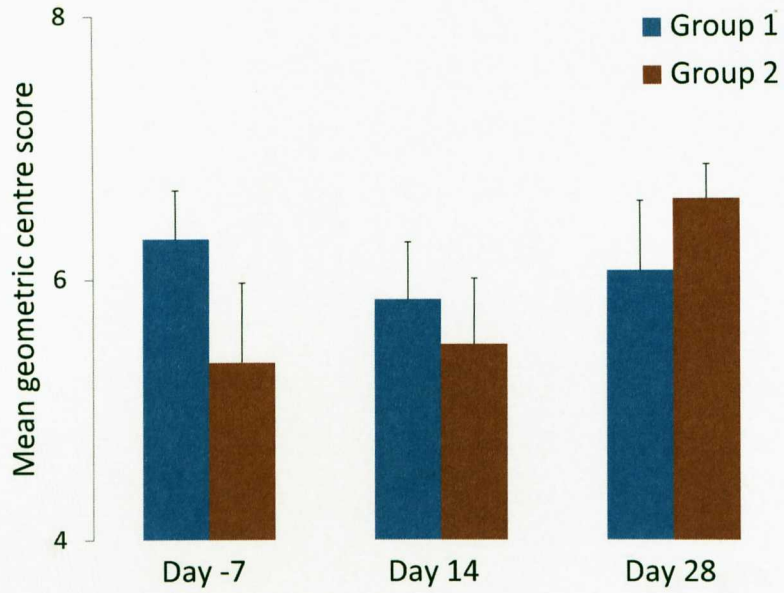


Figure (8.38): Graph showing the mean geometric centre of the capsules with the standard error across the three visits for Group 1 and Group 2.

2. Figure 8.39 shows the gender differences for the transit. There are no statistically significant differences.

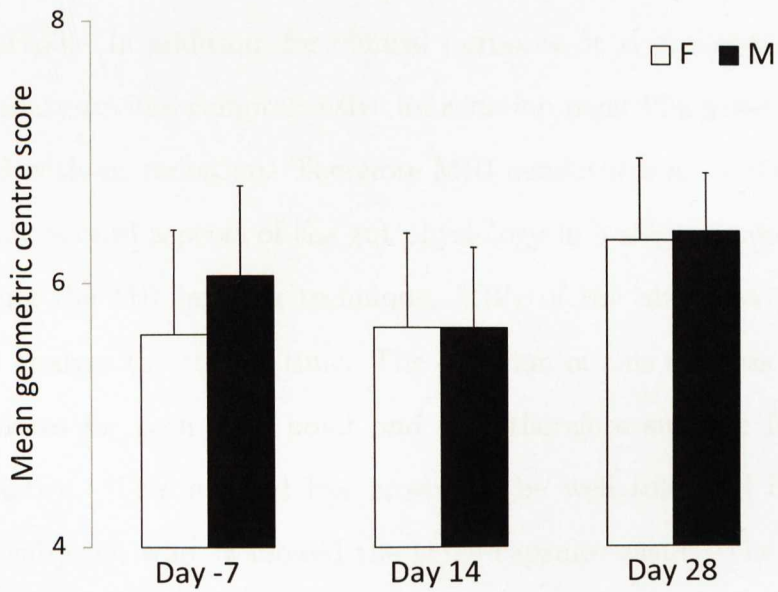


Figure (8.39): Gender differences for the mean geometric centre of the capsules with the standard error across the three visits.

### 8.8.4 Discussion and conclusion

Several techniques have been used to measure the colonic transit time including radio-opaque markers, isotopes, colored dyes, beads, and contrast agents [128–130]. However, there is no universally accepted or standardized technique.

This study showed that the double-labelled markers are a very useful method for the transit measurement in the gut, with the main advantage compared to alternative techniques being the absence of ionising radiation. The production of the capsules is also cheaper compared to other techniques such as the Smartpill. In addition, for clinical purposes, it is preferable to use a single test that provides comprehensive information regarding gastrointestinal transit, and without radiation. Therefore MRI constitutes an invaluable tool to investigate several aspects of the gut physiology in a single study day.

Regarding the MR imaging technique, MIPs of the abdomen were used in order to analyse the transit time. The duration of this analysis takes less than 5 minutes for each time point and it is therefore suitable for clinical routine practice. This method has proved to be well tolerated by a large number of subjects, who swallowed the three capsules easily. The detection of the capsules at 24 hours was easy and relatively quick thanks to the use of the gadolinium solution and the transit of the capsules was consistent among individuals, with all the capsules being found in the lower GI tract. However this technique showed several aspects that need further improvements. Firstly, the number of capsules may be too limited to correctly determine the transit in the gut and smaller capsules should be used to this aim. Also, because of the size and the weight of the capsules, they might not travel at the same rate as chyme along the gut, as shown in other studies [131]. It also has to be mentioned at this point that the fluorine detection has to be improved because the SNR is at the moment lower than the gadolinium. This would mean an improvement in the hardware and specifically in the coil itself and eventually

a further improvement of the sequences used in order to maximise the signal. With these improvements, the double-labelled markers technique would be a valid alternative compared to other techniques.

The present technique should be compared with other types of examinations such as conventional colonic transit using radiopaque markers and scintigraphy. The validation study is currently under way. Figure 8.40 shows the x-ray image of a phantom with the empty capsules behind.

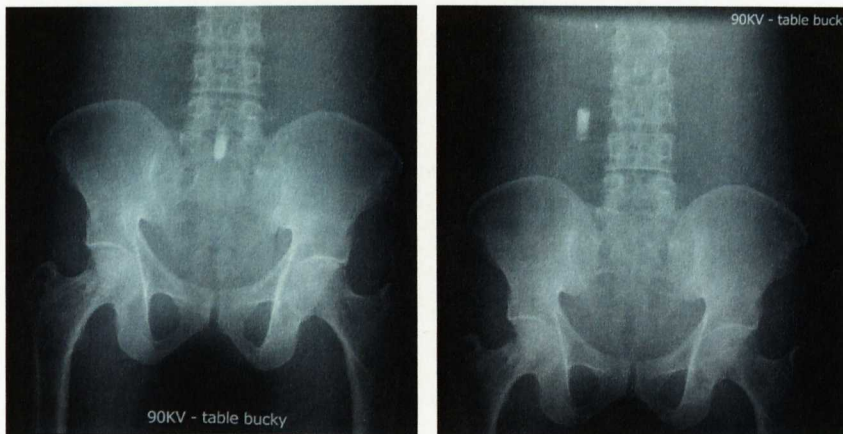


Figure (8.40): X-rays images of a phantom with the empty capsules behind. Courtesy of Dr Ching Lam.

We have found that the changes in transit scores after dosing with Moviprep were not significant for both Group 1 and Group 2. One main reason could be that the number of subjects per group was not sufficient as the effect of purging the bowel on transit is very variable between individuals. However, it was interesting to notice that the biggest changes in transit were in Group 2, corresponding to the single 2 litre dose of Moviprep in the same day. One could speculate that the considerable stretch of the colonic muscles may have a long-term effect on motility but further measurements are needed. Alternatively one could think that the colonic transit time is not effectively modified by a single purging event, as diarrhoea lasts longer in patients with IBS-like symptoms. Also, this measurement might not be sensitive enough as discussed above.

In addition, the transit scans have been performed only after 14 days from the Moviprep dose. There may have been a period of increased transit imme-

diately after the dosing days which was not investigated. This could be taken into account for future experiments.

## 8.9 Optimisation of the GI transit markers

### 8.9.1 Introduction

Following the studies described in the previous sections, further steps in the optimisation of the GI transit marker were undertaken. Firstly the size of the capsules was designed smaller so that their use could be easily extended to patients, also allowing the ingestion of an increased number. Secondly, the density of the capsules is to be considered. To this aim the filling of the capsules, i.e. the ratio between gadolinium solution and fluorine compound, is to be investigated. In order to address these points, a pilot study has been performed.

### 8.9.2 Methods

Small capsules were designed and produced with the same method and same shape as already described with final dimensions of 7 mm diameter and 20 mm length. They were filled with 0.2 ml of 15  $\mu$ M Gadoteridol solution in distilled water and 0.2 ml of PFOB. The total density of the capsules was 1.78. The capsules were filled and tested for leakage according to the SOP in appendix A.

This study was approved by the University of Nottingham Medical School Ethics Committee and all volunteers gave written informed consent. Two healthy volunteers were recruited and imaged on 3 consecutive days at multiple time points spread during the day. All images were acquired with a 3T Philips Achieva system using a range of MRI sequences for both proton and fluorine scans. The volunteers received a meal comprising a standard rice pudding at 8 pm on the first study day and they swallowed 5 capsules with water ad libitum. They were then scanned immediately after this and then at 13, 19, 24 and 37 hours. The same MRI sequences as the studies previously described were used

to image the stomach, bowels and the colon.

### 8.9.3 Results

The two volunteers swallowed the 5 capsules easily and there were no adverse event in the study. The capsules were detected in the gut on the proton images at all time points until evacuation. However, the fluorine images didn't show enough signal, therefore the results are based on the gadolinium detection only. Figure 8.41 summarises the results for the transit for both volunteers.

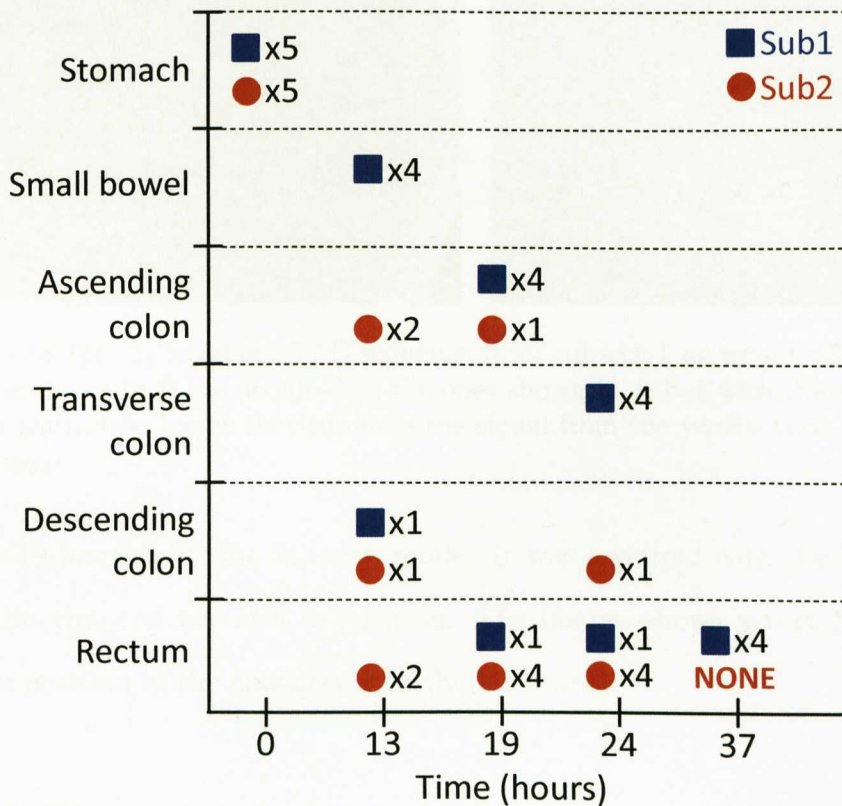


Figure (8.41): Position of the capsules for the 2 subjects over time. The capsules were detected in the gut for both volunteers at all time points until evacuation.

Figure 8.42A shows an example of the  $T_1$  weighted TFE sequence from subject 1. Figure 8.42B shows the same sequence on the same subject with the addition of the saturation bands in order to help the differentiation between capsules and other structures such as vessels.

Figure 8.43 shows the  $T_1$ -weighted TFE sequence acquired for subject 1 at

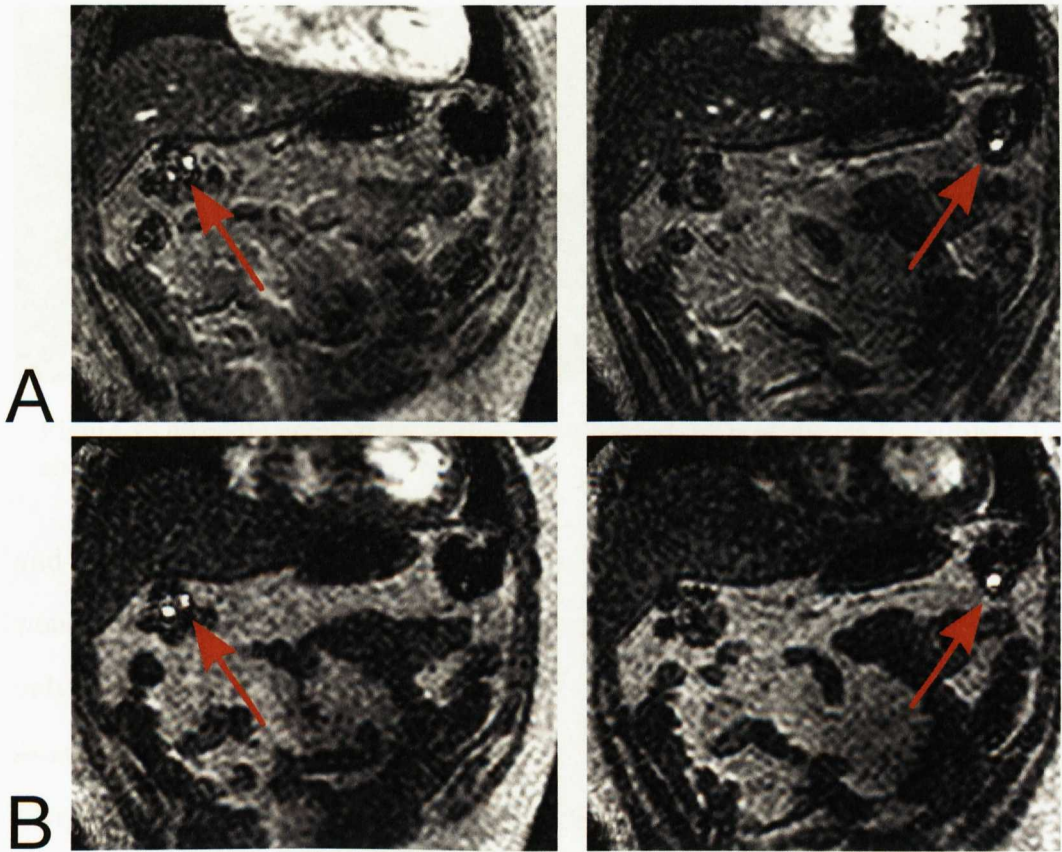


Figure (8.42):  $T_1$ -weighted TFE sequence from subject 1 at time  $t=24$  hours. Images shown in B are acquired as the ones shown in A but with the addition of the saturation bands that suppress the signal from the vessels such those in the liver.

time  $t=19$  hours with the 3D scan mode. It was acquired with the body coil as the fluorine coil was still in position. The images shows a very high SNR and the position of the capsules is easily detectable.

#### 8.9.4 Discussion and conclusion

This pilot study aimed at the optimisation of the double labelled capsules for their application with patients. To this aim smaller capsules were designed. However the internal volume of the capsules, equal to 0.4 ml, was found to be not enough for the detection of fluorine signal. On the contrary, the amount of gadolinium solution, equal to the previous studies, was enough for the easy detection of the capsules in the different regions of the gut. Further improvements of the proton sequences will consider the use of the saturation bands



Figure (8.43): 3D acquisition for the  $T_1$ -weighted TFE sequence for subject 1 showing an increased SNR.

and the use of 3D acquisitions. In this last case, the use of a SENSE coil would be necessary in order to acquire the data in one or two breath holds only. However, this would be feasible only if the fluorine coil is not used at the same time. For these reasons it may be concluded that for gut transit measurements the use of these plastic capsules filled with the gadolinium solution only is effective. The numerous advantages of using fluorine based compounds still apply for absorption studies, e.g. as a marker for liver absorption studies, as the gadolinium wouldn't be as effective. The main concern about using the fluorine compounds is still their safety. In case chemical industries will start producing PFOB, or similar compounds, approved for human use as it was the case for the Imagent GI (Alliance Pharmaceutical, San Diego, California) used by Mattrey et al. in the past [100], the possible applications of fluorine in gut imaging would be countless.

# Chapter 9

## Conclusions

The work described in this thesis was directed towards developing and applying MRI techniques for the investigation of colon function under any conditions non invasively and without any bowel preparation. It has been shown that these methods can find their applications in medical research, pharmaceutical trials as well as in studies of the gut physiology.

Chapter 6 presented the first in vivo study of colonic response to an experimental model of human diarrhoeal disease using MRI. This study was used to understand the time course of the physiological response of the gut and it allowed observation of the colon under physiological and pathological conditions. Colon function was monitored using a multimodal MRI approach. The water content was measured extending the method introduced by Hoad et al. [38] to the colonic water contents. It was found that after a mannitol drink, which is an unabsorbable osmotically active solution that causes secretion in the small bowel, the amount of water in the ascending colon increased significantly, together with the geometrical volume, with a first peak at 90 minutes after the drink and a successive peak soon after the solid meal.  $T_1$  and  $T_2$  were also measured in vitro to understand colonic content properties. In addition, a texture analysis based method was developed for the objective assessment of

colonic contents. It was found that texture features such as contrast and homogeneity are an effective and robust method to assess the heterogeneity and the mesoscopic structure of the colon. A possible extension of this work is the application of texture analysis to patients in order to have more information on the colonic content structure under various conditions. Also, more data would be desirable for the estimation of  $T_1$  and  $T_2$  in vitro. Another aspect that would need further improvements is the study of the motility of the ascending colon, with the optimization of MRI sequences to overcome the artifacts due to breathing.

Chapter 7 used the techniques developed in chapter 6 to investigate the colonic function under pharmacological interventions. The MRI protocol developed proved to be powerful and well tolerated for studying the gastrointestinal tract response to anticonstipation and antidiarrhoeal agents. In particular it was found that the antidiarrhoeal agent loperamide, administered alone or combined with simethicone, increased the gastric emptying rate of the non-nutrient mannitol meal, decreased the small bowel water content and the net secretion in the gut over time, and delayed the arrival of fluids in the ascending colon. Finally, the drugs also reduced significantly the contrast homogeneity ratio calculated.

Chapter 8 described a novel methodology for directly monitoring transit through the gut. This was achieved by using fluorinated compounds encapsulated in ad hoc built plastic capsules safe for human use. The choice of the best compound, the optimisation of MRI sequences and the development of the best capsules for a safe use in vivo, were the main object of the last chapter. This methodology, which is currently filed as a patent<sup>1</sup>, has also been applied in vivo for the investigation of an osmotic laxative commonly used in the clinical practice for the bowel preparation. Future work on this topic would involve the use of other markers for a broader application of the method

---

<sup>1</sup>Application Title: Magnetic resonance imaging methods and apparatus for use in such methods. Application Number:GB1109268.1 Application Date: 02/06/11.

and the further optimisation of the sequences and the hardware available for the improved detection of the fluorine signal. This would guarantee the successful application of this method with better results compared to the use of gadolinium only, which at the moment would be the easier and effective solution. A validation study for the double labelled markers is currently under way comparing this technique with radiopaque markers and scintigraphy. Possible collaborations with companies for the distribution of this methodology are also being pursued.

In conclusion, the MRI methods presented here proved to constitute an invaluable tool to investigate several aspects of the gut physiology and the colon function in a single study day.

# Appendix A

## Standard operating procedure for the capsules manufacture for in vivo studies

### A.1 Manufacture of the capsules

The manufacture of the capsule has been performed in the workshop of the SPMARC by Mr Ian Thexton. The raw material used is Polyoxymethylene (commonly referred to as POM and also known as polyacetal or polyformaldehyde), supplied by DuPont's under their trade name Delrin. The plastic rod is milled (figure A.1) and lathed (figure A.2), with hemispherical ends until it has these dimensions: 8 mm in diameter, and 22 mm long with hemispherical ends, with wall thickness of 1 mm and with a small hole drilled in one end 1 mm in diameter. The cuff with the hole is 3 mm thick; the other one is 1.5 mm (see figure 8.17). The capsules are then kept in the workshop in a clean bowl until the whole lot has been completed. Screws are also provided, purchased from RS, standard M2 nylon capsules.

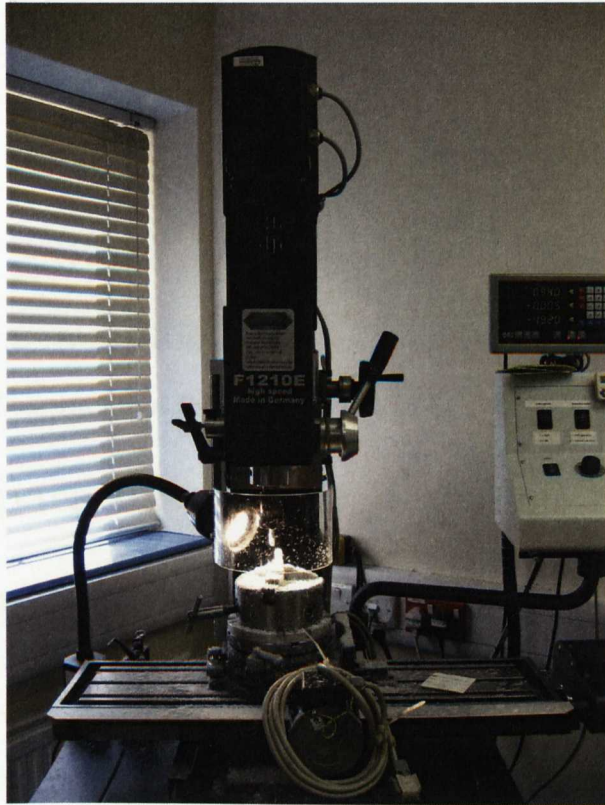


Figure (A.1): CNC control milling machine.

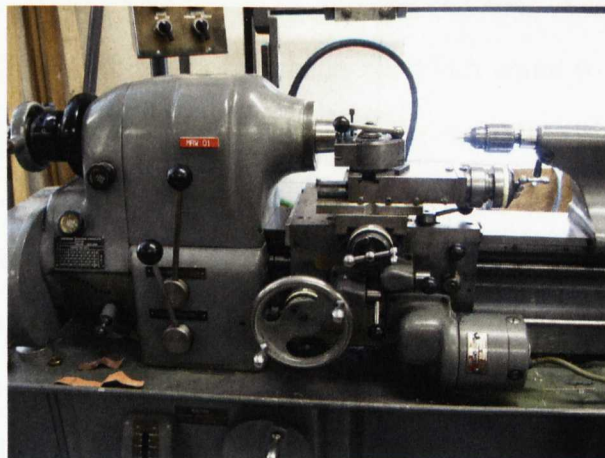


Figure (A.2): Hardinge lathing machine

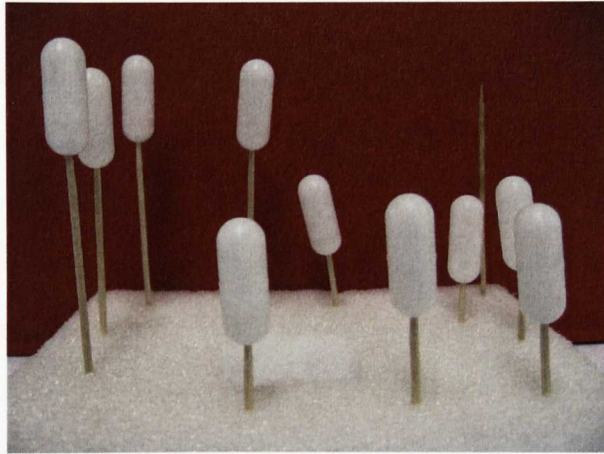


Figure (A.3): Illustration of the capsules left to dry on the sticks after sealing.

## A.2 Preparation of the capsules for in vivo studies

The preparation of the capsule for the in vivo experiments presented in chapter 8 follows the procedure below and it has been held in the prep room of the SPMRC, University of Nottingham.

### Day 1

Prepare the material: capsules, superglue, gloves, goggles, lab coat, tissues, sticks and foam. Wear gloves, goggles and the lab coat. Clean the work area before starting. Put a number of sticks in the foam equal to the total number of capsules to fill. Leave a spare stick to help spreading the glue uniformly. Glue the external part of the capsule that needs to be put in the other half, trying to make it as uniform as possible with the spare stick. Promptly push the matching half together to make a tight fit. Clean the capsule with a tissue so that little glue is left on the exterior of the capsule. Put the capsule on the stick via the hole on top (figure A.3). Repeat the same procedure for all the capsules. Leave them to dry for a day in prep room and label them as “do not touch”. Clean up work area.

## Day 2

To prepare the 15  $\mu\text{M}$  Gd solution disperse 1 ml of Gadoteridol using a new syringe and mix it with 33 ml of distilled water.

Prepare the materials required to fill the capsules: bottle of PFOB, gadolinium solution, 2 syringes with needles, plastic screws, grid to hold the capsules, tissues and blue dye for food. Wear gloves, goggles and the lab coat. Check that the capsules are dry. Take randomly 20% of the capsules and leave them apart for the leakage test.

### *Capsules for experiment*

Put the remaining capsules in the grid provided, standing them in upright position with the hole on top. Use a syringe to measure 0.6 ml of PFOB. Inject it in the hole carefully and slowly. Leave the syringe on a tissue on the table with the cap on. Take a new syringe and inject 0.2 ml of the gadolinium solution slowly into the capsule. Take the screw and put a drop of superglue on it and screw it in. Remove any residual glue from the capsule with a tissue. Repeat the same procedure for the other capsules. Leave them to dry for a day in prep room and label them as "do not touch". Clean up work area.

### *Capsules for leakage test*

Put the capsules in the grid provided, making them stand in an upright position with the hole on top. Using a new syringe inject 0.8 ml of blue dye into the capsule via the hole in the top carefully and slowly. Leave the syringe on a tissue on the table with the cap on. Take the screw and put a drop of superglue on it and screw it in. Repeat the same procedure for the other capsules. Leave them to dry for a day in prep room and label them as do not touch. Clean up work area.

## Day 3

Prepare the material: all capsules, cutter, file, glue approved for human use (BLUE Histoacryl® by Brown). Wear gloves, goggles and the lab coat. Cut

the top of the screw off the capsule so that the surface is nice and round. Use a file, if necessary, to smooth the surface of the capsule. Clear the exterior of the capsules of any unwanted material. Open the Histoacryl and pour a drop on the top of the capsules where the screw has just been cut. Leave it to dry. Repeat with all the capsules. Leave them to dry for a day in prep room and label them as do not touch. Clean up work area.

#### Day 4

Check that the capsules are dry and clear the exterior of the capsules of any unwanted material.

##### *Capsules for experiment*

Keep the capsule in a covered plastic dish, and label the dish with date and contents of the capsules. 30 minutes before giving the capsules to the subject prepare a plastic bowl with 2.5 l of tap water and dilute a half cupful of Milton disinfectant in it and leave the capsules in the bowl for at least 20 minutes. Be careful not to touch the capsules with dirty hands, rinse once and serve in the reception room in a paper dish with some napkins. Subject are allowed to drink as much water as they want to help them swallow the capsules but this will have to be checked for each experiment.

##### *Capsules for leakage test*

Prepare the material: capsules, 50 ml plastic test tubes with lid, water bath, thermometer for the water bath, tube rack for the water bath, eppendorfs. Fill the water bath with water and set the temperature to be 37°C. Leave it until it reaches the desired temperature (check with the thermometer). Fill each test tube with 45 ml tap water and put one capsule in. Close the test tube and put it in the test rack in the water bath. Take a 1 ml sample from each test tube and put it in different eppendorfs and label them. Repeat this step every 3 hours up to 72 hours.

### A.3 Leakage test with the spectrophotometer

Prepare the material (after collecting all the samples): UV-Vis spectrometer (figure A.4), labelled eppendorfs, syringe, eppendorfs provided specific for the spectrometer analysis. Turn the spectrometer on and leave it for 15 minutes to allow the lamp to warm up prior to use.

Calibration: Place a blank solution (1 ml distilled water) in the eppendorf and insert it in the cell holder. Close the sample chamber lid and select the required wavelength (400nm). Select Abs by use of the MODE keypad. Press the CAL keypad. The display will update to zero. Select %T by use of the MODE keypad. Press the CAL keypad. The display will update to 100.0. The unit is now ready to measure.

Place the first sample in the cell holder, close the sample chamber lid and write down the values for Abs and %T. Repeat for each sample without changing the wavelength. At the end put the blank solution (distilled water) in the cell holder and write down the values for Abs and %T to check for the stability. The test is now complete, clean up work area.

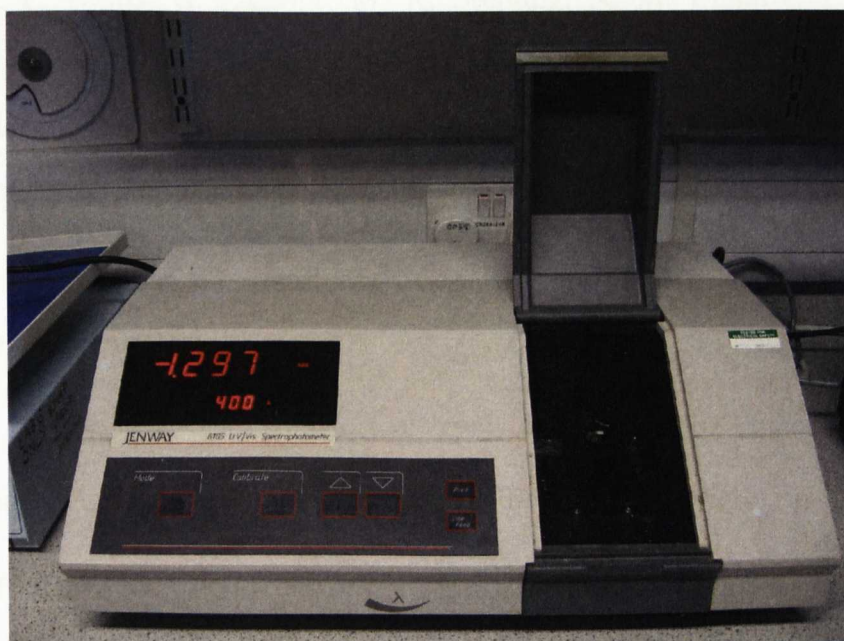


Figure (A.4): UV/VIS spectrophotometer Jenway Model 6105 (courtesy of Nottingham Digestive Diseases Centre NIHR Biomedical Research Unit, University of Nottingham) used to establish the presence of colour in the samples.

# Bibliography

- [1] P. Mansfield and P. K. Grannell. Nmr 'diffraction' in solids?. *J. Physics D*, 6:422–426, 1973.
- [2] P. C. Lauterbur. Image formation by induced local interactions: examples employing nuclear magnetic resonance. *Nature*, 242:190–191, 1973.
- [3] M. K. Stehling, D. F. Evans, G. Lamont, R. J. Ordidge, A. M. Howseman, B. Chapman, R. Coxon, P. Mansfield, J. D. Hardcastle, and R. E. Coupland. Gastrointestinal tract: dynamic mr studies with echo-planar imaging. *Radiology*, 171(1):41–46, Apr 1989.
- [4] D. F. Evans, G. Lamont, M. K. Stehling, A. M. Blamire, P. Gibbs, R. Coxon, J. D. Hardcastle, and P. Mansfield. Prolonged monitoring of the upper gastrointestinal tract using echo planar magnetic resonance imaging. *Gut*, 34(6):848–852, Jun 1993.
- [5] A. Lembo and M. Camilleri. Chronic constipation. *N Engl J Med*, 349(14):1360–1368, Oct 2003.
- [6] R. D. Madoff, S. C. Parker, M. G. Varma, and A. C. Lowry. Faecal incontinence in adults. *Lancet*, 364(9434):621–632, 2004.
- [7] M. H. Levitt. *Spin dynamics: basics of nuclear magnetic resonance*. 2001.

- 
- [8] P. T. Callaghan. *Principles of Nuclear Magnetic Resonance Microscopy*. Oxford Science Press, 1991.
- [9] P. G. Morris. *Nuclear Magnetic Resonance Imaging in Medicine and Biology*. Oxford Science Press, 1986.
- [10] P. Mansfield and P. G. Morris. *NMR Imaging in Biomedicine*. Academic Press, 1982.
- [11] F. Bloch, W. W. Hansen, and M. Packard. Nuclear induction. *Physical Review*, 69:127, 1946.
- [12] E. M. Purcell, H. C. Torrey, and R. V. Pound. Resonance absorption by nuclear magnetic moments in a solid. *Physical Review*, 69:37–38, 1946.
- [13] R. M. Sanchez Panchuelo. *High resolution anatomical and functional imaging*. PhD thesis, University of Nottingham, 2009.
- [14] S. Meiboom and D. Gill. Modified spin echo method for measuring nuclear relaxation times. *Rev. Sci. Instrum.*, 29(8):688–691, 1958.
- [15] R. Turner, D. Le Bihan, C. T. Moonen, D. Despres, and J. Frank. Echo-planar time course mri of cat brain oxygenation changes. *Magn Reson Med*, 22(1):159–166, Nov 1991.
- [16] W. Schwizer, R. Fraser, H. Maecke, K. Siebold, R. Funck, and M. Fried. Gd-dota as a gastrointestinal contrast agent for gastric emptying measurements with mri. *Magn Reson Med*, 31(4):388–393, Apr 1994.
- [17] H. J. Weinmann, R. C. Brasch, W. R. Press, and G. E. Wesbey. Characteristics of gadolinium-dtpa complex: a potential nmr contrast agent. *AJR Am J Roentgenol*, 142(3):619–624, Mar 1984.
- [18] S. Laurent, L. V. Elst, and R. N. Muller. Comparative study of the physicochemical properties of six clinical low molecular weight gadolinium contrast agents. *Contrast Media Mol Imaging*, 1(3):128–137, 2006.

- [19] A.N. Garroway, P.K. Grannell, and P. Mansfield. Image formation in nmr by a selective irradiative process. *J. Phys. C*, 7:457–562, 1974.
- [20] P. Mansfield. Multi-planar image formation using nmr spin echoes. *J. Phys. C*, 10:55–58, 1977.
- [21] P. Mansfield and B. Chapman. Active magnetic screening of coils for static and time-dependent magnetic field generation in nmr imaging. *J. Phys. E*, 19:540–545, 1986.
- [22] P. Mansfield, A.M. Howseman, and R.J. Ordidge. Volumar imaging using nmr spin echoes - echo-volumar imaging (evi) at 0.1-t. *J. Phys. E*, 22:324–330, 1989.
- [23] R. H. Hashemi, W. G. Bradley, and C. Lisanti. *MRI The Basics*. 2004.
- [24] J. Hennig, A. Nauerth, and H. Friedburg. Rare imaging: a fast imaging method for clinical mr. *Magn Reson Med*, 3(6):823–833, Dec 1986.
- [25] M. Poole. *Improved Equipment and Techniques for Dynamic Shimming in High Field MRI*. PhD thesis, University of Nottingham, 2007.
- [26] P. Mansfield and B. Chapman. Active magnetic screening of coils for static and time-dependent magnetic field generation in nmr imaging. *J. Phys. E: Sci. Instrum.*, 19:540–545, 1986.
- [27] J.V.M. McGinley, V.C. Srivastava, and G.D. DeMeester. Passive shimming technique for mri magnets. *Mag. Res. Im.*, 15(3):XIX, 1997.
- [28] J. F. Debatin and M. A. Patak. Mri of the small and large bowel. *Eur Radiol*, 9(8):1523–1534, 1999.
- [29] <http://www.newworldencyclopedia.org/entry/digestivesystem>.
- [30] <http://www.virtualcancercentre.com>.

- [31] L. R. Johnson. Digestion and absorption. *Gastrointestinal physiology*, 6th edition:119–41, 2001.
- [32] <http://www.colorado.edu/intphys/class/iphy3430-200/image/21-31.jpg>.
- [33] A. Swidsinski, J. Weber, V. Loening-Baucke, L. P. Hale, and H. Lochs. Spatial organization and composition of the mucosal flora in patients with inflammatory bowel disease. *J Clin Microbiol*, 43(7):3380–3389, Jul 2005.
- [34] Watts. The transit rate of different-sized model dosage forms through the human colon and the effects of a lactulose-induced catharsis. *International Journal of Pharmaceutics*, 87:215–221, 1992.
- [35] G. Bassotti, G. de Roberto, D. Castellani, L. Sediari, and A. Morelli. Normal aspects of colorectal motility and abnormalities in slow transit constipation. *World J Gastroenterol*, 11(18):2691–2696, May 2005.
- [36] R. Hagger, D. Kumar, M. Benson, and A. Grundy. Colonic motor activity in slow-transit idiopathic constipation as identified by 24-h pancolonic ambulatory manometry. *Neurogastroenterol Motil*, 15(5):515–522, Oct 2003.
- [37] P. Boulby, P. Gowland, V. Adams, and R. C. Spiller. Use of echo planar imaging to demonstrate the effect of posture on the intragastric distribution and emptying of an oil/water meal. *Neurogastroenterol Motil*, 9(1):41–47, Mar 1997.
- [38] C. L. Hoad, L. Marciani, S. Foley, J. J. Totman, J. Wright, D. Bush, E. F. Cox, E. Campbell, R. C. Spiller, and P. A. Gowland. Non-invasive quantification of small bowel water content by mri: a validation study. *Phys Med Biol*, 52(23):6909–6922, Dec 2007.

- [39] Y. Takehara. Mr pancreatography: technique and applications. *Top Magn Reson Imaging*, 8(5):290–301, Oct 1996.
- [40] A. M. Connel. The motility of the pelvic colon. ii. paradoxical motility in diarrhoea and constipation. *Gut*, 3:342–348, Dec 1962.
- [41] A. Prior, D. G. Maxton, and P. J. Whorwell. Anorectal manometry in irritable bowel syndrome: differences between diarrhoea and constipation predominant subjects. *Gut*, 31(4):458–462, Apr 1990.
- [42] C. L. Hoad, E. F. Cox, and P. A. Gowland. Quantification of  $t(2)$  in the abdomen at 3.0 t using a  $t(2)$ -prepared balanced turbo field echo sequence. *Magn Reson Med*, 63(2):356–364, Feb 2010.
- [43] J. M. Bland and D. G. Altman. Statistical methods for assessing agreement between two methods of clinical measurement. *Lancet*, 1(8476):307–310, Feb 1986.
- [44] J. M. Bland and D. G. Altman. Measuring agreement in method comparison studies. *Stat Methods Med Res*, 8(2):135–160, Jun 1999.
- [45] J. M. Bland and D. G. Altman. Comparing methods of measurement: why plotting difference against standard method is misleading. *Lancet*, 346(8982):1085–1087, Oct 1995.
- [46] D. Gabor. Theory of communications. *Journal of Institution of Electrical Engineers*, 93:429–457, 1946.
- [47] M. R. Turner. Texture discrimination by gabor functions. *Biol Cybern*, 55(2–3):71–82, 1986.
- [48] J. K. Kamarainen, V. Kyrki, and H. Kalviainen. Local and global gabor features for object recognition. *Pattern Recognition and Image Analysis*, 17 (1):93–105, 2007.

- 
- [49] J. Ilonen, J.K. Kmrinen, and H. Klviinen. *Efficient computation of Gabor features*. Research Report 100, 2005.
- [50] B. E. Boser, I. Guyon, and V. Vapnik. A training algorithm for optimal margin classifiers. *Proceedings of the Fifth Annual Workshop on Computational Learning Theory*, pages 144–152, 1992.
- [51] C. Cortes and V. Vapnik. Support-vector network. *Machine Learning*, 20:273–297, 1995.
- [52] M. Aizerman, E. Braverman, and L. Rozonoer. Theoretical foundations of the potential function method in pattern recognition learning. *Automation and Remote Control*, 25:821837, 1964.
- [53] C. Chang and C. Lin. Libsvm : a library for support vector machines. *ACM Transactions on Intelligent Systems and Technology*, 2:1–27, 2011.
- [54] H. J. Brownlee. Family practitioner’s guide to patient self-treatment of acute diarrhea. *Am J Med*, 88(6A):27S–29S, Jun 1990.
- [55] W. F. Stewart, J. N. Liberman, R. S. Sandler, M. S. Woods, A. Stemhagen, E. Chee, R. B. Lipton, and C. E. Farup. Epidemiology of constipation (epoc) study in the united states: relation of clinical subtypes to sociodemographic features. *Am J Gastroenterol*, 94(12):3530–3540, Dec 1999.
- [56] <http://www.romecriteria.org>.
- [57] J. F. Johanson, A. Sonnenberg, and T. R. Koch. Clinical epidemiology of chronic constipation. *J Clin Gastroenterol*, 11(5):525–536, Oct 1989.
- [58] A. Ganeshan, E. M. Anderson, S. Upponi, A. C. Planner, A. Slater, N. Moore, H. D’Costa, and H. Bungay. Imaging of obstructed defecation. *Clin Radiol*, 63(1):18–26, Jan 2008.

- [59] M. Wyss, J. M. Froehlich, M. A. Patak, C. F. Juli, M. B. Scheidegger, C. L. Zollikofer, and K. U. Wentz. Gradient-enhanced volume rendering: an image processing strategy to facilitate whole small bowel imaging with mri. *Eur Radiol*, 17(4):1081–1088, Apr 2007.
- [60] A. Gutzeit, M. A. Patak, C. von Weymarn, N. Graf, A. Doert, E. Willemse, C. A. Binkert, and J. M. Froehlich. Feasibility of small bowel flow rate measurement with mri. *J Magn Reson Imaging*, 32(2):345–351, Aug 2010.
- [61] L. Marciani, E. F. Cox, C. L. Hoad, S. Pritchard, J. J. Totman, S. Foley, A. Mistry, S. Evans, P. A. Gowland, and R. C. Spiller. Postprandial changes in small bowel water content in healthy subjects and patients with irritable bowel syndrome. *Gastroenterology*, 138(2):469–77, 477.e1, Feb 2010.
- [62] F. Awouters, A. Megens, M. Verlinden, J. Schuurkes, C. Niemegeers, and P. A. Janssen. Loperamide. survey of studies on mechanism of its antidiarrheal activity. *Dig Dis Sci*, 38(6):977–995, Jun 1993.
- [63] M. A. Kaplan, M. J. Prior, R. R. Ash, K. I. McKonly, E. C. Helzner, and E. B. Nelson. Loperamide-simethicone vs loperamide alone, simethicone alone, and placebo in the treatment of acute diarrhea with gas-related abdominal discomfort. a randomized controlled trial. *Arch Fam Med*, 8(3):243–248, 1999.
- [64] L. R. Schiller, C. A. Santa Ana, S. G. Morawski, and J. S. Fordtran. Mechanism of the antidiarrheal effect of loperamide. *Gastroenterology*, 86(6):1475–1480, Jun 1984.
- [65] B. K. Sandhu, J. H. Tripp, D. C. Candy, and J. T. Harries. Loperamide: studies on its mechanism of action. *Gut*, 22(8):658–662, Aug 1981.

- [66] B. K. Sandhu, P. J. Milla, and J. T. Harries. Mechanisms of action of loperamide. *Scand J Gastroenterol Suppl*, 84:85–92, 1983.
- [67] A. Szilagyi, R. Salomon, and E. Seidman. Influence of loperamide on lactose handling and oral-caecal transit time. *Aliment Pharmacol Ther*, 10(5):765–770, Oct 1996.
- [68] V. Thodorou, J. Fioramonti, T. Hachet, and L. Buno. Absorptive and motor components of the antidiarrhoeal action of loperamide: an in vivo study in pigs. *Gut*, 32(11):1355–1359, Nov 1991.
- [69] G. Kachel, H. Ruppin, J. Hagel, W. Barina, M. Meinhardt, and W. Domschke. Human intestinal motor activity and transport: effects of a synthetic opiate. *Gastroenterology*, 90(1):85–93, Jan 1986.
- [70] A. L. Connor, H. Wray, J. Cottrell, and I. R. Wilding. A scintigraphic study to investigate the potential for altered gut distribution of loperamide from a loperamide-simethicone formulation in man. *Eur J Pharm Sci*, 13(4):369–374, Jul 2001.
- [71] G. Basilisco, G. Camboni, A. Bozzani, M. Paravicini, and P. A. Bianchi. Oral naloxone antagonizes loperamide-induced delay of orocecal transit. *Dig Dis Sci*, 32(8):829–832, Aug 1987.
- [72] P. A. Cann, N. W. Read, C. D. Holdsworth, and D. Barends. Role of loperamide and placebo in management of irritable bowel syndrome (ibs). *Dig Dis Sci*, 29(3):239–247, Mar 1984.
- [73] E. K. Yeoh, M. Horowitz, A. Russo, T. Muecke, T. Robb, and B. E. Chatterton. Gastrointestinal function in chronic radiation enteritis—effects of loperamide-n-oxide. *Gut*, 34(4):476–482, Apr 1993.

- [74] A. F. Hertz, C. J. Morton, F. Cook, A. N. Cox, H. Gardiner, E. G. Schlesinger, and A. H. Todd. The passage of food along the human alimentary canal. *Guy's Hospital Reports*, 61:389–427, 1907.
- [75] C. Compher, S. Rubesin, B. Kinosian, J. Madaras, and D. Metz. Non-invasive measurement of transit time in short bowel syndrome. *JPEN J Parenter Enteral Nutr*, 31(3):240–245, 2007.
- [76] J. M. Hinton, J. E. Lennord-Jones, and A. C. Young. A new method for studying gut transit times using radioopaque markers. *Gut*, 10:842–847, 1969.
- [77] R. H. Higgs, R. B. Ellis-Pegler, and H. P. Lambert. Assessment of simple methods of measuring intestinal transit times in children with gastroenteritis. *Gut*, 16(6):458–461, Jun 1975.
- [78] H. C. Lin, C. Prather, R. S. Fisher, J. H. Meyer, R. W. Summers, M. Pimentel, R. W. McCallum, L. M. Akkermans, V. Loening-Baucke, and A. M. S. Task Force Committee on Gastrointestinal Transit. Measurement of gastrointestinal transit. *Dig Dis Sci*, 50(6):989–1004, Jun 2005.
- [79] R.C. Spiller. Colonic manometry. *Wrightson Biomedical Publishing Ltd.*, pages 191–202, 1989.
- [80] J. H. Cummings and H. S. Wiggins. Transit through the gut measured by analysis of a single stool. *Gut*, 17(3):219–223, Mar 1976.
- [81] S. C. Rao, B. Kuo, R. W. McCallum, W. D. Chey, J. K. Dibaïse, W. L. Hasler, K. L. Koch, J. M. Lackner, C. Miller, R. Saad, J. R. Semler, M. D. Sitrin, G. E. Wilding, and H. P. Parkman. Investigation of colonic and whole gut transit with wireless motility capsule and radioopaque markers in constipation. *Clin Gastroenterol Hepatol*, Feb 2009.

- [82] T. Hahn, S. Kozerke, W. Schwizer, M. Fried, P. Boesiger, and A. Stein-  
goetter. Visualization and quantification of intestinal transit and motor  
function by real-time tracking of (19) f labeled capsules in humans. *Magn  
Reson Med*, Mar 2011.
- [83] E. Placidi, R. C. Spiller, and P. A. Gowland. Characterising a  
coil/sample system for monitoring gi transit using fluorine markers. In  
*ISMRM 2010*, 2010.
- [84] E. Placidi, C. L. Hoad, L. Marciani, A. C. Perkins, P. E. Blackshaw,  
R. C. Spiller, and P. A. Gowland. In vivo gastrointestinal transit study  
using double-labelled markers. In *ISMRM 2011*, 2011.
- [85] P. Bachert. Pharmacokinetics using fluorine nmr in vivo. *Progress in  
Nuclear Magnetic Resonance Spectroscopy*, 33:1–56, 1998.
- [86] H. K. Lee and O. Nalcioglu. Reduced-bandwidth method for f–19 imag-  
ing of perflubron. *J Magn Reson Imaging*, 2(5):563–568, 1992.
- [87] M. P. Krafft. Fluorocarbons and fluorinated amphiphiles in drug delivery  
and biomedical research. *Adv Drug Deliv Rev*, 47(2–3):209–228, Apr  
2001.
- [88] J. Ruiz-Cabello, B. P. Barnett, P. A Bottomley, and J. W. M. Bulte.  
Fluorine (19)f mrs and mri in biomedicine. *NMR Biomed*, Sep 2010.
- [89] L. C. Clark, J. L. Ackerman, S. R. Thomas, R. W. Millard, R. E. Hoff-  
man, R. G. Pratt, H. Ragle-Cole, R. A. Kinsey, and R. Janakiraman.  
Perfluorinated organic liquids and emulsions as biocompatible nmr imag-  
ing agents for 19f and dissolved oxygen. *Adv Exp Med Biol*, 180:835–845,  
1984.

- [90] L. C. Clark and F. Gollan. Survival of mammals breathing organic liquids equilibrated with oxygen at atmospheric pressure. *Science*, 152(730):1755–1756, Jun 1966.
- [91] J. G. Riess and M. P. Krafft. Fluorinated materials for in vivo oxygen transport (blood substitutes), diagnosis and drug delivery. *Biomaterials*, 19(16):1529–1539, Aug 1998.
- [92] M. P. Krafft, A. Chittofrati, and J. G. Riess. Emulsions and microemulsions with a fluorocarbon phase. *Current Opinion in Colloid and Interface Science*, 8:251–258, 2003.
- [93] M. P. Krafft, J. G. Riess, and J. G. Weers. The design and engineering of oxygen-delivering fluorocarbon emulsions. *Submicronic Emulsions in Drug Targeting and Delivery*, Harwood Academic Publishers, Amsterdam:235–333, 1998.
- [94] N. R. Bolo, Y. Hod, and J-P. Macher. Long-term sequestration of fluorinated compounds in tissues after fluvoxamine or fluoxetine treatment: a fluorine magnetic resonance spectroscopy study in vivo. *MAGMA*, 16(6):268–276, May 2004.
- [95] K. L. Meyer, M. J. Carvlin, B. Mukherji, H. A. Sloviter, and P. M. Joseph. Fluorinated blood substitute retention in the rat measured by fluorine-19 magnetic resonance imaging. *Invest Radiol*, 27(8):620–627, Aug 1992.
- [96] K. C. Lowe. Fluorinated blood substitutes and oxygen carriers. *Journal of Fluorine Chemistry*, 109:59–65, 2001.
- [97] R. F. Mattrey, P. C. Hajek, V. M. Gylys-Morin, L. L. Baker, J. Martin, D. C. Long, and D. M. Long. Perfluorochemicals as gastrointestinal contrast agents for mr imaging: preliminary studies in rats and humans. *AJR Am J Roentgenol*, 148(6):1259–1263, Jun 1987.

- [98] C. M. Anderson, J. J. Brown, D. M. Balfe, J. P. Heiken, J. A. Borrello, R. E. Clouse, and T. K. Pilgram. Mr imaging of crohn disease: use of perflubron as a gastrointestinal contrast agent. *J Magn Reson Imaging*, 4(3):491–496, 1994.
- [99] G. S. Bisset, K. H. Emery, M. P. Meza, N. K. Rollins, S. Don, and J. S. Shorr. Perflubron as a gastrointestinal mr imaging contrast agent in the pediatric population. *Pediatr Radiol*, 26(6):409–415, 1996.
- [100] R. F. Mattrey, M. A. Trambert, J. J. Brown, S. W. Young, J. N. Bruneton, G. E. Wesbey, and Z. N. Balsara. Perflubron as an oral contrast agent for mr imaging: results of a phase iii clinical trial. *Radiology*, 191(3):841–848, Jun 1994.
- [101] E. Pisani, N. Tsapis, J. Paris, V. Nicolas, L. Cattel, and E. Fattal. Polymeric nano/microcapsules of liquid perfluorocarbons for ultrasonic imaging: physical characterization. *Langmuir*, 22(9):4397–4402, Apr 2006.
- [102] J. Wolber, I. J. Rowland, M. O. Leach, and A. Bifone. Perfluorocarbon emulsions as intravenous delivery media for hyperpolarized xenon. *Magn Reson Med*, 41(3):442–449, Mar 1999.
- [103] C. H. Sotak, P. S. Hees, H. N. Huang, M. H. Hung, C. G. Krespan, and S. Raynolds. A new perfluorocarbon for use in fluorine-19 magnetic resonance imaging and spectroscopy. *Magn Reson Med*, 29(2):188–195, Feb 1993.
- [104] A. S. K. Dzik-Jurasz, M. O. Leach, and I. J. Rowland. Investigation of microenvironmental factors influencing the longitudinal relaxation times of drugs and other compounds. *Magn Reson Imaging*, 22(7):973–982, Sep 2004.

- [105] R. Schwarz, A. Kaspar, J. Seelig, and B. Knecke. Gastrointestinal transit times in mice and humans measured with  $^{27}\text{Al}$  and  $^{19}\text{F}$  nuclear magnetic resonance. *Magn Reson Med*, 48(2):255–261, Aug 2002.
- [106] R. Schwarz, M. Schuurmans, J. Seelig, and B. Knecke.  $^{19}\text{F}$ -mri of perfluorononane as a novel contrast modality for gastrointestinal imaging. *Magn Reson Med*, 41(1):80–86, Jan 1999.
- [107] R. P. Mason, W. Rodbumrung, and P. P. Antich. Hexafluorobenzene: a sensitive  $^{19}\text{F}$  nmr indicator of tumor oxygenation. *NMR Biomed*, 9(3):125–134, May 1996.
- [108] P. Parhami and P. M. Fung. Fluorine- $^{19}$  relaxation study of perfluorochemicals as oxygen carriers. *J Phys Chem*, 87:1928–1931, 1983.
- [109] V. Christmann, J. Rosenberg, J. Seega, and C. M. Lehr. Simultaneous in vivo visualization and localization of solid oral dosage forms in the rat gastrointestinal tract by magnetic resonance imaging (mri). *Pharm Res*, 14(8):1066–1072, Aug 1997.
- [110] E. T. Ahrens, R. F., H. Xu, and P. A Morel. In vivo imaging platform for tracking immunotherapeutic cells. *Nat Biotechnol*, 23(8):983–987, Aug 2005.
- [111] U. Nth, L. M. Rodrigues, S. P. Robinson, A. Jork, U. Zimmermann, B. Newell, and J. R. Griffiths. In vivo determination of tumor oxygenation during growth and in response to carbogen breathing using  $^{15}\text{C}_5$ -loaded alginate capsules as fluorine- $^{19}$  magnetic resonance imaging oxygen sensors. *Int J Radiat Oncol Biol Phys*, 60(3):909–919, Nov 2004.
- [112] A. N. Stevens, P. G. Morris, R. A. Iles, P. W. Sheldon, and J. R. Griffiths. 5-fluorouracil metabolism monitored in vivo by  $^{19}\text{F}$  nmr. *Br J Cancer*, 50(1):113–117, Jul 1984.

- [113] A. S. Dzik-Jurasz, D. J. Collins, M. O. Leach, and I. J. Rowland. Gallbladder localization of  $(19)\text{f}$  mrs catabolite signals in patients receiving bolus and protracted venous infusional 5-fluorouracil. *Magn Reson Med*, 44(4):516–520, Oct 2000.
- [114] D. J. O. McIntyre, F. A. Howe, C. Ladroue, F. Lofts, M. Stubbs, and J. R. Griffiths. Can localised  $(19)\text{f}$  magnetic resonance spectroscopy pharmacokinetics of 5fu in colorectal metastases predict clinical response? *Cancer Chemother Pharmacol*, Sep 2010.
- [115] S. Laukemper-Ostendorf, A. Scholz, K. Brger, C. P. Heussel, M. Schmittner, N. Weiler, K. Markstaller, B. Eberle, H. U. Kauczor, M. Quintel, M. Thelen, and W. G. Schreiber.  $19\text{f}$ -mri of perflubron for measurement of oxygen partial pressure in porcine lungs during partial liquid ventilation. *Magn Reson Med*, 47(1):82–89, Jan 2002.
- [116] Msds perfluorotributylamine. *Acros Organics*.
- [117] H. P. Shukla, R. P. Mason, D. E. Woessner, and P. P. Antich. A comparison of three commercial perfluorocarbon emulsions as high-field  $19\text{f}$  nmr probes of oxygen tension and temperature. *Journal of Magnetic Resonance*, 106:131–141, 1995.
- [118] B. Kuo, R. W. McCallum, K. L. Koch, M. D. Sitrin, J. M. Wo, W. D. Chey, W. L. Hasler, J. M. Lackner, L. A. Katz, J. R. Semler, G. E. Wilding, and H. P. Parkman. Comparison of gastric emptying of a nondigestible capsule to a radio-labelled meal in healthy and gastroparetic subjects. *Aliment Pharmacol Ther*, 27(2):186–196, Jan 2008.
- [119] S. Maqbool, H. P. Parkman, and F. K. Friedenberg. Wireless capsule motility: comparison of the smartpill gi monitoring system with scintigraphy for measuring whole gut transit. *Dig Dis Sci*, 54(10):2167–2174, Oct 2009.

- [120] H. P. Parkman. Assessment of gastric emptying and small-bowel motility: scintigraphy, breath tests, manometry, and smartpill. *Gastrointest Endosc Clin N Am*, 19(1):49–55, vi, Jan 2009.
- [121] C. Lohrmann, E. Foeldi, J-P. Bartholomae, and M. Langer. Gadoteridol for mr imaging of lymphatic vessels in lymphoedematous patients: initial experience after intracutaneous injection. *Br J Radiol*, 80(955):569–573, Jul 2007.
- [122] V. M. Runge, W. G. Bradley, M. N. Brant-Zawadzki, M. J. Carvlin, D. N. DeSimone, B. L. Dean, W. P. Dillon, B. P. Drayer, A. E. Flanders, and S. E. Harms. Clinical safety and efficacy of gadoteridol: a study in 411 patients with suspected intracranial and spinal disease. *Radiology*, 181(3):701–709, Dec 1991.
- [123] W. S. Ball, S. N. Nadel, R. A. Zimmerman, S. E. Byrd, R. B. Dietrich, E. C. Prenger, B. P. Drayer, M. D. Nelson, F. W. Morgan, and N. R. Altman. Phase iii multicenter clinical investigation to determine the safety and efficacy of gadoteridol in children suspected of having neurologic disease. *Radiology*, 186(3):769–774, Mar 1993.
- [124] J. C. Bousquet, S. Saini, D. D. Stark, P. F. Hahn, M. Nigam, J. Wittenberg, and J. T. Ferrucci. Gd-dota: characterization of a new paramagnetic complex. *Radiology*, 166(3):693–698, Mar 1988.
- [125] M. Allard, D. Doucet, P. Kien, B. Bonnemain, and J. M. Caill. Experimental study of dota-gadolinium. pharmacokinetics and pharmacologic properties. *Invest Radiol*, 23 Suppl 1:S271–S274, Sep 1988.
- [126] V. M. Korshunov, L. V. Potashnik, O. V. Korshunova, V. V. Smeianov, B. A. Efimov, K. Gyr, R. Frei, and H. Reber. [effect of the lavage of the digestive tract on microflora in patients with polyps in the large intestine]. *Zh Mikrobiol Epidemiol Immunobiol*, (3):76–80, 2001.

- [127] J. Belsey, O. Epstein, and D. Heresbach. Systematic review: oral bowel preparation for colonoscopy. *Aliment Pharmacol Ther*, 25(4):373–384, Feb 2007.
- [128] A. M. Metcalf, S. F. Phillips, A. R. Zinsmeister, R. L. MacCarty, R. W. Beart, and B. G. Wolff. Simplified assessment of segmental colonic transit. *Gastroenterology*, 92(1):40–47, Jan 1987.
- [129] Y. S. Nam, A. J. Pikarsky, S. D. Wexner, J. J. Singh, E. G. Weiss, J. J. Noguerras, J. S. Choi, and Y. H. Hwang. Reproducibility of colonic transit study in patients with chronic constipation. *Dis Colon Rectum*, 44(1):86–92, Jan 2001.
- [130] M. Camilleri and A. R. Zinsmeister. Towards a relatively inexpensive, noninvasive, accurate test for colonic motility disorders. *Gastroenterology*, 103(1):36–42, Jul 1992.
- [131] J. M. Hebden, P. J. Gilchrist, E. Blackshaw, M. E. Frier, A. C. Perkins, C. G. Wilson, and R. C. Spiller. Night-time quiescence and morning activation in the human colon: effect on transit of dispersed and large single unit formulations. *Eur J Gastroenterol Hepatol*, 11(12):1379–1385, Dec 1999.